

APPENDIX G

FLUID MASS CLOSURE

Closure of the fluid mass-conservation equations involves the net vapor (or liquid) generation between the phases. This mass transfer includes the following considerations: (1) the subcooled-boiling model, (2) the interfacial heat-transfer models, and (3) the effect of noncondensables. The effect of noncondensables might be divided further into two parts: (1) Dalton's law applied to the two-component mixture of steam and noncondensable gas and (2) the influence of noncondensables upon the condensation and evaporation of water.

Section 2.1. discussed the field equations and identified the mass-transfer terms present in the two-fluid formulation. Appendix F, Section F.1. further defined in detail how the mass transfer is determined as it results from the interfacial heat transfer. This appendix will further consider the mass transfer present in two-fluid formulation by investigating those portions of the models used in the mass-conservation equation.

To begin this section, it is instructive to note the code input variables that control the inclusion of a noncondensable. There are two input variables, IEOS and NOAIR, that affect how noncondensables are included within the equation set by the code. There are also two input variables, IGAS and IH2SRC, that specify which noncondensable is present. IEOS is the main data card number 2. NOAIR, IGAS, and IH2SRC are NAMELIST variables.

IEOS was the first attempt within the code to allow for noncondensables and represented an on/off switch to allow for purely noncondensable/liquid-water mixtures by setting IEOS = 1, i.e., no steam vapor present. The setting of this switch turns off the interfacial mass transfer caused by evaporation and condensation.

NOAIR is an option that was added to improve the calculational efficiency by specifying that the noncondensables will be present during the calculation so that additional equations may be eliminated. Setting NOAIR = 1 results in the partial pressure of noncondensables being set to zero and only the two-fluid equation set for steam water being considered. Setting NOAIR = 0 results in the solution of a system of equations, which includes a nonzero partial pressure of the noncondensable.

The NAMELIST variable IGAS specifies which noncondensable is present. If IGAS = 1, the noncondensable is air. If IGAS = 2, the noncondensable is hydrogen. Finally, if IGAS = 3, the noncondensable is helium. IGAS = 1 is the default value. An additional NAMELIST variable IH2SRC allows a hydrogen source to be present. If the hydrogen source flag is on (that is, IH2SRC is nonzero), NOAIR is reset to zero, and IGAS is reset to 2. The basis for the models used for closure of the fluid mass-conservation equations involves the net vapor (or liquid) generation arising between the phases. The introduction of Appendix F, Section F.1. discussed the vapor generation rate per unit volume. The final expression for total vapor generation rate per unit volume is given by

$$\Gamma = \Gamma_i + \Gamma_{\text{sub}} \quad , \quad (\text{G-1})$$

where Γ_i and Γ_{sub} are the vapor generation rates per unit cell volume resulting from interfacial heat transfer and subcooled boiling, respectively. The following nomenclature is used within Appendix G.

NOMENCLATURE

A :	area
B_{cell} :	cell volume
$C_{p,l}$:	liquid specific heat
D_H :	hydraulic diameter
F_e :	evaporation fraction
G :	mass flux
h :	specific enthalpy
h_{ig} :	gas-to-interface heat-transfer correlation
h_{il} :	liquid-to-interface heat-transfer correlation
h_{ld} :	liquid specific enthalpy at the point of bubble departure
$h_{l,\text{sat}}$:	saturated liquid specific enthalpy
h_{Γ} :	subcooled-boiling heat-transfer coefficient
H_{ALV} :	liquid-side heat-transfer factor during flashing
H_{ALVE} :	liquid-side heat-transfer factor during evaporation and condensation
H_{CHT} :	vapor-side heat-transfer factor
k :	thermal conductivity
m :	mass
N :	number of moles
P :	total pressure (Pa)
q :	heat-transfer rate
q_{ig} :	gas-to-interface heat-transfer rate
q_{il} :	liquid-to-interface heat-transfer rate
q_{sub} :	subcooled-boiling heat-transfer rate
q_{wl} :	wall-to-liquid heat-transfer rate
R :	universal gas constant
T :	temperature
T_{ld} :	liquid temperature at the point of bubble detachment
T_{sv} :	saturation temperature corresponding to steam partial pressure
v :	specific volume
v'_r :	pseudo-reduced specific volume

V :	volume
W_{sb} :	subcooled-boiling weighting factor
y_i :	mole fraction of component i
Z :	compressibility factor
α :	void fraction
Γ :	total phase change rate per unit volume

Subscripts

c :	critical
g :	gas phase
i :	interfacial
l :	liquid phase
r :	reduced
s :	steam
sat:	saturation
sub, sb :	subcooled boiling
w :	wall

Dimensionless Groups

Nu :	Nusselt number
Nu^* :	modified Nusselt number
Pe :	Peclet number
St :	Stanton number

G.1. Subcooled-Boiling Model

To properly predict the void fraction in heated cells near the saturation point, the effect of subcooled boiling must be accounted for. Normally one thinks that boiling will start when the local liquid temperature exceeds the local saturation temperature. In a computer simulation code such as TRAC, however, microscopic local temperatures are not available. Instead, the liquid temperature over a region as defined by a computational cell are in effect averaged to yield a liquid temperature that represents the conditions in that cell. In reality, the true liquid temperature near the hot wall will be greater than the cell-averaged liquid temperature, and could be greater than the saturation temperature. If this were the case, vapor could be formed at the wall even though the cell-averaged liquid temperature is subcooled. This is referred to as subcooled boiling. The vapor generation resulting from subcooled boiling is formulated as

$$\Gamma_{\text{sub}} = \frac{q_{\text{sub}}}{B_{\text{cell}}(h_g - h_l)} \quad (G-2)$$

where

$$q_{\text{sub}} = h_r A_w (T_w - T_l) \quad (G-3)$$

In previous TRAC-PF1/MOD1 versions (Ref. G-1.), subcooled boiling was accounted for only in cells containing ROD or SLAB components. It was done by adjusting the evaporation rate when both the wall temperature was greater than the saturation temperature, and the convective heat-transfer coefficient was higher than that predicted by the Dittus-Boelter equation. For TRAC-PF1/MOD2 (and TRAC-M), we use a different approach that applies to all cells containing heat structures.

G.1.1. Basis for the Correlation

The approach suggested by the Saha-Zuber correlation (Ref. G-2.) is used in TRAC-PF1/MOD2 (and TRAC-M). In Ref. G-2., Saha and Zuber pointed out that subcooled boiling occurs in two regimes—thermally controlled and hydrodynamically controlled. At low mass fluxes, it has been found that the point of net vapor generation is dependent only on local thermal conditions, which determine the rates of vapor condensation and evaporation at the wall. To make an estimate of these two rates it was assumed that the rate of evaporation at the wall will be proportional to heat flux, whereas the rate of condensation will be proportional to the local subcooling. Thus, the similarity parameter was taken to be the local Nusselt number

$$Nu = \frac{q_{wl} D_H}{k_l (T_{\text{sat}} - T_l)} \quad (G-4)$$

For the high mass fluxes, the phenomenon is hydrodynamically controlled, and the appropriate similarity parameter is the local Stanton number defined as

$$St = \frac{q_{wl}}{G C_{\rho,l} (T_{\text{sat}} - T_l)} \quad (G-5)$$

The Peclet number, which by definition is the ratio of the Nusselt number and the Stanton number,

$$Pe = \frac{Nu}{St} = \frac{G D_H C_{\rho,l}}{k_l} \quad (G-6)$$

was selected to be the correlation-independent parameter with the Stanton number as the dependent parameter. Data from 10 different sources were plotted as shown in the Fig. G-1.

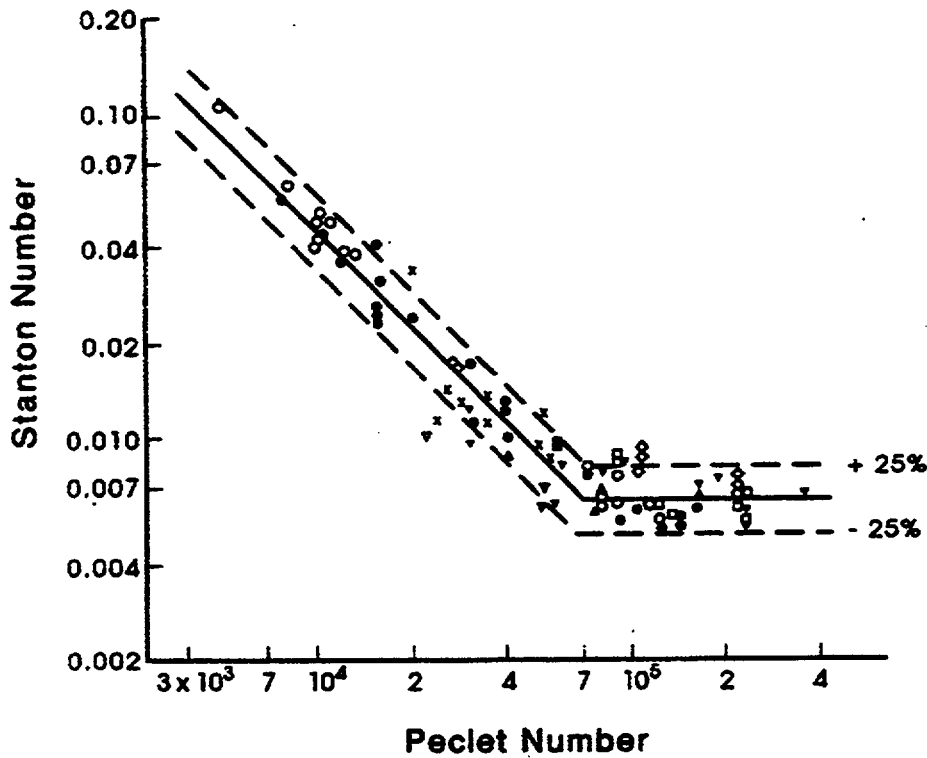


Fig. G-1. Original database of Saha-Zuber correlation.

The two distinct regions can easily be identified. Up to a Peclet number of 70000, the data fall in a straight line having the slope of minus one, which implies a constant value for the local Nusselt number. This is the thermally controlled region. Beyond a Peclet number of 70000, the data fall on a constant Stanton number, which is referred to as the hydrodynamically controlled region. The entire correlation for the point of net vapor generation is expressed as

$$Nu = 455, \text{ if } Pe \leq 70000$$

and

$$St = 0.0065, \text{ if } Pe > 70000.$$

This correlation is interpreted by the authors as follows. In the thermally controlled region, the bubbles stay attached to the walls until a characteristic roughness parameter is reached, at which point they detach from the surface (as soon as the local Stanton number becomes 0.0065). Since the local subcooling is still high, the bubbles are forced to stay near the heated wall and flow downstream until the local Nusselt number becomes 455. At this point, the local subcooling is low enough to initiate a rapid increase in void fraction. For the hydrodynamically controlled region, the Stanton number reaches the

value of 0.0065 at a point where the Nusselt number is already higher than 455. Thus, as soon as the bubbles are detached from the wall they can move to the liquid core without being rapidly condensed. This results in a rapid increase in vapor void fraction at the point of bubble detachment.

Once it has been determined that subcooled boiling is taking place, the energy must be partitioned between the energy going into raising the temperature of the liquid and the energy going into vaporization. The Lahey mechanistic model (Ref. G-3.) is used for this purpose. This model takes the form

$$q_{sub} = q_{wl} \times \left(\frac{h_l - h_{ld}}{h_{l,sat} - h_{ld}} \right) , \quad (G-7)$$

where q_{sub} is the subcooled-boiling heat flux, q_{wl} is the total heat flux, h_l is the liquid specific enthalpy, h_{ld} is the liquid specific enthalpy at the point of bubble departure, and $h_{l,sat}$ is the saturated liquid enthalpy.

Part of the vapor generated near the wall condenses because of contact with subcooled liquid. This effect of subcooled boiling on interfacial condensation is described in Appendix F, Section F.1.1.3.

G.1.2. Database of the Original Correlation

The data shown plotted in Fig. G-1 include data for water, freon-22, and freon-114, and cover a wide range of pressure, mass flow rate, heat flux, and channel geometries in either horizontal or upflow conditions.

G.1.3. Changes to Original Correlation

Developmental-assessment-calculation comparisons were made using preliminary versions of TRAC-PF1/MOD2 against flow-rate and pressure-drop data taken at Columbia University in support of the Savannah River Production Facility (Ref. G-4.). Developmental assessment calculations were also made against the Savannah River Laboratory Subcooling Boiling Tests (Ref. G-5.). The objective of this analysis was to assess the adequacy of TRAC to adequately model the flow instability phenomenon in downflow situations. It was found that early versions of TRAC-PF1/MOD2 tended to predict the onset of the flow instability at too low a mass flux. It was reasoned that the transition between the thermally controlled region and the hydrodynamically controlled region could be altered when the flow went from horizontal to vertical downflow. Using the Savannah River Heat Transfer Laboratory tube test data for downflow geometries, the correlation was altered as follows:

$$Nu = 74.55 \text{ if } Pe \leq 7000$$

and

$$St = 0.01065 \text{ if } Pe > 7000.$$

The value of 0.01065 was determined by performing a weighted fit of the Savannah River Heat Transfer Laboratory downflow tube test data. These values are only used as part of the core reflood model (Section F.1.6.).

G.1.4. Correlation as Coded

For the core reflood model, the subcooled-boiling heat-transfer coefficient is calculated in subroutine HTVSSL using the modified Saha-Zuber correlation described in Section G.1.3. Once it has been determined that subcooled-boiling conditions may exist (the wall temperature is greater than the fluid saturation temperature with the liquid temperature less than saturation temperature), then the liquid heat-transfer coefficient is adjusted for subcooled boiling as follows:

$$h_r = W_{sb} h_{wl} F_e , \quad (G-8)$$

where W_s is the subcooled-boiling weighting factor and is coded as

$$0 \leq 5(0.7 - \alpha) \leq 1 , \quad (G-9)$$

using Fortran min and max functions.

The evaporation fraction, F_e , in Eq. (G-8) is computed from Lahey's mechanistic model as

$$0 \leq F_e = \frac{T_\ell - T_{ld}}{\max[1, (T_{sv} - T_{ld})]} \leq 1 , \quad (G-10)$$

where the liquid temperature at bubble detachment, T_{ld} , is computed from the modified Saha-Zuber model (as described in Section G.1.3.) as follows:

$$T_{ld} = T_{sv} - \frac{Nu^*}{0.01065 \times 7000} \text{ if } Pe \leq 7000,$$

and (G-11)

$$T_{ld} = T_{sv} - \frac{Nu^*}{0.01065 \times Pe} \text{ if } Pe > 7000,$$

where Nu^* is a modified Nusselt number that does not include a $(T_{sat} - T_l)$ term.

For HTSTR components that are not participating in the reflood logic, the subcooled-boiling heat transfer is calculated in subroutine HTCOR. The same equations [Eqs. (G-8) through (G-11)] are used, except that the Stanton number 0.0065 and the Peclet number 70000 are used in Eq. (G-11).

G.1.5. Scaling Considerations on Correlation

The original Saha-Zuber correlation covered a wide range of channel sizes and geometries, including 7-mm-i.d. and 13-mm-o.d. annular geometries through 63-mm channels. The correlation is expected to be independent of scale.

G.1.6. Input and Constants of Correlation

The constants of the Saha-Zuber correlation have been changed for the core reflood model, as described above. The original Saha-Zuber correlation is used in all other cases.

G.1.7. Parametric Range of the Coded Correlation

The original Saha-Zuber correlation covered a wide range of pressures (1.01 to 138 bar) and three different fluids (water, freon-22, and freon-114). The correlation is expected to cover the range of fluid conditions encountered in reactor safety analysis.

G.2. Interfacial Heat-Transfer Models

As discussed in the introduction of Appendix F, Section F.1., the vapor generation resulting from interfacial heat transfer is calculated through

$$\Gamma_i = \frac{q_{ig} + q_{il}}{B_{\text{cell}}(h_g - h_l)}, \quad (\text{G-12})$$

where

$$q_{il} = \underbrace{H_{\text{ALVE}}(T_l - T_{sv})}_{\text{evaporation or condensation}} + \underbrace{H_{\text{ALV}}\langle T_l - T_{\text{sat}} \rangle}_{\text{flashing}}, \quad (\text{G-13})$$

and

$$q_{ig} = \frac{P_s}{P} H_{\text{CHTI}}(T_g - T_{sv}). \quad (\text{G-14})$$

The interfacial heat-transfer factors, H_{ALV} , H_{ALVE} , and H_{CHTI} , are defined as

$$H_{\text{ALV}} = H_{\text{ALVE}} = h_{il}A_i \quad (\text{G-15})$$

and

$$H_{\text{CHTI}} = h_{ig}A_i, \quad (\text{G-16})$$

where the closure relationships for the convective heat-transfer coefficients and interfacial area are described in Appendix F, Section F.1.

Also note that, in TRAC-PF1/MOD1 (Ref. G-1.), evaporation and flashing were treated the same way. In TRAC-PF1/MOD2 and TRAC-M, flashing is superimposed on the energy equation through a singularity function $\langle T_1 - T_{sat} \rangle'$, as shown in Eq. (G-13). As shown in Fig. G-2, evaporation occurs if $T_{sv} < T_l < T_{sat}$ and flashing occurs if $T_l > T_{sat}$. A positive Γ_i indicates vapor generation and a negative Γ_i indicates liquid generation. Notice that, whereas q_{ig} is negative, q_{il} may be positive and vice versa. The net vapor or liquid generation is determined by the relative magnitude of these quantities and is illustrated in Fig. G-3.

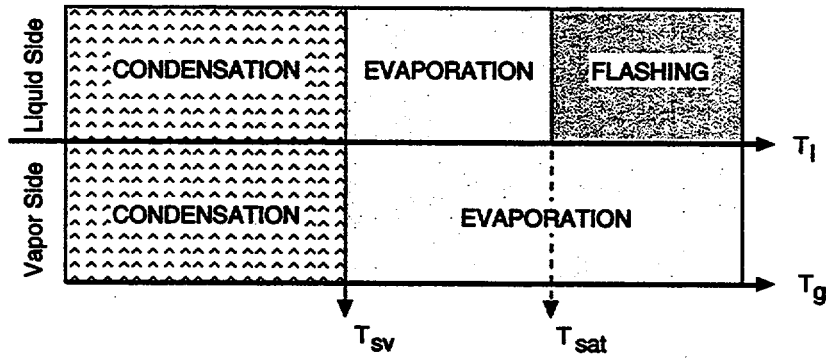


Fig. G-2. Graphical illustration of the selection logic for condensation, evaporation, and flashing.

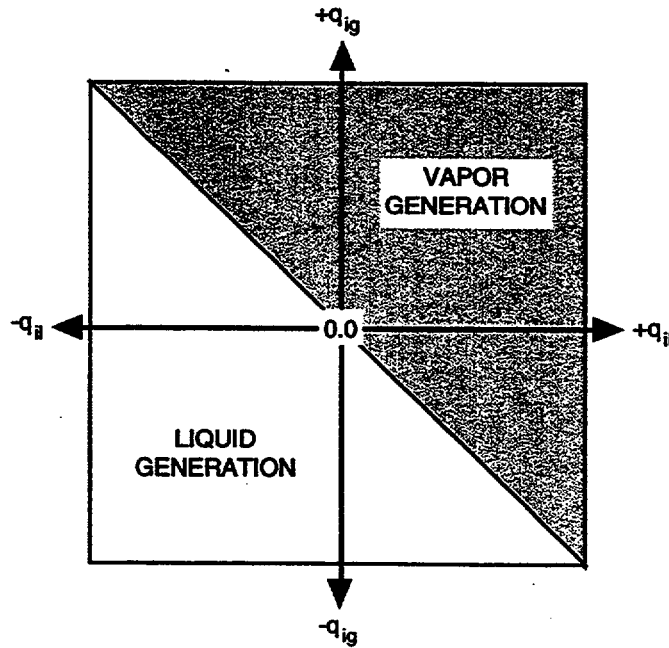


Fig. G-3. Interfacial mass-transfer map.

G.3. The Effect of Noncondensables

The effect of noncondensables will be divided further into two parts. The first includes Dalton's law applied to the mixture of steam and a noncondensable gas. The second includes the influence of the noncondensable upon the condensation or evaporation of water.

G.3.1. Dalton's Law

The partial pressure of a given component in a gas mixture is defined as (Ref. G-6., Eq. 3-20)

$$P_i \equiv y_i \times P , \quad (G-17)$$

where y_i is the mole fraction of component i and P is the total pressure. This choice of the definition of partial pressure makes the sum of partial pressures equal to the total pressure, even if the mixture is not ideal (see Ref. G-6., p. 115). Thus,

$$P = \sum P_i . \quad (G-18)$$

The term *partial pressure*, however, has a physical relevance only for ideal gases (Ref. G-7., p. 428). The "law of partial pressures" is obtained by applying the definition of partial pressure to the ideal gas equation given by

$$P_i V = NRT , \quad (G-19)$$

assuming that the mixture is at uniform temperature and each component occupies the entire volume by itself. The resulting relationship is also known as Dalton's law, which basically states that, "in a mixture, every gas is a vacuum to every other gas" (Ref. G-6., p. 116). This is consistent with the definition of an ideal gas.

The behavior of ideal gases can be explained by making two assumptions: (1) the molecules are so far apart that there are no molecular attractions, and (2) the size of the molecules is so small relative to the volume they occupy that the presence of the molecules can be neglected. When the pressure is increased with the temperature fixed, the molecules are forced closer together so that molecular attractions and molecular size become progressively more important and the gas departs from its ideal gas characteristics. If the temperature is raised with the pressure held constant, two effects result. First, the volume (and hence the distance between the molecules) will increase. Second, there is an increase in the kinetic energy of the molecules, thus helping overcome molecular attractions. Therefore, as the temperature of a gas is increased, it tends to behave more nearly as an ideal gas.

The pressure exerted by an ideal gas occupying a given volume is directly proportional to the product of the number of molecules of the gas and the mean molecular kinetic energy (temperature). This observation leads to the ideal gas law, or equation of state,

given by Eq. (G-19), where P = pressure, V = volume, N = number of moles of gas, T = temperature, and R = a proportionality constant known as the universal gas constant. If a second gas occupies the same volume at the same temperature as the first gas, no intermolecular attractions can exist so that each will exist independently. Gas A will exert the same pressure on the system as it did prior to the introduction of gas B. Likewise, gas B will exert a pressure equal to the pressure it would have had if it existed alone in the system. This observation resulted in Dalton's law of partial pressures for ideal gases, as given by Eq. (G-18).

In general, there is no sharp distinction between a vapor and a noncondensable gas. A noncondensable gas is frequently considered as being far removed from its liquid state, whereas the vapor is thought of as being readily liquefiable. A vapor also may be thought of as an actual gas requiring either a unique P - V - T relationship or the definition of its compressibility factors, where the compressibility factor is defined by

$$Z = \frac{PV}{NRT} \quad (G-20)$$

If $Z = 1$, the vapor can be represented as an ideal gas.

While the properties of steam have been measured over a wide range of the pressures and temperatures, those of many substances have not. If an accurate P - V - T formulation (that is, equation of state) has been found for a substance, it is possible through the Gibbs relationships to determine the changes of other properties such as internal energy, enthalpy, and entropy. For those substances, however, in which a P - V - T formulation is not available and the state conditions have thus most likely not been measured, the concept of corresponding states may be used to obtain an approximate value of the desired properties. Here, the concept of corresponding states will be used to look at the validity of the assumption of ideal gases within the steam/ noncondensable mixtures.

To consider the concept of corresponding states, reduced properties must be defined. A reduced property is the ratio of the property in a given state to the value of the property at the substance's critical state. Using the subscripts r to represent the reduced property and c for the critical property, the reduced pressure, reduced temperature, and reduced specific volume can be written as

$$P_r = P/P_c, \quad (G-21)$$

$$T_r = T/T_c. \quad (G-22)$$

and

$$v_r = v/v_c, \quad (G-23)$$

where $v = V/m$ = specific volume and m is the mass of the gas contained in volume V . Table G-1. gives the critical properties of the fluids currently modeled in TRAC.

TABLE G-1.
Critical Properties of TRAC Fluids

Substance	Critical Pressure (MPa)	Critical Temperature (K)	Critical Volume (cm ³ · g ⁻¹)
Air	3.772	133.0	2.86
Hydrogen	1.298	33.3	33.03
Helium	0.230	5.3	14.45
Water Vapor	22.089	647.3	3.16

When two gases are at the same reduced pressure and reduced temperature, they are said to be at corresponding states. An examination of various properties of various gases shows that gases at the same corresponding states have approximately the same reduced properties in addition to pressure and temperature. Nelson and Obert (Ref. G-8.) applied the concept of corresponding states to the determination of compressibility factors. They found that over an extensive region of temperatures and pressures, the compressibility factors for various substances did not deviate by more than a small percentage. They used a pseudo-reduced specific volume defined as

$$v'_r = Z T_r / P_r \quad (G-24)$$

so that

$$v'_r = f'(P_r / T_r) . \quad (G-25)$$

Figures G-4. and G-5. give the compressibility factor as a function of these reduced properties. From Fig. G-4., it can be seen that at very low pressures a so-called vapor may be treated as an ideal gas for most engineering purposes. On the other hand, from Fig. G-5., when a vapor exists at very high pressures it deviates from an ideal gas, even when its temperature is much higher than the boiling point.

Using the critical properties of substances of interest to TRAC given in Table G-1. and Figs. G-4. and G-5., we can determine how near to an ideal gas the vapors of interest are for some potential PWR pressure conditions. Table G-2. shows typical results for air and water vapor. In Table G-2., the air temperature is taken as that corresponding to saturated steam. The plus sign indicates that the volume is approximate. We can see that air can reasonably be approximated by an ideal gas. One potential region for this ideal gas approximation to become invalid for the noncondensables is at pressures above operational pressures for a PWR, 17.0 MPa, when a mixture has significant superheating. For this case, the error will increase above 10%. On the other hand, water vapor cannot be accurately approximated as an ideal gas once the pressure exceeds 1.0 MPa unless there is excessive superheating. Below 1.0 MPa, the ideal gas assumption for steam is acceptable.

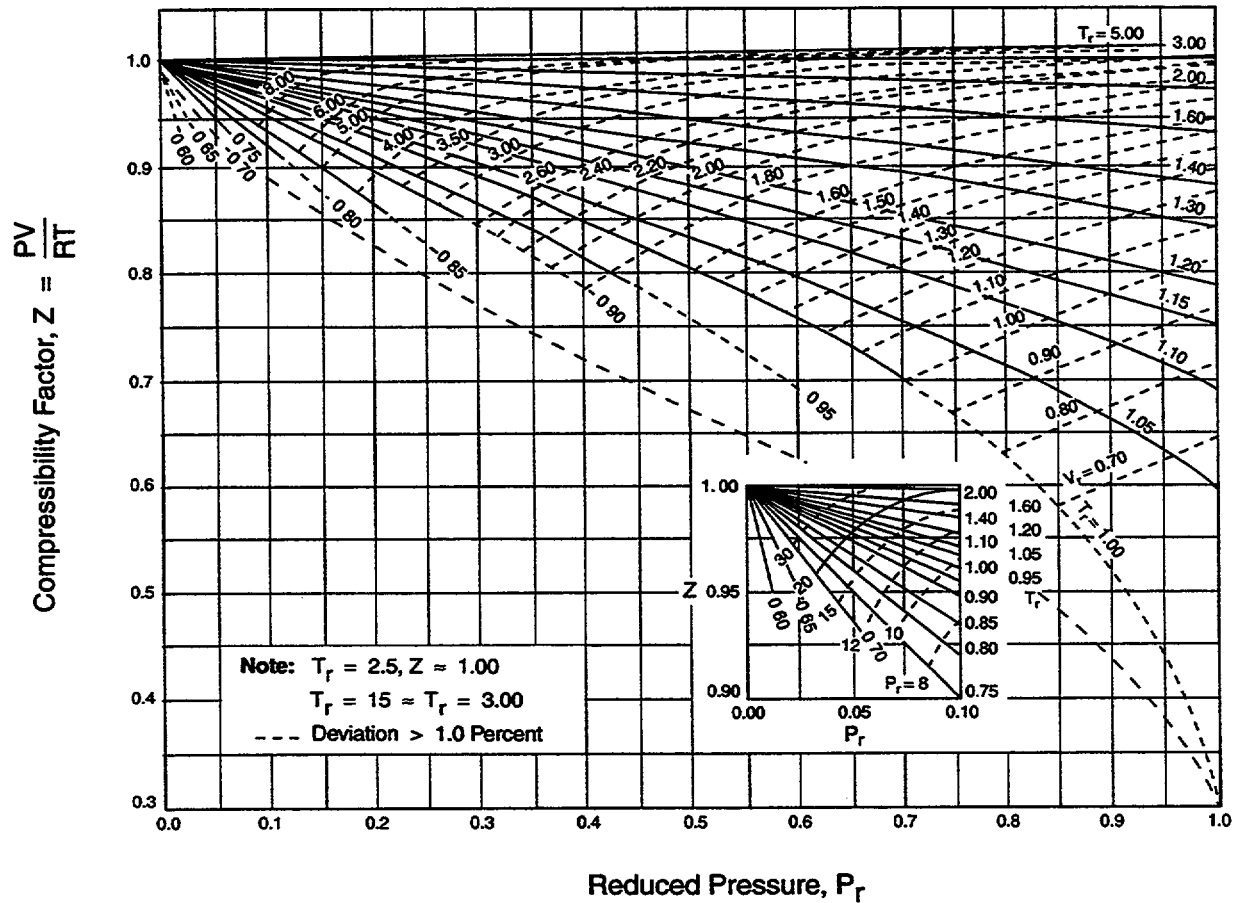


Fig. G-4. Compressibility factors for reduced pressures 0 to 1.0. (Reprinted from Ref. G-8. with permission.)

Using the critical properties of substances of interest to TRAC given in Table G-1. and Figs. G-4. and G-5., we can determine how near to an ideal gas the vapors of interest are for some potential PWR pressure conditions. Table G-2. shows typical results for air and water vapor. In Table G-2., the air temperature is taken as that corresponding to saturated steam. The plus sign indicates that the volume is approximate. We can see that air can reasonably be approximated by an ideal gas. One potential region for this ideal gas approximation to become invalid for the noncondensables is at pressures above operational pressures for a PWR, 17.0 MPa, when a mixture has significant superheating. For this case, the error will increase above 10%. On the other hand, water vapor cannot be accurately approximated as an ideal gas once the pressure exceeds 1.0 MPa unless there is excessive superheating. Below 1.0 MPa, the ideal gas assumption for steam is acceptable.

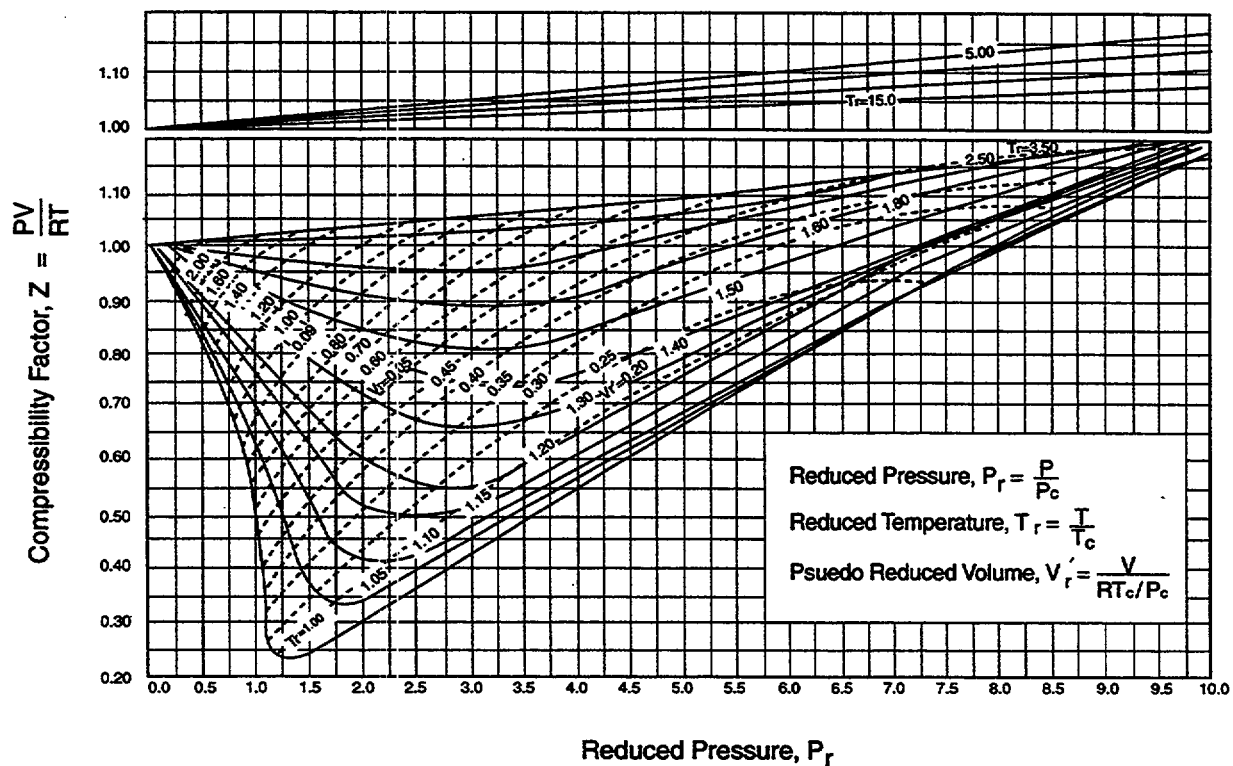


Fig. G-5. Compressibility factors for reduced pressures 0 to 10.0.
(Reprinted from Ref. G-8. with permission.)

From Fig. G-5, we can further observe that the worst case for a vapor is in the vicinity of its critical point. Assuming the pressure corresponds to the critical points of air and hydrogen and the temperature is that corresponding to saturation for steam, we can determine the nature of the two noncondensables at these states. This is shown in Table G-3. Because of the high reduced temperatures that result for both air and hydrogen, they can easily be approximated as ideal gases.

Thus, we have shown that the noncondensables can be treated typically as ideal gases, but that in general, the steam is a nonideal gas. The exception to this nonideal behavior occurs when steam is at lower pressures, i.e., less than 1 MPa. To apply Dalton's law, we must assume that the mixture of one nonideal gas with ideal gases still allows the use of Dalton's law provided the proper equation of state is used for the actual vapor. Such is the case in TRAC.

G.3.2. Influence of Noncondensables Upon Evaporation and Condensation

The noncondensables influence the phase change by lowering the saturation temperature, and thus, the interface temperature. On the vapor side, no special models are used to account for the presence of the noncondensables. As given by Eq. (G-14), however, the vapor side interfacial heat-transfer factor is reduced by P_s/P . On the liquid

side, the existence of noncondensables triggers model changes. During evaporation, a simple diffusion-controlled model is used to calculate H_{ALVE} , as discussed in Appendix F, Section F.1.7.1.1.

TABLE G-2.
Typical Compressibility Factors of Air and Water

(Sat. Temp.)	Pressure (MPa)		Air	Water
(373 K)	0.1	P_r	0.026	0.005
		T_r	2.8	0.58
		Z	1.00+	0.98
(453 K)	1.0	P_r	0.27	0.045
		T_r	3.4	0.70
		Z	1.00+	0.93
(559 K)	7.0	P_r	1.86	0.31
		T_r	4.2	0.86
		Z	1.02+	0.78
(625 K)	17.0	P_r	4.5	0.77
		T_r	4.7	0.97
		Z	1.07	0.64
(647.3 K)	22.089	P_r	5.9	1.0
		T_r	4.9	1.0
		Z	1.09	0.3

TABLE G-3.
Compressibility Factors of Air and Hydrogen at $P_r = 1.0$

	Air	Hydrogen
Pressure (MPa)	3.772	1.298
Sat. Temp. (K)	520.0	464.7
Reference Temp.	3.9	13.95
Compressibility	1.01+	1.00+

During condensation, H_{CHT} is modified via the empirical correlation developed by Sklover and Rodivilin (Ref. G-9.). This correlation is further discussed in Appendix F, Section F.1.7.1.2.

G.4. Summary and Conclusions

Considerable improvements over TRAC-PF1/MOD1 have been made in terms of mass closure models. In subcooled boiling, the mechanistic model of Lahey (Ref. G-3.) is coupled with a model similar to the one suggested by Saha and Zuber (Ref. G-2.). The effect of noncondensables is made consistent between one- and three-dimensional components. Evaporation and flashing are accounted for using separate models. Evaporation is modeled as being diffusion controlled.

REFERENCES

- G-1. Safety Code Development Group, "TRAC-PF1/MOD1 Correlations and Models," Los Alamos National Laboratory document LA-11208-MS (NUREG/CR-5069) (December 1988).
- G-2. P. Saha and N. Zuber, "Point of Net Vapor Generation and Vapor Void Fraction in Subcooled Boiling," *Proc. 5th Int. Heat Transfer Conf.* (Tokyo, Japan, 1974), Paper B4.7.
- G-3. R. T. Lahey, "A Mechanistic Subcooled Boiling Model," *Proc. 6th Int. Heat Transfer Conf.* (Toronto, Canada, 1978), Vol. 1, pp. 293-297.
- G-4. D. M. Lee, "Additional Pressure-Drop-Flow Curves for Simulated Mark VII-AL Fuel Assembly," Supplement to Technical Note TN-XIV-1-63, Savannah River Laboratory report DFW2-883-XIV-3-63 (April 1963).
- G-5. B. S. Johnston, "Subcooled Boiling of Downward Flow in a Vertical Annulus," ASME Proc. 1989 National Heat Transfer Conf. (Philadelphia, 1989), *Multiphase Flow Heat and Mass Transfer*, HTD. Vol. 109, pp. 149-156.
- G-6. K. Denbigh, *The Principles of Chemical Equilibrium*, 3rd ed. (Cambridge University Press, Boston, 1971).
- G-7. G. J. Van Wylen and R. E. Sonntag, *Fundamentals of Classical Thermodynamics*, SI version, 2nd ed. (John Wiley & Sons, Inc. New York, 1976).
- G-8. L. C. Nelson and E. F. Obert, "Generalized P-V-T Properties of Gases," *Trans. ASME*, pp. 1057-1066 (1954).
- G-9. G. G. Sklover and M. D. Rodivilin, "Condensation of Water Jets with a Cross Flow of Steam," *Teploenergetika* 23, 48-51 (1976).

APPENDIX H

FLUID MOMENTUM CLOSURE

The TRAC field equations include the phasic momentum equations as described in Section 2.1. The code uses separate equations for the gas and liquid phases. These equations relate the total pressure drop between cell centers to the following:

1. temporal acceleration,
2. spatial acceleration,
3. gravitational acceleration,
4. interphasic momentum transfer caused by phase change,
5. interphasic momentum transfer caused by interfacial drag, and
6. wall drag.

The first three components of the momentum equations listed above are calculated as described in Section 2.1. The phase-change component, also incorporated as described in Section 2.1, requires the details of the calculation of the interphase mass-transfer rate provided in Appendix G. This section describes the calculation of the interfacial-drag term and the wall drag in Appendix H, Sections H.1 and H.2, respectively. The following nomenclature is used in Appendix H.

NOMENCLATURE

A :	flow area of the channel
A_t :	total surface area of rods
A_{pb} :	projected area of the bubble (m^2)
A_u :	unheated surface area of rods
c_{Db} :	bubble-drag coefficient
c_f :	coefficient of friction
c_{flo} :	single-phase liquid friction-factor correlation
c_{hwg} :	horizontal 1D wall-shear coefficient
c_{hwl} :	horizontal 1D wall-shear coefficient
c_i, C_i :	interfacial-drag coefficient ($kg \cdot m^{-4}$)
$c_{\sigma wg}$:	nonstratified 1D wall-shear coefficient
$c_{\sigma wl}$:	nonstratified 1D wall-shear coefficient
c_{wg} :	gas-phase wall drag
c_{wl} :	liquid-phase wall drag
C_0, C_1 :	bubble distribution parameters
$C_1 - C_5$:	correlation parameters in <u>Eq. (H-32)</u>

C, C' :	constants in bubble-height calculation [Eq. (H-89)]
C_{an} :	roughness parameter
C_d :	form drag coefficient for droplets
C_{wg} :	wall-gas drag coefficient
Ca :	capillary number
d, D, diam :	diameter
D_g :	hydraulic diameter for the gas phase
D_h :	hydraulic diameter (m)
D_l :	hydraulic diameter for the liquid phase
DX :	cell lengths
E :	relative entrainment
f :	friction factor
f_{fo} :	single-phase friction factor
f_{wg} :	wall-gas friction factor
$fc4$:	proportionality constant for pipe roughness
fc_{drop} :	constant
fd_{is} :	constant
ffd :	constant
ffs :	constant
fmd_{is} :	constant
frw :	constant
fsb :	constant
fsm :	constant
F_b :	force on the gas bubbles
F_d :	force on the droplets
F_u :	fraction of unheated surface area
FA :	cell-edge flow area
g, g_c :	magnitude of the gravity vector
G :	mass flux ($\text{kg} \cdot \text{m}^{-2} \cdot \text{s}^{-1}$)
h_t :	height of the stratified layer of liquid
HD :	hydraulic diameter (m) or average of the level height in Eq. (H-74)
j :	cell designator
j :	superficial velocity ($\text{m} \cdot \text{s}^{-1}$)
j^* :	dimensionless superficial velocity
k :	cell level index or dummy directional index
L :	length

L_0 :	Laplace coefficient
M :	drag force per unit volume ($\text{N}\cdot\text{m}^{-3}$)
NTSX:	number of azimuthal sectors
$N_{\mu g}$:	viscosity number
p :	pressure (Pa)
P :	equivalent perimeter
P_s :	profile slip factor
r :	radial position or bubble radius
r_d :	drag radius
r_{sm} :	Sauter mean radius
Re :	Reynolds number
s :	distance between bubbles
S_i :	width of the stratified interface (m)
S_r :	slip ratio
T :	temperature (K)
u :	liquid velocity parallel to the wall
vol:	cell volume
vol _b :	bubble volume
Vol _d :	droplet volume
V :	velocity ($\text{m}\cdot\text{s}^{-1}$)
V_{fd} :	liquid velocity combining the effects of both annular film and entrained droplets [Eqs. (H-57) and (H-58)]
\vec{V}_r :	vector-average velocity in the axial and radial directions
$\vec{V}_{g\theta}$:	vector-average velocity in the azimuthal direction
$\langle V_r \rangle$:	vector-average velocity at the r face for the ijk cell
$\langle V_z \rangle$:	vector-average velocity at the z face for the ijk cell
$\langle V_\theta \rangle$:	vector-average velocity at the θ face for the ijk cell
V_{gj} :	drift-flux velocity ($\text{m}\cdot\text{s}^{-1}$)
V_{gr} :	magnitude of gas velocity in the radial direction ($\text{m}\cdot\text{s}^{-1}$)
V_{gz} :	magnitude of gas velocity in the axial direction ($\text{m}\cdot\text{s}^{-1}$)
$V_{g\theta}$:	magnitude of gas velocity in the azimuthal direction ($\text{m}\cdot\text{s}^{-1}$)
V_{lr} :	magnitude of liquid velocity in the radial direction ($\text{m}\cdot\text{s}^{-1}$)
V_{lz} :	magnitude of liquid velocity in the axial direction ($\text{m}\cdot\text{s}^{-1}$)
$V_{l\theta}$:	magnitude of liquid velocity in the azimuthal direction ($\text{m}\cdot\text{s}^{-1}$)
V_{rr} :	magnitude of the relative velocity in the radial direction ($\text{m}\cdot\text{s}^{-1}$)
V_{rz} :	magnitude of the relative velocity in the axial direction ($\text{m}\cdot\text{s}^{-1}$)

$V_{r\theta}$:	magnitude of the relative velocity in the azimuthal direction ($\text{m} \cdot \text{s}^{-1}$)
W :	weighting factor
We :	Weber number
WF :	weighting factor
$WFHDS$:	weighting factor
$WFHF$:	weighting factor
$WFMDs$:	weighting factor
$WFRW$:	weighting factor
$WFSB$:	weighting factor
$WFSM$:	weighting factor
WX :	weighting factor
$xmdis$:	constant
X :	quality or polynomial curve-fit parameter defined in <u>Eq. (H-80)</u>
X_f :	flow quality
X_s :	static quality
XS :	weighting factor
y :	coordinate perpendicular to wall
Y :	polynomial curve-fit parameter defined in <u>Eq. (H-80)</u>
Y_b :	bubble height from the wall
z :	axial elevation
α :	volume fraction or void fraction
α_{AG} :	void fraction at the agitated/post-agitated IAF-regime transition
α_b :	bubble fraction
α_c :	gas-droplet-core area fraction
α_d :	droplet area fraction
$\alpha_{d d}$:	liquid dispersed droplet fraction
α_f :	liquid film area fraction
α_{fr} :	void fraction of bubbles traveling in the free stream
α_g :	void fraction associated with the gas phase
α_k :	area fraction of the k^{th} phase
α_l :	liquid fraction
α_w :	void fraction of bubbles attached to the wall
α_1, α_2 :	void-fraction parameters used to calculate the weighting factor for the total interfacial-drag coefficient in the transition regime
Δp :	pressure difference
Δt :	time step (s)

Δx :	cell length
Δz :	elevation difference or length
$\Delta \alpha$:	fractional difference
$\Delta \rho$:	liquid density minus gas density
δ_f :	liquid film thickness (mm)
γ :	ratio of densities
ε :	roughness parameter
μ :	viscosity ($\text{N} \cdot \text{s} \cdot \text{m}^{-2}$)
ρ :	density ($\text{kg} \cdot \text{m}^{-3}$)
ρ_c :	gas core density
ρ_m :	density of two-phase mixture
ξ :	cell-centered fluid property
θ :	azimuthal angle
$(\Phi^2)_{\omega}$:	TRAC effective two-phase multiplier
$(\Phi^2)_H$:	homogeneous two-phase multiplier
σ :	surface tension
τ :	shear stress
τ_f :	shear stress at the film-to-core interface
dp/dx :	pressure drop per unit length
Ω :	cell lengths adjoining the cell edge

Subscripts

a :	annular film
ag :	agitated flow
am :	annular mist
b :	bubble
bot :	bottom
bs :	bubbly slug flow
c :	core
CHF:	critical heat flux
d :	droplet
dd :	dispersed droplet
df :	highly dispersed flow
f :	film
fr :	free stream
g :	gas phase

<i>i</i> :	interfacial
<i>k</i> :	phase dummy index
<i>l</i> :	liquid phase
<i>m</i> :	modified or two-phase mixture
min:	minimum
max:	maximum
<i>old</i> :	old-time value
<i>pa</i> :	post-agitated IAF flow
<i>r</i> :	relative
<i>r</i> :	radial direction
<i>rw</i> :	rough-wavy IAF
sat:	saturation
<i>sb</i> :	subcooled nucleate boiling
<i>sm</i> :	smooth IAF
st:	stratified flow
<i>top</i> :	top
<i>tr</i> :	transition boiling
trans:	transition flow
<i>v</i> :	vapor
<i>w</i> :	wall
<i>z</i> :	axial direction
θ :	azimuthal direction

H.1. Interfacial Drag

The interfacial-drag term in the TRAC field equations accounts for the interfacial force that can occur as a result of the momentum interchange between the phases. The code assumes that this term is proportional to the square of the relative velocity. It calculates an interfacial-drag coefficient as the constant of proportionality. The interfacial-drag coefficient is dependent on the flow regime that is determined by the local total mass flux and the void fraction. (See [Appendix E](#) for a description of the flow-regime map.) The following discussion describes how the interfacial-drag coefficient is determined for bubbly slug flow, annular-mist flow, stratified flow, and the transitions among them. The special core-reflood model and other process models are described in detail. The CCFL model that modifies the interfacial shear in the VESSEL component at user-prescribed positions is described separately in [Appendix I, Section I.3](#).

During development of TRAC-PF1/MOD2, a major goal was to improve the interfacial-drag and heat-transfer relations that were being used in the MOD1 code. A detailed review of the MOD1 models and correlations produced a number of errors and

shortcomings and areas that needed improvement. This criticism is tempered with the fact that at the time of MOD1 development, many mechanistic models for interfacial drag as well as pertinent data were not available. The developers at that time sought to provide a robust efficient version of the code that would accommodate a wide range of two-phase flow processes. With this in mind, the developers adopted the use of simple, quasi-steady correlations that could be applied to a variety of geometric configurations and scales.

This approach has proved to be very attractive with regard to applicability and computation time, but has not been without its problems. Several cases occurred in which the code predicted incorrect phenomena and therefore, estimated the interfacial drag incorrectly. In the MOD2 version, we attempted to correct these problems. We have tried to reduce the number of engineering models and to use recent correlations from the literature wherever possible.

In essence, we have striven to provide a more realistic and accurate prediction of the actual phenomena, and therefore, make the code more justifiable. The major changes that were implemented into TRAC-PF1/MOD2 include the following:

- determination of the flow regime using a void fraction that is donor-celled on the vapor velocity,
- definition of the bubble diameter based on the Laplace coefficient rather than on the Weber number,
- definition of the droplet diameter based on a wave-crest-shear correlation rather than on the Weber number,
- addition of the profile slip effect to the bubble drag,
- momentum weighting of the droplet and film components in the annular-mist regime,
- addition of a stratified-flow regime in the VESSEL component,
- a complete rewrite of the core-reflood interfacial drag to model the physical phenomena as described in the recent literature, and
- the allowable change in the interfacial drag from one time step to the next, based on real time rather than on an average of new- and old-time values.

H.1.1. Bubbly Slug Flow Correlations

This section describes the calculation of interfacial drag for the bubbly slug regime. [As in Appendix E, here we will refer to bubbly flow, bubbly slug transition, and bubbly slug flow, as shown in Fig. F-3, collectively as the bubbly slug regime.] For mass fluxes less than $2000 \text{ kg} \cdot \text{s}^{-1} \cdot \text{m}^{-2}$, bubbly flow is assumed for void fractions up to 0.3, and slug

flow for void fractions between 0.3 and 0.5. (Physically, slug flow is more accurately described as bubbly slug flow as shown in Fig. F-3. To avoid confusion, we will use "slug flow" here.) For mass fluxes greater than $2700 \text{ kg} \cdot \text{s}^{-1} \cdot \text{m}^{-2}$, bubbly flow is assumed for void fractions up to 0.5. For mass fluxes between 2000 and 2700, bubbly flow is assumed up to a void fraction of 0.3, and an interpolation is made between bubbly and slug flows for void fractions between 0.3 and 0.5. (See Appendix E for a full description of the flow-regime map, and refer to Fig. E-1. in Appendix E to visualize the limits of this regime.)

The basic relations described here for this regime are used throughout the code in all 1D components and in the 3D VESSEL component. In some special cases, the interfacial drag is overridden or altered. These cases are

1. core reflood in the VESSEL component,
2. stratified flow in the VESSEL component,
3. flow in an upper plenum,
4. accumulator logic in the PIPE component,
5. stratified flow in 1D components,
6. user-defined CCFL in the VESSEL, and
7. complete phase-separation option in 1D components.

These special cases are described separately in subsequent sections. Except for these cases, and except for mass fluxes and void fractions outside the range of the bubbly slug regime, the model described below is used for the interfacial drag in each direction in the VESSEL component and in all 1D components.

H.1.1.1. Basis for the Model. We base the interfacial-drag prediction for bubbly slug flow in TRAC upon the following assumptions:

1. The interfacial drag on bubbles can be represented with the correlations commonly used for solid spherical particles. Therefore, no bubble distortion is assumed.
2. The transient is sufficiently slow that interfacial-drag phenomena are quasi-steady. Therefore, the transient forces during the acceleration of bubbles (apparent mass and Basset force) can be neglected.
3. The bubble diameter used for bubbly flow can be determined using the Laplace coefficient.
4. The increased slip due to the bubble distribution in a channel is accounted for.
5. The interfacial drag in the slug-flow regime can be represented with the correlations used for solid spherical particles, with the diameter increased up to the hydraulic diameter of the channel.

The method for determining the interfacial-drag force in the bubbly slug flow regime follows that of Ishii and Chawla (Ref. H-1, p. 12). Here, the interfacial force for the dispersed phase (in this case, gas bubbles) is given by

$$M_i = \frac{\alpha F_b}{\text{vol}_b} \quad . \quad (\text{H-1})$$

This relation assumes steady-state conditions; therefore, the force on the bubble is caused by skin friction and form drag only. We neglect the transient forces that occur during bubble or slug acceleration (apparent mass and the Basset force), but include the increased slip caused by the nonuniform distribution of bubbles in a channel (also known as profile slip because bubbles redistribute due to the velocity profile). Thus, the force on the bubble can be represented as

$$F_b = \frac{1}{2} c_{Db} \rho_\ell V_r |V_r| A_{pb} P_s \quad . \quad (\text{H-2})$$

Combining Eqs. (H-1) and (H-2) with the relations for the projected area and the volume of a sphere, we have

$$M_i = \frac{\frac{3}{4} c_{Db} \alpha \rho_\ell V_r |V_r| P_s}{D_b} \quad . \quad (\text{H-3})$$

Defining the interfacial-drag coefficient as

$$c_i = \frac{\frac{3}{4} c_{Db} \alpha \rho_\ell P_s}{D_b} \quad , \quad (\text{H-4})$$

the interfacial force becomes

$$M_i = c_i |V_r| V_r \quad . \quad (\text{H-5})$$

Equation (H-5) represents how the interfacial force appears in the TRAC momentum equations. Because it is calculated with the assumption of steady-state skin friction and form drag only, it is also called the interfacial-drag force, and the coefficient c_i , the interfacial-drag coefficient. The interfacial-drag force appears in the liquid and in the gas momentum equations, so that a drag force on one phase causes a pulling force of equal magnitude on the other phase. As shown in Eq. (H-5), the sign of the force (and therefore the direction) is determined by the relative velocity, which is defined as the gas velocity minus the liquid velocity.

To determine the interfacial-drag coefficient from Eq. (H-4), constitutive relations are required for the bubble diameter, the bubble-drag coefficient, and the profile slip factor.

A wide range of bubble diameters is observed in the literature. We used a simple expression suggested by Ishii (Ref. H-2.), as follows:

$$D_b = 2L_o , \quad (H-6)$$

where L_o is the Laplace coefficient defined as

$$L_o = \sqrt{\frac{\sigma}{g(\rho_l - \rho_g)}} . \quad (H-7)$$

Ishii suggested this expression as an approximate arithmetic average of minimum and maximum bubble diameters observed experimentally.

From Eq. (H-4), the interfacial-drag coefficient is inversely proportional to the bubble diameter, which therefore has a direct effect on the interfacial drag.

H.1.1.1.1. Bubbly Flow Interfacial-Drag Coefficient. To determine the bubble-drag coefficient (c_{Db}) we first calculate the bubble Reynolds number. This is defined as

$$Re_b = \frac{D_b V_r \rho_l}{\mu_l} . \quad (H-8)$$

The dependence of the bubble-drag coefficient on the bubble Reynolds number is calculated for three separate regimes: Stokes regime, viscous regime, and Newton's regime. The relations used are very similar to those proposed by Ishii and Chawla (Ref. H-1., pp. 13 and 14) for solid particles. Thus, this development assumes no bubble deformation and greatly simplifies the equations.

The three ranges of Reynolds numbers and their respective bubble-drag coefficients are as follows:

Stokes regime ($Re_b \leq 0.1031$) ,

$$c_{Db} = 240.0 ; \quad (H-9)$$

Viscous regime ($0.1031 < Re_b < 989.0$) ,

$$c_{Db} = \frac{24.0}{Re_b} (1.0 + 0.15 Re_b^{0.687}) ; \quad (H-10)$$

and

Newton's regime ($989.0 \leq Re_b$) ,

$$c_{Db} = 0.44 . \quad (H-11)$$

The constant-Stokes-regime drag coefficient is equivalent to $24.0/Re_b$, for $Re_b = 0.1$. Thus, at the very low bubble Reynolds numbers, this constant drag coefficient provides an upper limit on the drag equivalent to the well-known Stokes' drag law at $Re_b = 0.1$. Setting the drag coefficient equal to the constant value of 240.0 also prevents dividing by zero for the case in which the relative velocity (and therefore the Reynolds number) is zero. Bird, Stewart, and Lightfoot (Ref. H-3, p. 193) propose that Stokes flow can be assumed up to a Reynolds number of 0.1. Ishii and Chawla (Ref. H-1, p. 14) recommend a value of 1.0. In TRAC, a value of 0.1031 is used. This limit was adjusted from the 0.1 value so that the drag coefficient is essentially continuous with the viscous regime. [That is, using a value of 0.1031 for the bubble Reynolds number in Eq. (H-10) results in a drag coefficient of 240.1.]

The viscous-regime drag coefficient is an empirical relation proposed by Shiller and Nauman (Ref. H-4). The upper range of this regime is chosen to be a bubble Reynolds number of 989.0. This is greater than the value of 800.0 suggested by Shiller and Nauman (Ref. H-4), but less than the value of 1000.0 proposed by Ishii and Chawla (Ref. H-1, p. 14). The upper limit of 989.0 was chosen so that the drag coefficient was continuous with the Reynolds number at the transition to Newton's regime.

In Newton's regime, the drag force is approximately proportional to the square of the velocity of the fluid moving past the bubble, and the drag coefficient reaches an asymptotic value. We use a value of 0.44 as recommended by Bird, Stewart, and Lightfoot (Ref. H-3, p. 192). For comparison, a value of 0.45 is proposed by Ishii and Chawla (Ref. H-1). The Newton's-regime bubble-drag coefficient is assumed to exist for all Reynolds numbers greater than 989.0. Comparisons with data (Ref. H-1, p. 14, and Ref. H-3, p. 193) suggest that this is true for solid particles up to a Reynolds number of 2×10^5 .

H.1.1.1.2. Profile Slip in Bubbly Flow. In TRAC, we have added a factor to the interfacial-drag coefficient to account for the increased slip in channel flow that occurs as the bubbles redistribute in the velocity profile. Physically, the lighter phase (in this case bubbles) tends to migrate to a higher-velocity region of the channel, resulting in a higher void concentration in the central regime. In the two-fluid formulation, the additional slip between the phases can be accounted for by the introduction of a profile slip factor that appears in Eq. (H-4). Following Ishii (Ref. H-2), this is defined as

$$P_s = \frac{(C_1 V_g - C_0 V_\ell)^2}{(V_r)^2}, \quad (\text{H-12})$$

where the distribution parameters are given by

$$C_0 = 1.2 + 0.2 \sqrt{\frac{\rho_g}{\rho_\ell}} \quad (\text{H-13})$$

and

$$C_1 = \frac{1.0 - C_0 \alpha_b}{1.0 - \alpha_b}. \quad (\text{H-14})$$

This expression for the distribution parameter assumes fully developed turbulent flow in a circular channel (Ref. H-5.).

H.1.1.1.3. Slug-Flow Interfacial-Drag Coefficient. In TRAC, the interfacial-drag coefficient for slug flow is calculated in the same manner as for bubbly flow, but with a different bubble diameter. Referring to the flow-regime map (Fig. E-1. in Appendix E), the slug-flow regime is assumed to exist for local void fractions between 0.3 and 0.5, when the mass flux is less than $2000 \text{ kg} \cdot \text{s}^{-1} \cdot \text{m}^{-2}$. In this regime, the bubble diameter is calculated by linear interpolation between the bubble diameter from the Laplace coefficient [Eq. (H-6)] and the minimum of $40L_0$, or $0.9HD$. Kataoka and Ishii (Ref. H-6., p. 1933) cite that the slug bubbles cannot be sustained for channels with a diameter much larger than $40L_0$, because of interfacial instability. At this point, they form cap bubbles. This argument is also consistent with the data of Grace et al. (Ref. H-7.) and the analysis of Kitscha and Kocamustafaogullari (Ref. H-8.). Also, Ishii and Chawla (Ref. H-1., p. 25) limit the bubble size to 90% of the hydraulic diameter.

The interpolation uses the void fraction as the independent variable. Thus, the interfacial-drag coefficient used in the code for the slug-flow regime uses a solid spherical particle drag correlation, modified by increasing the diameter up to that of the channel hydraulic diameter. This has a significant effect on the interfacial drag because the calculated value is inversely proportional to the bubble diameter [Eq. (H-3)].

H.1.1.2. Input Required to Implement the Correlations. To calculate the interfacial drag, the relative velocity, void fraction, liquid density, vapor density, surface tension, and liquid viscosity are used as input [see Eqs. (H-4), (H-6), (H-7), (H-8), (H-12), (H-13), and (H-14)].

Because the interfacial drag is calculated at cell edges, these quantities must be calculated accordingly. The definitions are given below.

The relative velocity V , used in Eqs. (H-8) and (H-12) is required in the 3D VESSEL for all three directions. In this case, the code uses the magnitude of a vector-average relative velocity rather than the absolute value of the actual relative velocity at the interface. In this way, spatial averaging is achieved, and the potential for radical changes in the relative velocity is reduced. To present the definitions of the relative velocities, the same nomenclature for the 3D mesh-cell velocities given in Section 2.0. is used.

Referring to Section 2.1.5., the magnitude of the vector relative velocity that is used for the calculation of the interfacial drag in the axial direction is given by

$$\begin{aligned}
V_{rz} = & \left\{ \left[V_{gz}(r, \theta, z + \frac{1}{2}) - V_{lz}(r, \theta, z + \frac{1}{2}) \right]^2 \right. \\
& + \left[\left\{ V_{gr}(r + \frac{1}{2}, \theta, z) + V_{gr}(r - \frac{1}{2}, \theta, z) \right\} / 2 \right. \\
& \left. \left. - \left\{ V_{lr}(r + \frac{1}{2}, \theta, z) + V_{lr}(r - \frac{1}{2}, \theta, z) \right\} / 2 \right]^2 \right. \\
& + \left[\left\{ V_{g\theta}(r, \theta + \frac{1}{2}, z) + V_{g\theta}(r, \theta - \frac{1}{2}, z) \right\} / 2 \right. \\
& \left. \left. - \left\{ V_{l\theta}(r, \theta + \frac{1}{2}, z) + V_{l\theta}(r, \theta - \frac{1}{2}, z) \right\} / 2 \right]^2 \right\}^{0.5}. \tag{H-15}
\end{aligned}$$

Thus, this relative velocity contains an arithmetic average of the surrounding relative velocities in the three directions. Recall from [Section 2.0](#) that the g and l subscripts refer to the gas and liquid phases, respectively; the z , r , and θ subscripts refer to the axial, radial, and azimuthal directions, respectively; and the $+1/2$ or $-1/2$ positions refer to the cell-edge locations. To avoid divisions by small numbers and to prevent the calculation of nonphysical, interfacial-drag coefficients at the start of transients (the relative velocity may be identically 0.0), the relative velocity given in [Eq. \(H-15\)](#) is not allowed to be less than 0.01.

In the radial direction, the magnitude of the vector relative velocity is given by

$$\begin{aligned}
V_{rr} = & \left\{ \left[V_{gr}(r + \frac{1}{2}, \theta, z) - V_{lr}(r + \frac{1}{2}, \theta, z) \right]^2 \right. \\
& + \left[\left\{ V_{gz}(r, \theta, z + \frac{1}{2}) + V_{gz}(r, \theta, z - \frac{1}{2}) \right\} / 2 \right. \\
& \left. \left. - \left\{ V_{lz}(r, \theta, z + \frac{1}{2}) + V_{lz}(r, \theta, z - \frac{1}{2}) \right\} / 2 \right]^2 \right. \\
& + \left[\left\{ V_{g\theta}(r, \theta + \frac{1}{2}, z) + V_{g\theta}(r, \theta - \frac{1}{2}, z) \right\} / 2 \right. \\
& \left. \left. - \left\{ V_{l\theta}(r, \theta + \frac{1}{2}, z) + V_{l\theta}(r, \theta - \frac{1}{2}, z) \right\} / 2 \right]^2 \right\}^{0.5}. \tag{H-16}
\end{aligned}$$

The magnitude of the vector relative velocity that is used for the calculation of the interfacial drag in the azimuthal direction is defined differently because the interface is adjacent to locations in sectors θ and $\theta + 1$. The code calculates this velocity as

$$\begin{aligned}
V_{r\theta} = & \left\{ \left[\frac{V_{gz}(r, \theta, z + \frac{1}{2}) + V_{gz}(r, \theta, z - \frac{1}{2}) + V_{gz}(r, \theta + 1, z + \frac{1}{2}) + V_{gz}(r, \theta + 1, z - \frac{1}{2})}{4.0} \right. \right. \\
& \left. \left. \frac{V_{lz}(r, \theta, z + \frac{1}{2}) + V_{lz}(r, \theta, z - \frac{1}{2}) + V_{lz}(r, \theta + 1, z + \frac{1}{2}) + V_{lz}(r, \theta + 1, z - \frac{1}{2})}{4.0} \right]^2 \right. \\
& + \left[\frac{VVR13 / 2.0 + [V_{gr}(r + \frac{1}{2}, \theta, z) + V_{gr}(r + \frac{1}{2}, \theta + 1, z)]}{4.0} \right. \\
& \left. \left. \frac{VLR13 / 2.0 + [V_{lr}(r + \frac{1}{2}, \theta, z) + V_{lr}(r + \frac{1}{2}, \theta + 1, z)]}{4.0} \right]^2 \right. \\
& \left. + \left[V_{g\theta}(r, \theta + \frac{1}{2}, z) - V_{l\theta}(r, \theta + \frac{1}{2}, z) \right]^2 \right\}^{0.5} . \tag{H-17}
\end{aligned}$$

In the above equation, the terms *VVR13* and *VLR13* have special meaning, depending on the ring number and the number of azimuthal sectors. For convenience, the chosen variable names, *VVR13* and *VLR13*, are identical to the actual coding. For the innermost ring, *VVR13* and *VLR13* have the same definition except that *VVR13* refers to the gas phase and *VLR13* refers to the liquid phase. Thus, the definition given below for *VVR13* is identical for the liquid phase, with the liquid subscript used in place of the gas subscript. In the innermost ring, the code averages in the velocities in the radial direction on the opposite side of the apex of the cylindrical geometry 3D mesh cell. Thus,

$$\begin{aligned}
VVR13 = & \left[V_{gr}(r + \frac{1}{2}, \theta, z) + V_{gr}(r + \frac{1}{2}, \theta + \frac{1}{2}, z) \right] / 4.0 \\
& - \left[V_{gr}(r + \frac{1}{2}, \theta + \frac{NTSX}{2}, z) + V_{gr}(r + \frac{1}{2}, \theta + 1 + \frac{NTSX}{2}, z) \right] RS / 2.0 , \tag{H-18}
\end{aligned}$$

where

$$\begin{aligned}
NTSX &= \text{number of azimuthal sectors,} \\
RS &= 0.0 \quad \text{if } NTSX = 1, \text{ and} \\
RS &= 0.5 \quad \text{if } NTSX > 1.
\end{aligned}$$

The above equation holds for the case in which *NTSX* is an even number (which is typical for most input decks). In the case in which *NTSX* is odd, the following relation for *VVR13* is used:

$$VVR13 = \left[V_{gr}(r + \frac{1}{2}, \theta, z) + V_{gr}(r + \frac{1}{2}, \theta + \frac{1}{2}, z) \right] / 4.0 \\ - \left[V_{gr}(r + \frac{1}{2}, \theta + 1 + \frac{NTSX}{2}, z) \right] RS \quad , \quad (H-19)$$

where RS and $NTSX$ have the same meanings as above. As noted above, Eqs. (H-13) and (H-14) are identical for $VLR13$ except for the change in subscript from g to l .

For rings outside of the innermost ring (i.e., rings 2, 3, 4, . . .), the variables $VVR13$ and $VLR13$ take on different definitions. In this case, $VVR13$ is defined as

$$VVR13 = \left[V_{gr}(r - \frac{1}{2}, \theta, z) + V_{gr}(r - \frac{1}{2}, \theta + 1, z) \right] / 2.0 \quad . \quad (H-20)$$

Thus, combining Eq. (H-15) with Eq. (H-12), we see that the radial gas velocity contribution is simply the arithmetic average of the four components near the azimuthal interface. The code calculates $VLR13$ in this case with special weighting factors on the liquid velocities to take into account the momentum of the liquid. Thus,

$$VLR13 = (FWTK)(FV1)V_{lr}(r - \frac{1}{2}, \theta, z) + (FWTE)(FV2)V_{lr}(r - \frac{1}{2}, \theta + 1, z) \quad , \quad (H-21)$$

where

$$FWTK = [1.00001 - \alpha(r, \theta, z)] \text{vol}(r, \theta, z) \\ / \{ [1.00001 - \alpha(r, \theta, z)] \text{vol}(r, \theta, z) \\ + [1.00001 - \alpha(r, \theta + 1, z)] \text{vol}(r, \theta + 1, z) \} \quad ,$$

$$FWTE = [1.00001 - \alpha(r, \theta + 1, z)] \text{vol}(r, \theta + 1, z) \\ / \{ [1.00001 - \alpha(r, \theta, z)] \text{vol}(r, \theta, z) \\ + [1.00001 - \alpha(r, \theta + 1, z)] \text{vol}(r, \theta + 1, z) \} \quad ,$$

$$FV1 = \left[\text{VOLG}(r, \theta, z) \text{FA}_r(r - \frac{1}{2}, \theta, z) (1.0 - \alpha(r - 1, \theta, z)) \right] \\ / \left[\text{vol}(r, \theta, z) \text{FAG}_r(r - \frac{1}{2}, \theta, z) (1.00001 - \alpha(r, \theta, z)) \right] \quad ,$$

and

$$FV2 = \left[\text{VOLG}(r, \theta + 1, z) \text{FA}_r(r - \frac{1}{2}, \theta + 1, z) (1.0 - \alpha(r - 1, \theta + 1, z)) \right] \\ / \left[\text{vol}(r, \theta + 1, z) \text{FAG}_r(r - \frac{1}{2}, \theta + 1, z) (1.00001 - \alpha(r, \theta + 1, z)) \right] \quad .$$

The code restricts $FV1$ and $FV2$ to be less than or equal to 1.0. As in the case of the axial and radial directions, the magnitude of the vector-average relative velocity used for the interfacial drag in the azimuthal direction is not allowed to drop below a value of 0.01.

In the 1D components, the definition of the relative velocity for use in the interfacial-drag calculations is much simpler because only one direction is considered. Thus,

$$V_r = V_g(j + \frac{1}{2}) - V_\ell(j + \frac{1}{2}) \quad . \quad (H-22)$$

The void fraction that is used for Eq. (H-4) is averaged spatially. This is required because the void fraction is a cell-centered quantity, whereas the interfacial drag is calculated at the cell edges. The averaging technique is the same regardless of the flow direction and is the same for the 3D VESSEL component as well as for the 1D components. The spatially averaged void fraction is defined as

$$\langle \alpha \rangle = \frac{\Omega(j)\alpha(j) + \Omega(j+1)\alpha(j+1)}{\Omega(j) + \Omega(j+1)} \quad . \quad (H-23)$$

The Ω_s used in the equation above are the input cell lengths adjoining the cell edge. For instance, in the axial direction in the vessel, the Ω_s represent the heights of the cells. In the radial direction, this is the thickness of the rings and in the azimuthal direction, this is the average azimuthal thickness of the adjacent cells. In the 1D components, this is the input cell lengths. The void fraction is restricted to the range 0.00001 to 0.9999 in all components to avoid division by zero.

The other variables that are required to compute the bubbly slug interfacial drag are the following properties: liquid density, vapor density, surface tension, and liquid viscosity. In all directions in the 3D VESSEL, the code uses an arithmetic average of the adjacent cell-center values. For instance, in the azimuthal direction the average surface tension is given by

$$\sigma = [\sigma(r, \theta, z) + \sigma(r, \theta + 1, z)] / 2.0 \quad . \quad (H-24)$$

In the 1D components, the code uses a weighted average of the liquid and vapor density with the adjacent cell lengths. Thus, for example, the liquid density is given by

$$\langle \rho_\ell \rangle = \frac{\rho_\ell(j)DX(j) + \rho_\ell(j+1)DX(j+1)}{DX(j) + DX(j+1)} \quad . \quad (H-25)$$

The surface tension, liquid viscosity, and vapor viscosity are donor-celled. For surface tension and liquid viscosity, the upstream values are used, depending on the sign of the liquid velocity. Therefore,

$$\begin{aligned}\sigma &= \sigma(j) \text{ if } V_\ell \left(j + \frac{1}{2} \right) \geq 0 \quad , \\ \sigma &= \sigma(j+1) \text{ if } V_\ell \left(j + \frac{1}{2} \right) < 0 \quad , \\ \mu_\ell &= \mu_\ell(j) \text{ if } V_\ell \left(j + \frac{1}{2} \right) \geq 0 \quad ,\end{aligned}$$

and

$$\mu_\ell = \mu_\ell(j+1) \text{ if } V_\ell \left(j + \frac{1}{2} \right) < 0 \quad . \quad (\text{H-26})$$

In the above definitions, a special case occurs in the 3D VESSEL at the boundaries of the component. For instance, at the top level it is sufficient to say that the void fraction in a cell in level $k + 1$ must be set to the value for a corresponding cell in level k , because level $k + 1$ does not exist. Similar situations occur at the bottom level and in the outermost ring. Thus, the required properties and void fraction are revised when the adjacent cell of interest lies outside the boundary of the vessel.

H.1.1.3. Model as Coded. For the 1D components, the interfacial-drag coefficients are determined in subroutine StbVel1D (FEMOM in TRAC-M/F77). In the 3D VESSEL component, they are calculated in subroutine CIF3. The interfacial-drag force is calculated at the cell edges rather than the cell centers because the velocities and the momentum equations are defined here. The models are identical in all three directions in the 3D VESSEL and in the 1D components. Thus, Eqs. (H-4) through (H-14) are used in all cases, and their implementation varies only in the definition of the local relative velocities, void fractions, and properties. These differences are described in Section H.1.1.2. above.

The code calculates the interfacial-drag coefficient explicitly. That is, for the input velocities and properties, the values from the previous time step are used. No iterations are performed.

In the coding, the $3/4$ factor appearing in Eq. (H-4) is combined with the constants that appear in Eqs. (H-9), (H-10), and (H-11). Therefore, if one inspects the actual coding, one will find that Eqs. (H-9), (H-10), and (H-11) are written with the constants 180.0, 18.0, and 0.33, respectively.

The interfacial drag is a flow-regime-dependent quantity. Thus, the bubbly slug correlations described in this section are only used when the total mass flux and void fraction are in a certain range. The limits are given at the beginning of Section H.1.1. but are repeated here for completeness.

For mass fluxes less than $2000 \text{ kg} \cdot \text{s}^{-1} \cdot \text{m}^{-2}$, bubbly flow is assumed for void fractions up to 0.3, and slug flow between a void fraction of 0.3 and 0.5. For mass fluxes greater than $2700 \text{ kg} \cdot \text{s}^{-1} \cdot \text{m}^{-2}$, bubbly flow is assumed for void fractions up to 0.5. For mass fluxes

between 2000 and 2700, bubbly flow is assumed up to a void fraction of 0.3, and an interpolation is made between bubbly and slug for void fractions between 0.3 and 0.5. (See Appendix E for a full description of the flow-regime map, and refer to Fig. E-1 in Appendix E to visualize the limits of this regime.)

A change between TRAC-PF1/MOD2 and MOD1 in the flow-regime determination is that in MOD2, the void fraction that is used to determine the flow regime is donor-celled with the vapor velocity. Physically this makes sense because the cell-edge interfacial drag should represent the fluid that is passing through it.

H.1.1.4. Weighting, Magnitude Limits, and Rate Limits. Several limits are imposed to prevent unreasonably large or small numbers from occurring and thus, to prevent numerical difficulties. These are applied to the bubble diameter, D_b , to the interfacial-drag coefficient, c_i , to the relative velocity, and to the void fraction. We chose the limits based on the range of data provided in the literature and on experience obtained during the course of code development.

H.1.1.4.1. Bubble-Diameter Weighting and Limits. In the bubbly flow regime, the bubble diameter is not allowed to be less than 0.0001 m and is not allowed to be greater than the minimum of $40L_o$ or $0.9HD$ [where, because of Eq. (H-6), $0.9HD$ will be the controlling limit]. In the slug regime, the diameter is interpolated with a weighting factor between the bubble diameter determined from the Laplace coefficient and the minimum of $40L_o$ or $0.9HD$. As described in Appendix E, the slug regime is allowed for void fractions between 0.3 and 0.5 and mass fluxes less than $2000 \text{ kg} \cdot \text{s}^{-1} \cdot \text{m}^{-2}$. The weighting factor is 0.0 at void fraction 0.3 and below, 1.0 at void fractions 0.5 and above, and is increasing between the extremes.

For mass fluxes between 2000 and $2700 \text{ kg} \cdot \text{s}^{-1} \cdot \text{m}^{-2}$ and void fractions between 0.3 and 0.5, the code alters the weighting factor with a linear interpolation in mass flux between the 2000 and $2700 \text{ kg} \cdot \text{s}^{-1} \cdot \text{m}^{-2}$ values. After the weighting factor is limited between the values of 0.0 and 1.0, the code calculates a bubbly slug equivalent bubble diameter that is used to find the interfacial drag as

$$D_b = D_b(1.0 - XS) + \min(40L_o, 0.9HD)(XS) , \quad (\text{H-27})$$

where XS is the weighting factor. A plot of this weighting factor for the 3D VESSEL is presented in Fig. H-1, for mass fluxes below the $2000 \text{ kg} \cdot \text{s}^{-1} \cdot \text{m}^{-2}$ limit, above the $2700 \text{ kg} \cdot \text{s}^{-1} \cdot \text{m}^{-2}$ limit, and at an intermediate value of $2350 \text{ kg} \cdot \text{s}^{-1} \cdot \text{m}^{-2}$

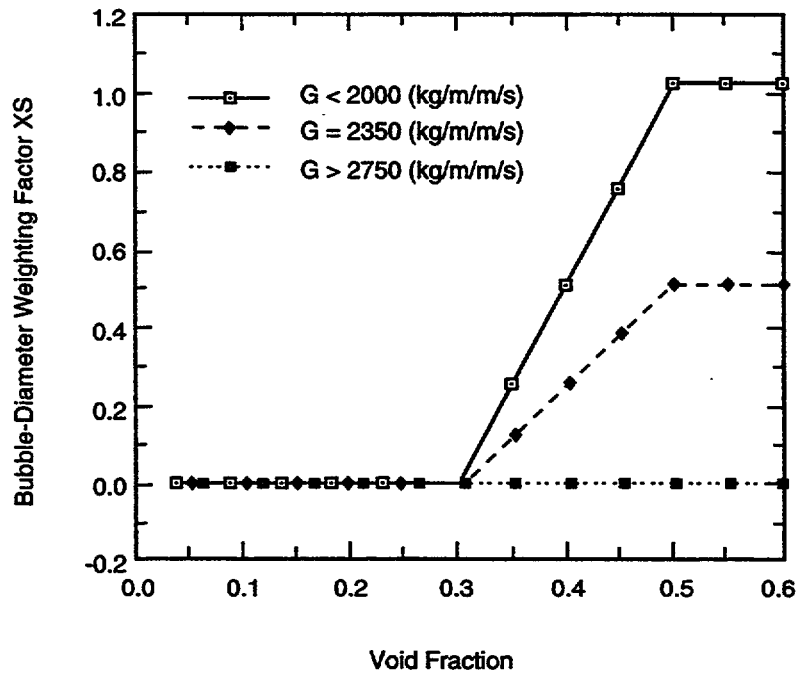


Fig. H-1. Bubble-diameter weighting factor in the bubbly slug regime for the 3D VESSEL.

H.1.1.4.2. Relative Velocity Limits. For calculations of the bubble Reynolds number in a 3D VESSEL, the relative velocity is limited to be greater than $0.01 \text{ m} \cdot \text{s}^{-1}$. As shown in Section H.1.1.2., the relative velocity used in calculating the interfacial drag is always positive. The limit ensures that, for instance, at the start of transients or when a flow reversal occurs and the relative velocity is near zero, a very large drag coefficient is not calculated. This limit is imposed with the rate limit in mind because some iterations may be required to allow the interfacial drag to reach a reasonable number, if a very large number was calculated initially.

H.1.1.4.3. Rate Limit on the Interfacial Drag. The allowable change in the interfacial drag from one time step to the next is identical for both the 3D VESSEL and the 1D components. In a departure from the method used in MOD1 where a new-time and old-time average was taken, the allowable change in MOD2 is based on real time to eliminate the sensitivity to the time-step size. The maximum and minimum allowable changes in the interfacial drag are given by

$$c_{i,\max} = c_{i,\text{old}} 2^{20.0\Delta t} \quad (\text{H-28})$$

and

$$c_{i,\min} = c_{i,\text{old}} 0.5^{20.0\Delta t} \quad (\text{H-29})$$

Thus, the amount of transient time required for the interfacial drag to double or halve is 0.05 s. The maximum allowable change is limited to be less than 2.0, and the minimum allowable change is limited to be greater than 0.4. For the special case of steady-state calculations, the new-time interfacial drag is a weighted average of 90% old time and 10% new time to provide stable convergence.

H.1.1.4.4. Interfacial Drag for Zero Flow Area and Zero Volume. If the flow area of the cell edge of interest is less than $1.0 \times 10^{-10} \text{ m}^2$ or the cell volume is less than $1.0 \times 10^{-12} \text{ m}^3$, the interfacial drag is set to zero to avoid extra computation.

H.1.1.4.5. Limits on the Void Fraction. The void fraction used to calculate the interfacial drag is restricted to the range 0.00001 to 0.9999 in all components.

H.1.1.5. Variations in the Application of the Correlations. The basic relations described here for the bubbly slug regime are used throughout the code in all 1D components and in the 3D VESSEL component. In some special cases, the interfacial drag is overridden or altered. These cases are

1. core reflood in the vessel (Section H.1.5.),
2. accumulator logic in the PIPE component (Sections H.1. and H.2.),
3. stratified flow in 1D components (Section H.1.3.),
4. user-defined CCFL in the vessel (Appendix J, Section J.4.),
5. complete phase-separation option in 1D components (Section H.1.6.1.),
6. stratified flow in the vessel (Section H.1.3.), and
7. two-phase flow in the upper plenum of the vessel (Section H.1.1.10.).

H.1.1.6. Consistency with the Interfacial Heat Transfer. In the development of Eq. (H-4), it is noted that instead of the actual interfacial area, the projected bubble area is used. For spherical geometry, the projected area is one-quarter times the surface area. In the calculation of the interfacial heat transfer, the code calculates the bubble diameter using Eq. (H-6), and the bubble surface area is used to calculate the interfacial heat-transfer area. Thus, in all cases (each direction in the 3D VESSEL and in the 1D components), the method is consistent in the calculation of both the interfacial drag and heat transfer in the bubbly regime because the same method is used in the calculation of the bubble diameter. However, differences do occur in the definition of the transport properties and in the calculation of the slug-regime interfacial area.

In general, the flow regime used in the interfacial heat transfer is determined using the local cell-center quantities. The case of stratified flow is one exception: the cell-edge, stratified-flow weighting factors that are calculated for the interfacial drag at the cell edges are averaged and used in the interfacial heat-transfer calculation.

With respect to the surface tension and densities used in the calculation of the bubble diameter, the cell-centered quantities are used in the interfacial heat-transfer calculation because this is also a cell-centered quantity. The differences that arise between it and the interfacial-drag calculation bubble diameter are expected to be small.

In the determination of the slug-regime interfacial heat transfer, a correlation from the literature is used for the interfacial area that takes into account the range in possible bubble diameters trailing the slug. In our determination of the interfacial drag, the trailing bubbles are neglected because of the domination of the slug on the drag.

H.1.1.7. Assessment of the Correlations. For this report, most of the individual bubbly slug, interfacial-drag correlations are not directly assessed against data, but rather the code as a whole is assessed. An effort was made to find previous assessments of the correlations if available, to perform some new data assessments, and to show comparisons with other interfacial-drag methods. The primary contributions to the calculation of the interfacial-drag coefficient are from the bubble diameter and the drag coefficient. In the discussion below, we try to separate the effects by first providing assessment of the drag coefficient.

H.1.1.7.1. Previous Assessment. In the Stokes regime for bubbly flow, a constant drag coefficient is used [Eq. (H-8)]. This gives a coefficient equivalent to Stokes' drag law for a bubble Reynolds number of 0.1, but underpredicts the drag for Reynolds numbers less than this value. Stokes' drag law gives excellent agreement with data as shown by many in the literature (Refs. H-1, H-3, and H-9). Except for rare conditions (such as at the start of transients when the relative velocity is near zero), this regime is not encountered in normal two-phase flow experiments, or in typical reactor-safety accidents. Thus, the constant value chosen gives a reasonable maximum value of the drag coefficient at such low velocities and prevents very large numbers from being calculated.

The viscous-regime drag coefficient is an empirical relation proposed by Shiller and Nauman (Ref. H-4). It was determined by Clift et al. (Ref. H-10, p. 111) that this relation is in agreement with the drag data for spheres within +5% to -4%. The Shiller and Nauman correlation is very similar to a relation proposed by Ishii and Chawla (Ref. H-1, p. 14),

$$c_{Db} = \frac{24.0}{Re_b} (1.0 + 0.1Re_b^{0.75}) \quad , \quad (H-30)$$

which they show to provide excellent agreement with solid particle data (Ref. H-1, p. 27). A comparison between the two relations is given in Fig. H-2. Because both correlations provide nearly identical bubble-drag coefficients, the viscous-regime drag coefficient used in TRAC should give good agreement with the data shown in Ishii and Chawla.

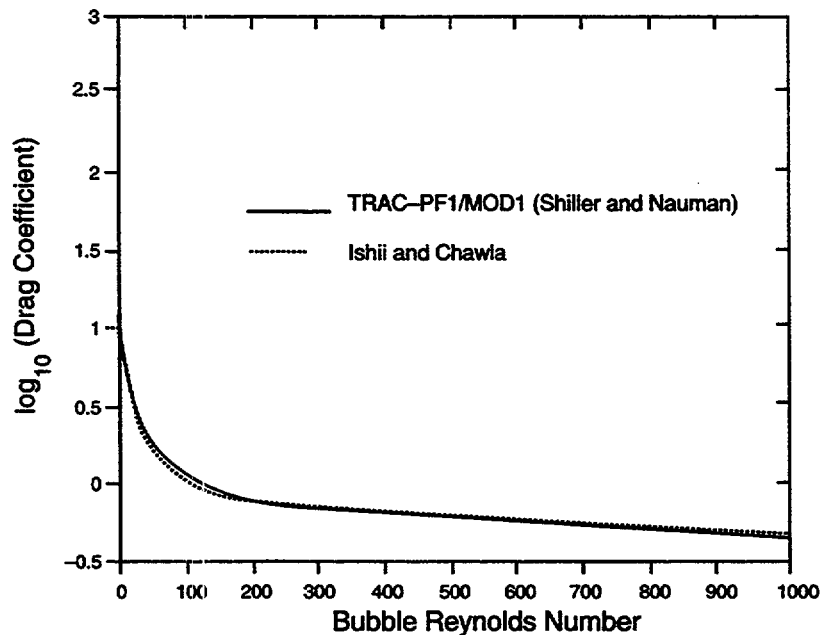


Fig. H-2. Comparison of the viscous-regime drag coefficient from Shiller and Nauman with the correlation proposed by Ishii and Chawla.

As mentioned above in Section H.1.1.1., in Newton's regime the code assumes a drag coefficient of 0.44. Bird et al. (Ref. H-3., p. 193) have shown this value to provide excellent agreement with solid particle data.

From the discussion above, it is apparent that the correlations used in TRAC for the bubble drag have a solid foundation of data to support them, if the particles are spherical. Since these correlations are used in dispersed bubbly flow, the conditions of bubble distortion and distribution are not accounted for. For this reason, some new assessment against other two-phase flow correlations was performed and is described in the following subsection.

H.1.1.7.2. Comparison to Other Correlations. The TRAC bubbly slug interfacial-drag coefficient [as defined by Eq. (H-4)] is compared to those given by Ishii and Chawla (Ref. H-1., Eq. 40, p. 22) and Chexal and Lellouche [Ref. H-11., Eqs. (2-1) through (2-5), pp. 2-3]. For this discussion, the three models are referred to as TRAC, Ishii, and Chexal, respectively. The comparison to Ishii is direct, since this is a two-fluid model. However, the Chexal correlation was developed using the drift-flux momentum equation, and some manipulation is required to make a direct comparison. Following the development of Anderson and Chu (Ref. H-12.), the following equation is used to calculate the interfacial-drag coefficient using a drift flux and a void fraction predicted from the Chexal model:

$$c_i = \frac{g(\rho_l - \rho_g)(1 - \alpha)^3 \alpha}{|V_{gj}|V_{gj}} \quad (\text{H-31})$$

The Chexal model has been assessed against a wide range of data (Ref. H-13.). Because of the database supporting the correlation, it was chosen for this comparison. The range in the data used to develop and assess the Chexal model is given in Table H-1.

The comparison among the Ishii, TRAC, and Chexal interfacial-drag predictions for a superficial liquid velocity (j_l) of $0.1 \text{ m}\cdot\text{s}^{-1}$, a pressure of 0.4 MPa, and a hydraulic diameter of 0.011 m is given in Fig. H-3. The values presented in the figures were calculated with a small driver code (approximately 700 Fortran statements). To avoid forcing the correlations used in TRAC and in Ishii into nonphysical situations, the following method was used. Using the fixed j_l and the physical properties, the superficial gas velocity (j_g) was varied between 0.0 and $25.0 \text{ m}\cdot\text{s}^{-1}$. For each j_g and j_l , the void fraction was determined by iteration using the Chexal correlation. Using the computed void fraction, the TRAC and Ishii drag coefficients were determined explicitly. The Chexal drag coefficient was then determined using Eq. (H-31), for the void fraction and the drift flux predicted by the correlation. The drag coefficient is presented as a logarithm for easier comparison. Note also that the interfacial-drag coefficient has the units $\text{kg}\cdot\text{m}^{-4}$ [Eq. (H-4)].

The comparison in Fig. H-3 shows that in the bubbly slug regime, the TRAC-calculated interfacial-drag coefficient lies between the Chexal and Ishii values. This result is a significant improvement over the MOD1 prediction that predicted values above that of Ishii's value for bubbly flow. The use of a more realistic bubble-diameter correlation (rather than the Weber number criterion) and the addition of the profile slip are the reasons for the improvement. For a hydraulic diameter of 0.01968 m, the comparison is very similar (Fig. H-4). This diameter was chosen because it is typical of the steam-generator tubes in a full-size plant. For a hydraulic diameter of 0.738 m (Fig. H-5), the TRAC prediction in the bubbly regime is in excellent agreement with Chexal. In the slug

TABLE H-1.
Range of Data Supporting the EPRI Correlation (Ref. H-11.)

Parameter	Range
Pressure	0.1–16.0 MPa
Pipe Diameter	0.16–0.457 m
Bundle Geometry:	
Rods/Bundle	6–161
Hydraulic Diameter	0.0097–0.047 m

regime, however, the code underpredicts the drag as the bubble diameter is allowed to increase up to about 0.1 m. This diameter is typical of hot-leg and cold-leg piping in full-size plants. Thus, for a variety of diameters, and at conditions similar to large-break LOCAs, the code is in very good agreement with the Chexal model and is an improvement over the MOD1 code.

H.1.1.8. Use of TRAC Bubbly Slug Correlations Outside the Database. The TRAC bubbly slug interfacial-drag-coefficient correlations are based on the assumptions that the bubbles (and slugs) are spherical (see [Section H.1.1.1.](#) for a full description). The database for the spherical geometry correlations is in general for single, solid particles in open channels with no effect on the drag from the distortion of the spheres. Thus, the database does not include the effect of bubble distortion. Also for very large channels, the TRAC correlations are being used outside the database. In [Fig. H-6.](#), the comparison of TRAC with Ishii and Chexal for large diameter (0.738 m) and higher pressure (1.0 MPa) shows that TRAC and Chexal are in reasonable agreement for the bubbly regime. A similar comparison is evident at 7.0 MPa ([Fig. H-7.](#)). This large diameter is typical of PWR primary-system piping and is outside the range of the Chexal correlation ([Table H-1.](#)). However, the comparison indicates that the TRAC-calculated drag coefficient is reasonable at these large diameters.

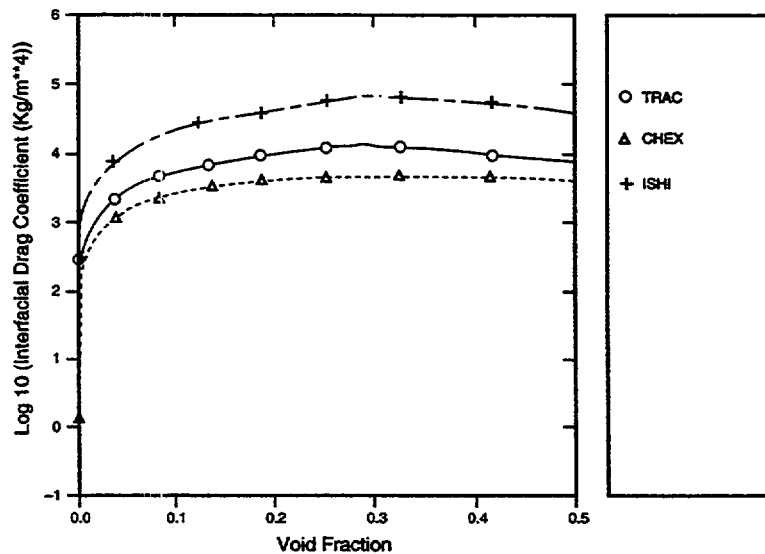


Fig. H-3. Comparison of the TRAC-calculated interfacial-drag coefficient (solid line) to the prediction by Ishii and Chawla (long dash) and the prediction by Chexal and Lellouche (dashed line) for a superficial liquid velocity of $0.1 \text{ m} \cdot \text{s}^{-1}$, a pressure of 0.4 MPa, and a hydraulic diameter of 0.011 m.

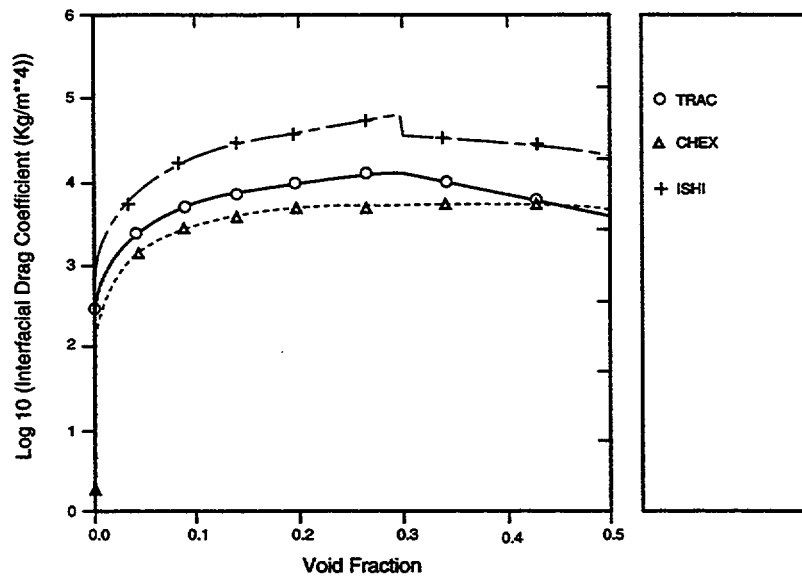


Fig. H-4. Comparison of the TRAC-calculated interfacial-drag coefficient (solid line) to the prediction by Ishii and Chawla (long dash) and the prediction by Chexal and Lellouche (dashed line) for a superficial liquid velocity of $0.1 \text{ m}\cdot\text{s}^{-1}$, a pressure of 0.4 MPa, and a hydraulic diameter of 0.0197 m.

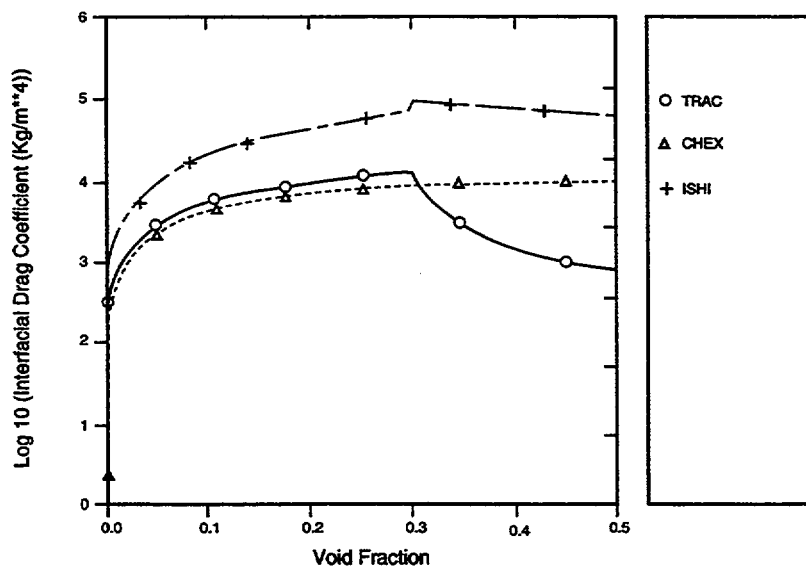


Fig. H-5. Comparison of the TRAC-calculated interfacial-drag coefficient (solid line) to the prediction by Ishii and Chawla (long dash) and the prediction by Chexal and Lellouche (dashed line) for a superficial liquid velocity of $0.1 \text{ m}\cdot\text{s}^{-1}$, a pressure of 0.4 MPa, and a hydraulic diameter of 0.0738 m.

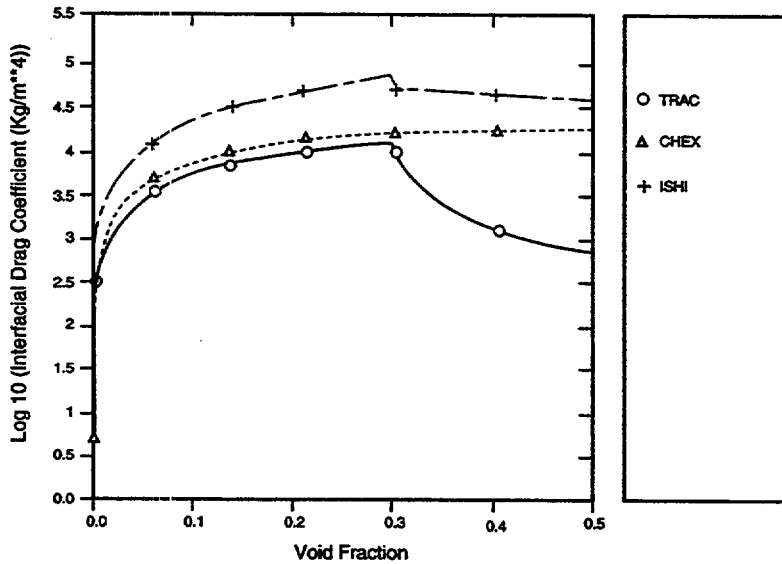


Fig. H-6. Comparison of the TRAC-calculated interfacial-drag coefficient (solid line) to the prediction by Ishii and Chawla (long dash) and the prediction by Chexal and Lellouche (dashed line) for a superficial liquid velocity of $0.1 \text{ m} \cdot \text{s}^{-1}$, a pressure of 1.0 MPa, and a hydraulic diameter of 0.0738 m.

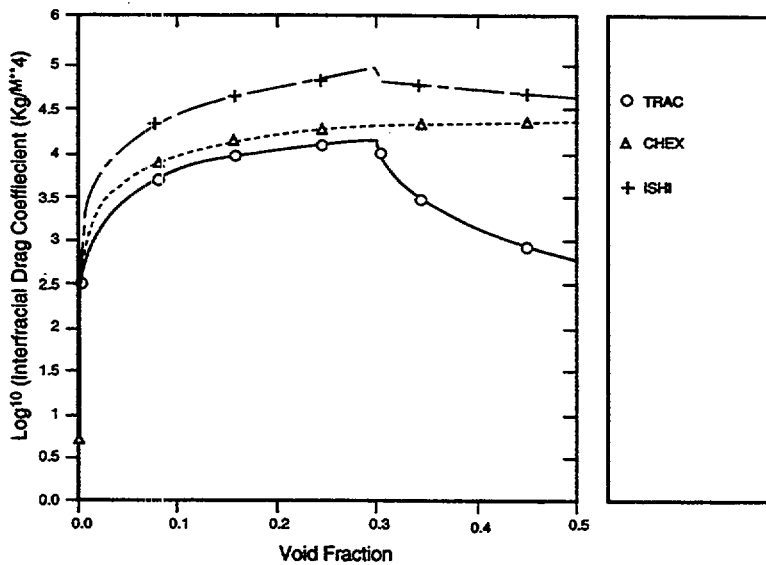


Fig. H-7. Comparison of the TRAC-calculated interfacial-drag coefficient (solid line) to the prediction by Ishii and Chawla (long dash) and the prediction by Chexal and Lellouche (dashed line) for a superficial liquid velocity of $0.1 \text{ m} \cdot \text{s}^{-1}$, a pressure of 7.0 MPa, and a hydraulic diameter of 0.0738 m.

H.1.1.9. Scaling Considerations. The correlations for the interfacial-drag coefficient for bubbly flow used in TRAC were developed based on the data for single spherical particles. Assessment results given in [Section H.1.1.7](#), show that, depending on the bubble diameter calculated by the Laplace coefficient criterion, TRAC can provide a reasonable estimate for the interfacial drag and therefore, can predict the relative velocity between the phases. For most applications, the bubble Reynolds number is greater than 1000.0. Thus, the drag coefficient is a constant value of 0.44, independent of hydraulic diameter and pressure. A significant part of the prediction, therefore, is the Laplace coefficient criterion that is used to predict the bubble diameter. The form of this relation includes the effect of increased pressure on the change in surface tension and liquid density [see [Eq. \(H-6\)](#)]. We have shown previously that for large hydraulic diameters at high pressure, the bubbly regime interfacial drag predicted by TRAC is in reasonable agreement with Ishii and Chexal (Figs. [H-6](#), and [H-7](#)). At small diameters and low pressure, the comparison is also very good and shows that the bubble concentration is taken into account accurately with the new profile slip factor. A comparison of TRAC with the other correlations for a small diameter and high pressure again shows a reasonable comparison ([Fig. H-8](#)). Thus, as the pressure increases, TRAC provides a reasonable prediction for the bubbly interfacial drag. This pressure effect at a single hydraulic diameter of 0.01968 m is shown in [Fig. H-9](#), for the pressure range 0.1 to 7.0 MPa (1.0 to 70.0 bar).

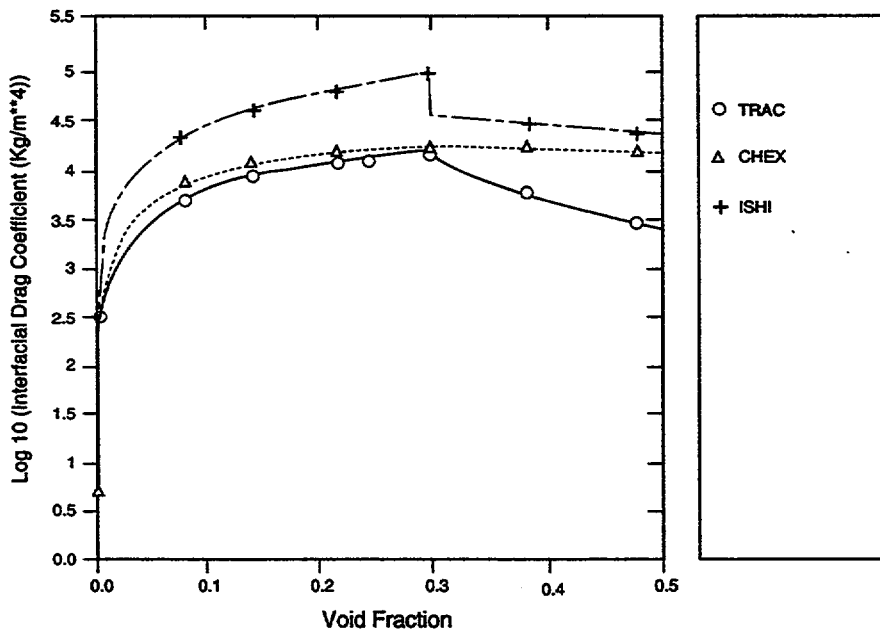


Fig. H-8. Comparison of the TRAC-calculated interfacial-drag coefficient (solid line) to the prediction by Ishii and Chawla (long dash) and the prediction by Chexal and Lellouche (dashed line) for a superficial liquid velocity of $0.1 \text{ m} \cdot \text{s}^{-1}$, a pressure of 7.0 MPa, and a hydraulic diameter of 0.01968 m.

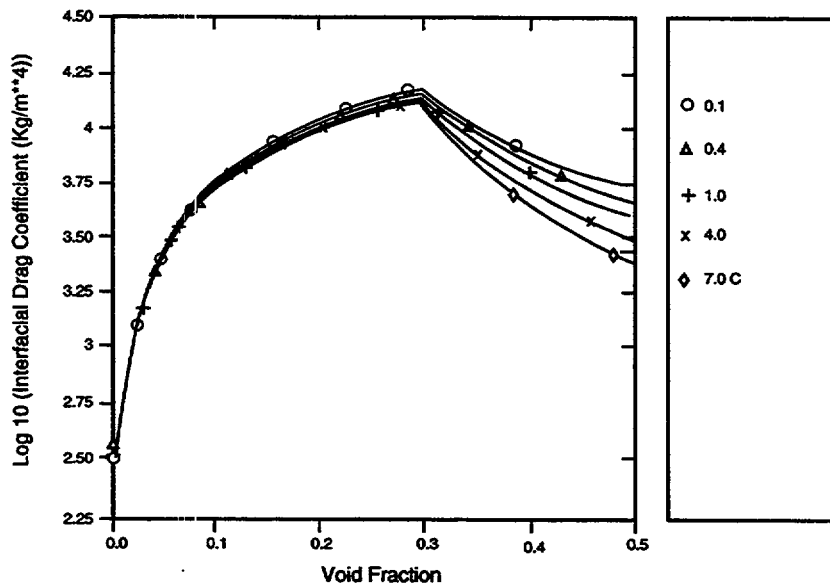


Fig. H-9. Comparison of the TRAC-calculated interfacial-drag coefficient for a superficial liquid velocity of $0.1 \text{ m} \cdot \text{s}^{-1}$, a hydraulic diameter of 0.01968 m , and a range in pressure of $0.1\text{--}7.0 \text{ MPa}$.

The effect of increased scale is discussed in the previous section. It is shown there that as the hydraulic diameter is increased, the TRAC prediction for the bubbly drag is reasonable in comparison with Ishii and Chexal.

H.1.1.10. Special Model for Bubbly Flow in the Upper Plenum. Through the input, the user can describe which regions of the VESSEL component are in the core, lower plenum, downcomer, and upper plenum. If there is bubbly slug flow in the upper plenum, a special void-fraction correlation is used to determine the interfacial-drag coefficient. The model of choice is the Wilson correlation (Ref. H-14.). This correlation is based on steam-water data in pipes of 0.1- and 0.48-m diameter at pressures between 2.0 and 5.5 MPa , and additional data obtained in 0.46- and 0.914-m -diameter pipes between pressures of 4.1 and 13.8 MPa . The tests were done with either zero liquid-flow rate (stagnant pool-type conditions) or at small liquid-flow rates established by natural circulation. The correlation has the following form:

$$\alpha_w = C_1 \left(\frac{\rho_g}{\rho} \right)^{C_2} k u_g^{C_3} \left(\frac{\sqrt{\sigma / g_c \Delta \rho}}{HD} \right)^{C_4} \left(\frac{j_g}{j} \right)^{C_5} \quad (\text{H-32})$$

where

$$ku_g = \frac{j_g}{\left(\frac{\sigma g_c}{\Delta\rho}\right)^{0.25}} ,$$

$$C_2 = 0.12, C_4 = 0.1, C_5 = 0.6 ,$$

and

$$\left. \begin{array}{l} C_1 = 0.564 \\ C_3 = 0.67 \end{array} \right\} ku_g \leq 1.5$$

$$\left. \begin{array}{l} C_1 = 0.619 \\ C_3 = 0.47 \end{array} \right\} ku_g > 1.5.$$

This model is implemented into TRAC using the relation

$$C_i = g_c \Delta\rho \alpha_w (1 - \alpha) / (j_g / \alpha_w)^2 , \quad (\text{H-33})$$

which is developed by solving for the interfacial drag from the steady-state two-fluid momentum equations.

To perform an assessment of the correlation, we used the same method as before (i.e., comparisons to the Chexal and Ishii correlations). Assuming prototypical upper-plenum conditions (3.5-m diameter, low liquid flow), the comparisons are shown in Figs. H-10 and H-11. for 0.1 and 0.4 MPa, respectively. The results show very good agreement with the Chexal correlation, but this agreement is much lower than the prediction of the Ishii model. This is to be expected because the Chexal model was developed against larger-diameter data, whereas the Ishii model was developed against smaller-diameter data.

H.1.1.11. Summary and Conclusions. The correlations used to predict the interfacial-drag force in the calculation of the bubbly slug flow regime in TRAC have been fully described. Many changes have been made since MOD1 was released. These changes represent a significant improvement and were recommended through the detailed assessment efforts that occurred in the 2D/3D, MIST, and ICAP programs associated with USNRC research. The assessments have been very beneficial because of the many recommendations that have been incorporated. The primary improvements were in the calculation of the bubble diameter (elimination of the Weber number criterion) and the implementation of the profile-slip effect. Both changes tended, in most cases, to reduce the drag.

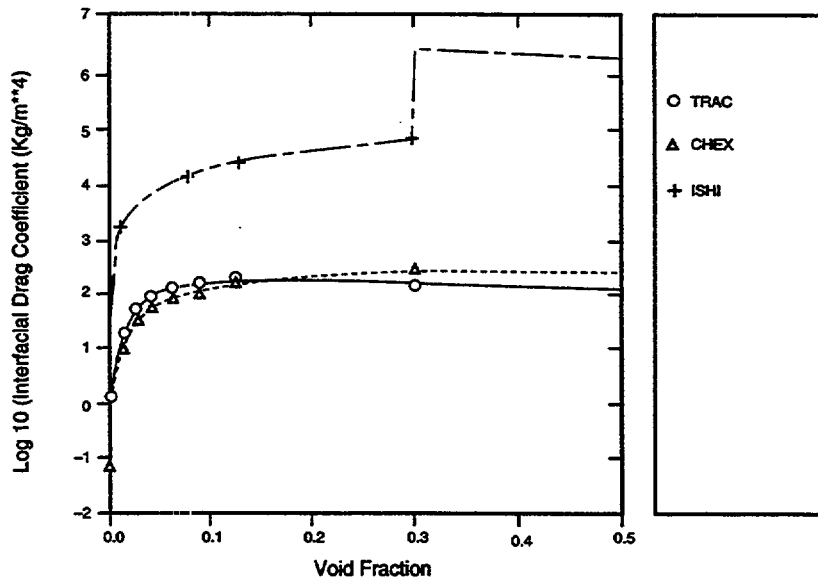


Fig. H-10. Comparison of the TRAC-calculated interfacial-drag coefficient (solid line) to the prediction by Ishii and Chawla (long dash) and the prediction by Chexal and Lellouche (dashed line) for a superficial liquid velocity of $0.1 \text{ m} \cdot \text{s}^{-1}$, a pressure of 0.1 MPa , and a hydraulic diameter of 3.5 m .

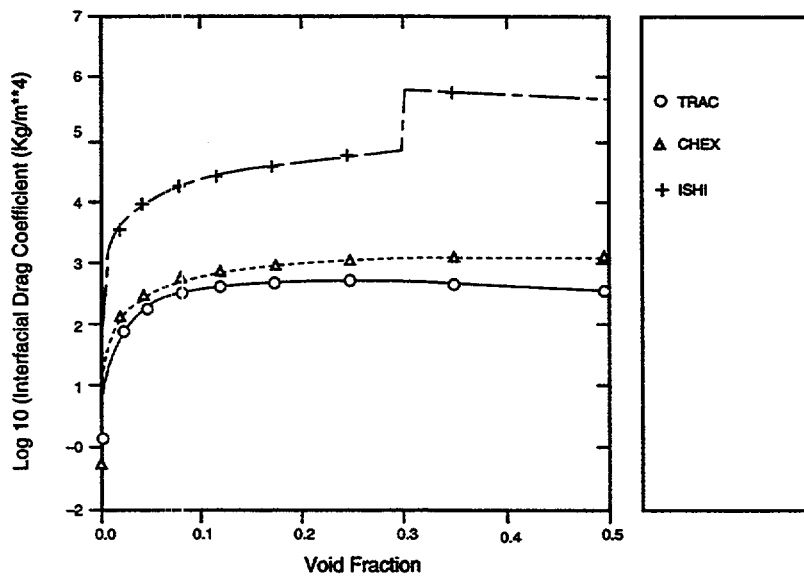


Fig. H-11. Comparison of the TRAC-calculated interfacial-drag coefficient (solid line) to the prediction by Ishii and Chawla (long dash) and the prediction by Chexal and Lellouche (dashed line) for a superficial liquid velocity of $0.1 \text{ m} \cdot \text{s}^{-1}$, a pressure of 0.1 MPa , and a hydraulic diameter of 3.5 m .

We believe that the current models are up to date, consistent, and as realistic as possible. However, we fully expect that there will continue to be discrepancies in future assessments because of the complex nature of two-phase flow and the dependence on the local geometry.

H.1.2. Annular-Mist Correlations

Annular-mist flow is assumed to exist if the void fraction is greater than 0.75. Exceptions to this are stratified flow, flow in the upper plenum of the vessel, core reflood, flow in the accumulator, and CCFL. Major improvements were made to the calculation of the annular-mist interfacial drag in the development of the MOD2 code. The most significant changes were the replacement of the static combination of the droplet and film contributions with an area-weighted average and the use of a recent droplet-diameter correlation from the literature. This provides for a more realistic estimate of the drag and for better comparisons with the data than was possible with the MOD1 code. The calculation of the interfacial drag is identical for the three directions in the 3D VESSEL and for all the 1D components. The description below applies to all components unless specified otherwise.

H.1.2.1. Basis for the Model. The interfacial-drag prediction for annular mist flow in TRAC was based upon the following assumptions:

1. The transient is sufficiently slow so that the interfacial-drag phenomenon is quasi-steady. Therefore, transient forces, such as the apparent mass and the Basset force, are neglected.
2. The effective interfacial-drag coefficient for annular mist can be determined by the addition of the contributions due to the annular film and the entrained drops weighted by their respective area fractions.
3. For the droplet contribution, the interfacial drag can be represented with correlations developed for a solid spherical particle. Therefore, no droplet distortion is assumed. The average droplet diameter can be determined from a correlation as a function of the Weber number based on a roll-wave shearing mechanism.
4. For annular film, the interfacial drag can be represented with a friction-factor correction developed from annular-flow data. In addition, the film thickness is limited by a minimum value so that a transition to rivulet flow will occur.

The annular-mist regime implies the existence of the liquid phase as a combination of annular film and entrained droplets. The code calculates the amount of entrainment based on correlations from Kataoka and Ishii (Ref. H-6.). It calculates the amount of liquid existing as a film by subtracting the entrained liquid from the total amount of liquid. An interfacial-drag coefficient is calculated for the droplets in a manner similar to bubbly flow by assuming there is no droplet distortion. Thus, it follows the theory developed by Ishii and Chawla (Ref. H-1.), Bird, Steward, and Lightfoot (Ref. H-3.), and Shiller and Nauman (Ref. H-4.). A separate interfacial-drag coefficient is calculated for

the liquid film using a correlation proposed by Wallis (Ref. H-15.). The two coefficients are combined with an area-weighted average and divided by a drift velocity developed by Kataoka and Ishii (Ref. H-16.) to determine the interfacial-drag coefficient for annular-mist flow. Since only one liquid field exists in the current version of TRAC, this interfacial-drag coefficient must represent the combined effect of the annular film and the entrained droplets.

As in the case of bubbly slug flow (Section H.1.1.), the pressure drop for the k^{th} phase is proportional to interfacial force per unit volume. Following the theory developed by Ishii and Chawla (Ref. H-1, pp. 13 and 14),

$$\alpha_k \frac{dp}{dz} \sim M_{ik} , \quad (\text{H-34})$$

where α_k is the area fraction of the k^{th} phase and is equal to A_k/A . The force is assumed to be proportional to the square of the relative velocities

$$M_i = C_i |V_r| V_r , \quad (\text{H-35})$$

where C_i is the total interfacial-drag coefficient and has units of $\text{kg} \cdot \text{m}^{-4}$. The total interfacial drag force for the annular-mist-flow regime consists of two components. One component is the contribution from droplets and the other is the contribution from the annular film, i.e., $M_i = M_{id} + M_{ia}$. Before we proceed to calculate the total interfacial-drag coefficient, we need to obtain the individual interfacial-drag coefficients for the components.

The basis for the interfacial-drag coefficient for the droplets follows that of Ishii and Chawla (Ref. H-1.). The drag force on the droplets balances with the total pressure drop as

$$M_{id} \sim \alpha_d \frac{dp}{dz} , \quad (\text{H-36})$$

where

$$M_{id} = \frac{\alpha_d F_d}{Vol_d} . \quad (\text{H-37})$$

For the dispersed flow, we use the drag-force equation given by Ishii and Mishima (Ref. H-17.) as

$$M_{id} = a_i \left[\frac{C_d}{4} \left(\frac{r_{sm}}{r_d} \right) \frac{\rho_g (V_g - V_d)^2}{2} \right] , \quad (\text{H-38})$$

where

$$a_i = \frac{\alpha}{1 - \alpha_d} \frac{3\alpha_d}{r_{sm}} \quad , \quad (\text{H-39})$$

α_d is the droplet area fraction, r_{sm} is the Sauter mean radius, and r_d is the drag radius. The ratio of the Sauter mean radius to the drag radius is defined as a shape factor. For a spherical particle, the shape factor is one. The Sauter mean radius is related to the droplet diameter (Ref. H-16.) by

$$r_{sm} = 0.796 \frac{D_d}{2} \quad . \quad (\text{H-40})$$

Then to determine the drag force, estimates are required for the droplet diameter, for the area fraction of droplets, and for the droplet-drag coefficient. To estimate the droplet diameter, we use a correlation for the volume mean diameter of droplets developed by Kataoka, Ishii, and Mishima (Ref. H-18.). The mechanism assumed for the generation of the droplets is that of shearing from wave crests, such as those produced in annular-mist flow. The droplet diameter is given by

$$D_d = \frac{2.0}{\rho_g j_g^2} \left[0.005 \sigma \left(\frac{\mu_g}{\mu_l} \right)^{2/3} Re_g^{2/3} \left(\frac{\rho_g}{\rho_l} \right)^{1/3} \right] \quad . \quad (\text{H-41})$$

To estimate the droplet-drag coefficient, we use a correlation recommended by Ishii and Chawla (Ref. H-1.). The correlation is given by

$$C_d = \frac{24}{Re_d} (1.0 + 0.1 Re_d^{0.75}) \quad , \quad (\text{H-42})$$

where the droplet Reynolds number is given by

$$Re_d = \frac{D_d \rho_g |V_g - V_d|}{\mu_m} \quad (\text{H-43})$$

and the modified viscosity is

$$\mu_m = \frac{\mu_g}{(1 - \alpha_d)^{2.5}} \quad . \quad (\text{H-44})$$

In annular-dispersed flow, most droplets are in the wake regime because of their relatively small size. We use a relative velocity by Ishii (Ref. H-5.) given by

$$V_g - V_d = D_d \left[\frac{(g\Delta\rho)^2}{\mu_g \rho_g} \right]^{1/3} \alpha_d (1 - \alpha_d)^{1.5} \text{ for} \quad (H-45)$$

$$j > 1.456 \left(\frac{\sigma g \Delta\rho}{\rho_g^2} \right)^{1/4} \left[\frac{\mu_g^2}{\rho_g \sigma (\sigma / g \Delta\rho)^{1/2}} \right]^{-1/12}$$

or

$$V_g - V_d = \sqrt{2} \left(\frac{\sigma g \Delta\rho}{\rho_g^2} \right)^{1/4} \alpha_d (1 - \alpha_d)^{1.5} \quad (H-46)$$

To estimate the droplet area fraction, we use an entrainment correlation developed by Kataoka and Ishii (Ref. H-16.). The correlation is given by

$$E = \tanh(7.25 \times 10^{-7} We_d^{1.25} Re_\ell^{0.25}) \quad (H-47)$$

where the liquid Reynolds number is given by

$$Re_\ell = \frac{\rho_\ell j_\ell D}{\mu_\ell} \quad (H-48)$$

and the droplet Weber number is

$$We_d = \frac{\rho_g j_g^2 D}{\sigma} \left(\frac{\Delta\rho}{\rho_g} \right)^{1/3} \quad (H-49)$$

where

$$\Delta\rho = \rho_\ell - \rho_g$$

For a small droplet, the area fraction of droplets is related to the entrainment by [see Ref. H-16., Eq. (90)]

$$\alpha_d = \frac{j_\ell E}{j_g} \quad (H-50)$$

The basis for the interfacial-drag coefficient for the annular film follows a force balance for a segment of liquid film as shown in Fig. H-12. By integrating the shear stress at the core-to-film interface over a length Δz , we obtain

$$\pi D_c \Delta z \tau_f = \frac{\pi}{4} D^2 \alpha_f \Delta p . \quad (\text{H-51})$$

Here, D_c is the diameter of the core that, from geometric considerations, is given as

$$D_c = \alpha_c^{1/2} D , \quad (\text{H-52})$$

where α_c is the core area fraction [$\alpha_c = \alpha / (1 - \alpha_d)$], α_f is the film area fraction ($\alpha_f = 1 - \alpha_c$), and τ_f is the shear stress at the film-to-core interface.

Similar to the wall-shear stress in single-phase channel flow, the shear stress at the film-to-core interface is given by

$$\tau_f = \frac{1}{2} f_i \rho_c (V_g - V_f)^2 , \quad (\text{H-53})$$

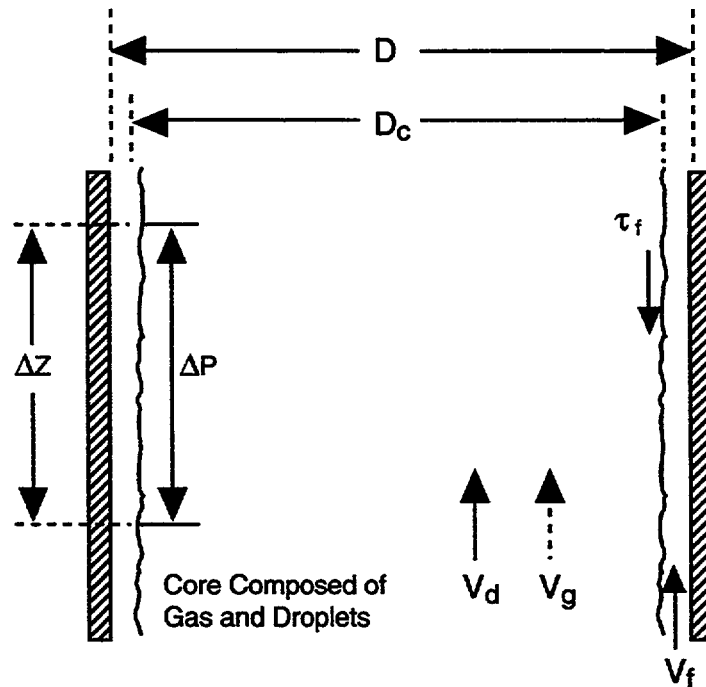


Fig. H-12. Core-to-film momentum balance.

where the density term refers to the gas core and f_i is the film-interface friction factor obtained from correlations. Wallis (Ref. H-15.) provided an empirical relationship for the friction factor in Eq. (11.19) of the reference,

$$f_i = 0.005[1 + 75(1 - \alpha_f)] , \quad (\text{H-54})$$

where, as previously noted, α_f is the film area fraction.

For annular-mist flow, we use the model developed by Ishii and Mishima (Ref. H-17.). The total interfacial shear force denoted by M_i has two sources, namely, the generalized drag M_{id} and the interfacial shear and void gradient M_{ia} . The M_{id} for droplets is given by Eq. (H-38). Ishii and Mishima showed that the interfacial shear and void gradient for annular flow in a tube is

$$M_{ia} = (\Delta\alpha_k \cdot \tau_i) = \alpha_{if} \cdot \tau_f , \quad (\text{H-55})$$

where

$$\alpha_{if} = \frac{4C_{an}}{D} \sqrt{\frac{\alpha}{1 - \alpha_d}} . \quad (\text{H-56})$$

The term τ_f is given by Eq. (H-53) and C_{an} is the roughness parameter due to waves in the film ($C_{an} \geq 1$). By definition, we have

$$M_i = C_{iam} \cdot (V_g - V_{fd}) |V_g - V_{fd}| , \quad (\text{H-57})$$

where C_{iam} is the overall interfacial-drag coefficient for annular-mist flow. In the above equation, we need a formulation for the relative velocity ($V_g - V_{fd}$) to calculate the interfacial-drag coefficient C_{iam} . Kataoka and Ishii (Ref. H-16.) developed a correlation for the relative velocity ($V_g - V_{fd}$) based on the drift-flux model (Ref. H-5.). The correlation is given as

$$V_g - V_{fd} = \frac{1}{\alpha_c + \left[\frac{1+75(1-\alpha_c)\rho_g}{\sqrt{\alpha_c} \rho_\ell} \right]} \left\{ j + \sqrt{\frac{\Delta\rho g_c D(1-\alpha_c)}{0.015\rho_\ell}} \right\} \cdot (1-\alpha_c) + \frac{r_d}{2} \left[\frac{(g_c \Delta\rho)^2}{\mu_g \rho_g} \right]^{1/3} \alpha_d (1-\alpha_d)^{1.5} , \quad (\text{H-58})$$

where, as before,

$$\alpha_c = \frac{\alpha}{1 - \alpha_d} . \quad (\text{H-59})$$

H.1.2.2. Input Required for Implementation. To calculate the interfacial drag using Eqs. (H-38) through (H-58), the void fraction, hydraulic diameter, gas density, liquid density, surface tension, gas viscosity, liquid and vapor viscosity, and relative velocity need to be input.

The definitions are first given for the 1D components. Here, the void fraction is spatially averaged as

$$\langle \alpha \rangle = \frac{\Omega(j)\alpha(j) + \Omega(j+1)\alpha(j+1)}{\Omega(j) + \Omega(j+1)}, \quad (\text{H-60})$$

where the Ω s used in the equation above represent the cell lengths adjoining the cell edge.

The gas density and gas viscosity are donor-celled based on the direction of the gas velocity. The liquid density, surface tension, and liquid viscosity are donor-celled based on the direction of the liquid velocity. [See Eq. (H-24) in Section H.1.1.2. for an example.] The gas velocity used to calculate entrainment is the absolute value of the velocity at the cell edge. The relative velocity used is the absolute value of the difference of the gas and liquid velocities as given in Eq. (H-22).

In the 3D VESSEL, the definitions for the variables are similar to those given for the bubbly slug flow. The void fraction is spatially averaged as given in Eq. (H-60) with cell lengths taking on the values for the three respective directions. For instance, in the axial direction, the Ω s represent the heights of the cells; in the radial direction, the thickness of the rings; and in the azimuthal direction, the average azimuthal thickness of the adjacent cells.

The hydraulic diameter used for the axial and radial direction is the input value given for the axial direction. If the input hydraulic diameter is less than 1.0×10^{-5} , a calculation is made based on the slab heat-transfer area, rod heat-transfer area, and the flow area in the axial direction to provide an effective hydraulic diameter. In the azimuthal direction, the input value at the azimuthal cell edge is used. The azimuthal hydraulic diameter is not allowed to be less than 1.0×10^{-5} .

In the radial and axial directions, the phasic densities, surface tension, and phasic viscosities are the cell-centered values. In the azimuthal direction, the arithmetic average of the adjacent cell-centered values is calculated. [See Eqs. (H-19) and (H-20), for example.]

The relative velocity is required to calculate the Reynolds number for evaluating the droplet diameter [Eq. (H-41)]. In the VESSEL, the relative velocity is defined in the same way as in bubbly slug flow. Therefore, in the axial and radial directions, the V_r is given as described in Eqs. (H-15) and (H-16), respectively. In the azimuthal direction, the V_r is given as described in Eqs. (H-17) through (H-20).

The gas velocity used to calculate the entrainment in Eqs. (H-39) and (H-42) is defined as a vector-average velocity. In the axial and radial directions, this is given as

$$\bar{V}_r = (VVZAV^2 + VVTAV^2 + VVRAV^2)^{0.5} , \quad (\text{H-61})$$

where

$$VVZAV = V_{gz} \left(r, \theta, z + \frac{1}{2} \right) , \quad (\text{H-62})$$

$$VVRAV = \left[V_{gr} \left(r + \frac{1}{2}, \theta, z \right) + V_{gr} \left(r - \frac{1}{2}, \theta, z \right) \right] / 2 , \quad (\text{H-63})$$

and

$$VVTAV = \left[V_{g\theta} \left(r, \theta + \frac{1}{2}, z \right) + V_{g\theta} \left(r, \theta - \frac{1}{2}, z \right) \right] / 2 . \quad (\text{H-64})$$

In the azimuthal direction, a different definition is required because the cell edge adjoins the two cells at θ and $\theta + 1$:

$$\bar{V}_{g\theta} = (VVZAVT^2 + VVTAVT^2 + VVRAVT^2)^{0.5} , \quad (\text{H-65})$$

where

$$\begin{aligned} VVZAVT = & \left[V_{gz} \left(r, \theta, z + \frac{1}{2} \right) + V_{gz} \left(r, \theta, z - \frac{1}{2} \right) \right. \\ & \left. + V_{gz} \left(r, \theta, +1, z + \frac{1}{2} \right) + V_{gz} \left(r, \theta, +1, z - \frac{1}{2} \right) \right] , \end{aligned} \quad (\text{H-66})$$

$$VVRAVT = \left[VVR13 + 0.5 \left(V_{gr} \left(r + \frac{1}{2}, \theta, z \right) + V_{gr} \left(r + \frac{1}{2}, \theta + 1, z \right) \right) \right] / 2 , \quad (\text{H-67})$$

and

$$VVTAVT = \left[V_{g\theta} \left(r, \theta + \frac{1}{2}, z \right) \right] . \quad (\text{H-68})$$

As in the case of bubbly flow, the variable VVR13 is used to account for the special cases that occur in the innermost ring. This variable is defined in Eqs. (H-19) and (H-20).

H.1.2.3. Constants. In the case of the annular film, the constants are coded as they appear in Eq. (H-54). In determination of the entrainment, the Weber number is chosen to be a constant 4.0. This value was chosen based on acceptable developmental assessment results. Sensitivity tests on the effect of the droplet Weber number have shown that variations between 2 and 12 did not strongly influence the results. The work of Hinze (Ref. H-15.) suggests a value of 3.46.

H.1.2.4. Model as Coded. All the coding for the 3D VESSEL is in subroutine CIF3. The interfacial drag in the 1D components is calculated in subroutine StbVel1D (FEMOM in TRAC-M/F77). The model is coded as shown in Eqs. (H-38) through (H-59).

H.1.2.5. Weighting, Averaging, and Limits. Limits are imposed on the allowable droplet size to prevent the calculation of excessively large drag coefficients. In the 3D and 1D models, the droplet diameter is limited to the range 0.000042 to 0.002 m. Other limits imposed on the void fractions are identical to those used in bubbly slug flow. The void fraction used to calculate the interfacial drag is restricted to the range 0.00001 to 0.9999 in all the components.

The rate limits (i.e., allowable changes from one time step to the next) are imposed after the interfacial-drag coefficient computation is complete. Thus, this restriction is the same for all regimes and is fully described in Section H.1.1.4.3.

H.1.2.6. Variations in the Application of the Correlations. The basic relations described here for the annular-mist regime are used throughout the code in all 1D components and in the 3D VESSEL component. In some special cases the interfacial drag is overridden or altered. These cases are

1. core reflood in the vessel (Section H.1.5.),
2. accumulator logic in the PIPE component (Section H.1.6.2.),
3. inverted annular flow (Sections 3.5.5. and H.1.5.),
4. stratified flow in 1D components (Section H.1.3.),
5. user-defined CCFL in the vessel (Appendix I, Section I.3.), and
6. complete phase-separation option in 1D components (Section H.1.6.1.).

These special cases are described separately in the sections listed. Except for these cases and for mass fluxes and void fractions outside the range of the annular-mist regime, the models described here are used for the interfacial drag in each direction in the VESSEL component and in all 1D components.

H.1.2.7. Consistency with the Interfacial Heat Transfer. The interfacial heat-transfer calculation depends directly on the value of the interfacial area. In this respect, the code is consistent, since the same method is used to calculate the entrainment fraction and the droplet diameter. In fact, the same low-level subroutine DEEQ is used in this regard. Differences may occur because the interfacial heat transfer is computed at

the cell centers, and cell-average quantities (such as densities and velocities) are used. Cell-edge quantities are used in the calculation of the interfacial drag.

H.1.2.8. Assessment. The data of Hossfeld and Barathan (Ref. H-19.) were chosen for the assessment calculations because pipe diameters of 0.051 and 0.152 m were both tested. A detailed description of the test facility and test conditions was given in the reference. A comparison of TRAC-calculated liquid fraction versus the dimensionless superficial gas velocity with the data is shown in Fig. H-13, where the dimensionless superficial gas velocity is given as

$$j_g^* = j_g \left(\frac{\rho_g}{g_c D \Delta \rho} \right)^{1/2} \quad (\text{H-69})$$

and

$$j_l^* = j_l \left(\frac{\rho_l}{g_c D \Delta \rho} \right)^{1/2} \quad (\text{H-70})$$

The TRAC results are in good agreement with the data in the middle and high ranges of the gas velocities but show a poor comparison at the low values.

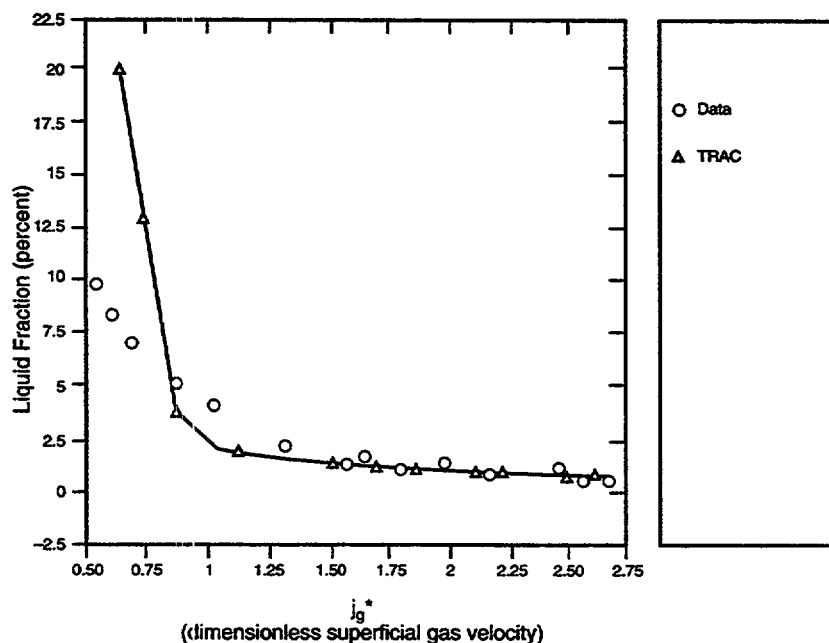


Fig. H-13. Liquid fraction comparison using the modified Wallis correlation.

H.1.2.9. Effects of Using the Correlations Outside the Database. As discussed in Section H.1.2.8., the database for the film-drag coefficient was small-scale pipe data. When applied to the case of downcomer geometry, the calculated interfacial drag appeared to be too small, thus allowing the excessive downflow of liquid at low gas velocities. At the higher gas velocities near the CCFL point, the prediction was in reasonable agreement with the data.

H.1.2.10. Scaling Considerations. The film-drag component of the annular-mist-flow regime is based on the Wallis correlation. Since this correlation was developed based on small-scale data, it may prove to be unacceptable at larger diameters associated with actual PWR hardware.

The droplet-drag component of the annular-mist-flow regime should scale appropriately if we assume that the droplet diameter and entrainment rate are accurately predicted.

H.1.2.11. Summary and Conclusions. As indicated in Section H.1.2.8., TRAC overpredicted the liquid fraction in the low dimensionless superficial gas velocities. In the future, we need to improve the model in the low dimensionless superficial gas velocity range. The interfacial-drag coefficient in the annular-mist-flow regime is calculated using a film-drag coefficient combined with a droplet-drag coefficient. The contributions of each are weighted with their respective liquid fractions based on the computed entrainment. An alternative method for combining the drag coefficients should be investigated to better represent the total movement of liquid.

H.1.3. Stratified-Flow Correlation

In the 1D components, the code calculates a stratified-flow interfacial-drag coefficient if the cell-edge velocities are less than critical values and if the angle that the cell edge makes with the horizontal is within certain limits. In the 3D VESSEL, stratified flow is allowed if there is a certain gradient in the void fraction and if the vapor flow from the bottom is below a certain limit. The limits for both the 1D and 3D models are described in Appendix E, Section E.2.7. This section describes the interfacial-drag coefficient in stratified flow.

H.1.3.1. Basis for the Model. The calculation of the stratified-flow interfacial-drag coefficient is based on Taitel and Dukler (Ref. H-20.) and Ohnuki et al. (Ref. H-21.).

As in the case of bubbly slug and annular-mist flows, we assume that the stratified flow is quasi-steady and that the transient forces can be neglected. In the code we assume that the stratified-flow regime can occur in the 1D components and the 3D VESSEL. Temporal changes in the stratified-flow interfacial-drag coefficient are limited in the same manner as the bubbly slug and annular-mist coefficients.

The stratified-flow interfacial-drag coefficient is derived from the method given in Taitel and Dukler (Ref. H-20.). In the reference, the momentum equations for the liquid and gas phases are combined through the elimination of the pressure drop. In TRAC the momentum equations are solved separately. Therefore, to demonstrate the derivation of

the interfacial-drag coefficient, we consider the gas-phase momentum equation only. From Taitel and Dukler (Ref. H-20, Eq. 2), the pressure drop in the gas caused by interfacial drag with the liquid is given by

$$\frac{dp}{dx} = \frac{1}{2} f_i \rho_g V_r^2 \frac{S_i}{A_g} \quad , \quad (\text{H-71})$$

where

- $\frac{dp}{dx}$ is the pressure drop,
- f_i is the interfacial friction factor,
- ρ_g is the density of the gas,
- V_r is the relative velocity,
- S_i is the width of the stratified interface, and
- A_g is the gas phase flow area.

In the reference, Taitel and Dukler assume that the liquid velocity is small, so that the relative velocity is approximated by the gas velocity. In the code, however, we use the relative velocity.

The TRAC gas momentum equation [Section 2.1.1, Eq. (2-6)] gives the same pressure drop as

$$\frac{dp}{dx} = \frac{c_i V_r^2}{\alpha} \quad , \quad (\text{H-72})$$

where

- c_i is the interfacial-drag coefficient ($\text{kg} \cdot \text{m}^{-4}$) and
- α is the gas fraction.

Note that the term $c_i V_r^2$ is the volumetric interfacial force ($\text{N} \cdot \text{m}^{-3}$) described in Section H.1.1.1. Combining Eqs. (H-71) and (H-72) and solving for c_i yields

$$c_i = \frac{1}{2} f_i \rho_g \frac{S_i}{FA} \quad , \quad (\text{H-73})$$

where A_g has been replaced with the product of the total flow area of the channel (FA) and the void fraction (α).

This is the equation used in the 1D components and is consistent with the assumption of circular pipe geometry. In the 3D VESSEL, however, the ratio of the width of the stratified interface to the available flow area is equivalent to a hydraulic diameter, or in this case, the height of the flow channel that exists in the radial and azimuthal directions. Therefore, in this situation we use

$$C_i = \frac{1}{2} \frac{f_i \rho_g}{HD} \quad , \quad (\text{H-74})$$

where HD is the average of the level height in the level of interest and the level above. If there is a zero flow in the radial or azimuthal direction or in the level above, HD is calculated by multiplying the current level height by the local void fraction. A situation like this may occur in the region between the lower plenum and the downcomer skirt. In this situation, a stratified-flow interfacial-drag coefficient is significantly lower than that of bubbly flow and would allow far less sweep-out during blowdown.

In the code, f_i is determined using the Ohnuki correlation as

$$f_i = 1.84 f_{wg} \quad , \quad (\text{H-75})$$

where

$$\begin{aligned} f_{wg} &= \frac{16.0}{Re_g} && \text{if laminar,} \\ f_{wg} &= \frac{0.079}{Re_g^{0.25}} && \text{if } Re_g < 10^5, \\ f_{wg} &= 0.0008 + \frac{0.05525}{Re_g^{0.237}} && \text{if } Re_g \geq 10^5, \text{ and} \end{aligned} \quad (\text{H-76})$$

Re_g = the liquid Reynolds number.

This correlation provides the best assessment results of the available correlations found in the literature.

H.1.3.2. Input Required to Implement the Correlation. To calculate the interfacial-drag coefficient as given in Eq. (H-74), it is necessary to define the gas density, the void fraction, the flow area of the channel, and the width of the stratified interface. In the 1D model, the gas density used is distance-weighted with the lengths of the cells on either side of the interface as follows:

$$\langle \rho_g \rangle = \frac{\rho_g(j)DX(j) + \rho_g(j+1)DX(j+1)}{DX(j) + DX(j+1)} \quad , \quad (\text{H-77})$$

where

$DX = \text{cell lengths}$

and the j and $j + 1$ indexes refer to the cell locations adjacent to the cell edge or interface.

The void fraction used is calculated in the same manner as in Eq. (H-77), with the additional constraint that it is not allowed to be greater than 0.9999 or less than 1.0×10^{-5} to avoid divisions by zero.

The channel cross section in the 1D model is assumed to be circular. The flow area is calculated from

$$FA = \frac{\pi}{4} \text{diam}^2 \quad , \quad (\text{H-78})$$

where

$$\text{diam} = \max[\text{diam}(j + 1), \text{diam}(j)] \quad ,$$

$$\text{diam}(j) = \left(\frac{4\text{vol}(j)}{\pi DX(j)} \right)^{0.5} \quad ,$$

$$\text{diam}(j + 1) = \left(\frac{4\text{vol}(j + 1)}{\pi DX(j + 1)} \right)^{0.5} \quad ,$$

$\text{vol}(j) = \text{volume of cell } j$, and

$\text{vol}(j + 1) = \text{volume of cell } j + 1$.

Thus, the flow area used is the maximum of the cells on each side of the interface (as designated by the j and $j + 1$ indexes). The width of the stratified interface is calculated from

$$S_i = \text{diam} \left[1.0 - \left(\frac{2h_\ell}{\text{diam}} - 1.0 \right)^2 \right]^{0.5} \quad , \quad (\text{H-79})$$

where h_ℓ is the height of the stratified layer of liquid lying in the bottom of the pipe. In the code, h_ℓ is calculated from the void fraction using a polynomial curve fit as follows:

if $\alpha \leq 0.5$ then $X = \alpha$ and

$h_\ell = Y$, or

if $\alpha > 0.5$ then $X = 1.0 - \alpha$ and

$h_\ell = \text{diam} - Y$,

where

if $X \leq 0.001$ then

$$Y = (1.0 - 7.612668 \cdot X) \cdot \text{diam}, \quad \text{or} \quad (\text{H-80})$$

if $0.001 < X \leq 0.5$ then

$$Y = (1.0 - 0.70269591 \cdot X^{0.6666666667} - 0.034146667 \cdot X - 0.161023911 \cdot X^{2.0}) \cdot \text{diam}.$$

The void fraction used above is the distance-weighted value described above, and the diameter is as given in Eq. (H-78). The value of h_l is not allowed to be less than 0.001 times the diameter (diameter). As noted above, in the 3D model the horizontal direction hydraulic diameter is used rather than the S_i and FA used in the 1D model.

H.1.3.3. Constants. The value of π used in Eq. (H-78) is a constant 3.14159.

H.1.3.4. Model as Coded. The model is coded as shown in Eq. (H-74) in subroutine StbVel1D (FEMOM in TRAC-M/F77) for the 1D component, and in subroutine CIF3 for the 3D component. The calculation of the stratified liquid level is determined as shown in Eq. (H-80) in subroutine LEVEL.

H.1.3.5. Weighting, Averaging, and Limits. The gas density and void fraction are averaged over distance as shown in Eq. (H-77). The height of the liquid level [Eq. (H-80)] is limited to 0.001 times the diameter [diameter given in Eq. (H-78)]. The void fraction is limited to a range less than or equal to 0.9999, and greater than or equal to 1.0×10^{-5} . These limits avoid divisions by zero. The final interfacial-drag coefficient used in the momentum equation is as shown in Eq. (H-74) if the gas and liquid velocities are below the critical values (described in Appendix E). If the critical values are exceeded, then the transition from stratified flow is calculated with weighting factors using the phasic velocities as the independent variable. The weighting factor is calculated in Appendix E.

The weighting factors are applied to calculate the final interfacial-drag coefficient and are combined with the bubbly slug or annular-mist interfacial-drag coefficients if the transition is occurring. The application of the weighting factors and the limits on the final interfacial-drag coefficient are described in the section on transitions (Section H.1.4).

H.1.3.6. Consistency with Interfacial Heat Transfer. The calculation of the interfacial heat transfer in stratified flow is determined using an interfacial area, a heat-transfer coefficient, and the temperature difference between the steam and the liquid. To be consistent with the interfacial-drag calculation, the interfacial area calculation must be similar, but because the interfacial drag is calculated at the cell edges and the heat transfer is calculated at the cell centers, small inconsistencies may exist. The interfacial area is calculated from the definition of the width of the stratified interface and the length of the cell. The width of the stratified interface is calculated in the same manner as given in Eq. (H-79). The value for the height of the liquid level used in Eq. (H-79) may be

slightly different since the cell-centered quantities for the void fraction and the diameter may in some cases be different from the cell-edge average quantities used in the calculation of the interfacial drag.

In addition, for the calculation of the interfacial heat transfer, the determination of the critical velocities is based on the cell-average quantities rather than the cell-edge quantities. To make the models more consistent, the weighting factor *WFHF* is saved during the interfacial-drag calculation and used in the calculation of the interfacial heat transfer.

H.1.3.7. Assessment of the Correlation. In this section we present the assessment of the code against full-scale countercurrent flow data recently obtained in the Upper Plenum Test Facility (UPTF). Therefore, although the interfacial friction factor is not assessed directly, this work is a verification of the two-fluid model with the calculation of the interfacial shear as a dominant term in the momentum equations.

The test setup for the countercurrent flow test in the UPTF hot leg is shown in Fig. H-14. Saturated water is injected into the inlet plenum of the steam-generator simulator and flows through the hot leg towards the vessel (not shown). Steam is injected through the core simulator in the vessel, and because of the configuration of the facility, is forced to flow countercurrent to the liquid in the hot leg. This situation is similar to what is hypothesized to occur in the event of a small-break LOCA in a PWR, in which steam produced in the core flows into the steam generator, is condensed on the tubes, and then flows back towards the vessel as condensate. This phenomenon is referred to as "reflux condensation." It is important to determine whether TRAC can predict the countercurrent flow of liquid in such a situation.

The test procedure is depicted in Fig. H-15. First the water flow in the hot leg was established, and then the steam flow. Both were held constant for the duration of the test. Each test run lasted about 100 to 150 s. The TRAC calculations were run in the same manner. In addition to testing the constant friction factor used in TRAC, we also tested other correlations for the purpose of comparison, using an experimental version of the code. The other correlations tested were Lee and Bankoff, Ohnuki et al. (Ref. H-21.), Kim (Ref. H-22.), and Linehan (Ref. H-23.).

The following Kim and Linehan correlations are similar in that they are dependent on the liquid Reynolds number:

$$f_i = a Re_\ell + b \quad , \quad (H-81)$$

where

$$a = 0.14 \times 10^{-5} \quad , \quad b = 0.021 \quad , \quad \text{Kim} \quad ,$$
$$a = 0.23 \times 10^{-5} \quad , \quad b = 0.013 \quad , \quad \text{Linehan} \quad .$$

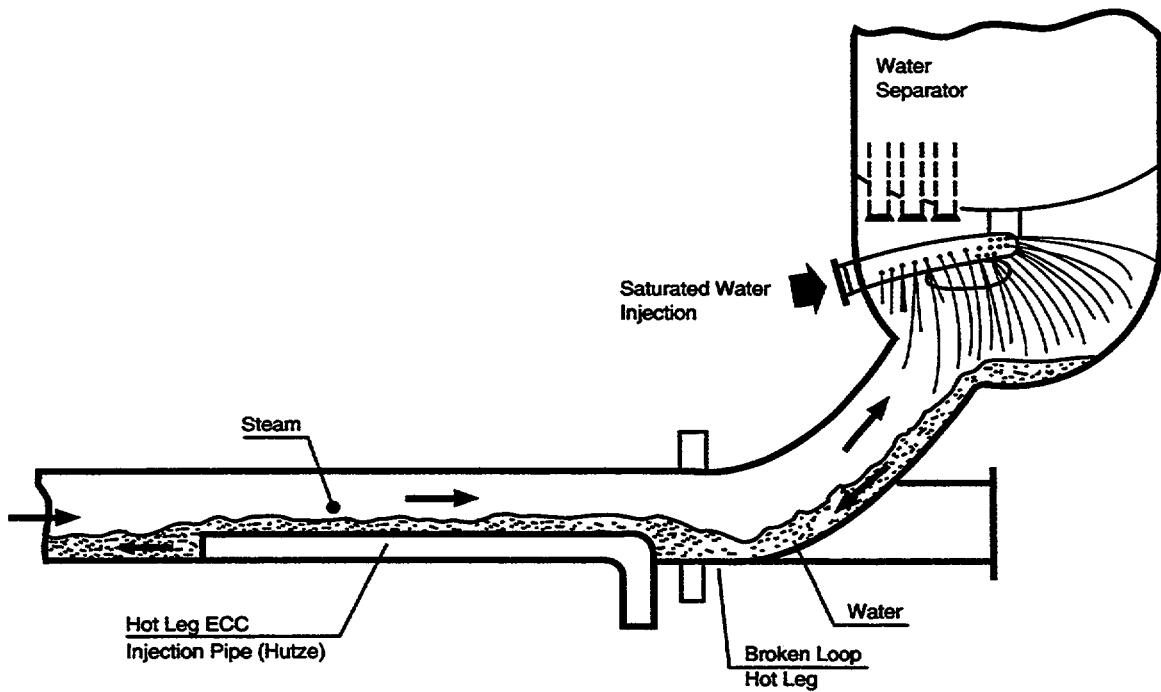


Fig. H-14. Test setup for the UPTF hot-leg countercurrent flow test.

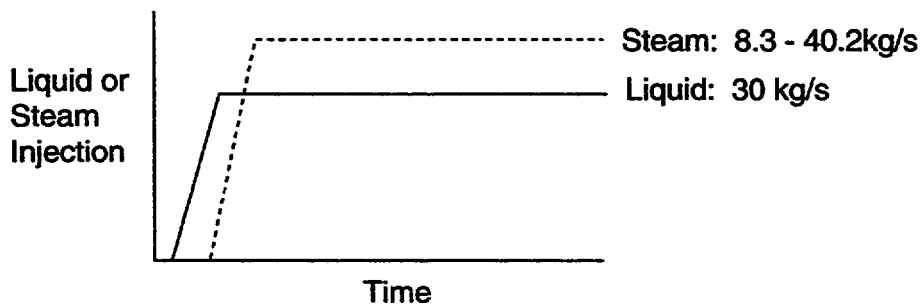


Fig. H-15. Procedure used for the injection of steam and water for the hot-leg countercurrent flow test.

The results for the assessment against the data at 1.5 MPa are shown in [Table H-2](#). Here, the liquid downflow rate is presented at the various steam flows. In all test runs (except Run 037), the liquid-injection rate was 30 kg/s. In test Run 037 a liquid-injection rate of 9.8 kg/s was used to model the actual PWR conditions during reflux condensation. As shown in the table, the liquid downflow rate in the experiment decreased as the steam flow was increased. For TRAC-PF1/MOD1, the complete liquid delivery at the reflux condensation conditions was predicted. However, the liquid delivery at the low

steam flows was overpredicted, and the CCFL point was underpredicted. The MOD2 code using the Ohnuki correlation predicts the CCFL point, but still overpredicts the downflow of liquid at the low steam-flow rates. The Lee and Bankoff and the Kim and Linehan correlations overpredicted the interfacial friction factor, and prevented the downflow of liquid except at the very low steam-injection rate of 8.3 kg/s. This is caused by the fact that at full-scale, high-pressure conditions, the gas Reynolds number for this test is on the order of 1.0×10^6 , and the liquid Reynolds number is on the order of 1.0×10^5 . Thus, all three correlations produce very high friction factors and cause the early turnaround as shown in the table.

TABLE H-2.
Comparison to Data

- UPTF Test no. 11, Phase A
- Pressure = 1.5 MPa
- Saturated Steam and Water Injection
- Water Injection 30 kg/s (except Run 037, 9.8 kg/s)

-UPTF Test No.	Steam Injection Rate (kg/s)	Water Downflow Rate (kg/s)				
		UPTF Test Result	MOD1 $f_i=0.02$	MOD2 f_i based on Ohnuki	MOD2 f_i based on Lee, Bankoff	MOD2 f_i based on Kim, Linehan
037 ^a	8.3	9.8	9.8	9.8	9.8	9.8
038	18.1	30.0	30.0	30.0	0.0	0.0
039	24.0	25.2	30.0	30.0	0.0	0.0
045	28.0	14.2	22.2	22.2	0.0	0.0
040	31.0	5.4	21.8	22.0	0.0	0.0
043	33.5	2.0	0.0	20.0	0.0	0.0
042	36.0	0.6	0.0	15.0	0.0	0.0
041	40.2	0.0	0.0	0.0	0.0	0.0

a. Typical PWR reflux condensation conditions.

The use of the Ohnuki correlation shows a better prediction of the CCFL point and does not produce the large friction factors associated with the other correlations tested. When we compare this correlation to the constant value used in MOD1 at typical gas Reynolds numbers (Fig. H-16.), we observe that at the higher values of gas flow, the MOD1 friction factor is too large. This is consistent with the assessment result in Table H-2., where the CCFL point is calculated at a lower steam flow than occurred in the data. Based on this assessment, we conclude that at full-scale conditions, the constant value of the friction factor provides an overall reasonable estimate of the interfacial drag. However, the prediction of the CCFL point is improved with the use of the Ohnuki correlation. This correlation was therefore chosen for use in MOD2.

H.1.3.8. Effects of Applying the Model Outside the Database. The Ohnuki correlation is applicable to a very large Reynolds number range and, therefore, should be applicable in most situations.

H.1.3.9. Scaling Considerations. Although the Ohnuki correlation was developed from small-scale data, assessment against full-scale UPTF data is favorable. Therefore, the scaling of the correlation appears promising.

H.1.3.10. Summary and Conclusions. The method used for the calculation of the interfacial drag in stratified flow follows that of Taitel and Dukler and Ohnuki. Assessment shows that the correlation proposed by Ohnuki for the friction factor better predicts the CCFL point. Based on our assessment, the MOD2 and TRAC-M codes should provide a reasonable simulation of full-scale PWR stratified flow.

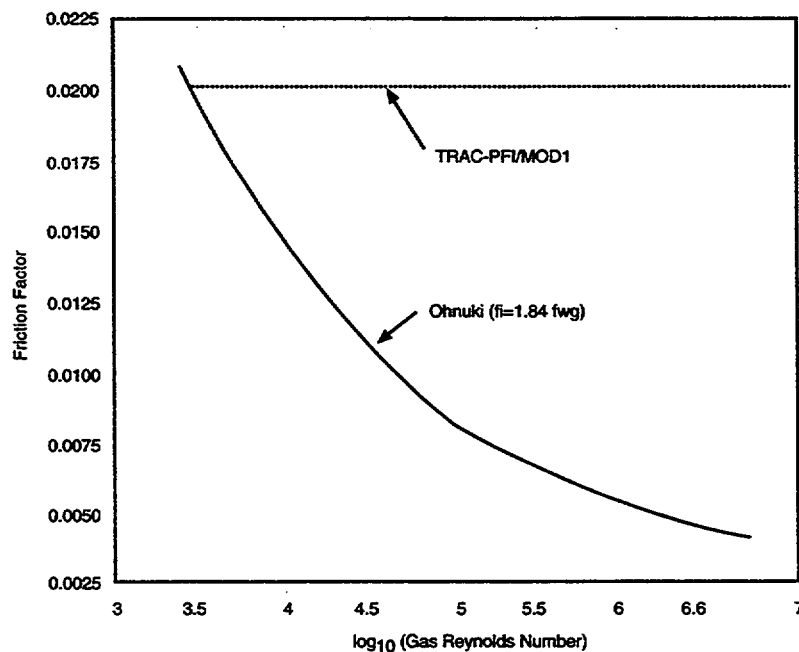


Fig. H-16. Comparison of the Ohnuki correlation with TRAC.

H.1.4. Transitions Between Bubbly Slug, Annular-Mist, and Stratified Flows

In the void-fraction range 0.5 to 0.75, the transition is made between the bubbly slug and annular-mist-flow regimes. This is sometimes referred to as churn-turbulent flow. In the code, a separate correlation for the interfacial drag is not used; rather, we average the bubbly slug interfacial-drag coefficient with the annular-mist interfacial-drag coefficient.

H.1.4.1. Transition Between Bubbly Slug and Annular-Mist Flows. The code calculates an interfacial-drag coefficient assuming the bubbly slug flow regime if the void fraction is ≤ 0.5 . If the void fraction is ≥ 0.75 , the annular-mist-flow regime is assumed. If the void fraction is between 0.5 and 0.75, the interfacial drag is calculated from the following average:

$$c_{itrans} = c_{iam}(WX) + c_{ibs}(1 - WX) \quad , \quad (H-82)$$

where

- c_{itrans} = transition interfacial-drag coefficient,
- c_{iam} = annular-mist interfacial-drag coefficient,
- c_{ibs} = bubbly slug interfacial-drag coefficient,
- WX = $4\alpha - 2$, and
- α = the distance-weighted void fraction.

The weighting factor WX is limited to be between 0.0 and 1.0. From the above equations we note that at a void fraction of 0.5, WX is 0.0. At a void fraction of 0.75, WX is 1.0. The method of calculating the transition interfacial-drag coefficient is identical in each of the three directions in the 3D. The differences occur in the distance weighting of the void fraction, which is directionally dependent, as described in [Section H.1.1.2](#). The annular-mist drag coefficient (c_{iam}) is calculated in the method as described in [Section H.1.2.1](#). The bubbly slug drag coefficient (c_{ibs}) is calculated using the method described in [Section H.1.1.1](#).

H.1.4.2. Transition to Stratified Flow. Transition to stratified flow is also linear, depending on the critical velocity. Stratified flow may occur in any 1D component or in the 3D VESSEL in the radial or azimuthal direction. As described above in [Section H.1.3.5](#), the weighting factor ($WFHF$) is calculated as the velocity drops below the critical velocity required for stratified flow to exist. For transition to stratified flow, the total interfacial drag is calculated by

$$c_i = (1 - WFHF)(c_{ibs} + c_{iam} + c_{itrans}) + WFHF(c_{ist}) \quad , \quad (H-83)$$

where c_{ibs} , c_{iam} , and c_{itrans} are set to 0.0 unless the void fraction dictates their respective regimes.

H.1.5. The Core-Reflow Interfacial-Drag-Coefficient Model

During postulated severe accidents in PWRs, the core can become uncovered, lose its cooling, and eventually heat up due to the decay heat of the fission process. Emergency core-cooling systems are designed to replenish the water that was lost from the system, and in the case of core uncover, reflow it. The reflooding rates are typically large (greater than 2.54 cm/s), and the water usually contains a large amount of subcooling (liquid temperature of 300 K, with the saturation temperature near 400 K). Experiments have shown that for typical conditions, one can expect inverted annular flow to exist in the core region as it refloods (see [Appendix F, Section F.1, Fig. F-25.](#)) A quench front is established that eventually moves up the core as the rods cool. The heat-transfer regimes from bottom to the top are listed as forced convection to liquid, subcooled nucleate boiling, transition boiling near the quench front, inverted annular-flow film boiling, and dispersed-flow film boiling as shown in [Fig. F-25.](#) in [Appendix F, Section F.1.](#) The location of the critical heat flux is at the top of the transition boiling region.

Ishii and DeJarlais ([Ref. H-24.](#)) performed visualization experiments of inverted annular flow (IAF) in the central channel of a heated double-quartz tube. A summary of their qualitative results is depicted in [Fig. F-25.](#) (see [Appendix F, Section F.1.](#)) The inverted annular region was initiated using a concentric injection nozzle. Motion pictures, as well as still photographs, were taken to identify the flow-regime characteristics. In a region directly downstream of the nozzle, a smooth liquid core was observed. This was followed by an inverted annular region with wave development on the liquid surface. The wavelengths were of the order 10 mm, with droplets being sheared from the wave crests. Also observed (although not shown in the figure) was a thin, highly agitated annulus of liquid near the heated wall. Above this region, an agitated slug/churn region was observed. Droplets (0.003-m diameter) swept past the slugs. The slugs were deformed into multiple ligaments and eventually broke up. In the dispersed region, the droplets evaporated and acted to de-superheat the steam. Several droplet sizes were observed originating from the agitated liquid annulus (0.00005 m), from the wave crests (0.0002 m), and from the slug break-up (0.0006 to 0.003 m).

Ishii and DeJarlais ([Ref. H-25.](#)) derived flow-regime transition models for their double-quartz tube experiment. Also, it was observed that the interfacial waves in the agitated region moved at a velocity 5 to 10 times the liquid injection velocity.

Obot and Ishii ([Ref. H-26.](#)) derive the transition criteria based on the visualization experiments. The final results are put in terms of the capillary number and the length above the quench front as follows:

$$\text{Smooth Section: } L / D \leq 60 \text{ Ca}^{1/2} , \quad (\text{H-84})$$

$$\text{Rough Wavy: } 60 \text{ Ca}^{1/2} < L / D \leq 295 \text{ Ca}^{1/2} , \quad (\text{H-85})$$

$$\text{Agitated: } 295 \text{ Ca}^{1/2} < L / D \leq 595 \text{ Ca}^{1/2} , \text{ and} \quad (\text{H-86})$$

$$\text{Dispersed: } 595 \text{ Ca}^{1/2} < L / D , \quad (\text{H-87})$$

where

$$\text{Ca} = \text{Capillary Number} = \frac{\mu_l V_l}{\sigma} \quad (\text{H-88})$$

Obot and Ishii observed large droplets in the dispersed flow. These large droplets get smaller and smaller when the void fraction increases further downstream of the agitated region. Thus, the dispersed flow in the TRAC core-reflood model is considered to consist of a dispersed-flow regime with large droplets (post-agitated region) and of a highly dispersed flow regime with fine droplets. The highly dispersed flow regime is assumed to occur when the cell void fraction is greater than 98%.

Models for the interfacial drag in a reflooding core are developed based on the inverted-annular-flow map, as shown in Fig. F-25. of Appendix F, Section F.1., proposed by Ishii and his coworkers (Refs. H-24., H-25., and H-26.). For each flow regime shown in Fig. F-25., a separate interfacial-drag model is developed. Furthermore, models for each flow regime are redefined in the flow-regime void-fraction plane based upon the cell void fraction, as in Fig. H-17a. Three void-fraction regions are identified: (1) the low-void-fraction region characterized by void fractions less than 75%; (2) the high-void-fraction region characterized by void fractions higher than 98%; and (3) the intermediate void-fraction region between high- and low-void-fraction regions. Fig. H-17b. shows the interfacial-drag coefficient (IFDC) selection logic used in the TRAC core-reflood model. The core-reflood IFDC model is coded in subroutine CIF3, which is called by VSSL1 for each level in the VESSEL component. In the following section, the interfacial-drag models for each IAF regime are presented from the bottom to the top of the channel in the following order: subcooled boiling, smooth inverted annular, rough-wavy inverted annular, agitated, dispersed (or post-agitated region), and highly dispersed flow. The assessment of individual models is not discussed in each section. The last section discusses the assessment of overall core-reflood drag models with CCTF Run-14 data.

H.1.5.1. Subcooled-Boiling Interfacial-Drag Model.

H.1.5.1.1. Basis for the Model. The subcooled-boiling models are characterized by two regions: (1) the partial boiling region, in which the bubbles remain attached to the wall, and (2) the fully developed boiling region, where bubbles enter the free stream and eventually collapse due to condensation (Ref. H-27.). In the partial boiling region, the wall is sufficiently hot to cause a layer of superheated liquid to exist in the vicinity of the surface and cause bubble formation. The bulk fluid remains subcooled, hence the term "subcooled boiling". As shown in Fig. H-18., the dominant forces on a bubble are buoyancy, drag, and surface tension.

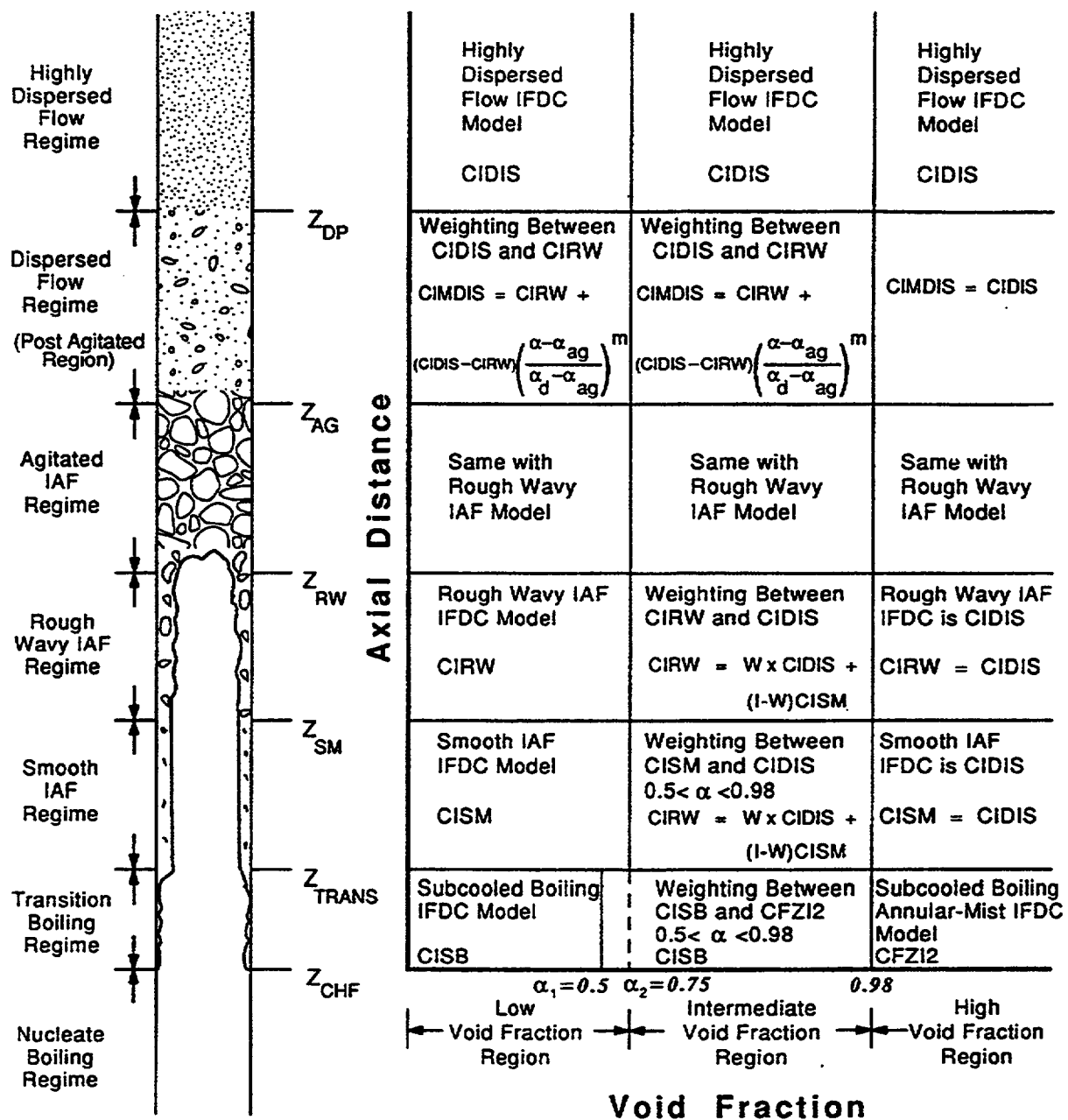


Fig. H-17a. The interfacial-drag coefficient model selection logic in the IAF regimes—void-fraction plane.

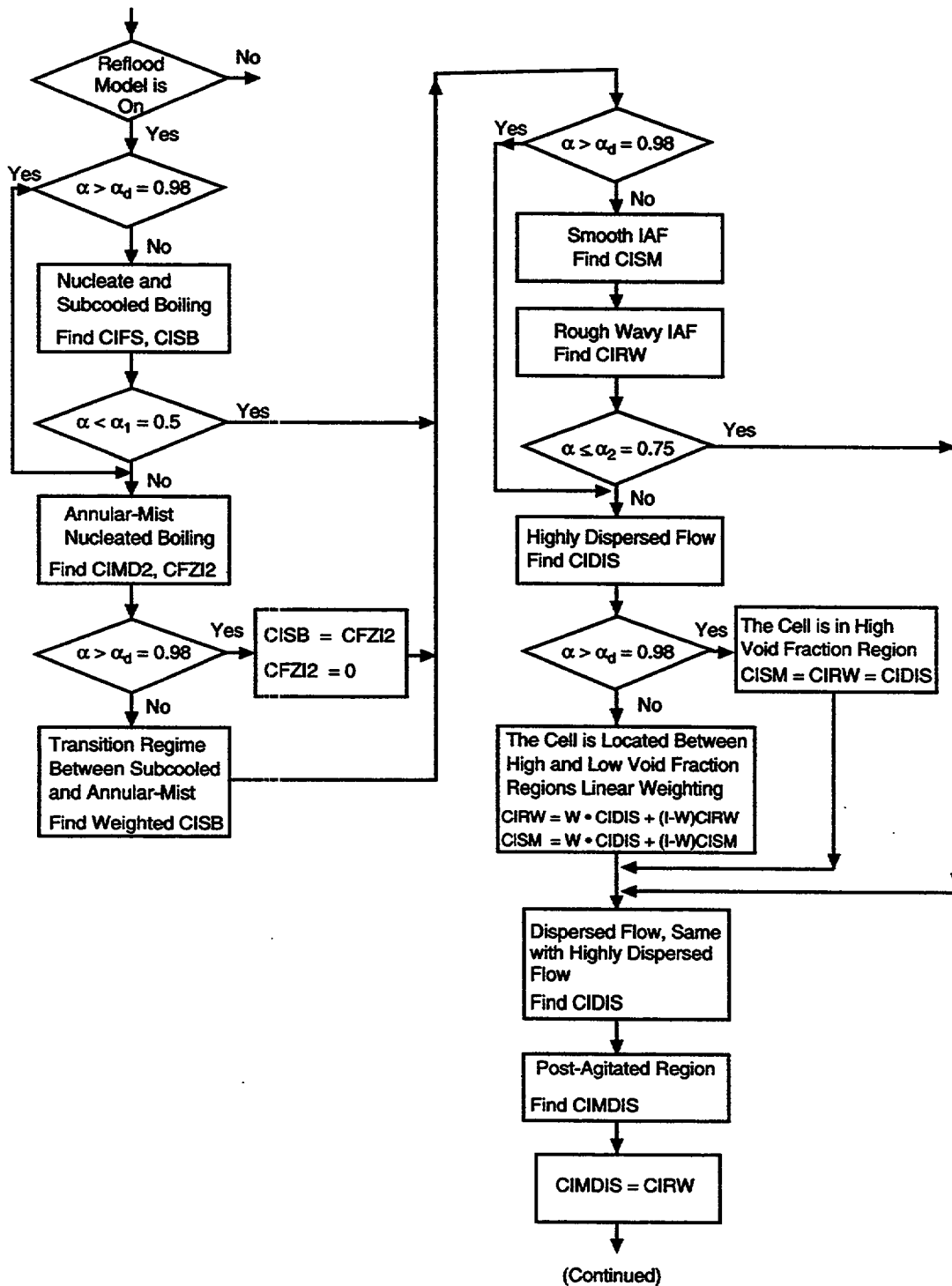


Fig. H-17b. The interfacial-drag coefficient model selection logic used in the core-reflood model.

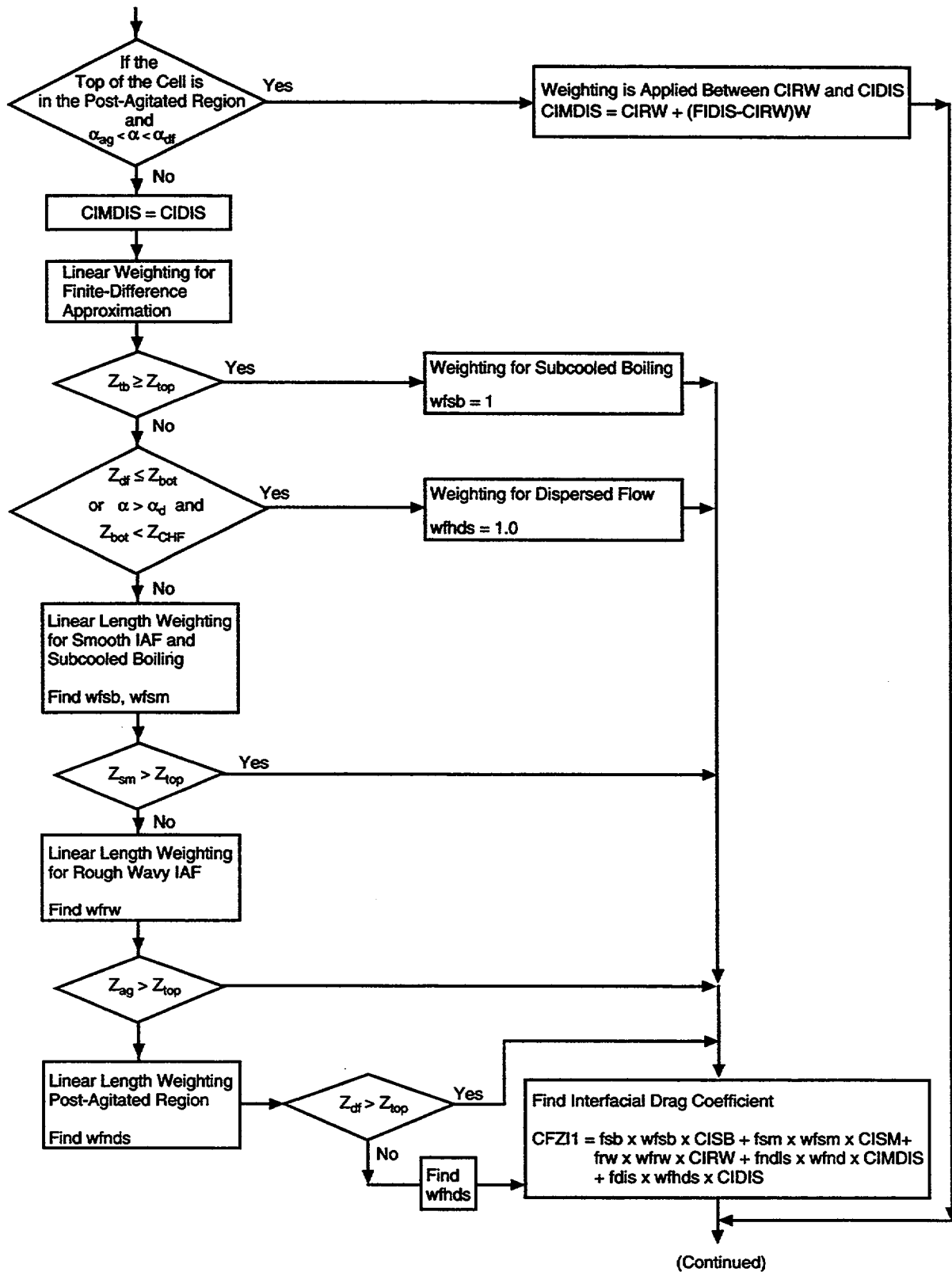


Fig. H-17b (cont). The interfacial-drag coefficient model selection logic used in the core-reflood model.

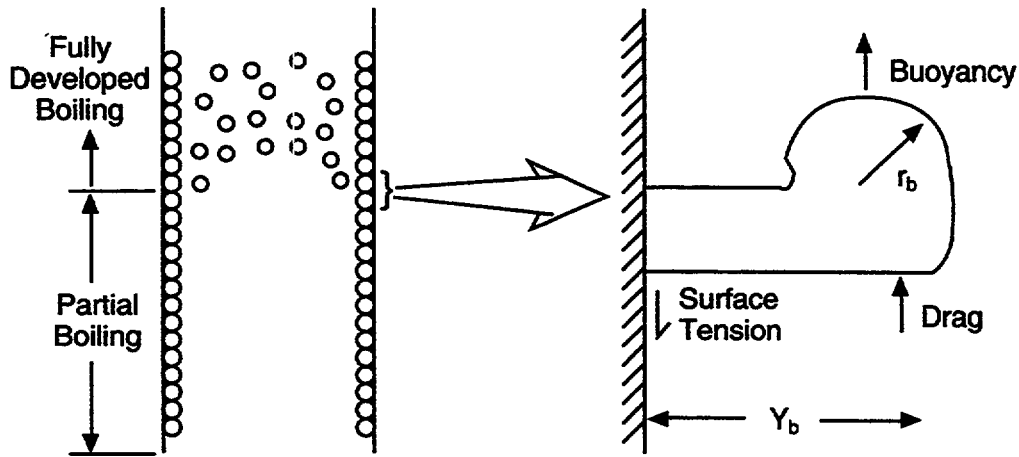


Fig. H-18. Bubble attached to wall in subcooled boiling (Ref. H-27.).

For a bubble of diameter 1 mm, near atmospheric pressure, the surface-tension force is of the order 60×10^{-6} N, and the buoyancy force about 10×10^{-6} N. The drag force depends on the liquid flow, bubble distortion, and other parameters, but it can be seen by this simple order-of-magnitude calculation that the surface-tension force can be significant, keeping the bubbles close to the wall. In addition, if many bubbles are closely packed, then the drag force should decrease due to the "shielding" effect of the surrounding bubbles. Collier (Ref. H-27.) indicates that the bubble height from the wall can be estimated by

$$Y_b = C \left[\frac{\sigma D_h}{\tau_w} \right]^{1/2} \left[1 + C' \left(\frac{g(\rho_l - \rho_g) D_h}{\tau_w} \right) \right]^{-1/2} \quad (\text{H-89})$$

for the case of closely packed bubbles.

Collier indicated that Levy evaluated the constants C and C' in Eq. (H-89) from experimental data and gave 0.015 and 0.0 for C and C' , respectively. The wall shear stress, τ_w in Eq. (H-89) is obtained from the relationship

$$\tau_w = \left[\frac{f_{f0} G^2}{2\rho_l} \right], \quad (\text{H-90})$$

where f_{f0} is the single-phase friction factor corresponding to a relative roughness of $\varepsilon/D_h = 10^{-4}$. Thus, based on the Colebrook correlation for fully turbulent flow over rough surfaces, the friction factor can be found as

$$f_{f0} = \frac{1}{(1.14 - 2 \log_{10} \frac{\varepsilon}{D_h})^2} = 0.01197037. \quad (\text{H-91})$$

To develop an interfacial-drag model for the subcooled-boiling region, one could attempt to analyze the partial boiling and fully developed boiling regions separately. In the fully developed region, the bubbles entering the free stream quickly collapse due to condensation, and the majority of the bubbles remain in the vicinity of the wall. Therefore, the bubbles for both regions are assumed to exist in a layer close to the wall, and models developed for the partial boiling region are assumed to apply to the fully developed region as well. However, if the liquid core becomes saturated or superheated, a model for IFDC is also developed to account for the interfacial drag resulting from bubbles flowing in the free stream.

In the partial boiling region, the surface-tension force that firmly attaches the bubbles to the wall is not taken into account for the two-fluid approximation. A modification to the interfacial-drag coefficient to account for this restoring force would require a negative value. This is clearly unacceptable due to the potential for destabilization of the solution. Sensitivity calculations show that a small positive value on the order of $1 - 10 \text{ kg/m}^4$ for C_i will allow for a reasonable prediction of the void fraction below the quench front.

If one assumes a bubble-drag model similar to the case of adiabatic flow in a channel, where the bubbles are dispersed, the calculated interfacial drag is very large (for a bubble size of 0.001 m , $C_i = 300\,000 \text{ kg/m}^4$). When applied to the two-fluid model, this would cause the bubbles to flow at or near the liquid velocity. A C_i of this magnitude is obviously inappropriate for the flow situation at hand.

If one assumes that the flow of the liquid in the subcooled-boiling region is very similar to the flow through a roughened pipe, a much smaller value of C_i is obtained. Using the Colebrook friction factor for turbulent flow and a completely rough zone, the shear stress is

$$\tau_i = \frac{1}{2} \rho_l V_\ell^2 \left[1.14 - 2.0 \log_{10} \left(\frac{\varepsilon}{D_h} \right) \right]^2 \quad (\text{H-92})$$

The roughness parameter is estimated to be a percentage of the time-averaged height of the growing bubbles (Ref. H-27.). We use the following relation for the roughness parameter:

$$\varepsilon = 0.01 Y_b \quad (\text{H-93})$$

To develop the interfacial-drag coefficient, we perform the following steady-state force balance on the channel:

$$\pi D_h \Delta z \tau_i = \frac{\pi}{4} D_h^2 \Delta p \alpha_l \quad (\text{H-94})$$

and

$$\alpha_t \frac{\Delta p}{\Delta z} = \frac{4\tau_i}{D_h}, \quad (\text{H-95})$$

where it is assumed that the hydraulic diameter is equivalent to the hydraulic diameter of the channel. From the liquid momentum equation,

$$\alpha_t \frac{dp}{dz} \sim C_{i, sb} V_r^2, \quad (\text{H-96})$$

so that $C_{i, sb}$ is found to be

$$C_{i, sb} = \frac{2\rho_\ell}{D_h} \left[1.14 - 2.0 \log_{10} \left(\frac{\varepsilon}{D_h} \right) \right]^{-2}. \quad (\text{H-97})$$

For a hydraulic diameter of 0.00129 m (typical of PWR cores), and a bubble diameter of 1 mm, equation Eq. (H-97) overestimates the drag coefficient. This is basically due to the liquid density used in the equation.

To determine an appropriate interfacial-drag coefficient, the following argument is proposed. The film of bubbles attached to the wall in subcooled boiling can be considered to be a film of vapor instead of individual bubbles. At the interface, the surface is rough or dimpled. The vapor is moving relative to the liquid and is now considered to be in the continuous phase. Thus, the vapor is seen to be flowing around a roughened liquid core with a diameter very similar to the diameter of the channel. Equation (H-97) then applies as before except that the liquid density is replaced with the vapor density:

$$C_{i, sb} = \frac{2\rho_g}{D_h} \left[1.14 - 2.0 \log_{10} \left(\frac{\varepsilon}{D_h} \right) \right]^{-2}. \quad (\text{H-98})$$

In the case where the liquid is saturated or superheated, the bubbles can exist in the free stream. Thus, the interfacial-drag-coefficient model should consist of two components: (1) the interfacial drag due to bubbles attached to the wall and (2) the interfacial drag due to bubbles traveling in the free stream. The contribution due to bubbles attached to the wall is calculated by Eq. (H-98), as discussed above. The contribution due to bubbles in the free stream is determined in the same fashion as for bubbly flow (see Section H.1.). For completeness, it is summarized below.

Collier (Ref. H-27.) indicated that if the bubbles attached to the wall are assumed to be packed in a square array and to interfere with each other when $r/s \approx 0.25$ (s is the distance between bubbles), then the void fraction at the wall can be given by

$$\alpha_w = \frac{\pi Y_b}{6 D_h} \quad . \quad (\text{H-99})$$

If the liquid temperature becomes saturated or greater than the saturation temperature, α_w becomes zero. For subcooled liquid conditions, α_w obtained from Eq. (H-99) is recorrected based upon the liquid temperature in order to make a smooth transition to the saturated conditions. This correction is done when the liquid temperature plus 5°C ($T_\ell + 5^\circ\text{C}$) is greater than or equal to the saturation temperature of the fluid and is given by

$$\alpha_w = \frac{\pi Y_b}{6 D_h} [0.2(T_{\text{sat}} - T_\ell)] \text{ for } T_{\text{sat}} - 5K \leq T_\ell < T_{\text{sat}} \text{ and} \quad (\text{H-100})$$

$$\alpha_w = 0 \quad \text{for } T_\ell \geq T_{\text{sat}} \quad .$$

Then, the void fraction of bubbles traveling in the free stream is expressed by

$$\alpha_{fr} = \alpha_g - \alpha_w \quad . \quad (\text{H-101})$$

Ishii (Ref. H-2.) gave the bubbly flow drag force by

$$M = -\frac{\alpha}{2} \left[\sqrt{\frac{g\Delta\rho}{\sigma}} f(\alpha) \right] \rho_\ell (C_1 V_v - C_0 V_\ell)^2 \quad . \quad (\text{H-102})$$

Thus, the free-stream drag coefficient can be obtained by equating Eq. (H-102) to $C_{i,fr} V_r^2$, and is given by

$$C_{i,fr} = \frac{\alpha_{fr}}{d_b} f(\alpha) \rho_\ell \frac{(C_1 V_v - C_0 V_\ell)^2}{(V_v - V_\ell)^2} \quad (\text{H-103})$$

where

$$f(\alpha) = \left[\frac{1 + 17.67(1 - \alpha_{fr})^{1.3}}{18.67(1 - \alpha_{fr})^{1.5}} \right]^2 \quad (\text{H-104})$$

and

$$d_b = 2 \sqrt{\frac{\sigma}{g\Delta\rho}} \quad . \quad (\text{H-105})$$

Finally, the total interfacial-drag coefficient for subcooled nucleate boiling is obtained as follows by a momentum-weighted equation as

If $T_\ell \geq T_{\text{sat}}$,

$$C_{i, sb} = \frac{C_{i, sb} V_\ell^2 + ffs \cdot C_{i, fr} V_r^2}{(\alpha_w + \alpha_{fr}) V_r^2}, \text{ if } \alpha_w > 0 \quad (\text{H-106})$$

$$C_{i, sb} = \frac{ffs C_{i, fr}}{\alpha_{fr}}, \text{ if } \alpha_w \leq 0, \quad (\text{H-107})$$

where the constant ffs , which multiplies the free-stream bubble IFDC, is assigned a value of 0.00175 to fit CCTF Run-14 pressure-drop data.

If $T_\ell < T_{\text{sat}}$, then (H-108)

$$C_{i, fr} = 0 \text{ and}$$

$$C_{i, sb} = C_{i, sb} \text{ [Eq. (H-98)]}.$$

The interfacial-drag model summarized above is used when the cell void fraction is between 0 and 0.5. For void fractions greater than 0.98, the interfacial-drag coefficient is calculated by the interfacial-drag model for the annular-mist-flow regime that is given in the previous section. For void fractions between 0.5 and 0.98, a linear weighting is used to obtain $C_{i, sb}$. The linear weighting is given by

$$C_{i, sb} = C_{i, sb} + (C_{i, am} - C_{i, sb})(WX)^{0.4}, \quad (\text{H-109})$$

where $C_{i, am}$ is the interfacial-drag coefficient for annular-mist flow in nucleate boiling and

$$WX = \frac{1}{\alpha_{df} - \alpha_1} \alpha - \frac{\alpha_1}{\alpha_d - \alpha_1}, \quad \alpha_1 = 0.5. \quad (\text{H-110})$$

H.1.5.1.2. Input Required for Implementation. Implementation of the subcooled interfacial-drag model requires the definition of fluid properties and the hydraulic diameter of the channel.

H.1.5.1.3. Constants. No changes were made to any of the numerical constants, and they are the same as in the references cited. The free-stream bubble IFDC is multiplied by a constant, ffs , of 0.00175 to fit CCTF Run-14 pressure-drop data.

H.1.5.1.4. Model as Coded. The core-reflood model is coded in subroutine CIF3. This subroutine is called by VSSL1 for each level in the VESSEL component. Several tests exist to determine whether the cell of interest resides in the core region. The subcooled

interfacial-drag model is used when the cell resides in the core region and the core-reflood model is turned on.

H.1.5.1.5. Weightings, Averaging, and Limits. The void fraction of bubbles attached to the wall is restricted, with a minimum value of 0.05 and maximum value of 0.3. The free-stream void fraction is also limited, with a minimum of 0.005 and a maximum of 0.5. The height of the bubble from the wall cannot be higher than 0.00001 m. If the liquid becomes saturated or superheated, the diameter of the bubbles calculated from Eq. (H-105) is limited by a maximum value of 0.9 times the hydraulic diameter, and the free-stream void fraction is limited by a minimum value of 0.001. No other weightings or limits are applied.

H.1.5.1.6. Scaling Consideration. The Colebrook friction-factor relation and the equation for the bubble height are given internal tube flows. Although the hydraulic diameter of the open channel used is similar to the tube diameter, the applicability of these equations to rod bundles is not verified and subject to further investigation.

H.1.5.1.7. Summary and Conclusions. The interfacial-drag coefficient for subcooled boiling is obtained by using the Colebrook friction factor for flows through roughened pipes. The bubbles attached to the wall in subcooled boiling are considered to be a film of vapor instead of individual bubbles. The vapor is thought to flow around a roughened liquid core with a diameter similar to the diameter of the channel. Therefore, the density of liquid is replaced by the density of vapor in Eq. (H-97). In the case where the liquid is superheated or saturated, the IFDC is considered to consist of two components: (1) the interfacial drag due to bubbles attached to the wall, and (2) the interfacial drag due to bubbles in the free stream. The free-stream contribution is obtained using Ishii's drag coefficient formulation for bubbly flows.

H.1.5.2. Smooth Inverted-Annular-Flow Model.

H.1.5.2.1. Basis for the Model. In this region, the interface is assumed to be smooth. Therefore, the following simple smooth-tube correlation for the interfacial friction factor is used (Ref. H-28.):

$$f_{i,sm} = \frac{16}{Re_g} \quad \text{for laminar flow, and} \quad (\text{H-111})$$

$$f_{i,sm} = 0.079 Re_g^{-0.25} \quad \text{for turbulent flow,} \quad (\text{H-112})$$

where

$$Re_g = \frac{(D_h - D_c) \alpha_g \rho_v V_v}{\mu_v}$$

To develop $C_{i,sm}$ a force balance is performed as before, using Fig. H-19. as follows:

$$\alpha_g \Delta p \frac{\pi}{4} D_h^2 = -\tau_i \pi D_c \Delta z - \tau_w \pi D_h \Delta z . \quad (\text{H-113})$$

From the vapor momentum equation, we have

$$\alpha_g \left(\frac{dp}{dz} \right) = C_i V_r^2 - C_{wg} V_g^2 . \quad (\text{H-114})$$

The core diameter can be determined from the geometric consideration as

$$D_c = \alpha_l^{1/2} D_h , \quad (\text{H-115})$$

and, from the definition of the friction factor, we have

$$\tau = \frac{1}{2} \rho V^2 f . \quad (\text{H-116})$$

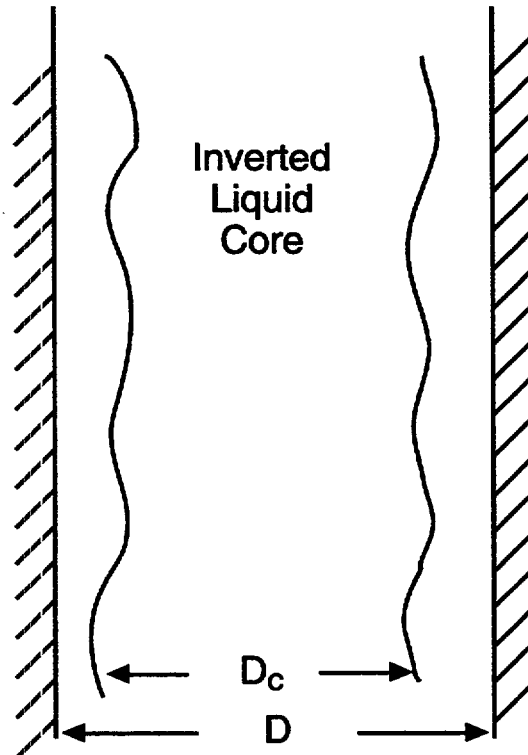


Fig. H-19. Representation of the smooth inverted annular regime.

The interfacial-drag coefficient then becomes

$$C_{i,sm} = 2\rho_g f_{i,sm} \frac{(1-\alpha_g)^{1/2}}{D_h} \quad (H-117)$$

The hydraulic diameter of the channel is used instead of the tube diameter in Eq. (H-117).

H.1.5.2.2. Input Required for Implementation. The fluid properties, channel hydraulic diameter, and the cell void fraction are the required input for the smooth IAF interfacial-drag model.

H.1.5.2.3. Constants. No changes were made to any of the numerical constants for friction-factor correlations, and they are the same as in the references cited.

H.1.5.2.4. Model as Coded. The interfacial-drag model for the smooth IAF is determined in subroutine CIF3 as a part of the core-reflood interfacial-drag model. This subroutine is called by VSSL1 for each level in the VESSEL component. Several tests exist to determine whether the cell of interest resides in the core region. The smooth IAF interfacial-drag model is used when the cell resides in the core region and the core-reflood model is turned on, and the cell void fraction is less than 98%.

H.1.5.2.5. Weightings, Averaging, and Limits. The void fraction at the smooth/rough-wavy IAF boundary is limited by a maximum value of 30% and a minimum value of 0.05%. The Reynolds number used in Eqs. (H-111) and (H-112) has a minimum value of 1.0. If $C_{i,sb} \times f_{sb}$ is less than $C_{i,sm} \times f_{sm}$ then, to prevent discontinuity, $C_{i,sm}$ is assumed to be

$$C_{i,sm} = C_{i,sb} \frac{f_{sb}}{f_{sm}}, \quad f_{sb} = 1 \text{ and } f_{sm} = 3.0 \quad (H-118)$$

The interfacial-drag coefficient is further redefined based upon the cell void fraction, as illustrated in Fig. H-17a. If the cell resides in the low-void-fraction region, $\alpha < 0.75$ (see Fig. H-17a), no adjustment is done, and the model mentioned above is used to estimate the interfacial-drag coefficient. If the cell is located in the high-void-fraction region, $\alpha > 0.98$, the interfacial-drag coefficient for the smooth IAF, $C_{i,sm}$, is assumed to be equal to that of the highly dispersed flow $C_{i,df}$. In the transition between the high- and low-void-fraction regions ($0.75 < \alpha < 0.98$), the following linear weighting based upon the void fraction is applied to avoid discontinuities between low- and high-void-fraction regions:

$$C_{i,sm} = C_{i,sm} + (C_{i,df} - C_{i,sm})W^{0.5}, \quad (H-119)$$

where

$$W = \frac{1}{(\alpha_{df} - \alpha_2)} \alpha_g - \left(\frac{\alpha_2}{(\alpha_{df} - \alpha_2)} \right)$$

The weighting, W , is limited by a maximum value of 1.0 and minimum value of 0.0, and $\alpha_{df} = 0.98$ and $\alpha_2 = 0.75$.

In summary, the interfacial-drag coefficient for the smooth IAF is determined by the following equations:

$$\begin{aligned} C_{i,sm} &= C_{i,df} && \text{if } \alpha_g > 0.98 \text{ or } C_{i,sm} < C_{i,df} \\ C_{i,sm} &= C_{i,sm} + (C_{i,df} - C_{i,sm})W && \text{if } 0.75 < \alpha_g < 0.98 \\ C_{i,sm} &= C_{i,sm} && \text{if } 0.75 > \alpha_g. \end{aligned} \quad (\text{H-120})$$

From sensitivity calculations and comparisons to reflood data, an appropriate value of $C_{i,sm}$ for this regime is of the order 1.0 to 5.0 kg/m⁴. If we apply Eqs. (H-111), (H-112), and (H-117), with typical PWR conditions ($D = 0.0129$ m, $p = 2.5$ bar, $V_g = 20$ m/s, and a void fraction of 10%), we obtain a value for $C_{i,sm}$ of 1.25 kg/m⁴. In this case, the vapor film is calculated to be turbulent. If we use the gap between the wall and liquid core as the characteristic diameter, we obtain a laminar vapor film and a $C_{i,sm}$ value of 4.5 kg/m⁴. Thus, the use of a smooth-tube-friction correlation in this regime appears to be valid, and it is expected that Eqs. (H-111), (H-112), and (H-117) will give an appropriate estimate of the interfacial drag. The interfacial drag is observed to be dependent on the definition of the hydraulic diameter. The use of the gap width is appropriate for the case of a small gap-to-diameter ratio as we have here.

H.1.5.2.6. Scaling Consideration. The smooth-tube friction factors for laminar and turbulent flows are given for internal flows. In the case of rod bundles, in which the flow is an external flow, the use of these equations is an engineering approximation. However, the hydraulic diameter of the open channel used in the model is similar to the rod diameter.

H.1.5.2.7. Summary and Conclusions. In the smooth IAF region, the smooth-tube-friction-factor correlations are used for the smooth IAF. The interfacial-drag coefficient is obtained from the force balance equation. The interfacial-drag coefficient depends on the definition of the hydraulic diameter. The sensitivity study indicated that for small gap-to-diameter ratios, the use of the gap width is appropriate. The IFDC for this flow regime is readjusted according to IFDC selection logic illustrated in Fig. H-17b. For the high void fractions ($\alpha_g > 0.98$), IFDC is identical to that of the highly dispersed flow. In the transition region ($0.75 < \alpha_g < 0.98$), IFDC for this flow regime is obtained by a linear weighting between IFDCs for the smooth and highly dispersed flow regimes. For low void fractions ($\alpha_g < 0.75$), the smooth IFDC model is used.

H.1.5.3. Rough-Wavy Inverted-Annular-Flow Model.

H.1.5.3.1. Basis for the Model. This regime is similar to the smooth IAF case. However, the interfacial friction is now increased due to the presence of waves and the shearing of droplets from the wave crests (Fig. H-20.).

The interfacial-drag coefficient for the rough-wavy inverted annular flow is formulated in the same way as the smooth inverted-annular-flow model. The interfacial-drag coefficient can be expressed with Eq. (H-117) as

$$C_{i,rw} = \frac{2\rho_v f_{i,rw} (1 - \alpha_g)^{1/2}}{D_h} \quad (\text{H-121})$$

In order to express the friction factor, $f_{i,rw}$ in Eq. (H-121), the turbulent, rough-pipe correlation suggested by Colebrook, given by Eq. (H-91), is used. The wavy vapor-liquid interface is considered to represent the pipe roughness in Eq. (H-91). The roughness is assumed to be proportional to the diameter of liquid droplets entrained from the wavy interface. Thus, the relative roughness in Eq. (H-121) becomes

$$\frac{\varepsilon}{D_h} = fc4 \times \frac{d_d}{D_h}, \quad (\text{H-122})$$

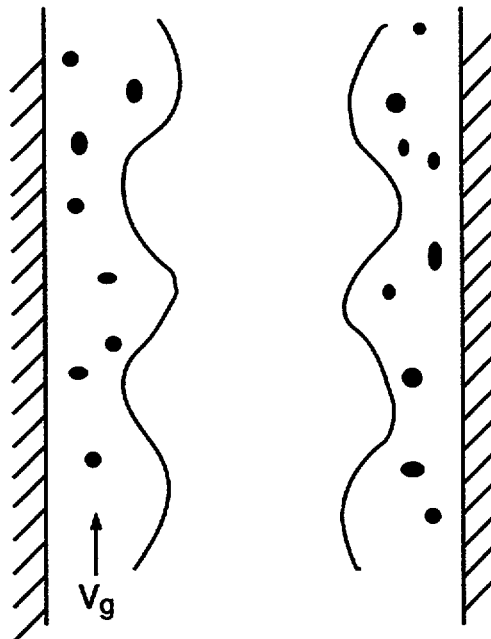


Fig. H-20. Representation of the rough-wavy IAF region.

where d_d is the droplet diameter. Ishii (Ref. H-2.) calculated droplet diameter for small droplets observed in inverted annular flow using

$$d_d = 0.613 \left(\frac{\sigma}{g\Delta\rho} \right)^{1/2} N_{\mu g} \quad , \quad (\text{H-123})$$

where

$$N_{\mu g} = \frac{\mu_g}{\left[\rho_g \sigma \sqrt{\frac{\sigma}{g\Delta\rho}} \right]^{1/2}} \quad . \quad (\text{H-124})$$

If $\varepsilon/D_h > 1$, then a constant of 0.77 is used for $f_{i,rw}$. If $\varepsilon/D_h < 1$, then $f_{i,rw}$ is calculated from Colebrook's equation, Eq. (H-91).

H.1.5.3.2. Input Required for Implementation. The fluid properties, hydraulic diameter, and the void fraction of the cell that is in the rough-wavy IAF are input into the model.

H.1.5.3.3. Constants. The proportionality constant for the pipe roughness was found to be 80 to fit best the CCTF pressure drop.

H.1.5.3.4. Model as Coded. The interfacial-drag model for the rough-wavy IAF is determined in subroutine CIF3 as a part of the reflow interfacial-drag model. If the cell void fraction is less than 98%, the interfacial-drag coefficient for the rough-wavy IAF is calculated as indicated in Fig. H-17b.

H.1.5.3.5. Weightings, Averaging, and Limits. The void fraction at the boundary between the rough-wavy and agitated IAF regimes is limited by a maximum value of 40% and minimum value of 30%. The interfacial-drag coefficient in the rough-wavy IAF regime is expected to be higher than that of the smooth IAF regime. If $C_{i,sm} \times fsm$ is found to be less than $C_{i,sm} \times frw$, then, to ensure smooth transition, $C_{i,sm}$ is multiplied by the ratio of frw/fsm . The constants frw and fsm are 1.25 and 3.0, respectively.

The interfacial-drag coefficient is further weighted based upon the cell void fraction as done before for the smooth IAF regime. If the cell is located in the low-void-fraction region, no adjustment is done, and the above-mentioned model, Eq. (H-121), is used to estimate the drag coefficient. If the cell is located in the high-void-fraction region, the interfacial-drag coefficient for the smooth IAF is assumed to equal that of the dispersed flow. In the transition between the high- and low-void-fraction regions, the following linear weighting is applied to accurately predict CCTF Run-14 pressure-drop data:

$$C_{i,rw} = C_{i,rw} + (C_{i,df} - C_{i,rw})W^{0.5} \quad , \quad (\text{H-125})$$

where

$$W = \frac{1}{\alpha_{df} - \alpha_2} \alpha_g - \frac{\alpha_2}{\alpha_{df} - \alpha_2}$$

The weighting, W , is limited by a maximum value of 1.0 and minimum value of 0.0, and $\alpha_{df} = 0.98$ and $\alpha_2 = 0.75$.

The interfacial-drag coefficient for the rough-wavy IAF regime is

$$\begin{aligned} C_{i,rw} &= C_{i,df} && \text{if } \alpha_g > 0.98, C_{i,rw} < C_{i,df} \\ C_{i,rw} &= C_{i,rw} + (C_{i,df} - C_{i,rw})W && \text{if } 0.75 < \alpha_g < 0.98 \\ C_{i,rw} &= C_{i,rw} && \text{if } 0.75 > \alpha_g \end{aligned} \quad (H-126)$$

H.1.5.3.6. Scaling Consideration. The Wallis correlation is given for internal tube flows. In the case of rod bundles in which the flow is an external flow, the use of these equations is an engineering approximation. However, the hydraulic diameter of the core channel is similar to the rod diameter.

H.1.5.3.7. Summary and Conclusions. The interfacial-drag model for the rough-wavy IAF is similar to Wallis' (Ref. H-15.) interfacial-drag model for annular-mist flow. The TRAC core-reflood model includes the gas void fraction instead of liquid fraction. The interfacial-drag coefficient obtained from the model is used in low-void-fraction regions. For the high-void-fraction region, the dispersed flow interfacial-drag coefficient is used, whereas between these low- and high-void-fraction regions, a linear weighting is applied.

H.1.5.4. Agitated Inverted Annular Region Model. This region is characterized by large liquid slugs of similar diameter to the tongue diameter in the rough-wavy region. Breakup of the slugs into smaller pieces and droplets eventually occurs. The region is quite chaotic. It may be similar to the churn-turbulent regime in adiabatic flow that is used to characterize the transition region between slug flow and annular mist. The interfacial drag should again be dominated by the mechanism of droplet entrainment and breakup of the inverted tongue. For this region, it is proposed to use the same correlation as the rough-wavy region, with possibly a constant multiplier to be determined from comparisons with data.

H.1.5.5. Highly Dispersed Flow Model. This region of IAF is characterized by liquid droplets, small in size, suspended in the vapor stream.

H.1.5.5.1. Basis for the Model. The dispersed region is comprised of droplets flowing up the channel. The liquid droplet size is determined by a correlation suggested by Ishii (Ref. H-2.). This correlation gives droplet sizes on the order of millimeters at reasonable reflood pressures, as given by

$$d_d = 1.838 \left(\frac{\sigma}{g(\rho_l - \rho_v)} \right)^{1/2} N_{\mu g}^{1/3} \quad (\text{H-127})$$

where $N_{\mu g}$ is the viscosity number,

$$N_{\mu g} = \frac{\mu_g}{\left[\rho_g \sigma \sqrt{\frac{\sigma}{g(\rho_l - \rho_g)}} \right]^{1/2}} \quad (\text{H-128})$$

An interfacial-drag coefficient for the droplet in this fully dispersed flow is found by a separate force balance on the droplet as

$$C_{i,dd} = \frac{\frac{3}{4} \alpha_{dd} \rho_g C_d}{d_d} \quad (\text{H-129})$$

where C_d is the form drag coefficient and α_{dd} is the liquid droplet fraction that is given below. The following equation, suggested by Ishii and Chawla (Ref. H-1.), is used for the spherical-drop form drag coefficient:

$$C_d = \frac{24(1 + 0.1 Re_d^{0.75})}{Re_d} \quad (\text{H-130})$$

where

$$Re_d = \text{Reynolds number} = \frac{\rho_v d_d V_r}{\mu_m}$$

$$V_r = \text{relative velocity} = V_v - V_d, \text{ and}$$

$$\mu_m = \text{viscosity of two-phase mixture} = \frac{\mu_v}{(1 - \alpha_{dd})^{2.5}}$$

An estimate of the droplet velocity can be obtained from a separate momentum balance, assuming the droplet-drag coefficient is 0.44 (Ref. H-29.), as

$$V_d = V_v - 2.462 \left[\frac{(\rho_l - \rho_v) g d_d}{2 \rho_v} \right]^{1/2} \quad (\text{H-131})$$

In actual reactor hardware, not all the surfaces are heated because control rods and structures are present at the periphery of the core. Thus, a liquid film may establish itself on the cold surfaces, adding significantly to the overall liquid fraction at the top of the core. A typical PWR core contains 45548 heated rods at 0.01073 m diameter and 3860 control rods of 0.0138 m diameter. Thus, the unheated surface for the control rods alone

accounts for 9.83% of the total heat-transfer surface area. From geometric considerations, one can calculate the local volumetric liquid fraction for a given film thickness. For the typical reactor hardware, Table H-3, presents such a calculation. This table shows that a liquid film thickness of 1 mm on the cold surface alone provides a total liquid fraction of about 3%. Thus the contribution of this film cannot be neglected since it can represent a significant portion of the total liquid fraction.

Williams (Ref. H-30.) has shown that the vapor velocities generated in the core during reflood are at about the correct value to cause countercurrent flow limitation. Thus, the drag and gravity forces balance, creating a "hanging" film condition. Figure H-21, depicts this condition from a top view.

In tests with only heated surfaces, exit-droplet liquid fractions are typically less than 1%. Thus the film on the unheated surfaces represents a significant component of the total volumetric liquid fraction. The overall drag coefficient must take into account both droplet and film. It is not possible to do this directly with the two-fluid approximation because only one liquid field is assumed, and the droplets flow at a much different velocity than the film.

The thickness of liquid film on a cold wall was derived by Pasamehmetoglu (Ref. H-31.). The following assumptions were made in deriving the formula:

1. the liquid flow is assumed laminar and incompressible,
2. the force balance includes gravity and interfacial shear only (i.e., wall shear and liquid momentum are negligible),
3. surface forces are negligible, and
4. the flow is fully developed and quasi-steady.

TABLE H-3.
Liquid Volume Fraction at Various Film Thicknesses

Film Thickness (m)	Liquid Volume Fraction (%)
0.0002	0.6
0.0005	1.5
0.001	3.2
0.002	6.9
0.003	11.0

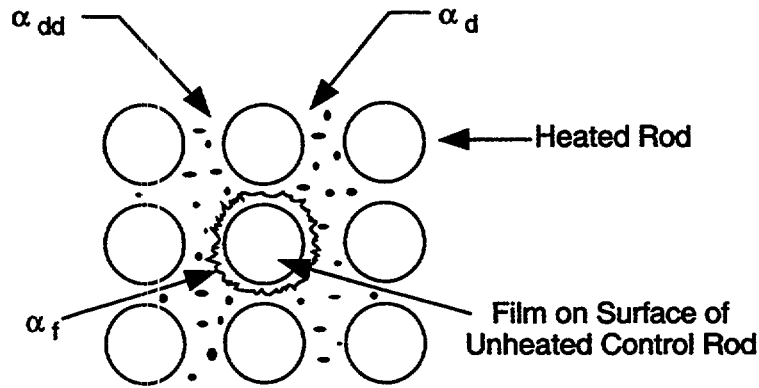


Fig. H-21. Proposed scheme for the dispersed region in reactor geometry.

The force balance on a differential liquid element gives

$$\mu_l \frac{\partial^2 u}{\partial y^2} = g \rho_l \quad , \quad (H-132)$$

where u is the liquid velocity parallel to the wall and y is the coordinate perpendicular to the wall. Thus, the velocity profile can be obtained as

$$u = \frac{1}{2} \frac{\rho_l g}{\mu_l} y^2 + \left[\frac{\tau_i}{\mu_l} - \frac{\rho_l g \delta_f}{\mu_l} \right] y \quad (H-133)$$

using the following boundary conditions:

$$\begin{aligned} \text{at } y = 0, \quad u &= 0 \\ \text{at } y = \delta_f, \quad \tau &= \tau_i \end{aligned} \quad (H-134)$$

The liquid film thickness can be expressed by

$$\delta_f = C \frac{\tau_i}{\rho_l g} \quad (H-135)$$

To determine C , the following criteria are proposed:

1. the velocity, u , is positive for all y , and
2. the volume flow rate in the axial direction is zero.

Using criterion 1, C is obtained as 1. The second criterion gives a value of 1.5 for C .

Substituting the Wallis interfacial shear correlation (Ref. H-15.) given by

$$\tau_i = \frac{1}{2} f_i \rho_g V_g^2 \quad , \quad (\text{H-136})$$

where the interfacial friction factor is

$$f_i = 0.005 \left(1 - 300 \frac{\delta_f}{D_h} \right) \quad , \quad (\text{H-137})$$

into Eq. (H-135), the liquid film thickness is obtained as

$$\delta_f = \frac{0.0025 C \rho_g V_g^2}{g \rho_l + \frac{0.75 C \rho_g V_g^2}{D_h}} \quad (\text{H-138})$$

Equation (H-138) is valid for

$$V_g < \sqrt{\frac{1.333}{C} \frac{\rho_l}{\rho_g} g D_h} \quad . \quad (\text{H-139})$$

This equation gives the maximum liquid thickness that can be sustained by the flowing vapor. If the thickness is larger, liquid will flow downwards due to gravity and if it is smaller, liquid will be carried with vapor. For unheated flow, under fully developed conditions, the deposition and entrainment will reach an equilibrium such that the deposition rate will be equal to the entrainment and yield a constant entrainment fraction. Thus, the film thickness will not be affected by entrainment and deposition. However, changes in vapor velocity in the flow direction will change the film thickness. the above equation is valid only if these changes are gradual because of fully developed flow assumptions.

For the typical reflooding conditions, $V_g = 10$ m/s, $p = 2$ bar, $D_h = 2$ cm, and Eq. (H-139) with $C = 1.5$ yields $\delta_f = 1.46$ mm. Because this thickness is small, the turbulence effects can be neglected. Equation (H-139) is also independent of viscosity; therefore, for homogeneous turbulence (where the eddies are uniform), the result would be the same. The result would be altered by turbulence only if the eddy viscosity is a function of y . The turbulence at the interface is accounted for by using Wallis' equation for the interfacial shear.

Then, the liquid film fraction is obtained from the geometrical consideration

$$\alpha_f = \frac{P\delta_f F_u}{A} \quad , \quad (H-140)$$

where

$$P = 4 \frac{A}{D_h} = \text{equivalent perimeter of the channel,}$$

$$\delta_f = \text{film thickness,}$$

$$F_u = \text{fraction of the unheated surface area in the core} = \frac{A_u}{A_t},$$

$$A = \text{flow area of the channel,}$$

$$A_u = \text{unheated surface area, and}$$

$$A_t = \text{total surface area.}$$

The liquid film fraction, α_f , can also be limited by the total liquid fraction, α_t , available to be deposited on the unheated surface area. If the liquid and the unheated surface area are homogeneously distributed within a control volume, the amount of liquid might be considered to be $F_u(1-\alpha_g)$. With cross flow between subchannels, however, and the ability of unheated surfaces to collect liquid and hold it, the amount of liquid "hanging" on an unheated wall may become greater than $F_u(1-\alpha_g)$. This effect is included in the following relationship, which has been developed using results from CCTF Run 14:

$$\alpha_f = F_u W (1 - \alpha_g) \quad , \quad (H-141)$$

where W is the cold-wall liquid fraction weighting that is defined as

$$W = 5 \left[\frac{0.98 - \alpha}{0.98 - \min(\alpha_{AG}, 0.7)} \right]^{0.35} \quad \text{if} \quad \min(\alpha_{AG}, 0.7) < \alpha < 0.98 \quad ,$$

$$W = 5 \quad \text{if} \quad \alpha \geq 0.98 \quad , \text{ and}$$

$$W = 0 \quad \text{if} \quad \alpha \leq \min(\alpha_{AG}, 0.7) \quad .$$

The weighting factor allows the limiting amount of liquid deposited on the cold wall to be an amount greater than the homogeneous fraction of the unheated surface area. We assumed that the weighting becomes unimportant when the void fraction is less than α_{AG} . The weighting also allows the maximum fraction of the liquid to be accumulated in the dispersed-flow regime. The liquid film fraction is selected to be the minimum of values obtained by Eqs. (H-140) and (H-141).

$$\alpha_f = \min\left(\frac{P\delta_f F_u}{A}, F_u W(1 - \alpha)\right) \quad (\text{H-142})$$

The liquid droplet fraction then becomes

$$\alpha_{dd} = 1 - \alpha_f - \alpha_g \quad (\text{H-143})$$

Using the modified Wallis relation (Ref. H-15.), the interfacial friction factor between the liquid film and the vapor is

$$f_{i,f} = 0.005(1 + 75\alpha_f) \quad (\text{H-144})$$

The interfacial drag on the film can be estimated using a relation similar to Eq. (H-117), except that the hydraulic diameter is replaced with the diameter of the cold rod and the weighting factor is applied as the fraction of the unheated surface area when the total heat-transfer area approaches zero. Then we have

$$C_{i,f} = \frac{2\rho_g f_{i,f}}{D_h} \quad (\text{H-145})$$

The linear relationship given in Eq. (H-140) assumes that the factor F_u has a value of 1.0 when the unheated surface area is 100% of the total. As discussed above, a value of 10% is typical of PWR geometry.

We can now calculate the total averaged interfacial drag for this regime by using an average momentum balance equation between the liquid and the gas (Ref. H-29.). Simplifying the relation by assuming that the film velocity is small compared to the vapor velocity, and that the total liquid velocity is similar to the film velocity, we have

$$C_{i,df} = \frac{C_{i,dd}V_r^2 + C_{i,f}V_v^2}{\left(V_v - \frac{\alpha_{dd}V_d}{(1-\alpha_g)}\right)^2} \quad (\text{H-146})$$

H.1.5.5.2. Input Required for Implementation. The fluid properties, hydraulic diameter, the fraction of unheated surface area in the core, and the void fraction of the cell that is in the rough-wavy IAF are input into the model.

H.1.5.5.3. Constants. The $C_{i,dd}$ obtained by Eq. (H-129) is multiplied by a constant, fc_{drop} , currently set to 0.015. The $C_{i,f}$, Eq. (H-145), is also multiplied by a constant, ffd , currently 0.5. This is done to fit best the CCTF Run-14 pressure-drop data. The constant, C , in Eq. (H-138) is set to 1.0. No other changes were made to any of the numerical constants for friction-factor correlations and they are the same as in the references cited.

H.1.5.5.4. Model as Coded. The highly dispersed flow interfacial-drag model is coded in subroutine CIF3, which is called by VSSL1. In the highly dispersed flow regime, evaluation of IFDC is performed in the following order. First, the droplet diameter is calculated. The velocity of the droplet is obtained from a momentum balance, assuming the droplet-drag coefficient is 0.44 [Eq. (H-131)]. The film thickness is evaluated from a force balance on the liquid film by Eq. (H-138). After calculating the droplet-drag coefficient and the friction factor for the film, the interfacial-drag coefficients for the film, droplet, and dispersed flow are obtained. Finally, the overall interfacial-drag coefficient for highly dispersed flow is obtained by Eq. (H-146).

H.1.5.5.5. Weightings, Averaging and Limits. There are several limits on various parameters to prevent numerical difficulties associated with Fortran coding and to prevent unacceptable conditions. The cell void fraction is limited by a minimum value of 30% for the dispersed flow. The droplet diameter estimated from Ishii's equation cannot be greater than 0.005 m or smaller than 0.0001 m. The diameter of the liquid slug is limited by a minimum value of 0.000001 m. The calculated droplet velocity and the relative velocity are restricted with a minimum value of 0.01 m/s. The calculated film thickness is also limited to a minimum value of 1×10^{-20} m and maximum value of 0.040 m. The droplet fraction cannot be smaller than zero. The droplet velocity calculated from Eq. (H-130) is limited by minimum value of 0.1. The relative droplet velocity is limited by a minimum of 0.05. No other weighting, averaging, or limits are applied to the model.

H.1.5.5.6. Scaling Consideration. The application of this model to rod bundles needs further investigation for various operating conditions different from those used in the development of this model.

H.1.5.5.7. Summary and Conclusions. The interfacial-drag model for the highly dispersed flow includes the IFDCs between the interface to droplet and interface to film, given by Eq. (H-146). The droplet IFDC is obtained from a force balance on the droplet. To determine the droplet-drag coefficient, the equation suggested by Ishii [Eq. (H-129)] is used. The friction factor for the film is calculated by the modified Wallis correlation [Eq. (H-144)].

H.1.5.6. Dispersed Flow with Large Droplets (Post-Agitated Region). This region is located downstream of the agitated IAF and extends until highly dispersed flow occurs and the droplets become smaller in size. In this region, the IFDC is obtained by performing a weighting based upon the void fractions and IFDCs between the rough-wavy and highly dispersed flow regimes. As shown in the flow-pattern/void-fraction map in Fig. H-17b., the IFDC is calculated by the following weightings for this region of IAF:

If $\alpha_{df} > \min(\alpha_{ag}, 0.7)$, $\alpha > \min(\alpha_{ag}, 0.7)$, and $z_{top} > z_{ag}$, then the interfacial-drag coefficient is given by

$$C_{i,pa} = C_{i,rw} \frac{frw}{fmdis} + \left(C_{i,df} \frac{fdis}{fmdis} - C_{i,rw} \frac{frw}{fmdis} \right) \left(\frac{\alpha - \min(\alpha_{ag}, 0.7)}{\alpha_{df} - \min(\alpha_{ag}, 0.7)} \right)^{xmdis} \quad (H-147)$$

if $C_{i,df} \times fdis < C_{i,rw} \times frw$ or by

$$C_{i,pa} = C_{i,rw} \frac{frw}{fmdis} \quad \text{if} \quad C_{i,df} \times fdis \geq C_{i,rw} \times frw . \quad (H-148)$$

If $z_{df} < z_{bot}$, then a simple correction is made as

$$C_{i,pa} = C_{i,df} \frac{fdis}{fmdis} . \quad (H-149)$$

If $\alpha < \min(\alpha_{ag}, 0.7)$ and $z_{ag} < z_{top}$, the correction is given by Eq. (H-148).

The coefficients used in above weightings are

$$\begin{aligned} frw &= 1.25 , \\ fmdis &= 1.0 , \\ fdis &= 1.0 , \text{ and} \\ xmdis &= 0.5 . \end{aligned}$$

H.1.5.7. Combinations of the Individual Drag Models.

H.1.5.7.1. Basis for the Model. The models developed for each region of the core during reflood must be brought together in to apply them to a finite-difference two-fluid approximation. In this situation the finite-difference mesh (typically 4 to 10 levels in the core region) is stationary, and the core-reflood quench front moves through it. The levels of each regime are calculated by subroutine ZCORE (see Appendix F, Section F.2. for more information). It is proposed to apply the models for the individual regions with the following method: (1) superimpose the level correlations above the quench for each of the regions and determine the amount of axial distance that each region occupies in a given hydrodynamic mesh, and then (2) average the lengths of the interfacial-drag coefficients in each mesh and apply the result at the top of the mesh cell (assuming positive vertical flow).

H.1.5.7.2. Constants. No constants are used.

H.1.5.7.3. Model as Coded. For each IAF regime, a linear weighting is defined based upon the axial distance. If the top of the cell, z_{top} is less than the elevation where transition boiling ends, z_{tr} then the weighting for subcooled boiling *WFSB* is set to 1. In this case, the cell resides completely in the transition boiling regime and the weightings for other flow regimes are zero.

If the cell resides in the dispersed-flow regime, $z_{bot} > z_{df}$ OR $z_{bot} < z_{CHF}$ the weighting for the highly dispersed flow regime, $WFHDS$, is set to 1 while the rest of the weightings for other regimes is zero.

If the cell is located in-between the transition boiling and the dispersed-flow regimes (inverted annular flow), $z_{tr} < z_{top}$ and $z_{df} > z_{bot}$, the following weightings are used for the subcooled boiling and smooth IAF regions:

$$WFSB = \frac{[\min(z_{tr}, z_{top}) - z_{bot}]}{dz} \quad (H-150)$$

and

$$WFSM = \frac{[\min(z_{sm}, z_{top}) - \max(z_{tr}, z_{bot})]}{dz} \quad (H-151)$$

In the case where the top of the cell is in the agitated region, $z_{top} > z_{sm}$, the weighting for the agitated region is

$$WFRW = \frac{[\min(z_{ag}, z_{top}) - \max(z_{sm}, z_{bot})]}{dz}; \quad (H-152)$$

otherwise $WFRW$ is zero.

If z_{top} is higher than z_{ag} , indicating that the cell has some parts located in the post-agitated region, the weighting for the post-agitated region is

$$WFMDS = \frac{[\min(z_{df}, z_{top}) - \max(z_{ag}, z_{bot})]}{dz}; \quad (H-153)$$

otherwise $WFMDS$ is zero.

The values of $WFSB$, $WFSM$, $WFRW$, and $WFMDS$ are constrained to be ≥ 0.0 and ≤ 1.0 .

Finally if $z_{top} > z_{df}$ and some part of the cell is in the highly dispersed flow, the weighting for the dispersed flow is

$$WFHDS = 1 - WFMDS - WFRW - WFSM - WFSB; \quad (H-154)$$

otherwise $WFHDS$ is zero.

The overall interfacial-drag coefficient for a cell is given by

$$C_i = WFSB \cdot f_{sb} \cdot C_{i, sb} + WFSM \cdot f_{sm} \cdot C_{i, sm} + WFRW \cdot f_{rw} \cdot C_{i, rw} \\ + WFMDS \cdot f_{mdis} \cdot C_{i, pa} + WFHDS \cdot f_{dis} \cdot C_{i, df} \quad (H-155)$$

The coefficients f_{sb} , f_{sm} , f_{rw} , f_{mdis} , and f_{dis} are currently set to 1.0, 3.0, 1.25, 1.0, and 1.0, respectively. These values are obtained to fit the CCTF Run-14 data.

H.1.5.8. Assessment. As mentioned in the introduction, the assessment of each individual model is not considered, since there is no available data for the reactor-core geometry. Therefore, the models developed for each inverted-annular-flow regime are used as an integral part of the core-reflood interfacial-drag package. To evaluate proper coefficients for weightings and drag coefficients, the CCTF Run-14 pressure-drop data are used.

In this section, therefore, we discuss only the overall results obtained when the overall core-reflood interfacial-drag model is used to predict CCTF Run-14 reflood data. Results presented in this section were obtained with MOD2, Version 5.3. The detailed assessment of the overall model that went into MOD2, Version 5.4, and subsequently into TRAC-M, is discussed in the TRAC-M/F77 Developmental Assessment Manual (Refs. H-40. and H-41.).

The CCTF facility (Ref. H-32.) is an experimental test facility designed to provide information on the thermal-hydraulic behavior of ECCS during the refill and reflood phases of a LOCA. It is an integrated test loop containing several features of a PWR such as core, downcomer, upper plenum, simulated steam generator, and pump. The CCTF Run-14 test procedure started with the preheating of the pressure vessel for initial conditions. After establishing initial conditions, the preheating was shut down and the lower plenum was filled to 0.87 m with near-saturated water before test initiation. The ECCS water was directly injected into the lower plenum after the heater rod surface temperature reached 502°C to prevent the possibility of rapid condensation. Later, the location of injection was changed to three intact cold legs. Typical operating conditions for this particular test were as follows:

Pressure	2.02 kg / cm ² ,
Power	9.36 kW ,
Cold - leg injection rate	30.2 m ³ / s , and
Cold - leg injection temperature	39°C .

The TRAC model of CCTF considers only the pressure vessel. A schematic of the model is shown in Fig. H-22. The TRAC model of CCTF consists of six components: fill, inlet-injection pipe, vessel, outlet pipe, break, and heat structures. The 1D vessel model includes a lower plenum cell located at the beginning of the vessel, 18 cells in the core region, and 6 cells in the upper plenum.

The calculated flooding rates were 0.0094 and 0.0044 m/s at the lower section and the mid-section of the core, respectively, which showed good agreement with the experimental data. The predicted wall temperature and quench times were in good agreement with the data, except at upper elevations where the wall heat flux was decreasing with the axial distance (chopped cosine power profile).

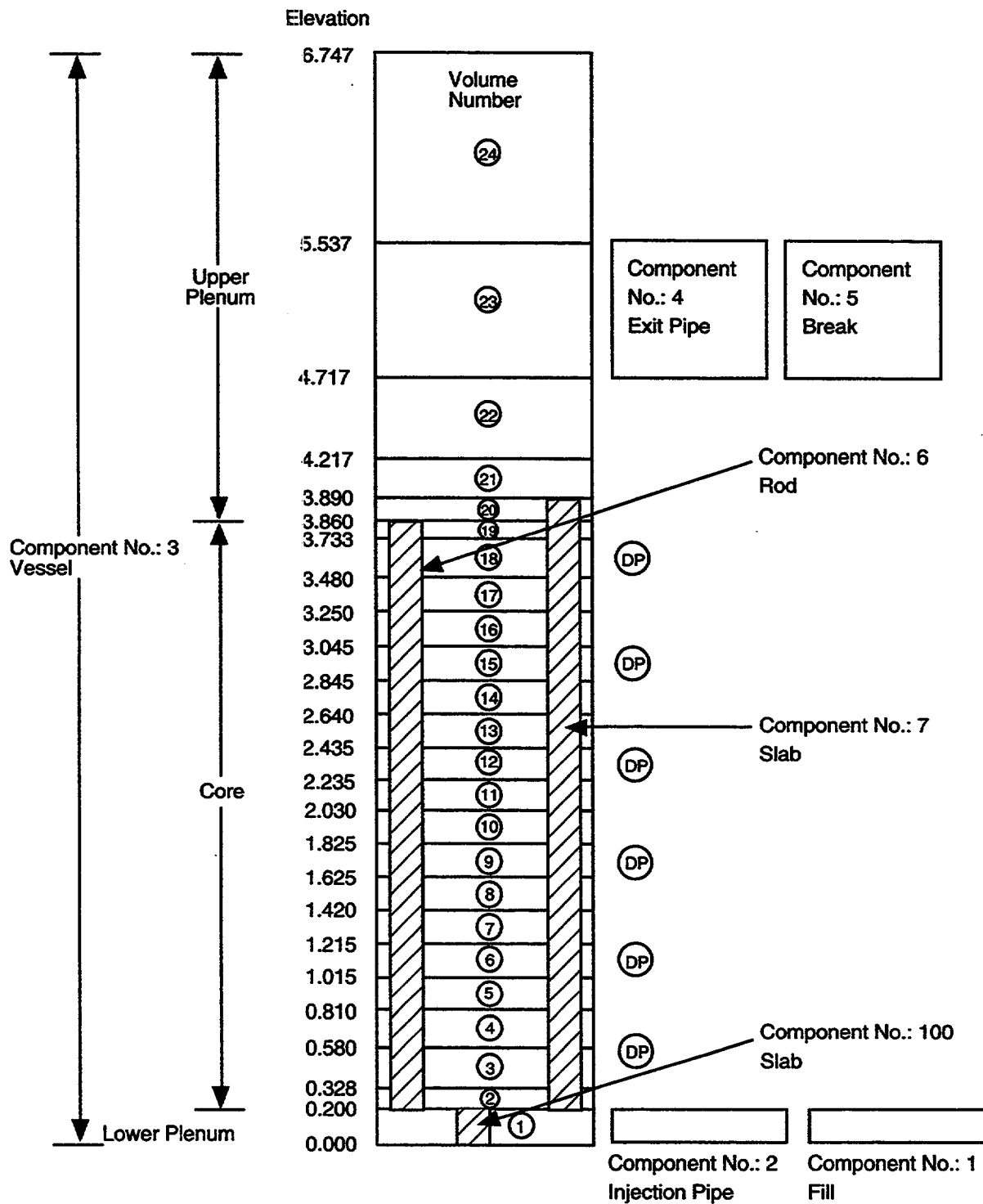


Fig. H-22. TRAC model for CCTF Run-14 test.

Comparisons of the calculated differential pressures at various elevations with the data are shown in Figs. H-23. to H-26. Figure H-23. shows the calculated and measured differential pressures between axial elevations of 0 and 0.61 m from the core inlet as a function of time. The calculated and measured differential pressure drops are in good agreement during the transient, with the exception of transient times between 10–80 s. At about 80 s in the transient, the quench front reaches the axial elevation of 0.38 m away from the inlet (corresponds to an axial location of 0.18 m from the beginning of the heated section). In this initial period of the transient, the interfacial-drag coefficient is slightly overestimated, which causes the liquid to be carried out to upper elevations, as seen in Figs. H-24. to H-26. These figures show pressure-drop peaks at higher elevations. However, this has a negligible effect on the prediction of pressure drop in the later times of the transient. In summary, the core-reflood interfacial-drag model provides a reasonable estimate of the pressure drop.

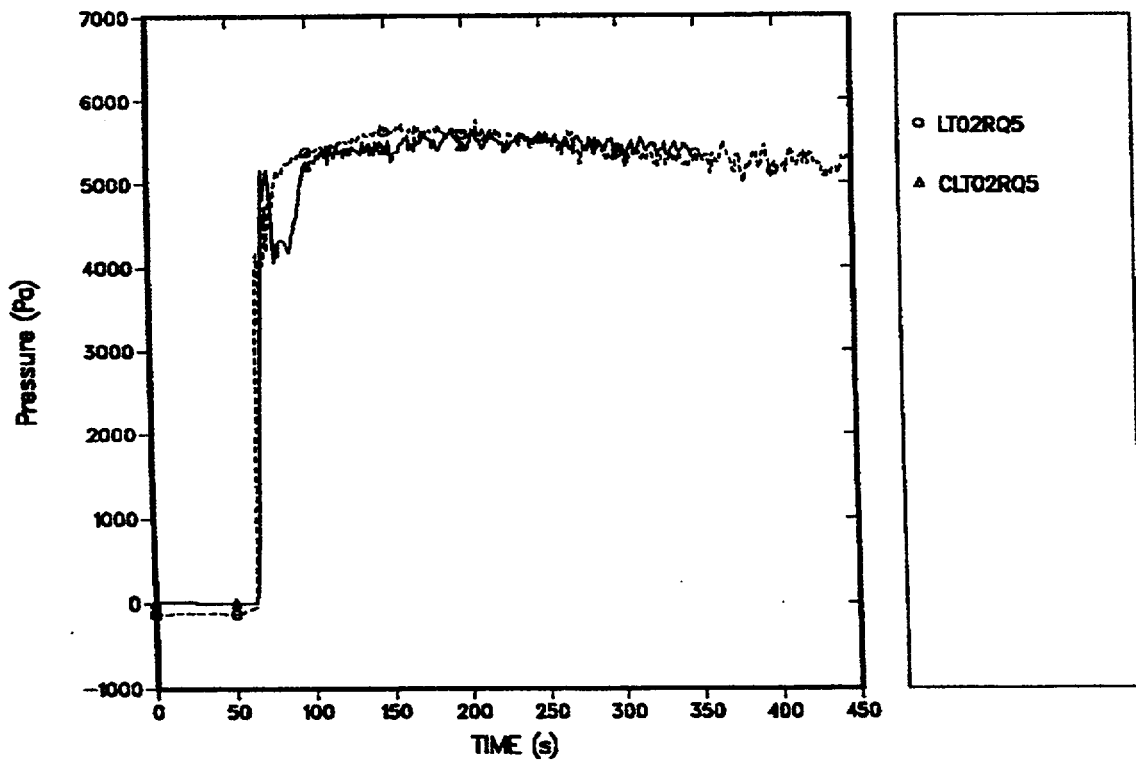


Fig. H-23. The predicted (solid) and measured (dashed) pressure-drop traces between axial elevations of 0–0.61 m.

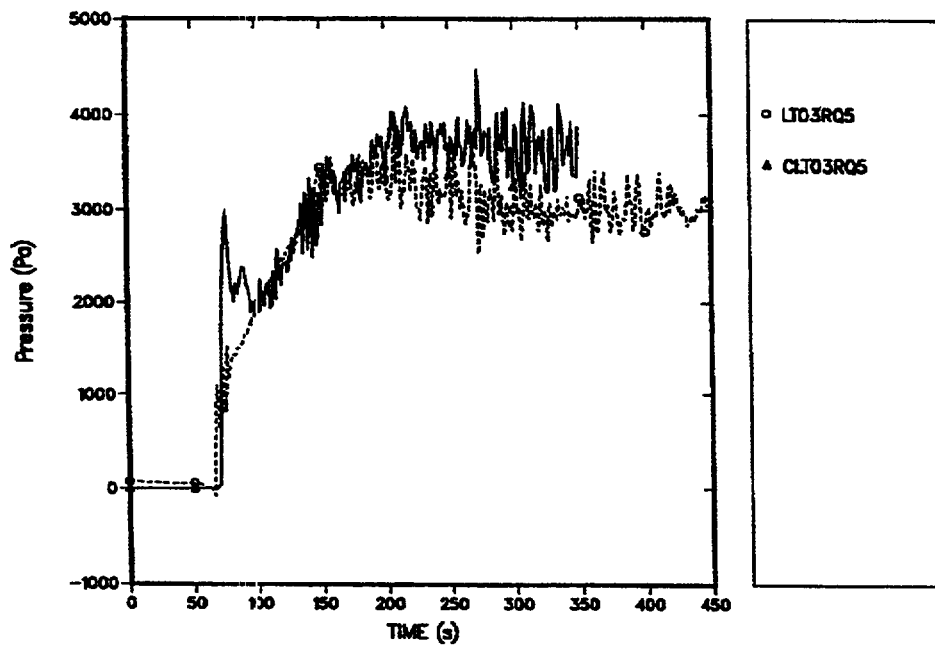


Fig. H-24. The predicted (solid) and measured (dashed) pressure-drop traces between axial elevations of 0.61–1.22 m.

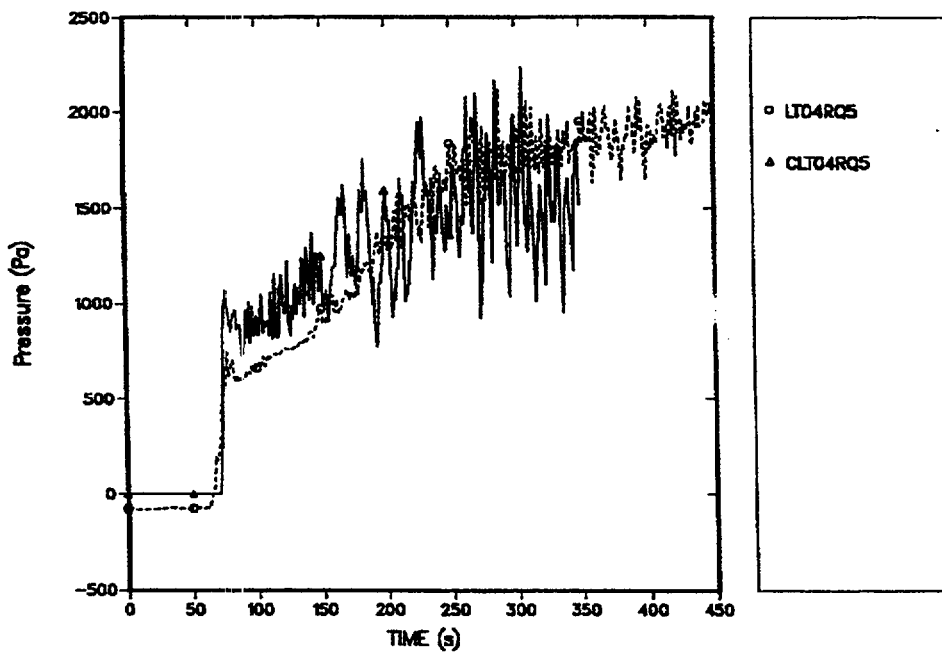


Fig. H-25. The predicted (solid) and measured (dashed) pressure-drop traces between axial elevations of 1.22–1.83 m.

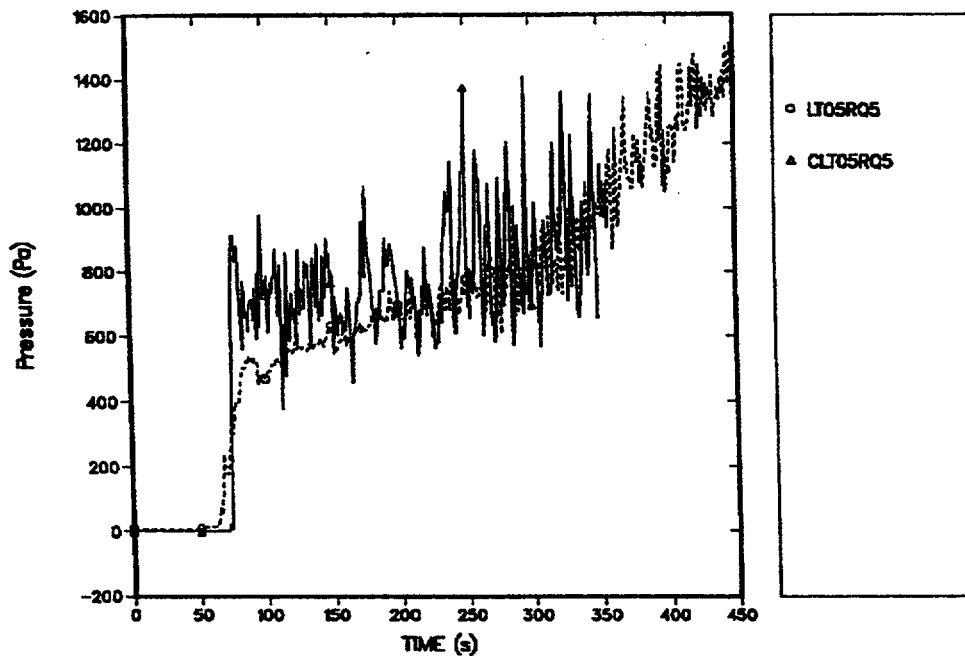


Fig. H-26. The predicted (solid) and measured (dashed) pressure-drop traces between axial elevations of 1.83–2.44 m.

H.1.5.9. Conclusion. The reflooding of a hot reactor core produces a quench front that passes through the core as the rods cool. Below the quench, subcooled boiling exists, and above the quench, regions of smooth inverted annular flow, rough-wavy flow, agitated flow, and dispersed flow exist. Transition correlations and visual images for each region above the quench are taken from the literature. Models are developed for the interfacial drag in each region for application to the two-fluid approximation. Order-of-magnitude analyses show that the various models provide values for the interfacial drag that are in the correct range.

In the subcooled-boiling region, a roughened pipe approach is recommended. Arguments are put forth to use the vapor as the continuous phase in this regime. In the smooth inverted annular region, smooth-tube correlations are used. In the rough-wavy region, the modified Wallis correlation is used. In the agitated region, for lack of correlations from the literature and details on the characteristics, it is recommended to use the models developed for the rough-wavy region. In the dispersed region, there is the possibility for a significant amount of liquid to exist as liquid film on the unheated surfaces. Thus, a method similar to that developed for annular-mist flow is recommended. To combine all the regions into a finite-difference scheme, we propose to use a length-weighted average of the components that exist within a given mesh. The coefficients used in the model for the drag coefficients and their weightings were obtained by fitting the CCTF Run-14 pressure-drop data. The comparison of the

calculated and predicted overall pressure drops at various elevations shows reasonable agreement when the overall model is used.

H.1.6. Process Models

In TRAC the interfacial-drag calculation is overridden for the case in which the user invokes the phase-separation logic or the accumulator logic. These two cases are described below.

H.1.6.1. Phase-Separation Option in 1D Components. The user invokes this option at any 1D component cell edge by setting the variable FRIC to a number greater than 10×10^{20} or less than -10×10^{20} . In the case where directional loss coefficients are input (variable NFRC1 is set to 2 in the NAMELIST input), then both values of FRIC must pass this test. If this test is passed, then the interfacial-drag coefficient is set to 0.0 to allow phase separation. Additionally, the code sets the liquid velocity at the interface to 0.

H.1.6.2. Accumulator Option. The user invokes this option by using a PIPE component in conjunction with the variable IACC = 1 or 2. IACC = 1 invokes an interface sharpener, which sets the interfacial drag to zero at user-selected cell internal interfaces. IACC = 2 invokes both a liquid separator model at the bottom of the PIPE and the interface sharpener. The separator model operates by manipulation of the FRIC array (i.e., the additive friction factor, which affects the phasic momentum solutions, but is not part of the interfacial logic per se), as described in Appendix J, Section J.7.

H.1.7. Conclusions Regarding Interfacial Drag

The correlations used to predict the interfacial-drag force in TRAC have been fully described. Many changes have been made since MOD1 has been released. These changes represent a significant improvement and are the result of the detailed assessment efforts that occurred in the 2D/3D, MIST, and ICAP programs associated with USNRC research. The assessments have been very beneficial because of the many recommendations that have been incorporated. The primary improvements were in the calculation of the bubble diameter (elimination of the Weber number criterion), the implementation of the profile slip effect, the addition of a realistic model for annular-mist flow, the addition of an inverted-flow regime for core reflow, the addition of stratified flow to the vessel, consistency with the interfacial heat transfer, and general code clean-up.

We believe that the current models are up to date, consistent, and as realistic as possible. However, we fully expect that there will continue to be discrepancies in future assessments because of the complex nature of the two-phase approach and the dependence on the local geometry. Nevertheless, the current models represent the best available data at this time and should provide a firm basis for any future improvements or additions.

H.2. Wall Drag.

The TRAC computer code models the pressure gradient caused by wall drag as the sum of the wall drag acting on the gas and liquid phases. TRAC models the wall drag acting

on the gas phase as a constant of proportionality times the momentum flux in the gas phase and the wall drag acting on the liquid phase as a constant of proportionality times the momentum flux in the liquid phase. This section will describe the TRAC wall-drag models for single-phase laminar and turbulent 1D flow, for two-phase vertical and horizontal-nonstratified 1D flow, for two-phase horizontal-stratified 1D flow, for single-phase laminar and turbulent 3D flow, and for two-phase 3D flow.

H.2.1. 1D Models

The TRAC-calculated pressure gradient caused by wall drag for two-phase 1D flow is given by the sum of the gas- and liquid-phase wall-drag terms

$$\left(\frac{dp}{dz}\right)_f = -c_{wg}|V_g|V_g - c_{wl}|V_l|V_l \quad , \quad (\text{H-156})$$

where

$$c_{wg} = \frac{\alpha_g \rho_g c_{fg}}{D_h} \quad , \quad (\text{H-157})$$

$$c_{wl} = \frac{\alpha_l \rho_l c_{fl}}{D_h} \quad , \quad (\text{H-158})$$

c_{fg} and c_{fl} are the gas and liquid friction factors, α_g is the void fraction associated with the gas phase, and α_l is the liquid fraction ($\alpha_l = 1 - \alpha_g$). From these equations, it can be seen that the constant of proportionality is c_{fg}/D_h for the gas phase and that the momentum flux for the gas phase is $\alpha_g \rho_g |V_g|V_g$. For the liquid phase, the constant of proportionality is c_{fl}/D_h and the momentum flux is $\alpha_l \rho_l |V_l|V_l$.

As the void fraction goes to zero, Eq. (H-156) will result in the correct single-phase liquid pressure gradient caused by wall drag consistent with c_{fl} , the liquid-phase friction factor. As the void fraction goes to one, Eq. (H-156) will result in the correct single-phase gas pressure gradient caused by wall drag consistent with c_{fg} , the gas-phase friction factor. Therefore, the single-phase correlations for c_{fl} and c_{fg} for laminar and turbulent flow will determine the single pressure gradient caused by wall shear.

For the purposes of comparison with correlations of known accuracy, the TRAC wall-drag model will be rewritten in terms of a two-phase multiplier (Ref. H-15, pp. 27-32, 49-68; Ref. H-27, Chapter-2). Division of Eq. (H-156) by the single-phase liquid wall drag flowing at the total mass flux yields the following effective two-phase multiplier for TRAC (Ref. H-15, Eq. 2.64, p. 28):

$$(\Phi^2)_{\ell o} = \left(\frac{dp}{dz} \right)_f = \frac{(\alpha_g \rho_g c_{fg} |V_g| V_g + \alpha_\ell \rho_\ell c_{f\ell} |V_\ell| V_\ell)}{c_{f\ell o} |G| G} \rho_\ell \quad , \quad (\text{H-159})$$

where $c_{f\ell o}$ is the single-phase liquid friction-factor correlation based on a liquid mass flux of $G = \rho_m V_m$. The gas and liquid friction factors in the above equation are based on different correlations depending upon the type of flow. The different correlations for each regime will be discussed in the following sections.

NFF is the user-input parameter for selecting 1D wall-drag options. Setting NFF equal to ± 1 selects the homogeneous wall-drag option. Setting NFF to zero results in constant wall friction with only the user-input values (FRIC array in input). A negative NFF results in the automatic calculation of an appropriate form loss coefficient (see [Appendix I, Section I.1.](#)) in addition to the selected two-phase-flow friction factor.

H.2.1.1. Homogeneous Model. If the user selects NFF equal to ± 1 , the homogeneous wall-drag model is used. This model is described below.

H.2.1.1.1. Basis for the Model. The friction-factor model for single-phase turbulent flow was chosen based on Churchill's model ([Ref. H-33.](#)),

$$f = 2 \left[\left(\frac{8}{Re} \right)^{12} + \frac{1}{(a+b)^{3/2}} \right]^{1/12} \quad , \quad (\text{H-160})$$

where

$$a = \left[2.457 \times \ln \left(\frac{1}{\left(\frac{7}{Re} \right)^{0.9} + \frac{0.27\epsilon}{D_h}} \right) \right]^{16} \quad (\text{H-161})$$

and

$$b = (37530/Re)^{16} \quad .$$

Churchill's equation represents a fit to the Moody curves, which include the laminar, transition, turbulent, smooth, and rough regimes in a single equation. The Reynolds number in the Churchill correlation is not allowed to go below 100 to prevent division by zero.

The TRAC two-fluid momentum equations result in a two-phase multiplier that includes the effect of slip without the modification for the single-phase friction factor.

The homogeneous wall-drag model alters the single-phase friction factor by using a two-phase viscosity (μ) defined in terms of the flow quality (X_f) [Ref. H-27., p. 33, Eq. (2-38)],

$$\mu = \left[\frac{X_f}{\mu_g} + \frac{(1-X_f)}{\mu_\ell} \right]^{-1} \quad (\text{H-162})$$

According to Ref. H-34., of the different methods for defining the two-phase viscosity, this method is more accurate than the methods of Owens (Ref. H-35.) or Cicchitti (Ref. H-36.), but is not as accurate as Dukler's method (Ref. H-37.). Whalley (Ref. H-38.) indicates that the standard deviation for the homogeneous wall-drag model with a two-phase viscosity based on Eq. (H-162) is ~38% for steam/water systems.

The coefficient of friction for the liquid phase is related to the Fanning friction factor by Eq. (H-163) and that for the gas phase by Eq. (H-164), such that

$$c_{f\ell} = 2f \quad \text{and} \quad (\text{H-163})$$

$$c_{fg} = c_{f\ell} \quad (\text{H-164})$$

Substitution of Eqs. (H-162), (H-163), and (H-164) into Eq. (H-159) yields

$$(\Phi)_{\text{to}}^2 = \left[\frac{(1-X_f)^2}{\alpha_\ell} + \frac{X_f^2 \rho_\ell}{\alpha_g \rho_g} \right] \left(\frac{c_f}{c_{f\text{to}}} \right) \quad (\text{H-165})$$

From Eq. (H-165), it can be seen that the TRAC effective two-phase multiplier is not equivalent to the homogeneous two-phase multiplier as defined in Wallis [Ref. H-15., p. 29, Eq. (2-70)],

$$(\Phi)_H^2 = \left[1 + X_f \left(\frac{\rho_\ell}{\rho_g} - 1 \right) \right] \left[1 + X_f \left(\frac{\mu_\ell}{\mu_g} - 1 \right) \right]^{-0.25} \quad (\text{H-166})$$

It can be shown that if the flow is homogeneous, and if $c_{f\ell} = c_{fg} = 0.158Re^{-0.25}$, then the TRAC homogeneous two-phase wall-drag model is equivalent to Eq. (H-166). Therefore, for slip ratios close to unity, the TRAC model will result in homogeneous two-phase multipliers consistent with Eq. (H-166).

H.2.1.1.2. Assumptions. In TRAC, the flow qualities in Eq. (H-162) are replaced with static quality to avoid discontinuities as $G \rightarrow 0$. More specifically,

$$X_f = \frac{\alpha_g \rho_g V_g}{(\alpha_g \rho_g V_g + \alpha_l \rho_l V_l)} = \frac{G_g}{G} = \frac{\alpha_g}{\alpha_g + \frac{\alpha_l}{\gamma S_r}} \quad (\text{H-167})$$

and

$$X_s = \frac{\alpha_g \rho_g}{(\alpha_g \rho_g + \alpha_l \rho_l)} \quad (\text{H-168})$$

where $S_r = V_g/V_l$ and $\gamma = \rho_g/\rho_l$. For slip ratios close to unity, this approximation is accurate. As the slip ratio increases, the difference between flow quality and static quality also increases.

The TRAC 1D homogeneous wall-drag model assumes that the wall drag acts on both phases, independent of whether both phases are in contact with the wall. When the liquid phase is in contact with the wall, it is assumed that some portion of the wall drag is transmitted to the gas phase. The total wall drag is apportioned between the liquid and the gas phases, based on the momentum flux in each phase.

H.2.1.1.3. Model as Coded. The homogeneous 1D wall-drag model is coded in subroutine FWALL, as described by Eqs. (H-160) through (H-164), except that the flow quality in Eq. (H-162) is replaced by the static quality, defined by Eq. (H-168). The quality is calculated in FWALL using

$$X = \frac{1}{1 + \frac{(1-\alpha_g)\rho_l}{\alpha_g \rho_g S_r}} \quad (\text{H-169})$$

with $S_r = 1$.

H.2.1.1.4. Weighting, Magnitude Limits, Rate Limits, and Averaging. The void fractions, densities, and viscosities used in the wall-drag correlations are volume-averaged. The momentum cell in TRAC is from cell center to cell center. The TRAC-calculated velocities are defined to be cell-edge quantities and the user-input hydraulic diameter is a cell-edge quantity. However, the TRAC-calculated fluid properties such as density, void fraction, and viscosity are cell-center quantities. The approach used in FWALL to obtain cell-edge quantities for the void fraction, density, and viscosity is to calculate a volume-average quantity using

$$\xi_{j+1/2} = \frac{\xi_j \text{vol}_j + \xi_{j+1} \text{vol}_{j+1}}{\text{vol}_j + \text{vol}_{j+1}} \quad (\text{H-170})$$

where ξ can be any cell-center fluid property. This process yields an averaged fluid property for the TRAC momentum cell.

FWALL also sets the calculated quality to zero when the volume-averaged void fraction is less than 0.001. This eliminates any divisions by zero in Eq. (H-169).

FWALL calculates the mass flux to be used in the calculation of the Reynolds number as the product of the volume-averaged mixture density and the absolute value of the two-phase mixture velocity. The absolute value of the mixture velocity is used to ensure that the Reynolds number is always positive. The mixture velocity is calculated in the PREPER routine with the following equation:

$$V_{mj+1/2} = \frac{\langle \alpha_g \rho_g V_g \rangle_{j+1/2} + \langle \alpha_l \rho_l V_l \rangle_{j+1/2}}{\rho_{mj+1/2}} \quad (\text{H-171})$$

In this expression, $\rho_{mj+1/2}$ is the donor-cell two-phase mixture density and $\langle \xi V \rangle_{j+1/2}$ is the donor-cell operator given by

$$\begin{aligned} \langle \xi V \rangle_{j+1/2} &= \xi_j V_{j+1/2} & \text{if } V_{j+1/2} \geq 0 \\ &= \xi_{j+1} V_{j+1/2} & \text{if } V_{j+1/2} < 0 \end{aligned} \quad (\text{H-172})$$

H.2.1.1.5. Assessment. The Churchill equation fits the Moody curves over the full range of the Moody curves. The Churchill equation includes the roughness effect and the laminar-flow regime.

To evaluate the TRAC effective homogeneous two-phase multiplier at a given pressure, mass flux, and void fraction, the relative velocity or slip ratio must be known. For all the comparisons to be made in this section of the report, the relative velocity at a given pressure, mass flux, and void fraction was determined by solving simultaneously the steady-state TRAC momentum equations and interfacial-shear model. Typical results for the calculated relative velocity based on the TRAC models are given in Figs. H-27 and H-28. These figures show two extreme hydrodynamic conditions: one at high pressure, high mass flux, and small hydraulic diameter, which all tend to reduce the TRAC-based relative velocity; the other at low pressure, low mass flux, and large hydraulic diameter, which all tend to increase the TRAC-based relative velocity. The hydraulic-diameter range spans the expected hydraulic diameters in a full-size four-loop Westinghouse plant. The pressure range spans the expected range of pressures for two-phase flow during a large-break LOCA in a Westinghouse four-loop plant. The high mass flux is approximately equal to the cold-leg and hot-leg steady-state mass flux for a Westinghouse four-loop plant, and the low mass flux was chosen so that the resulting phase velocities remained co-current.

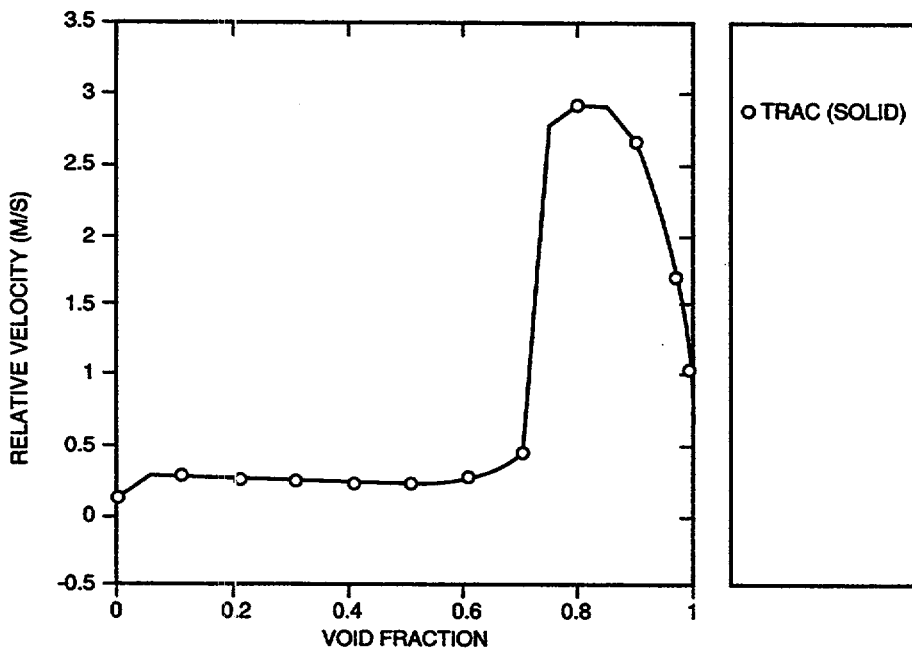


Fig. H-27. TRAC-calculated relative velocity for $p = 7.0$ MPa, $D_h = 0.011$ m, and $G = 10000$ $\text{kg} \cdot \text{m}^{-2} \cdot \text{s}^{-1}$.

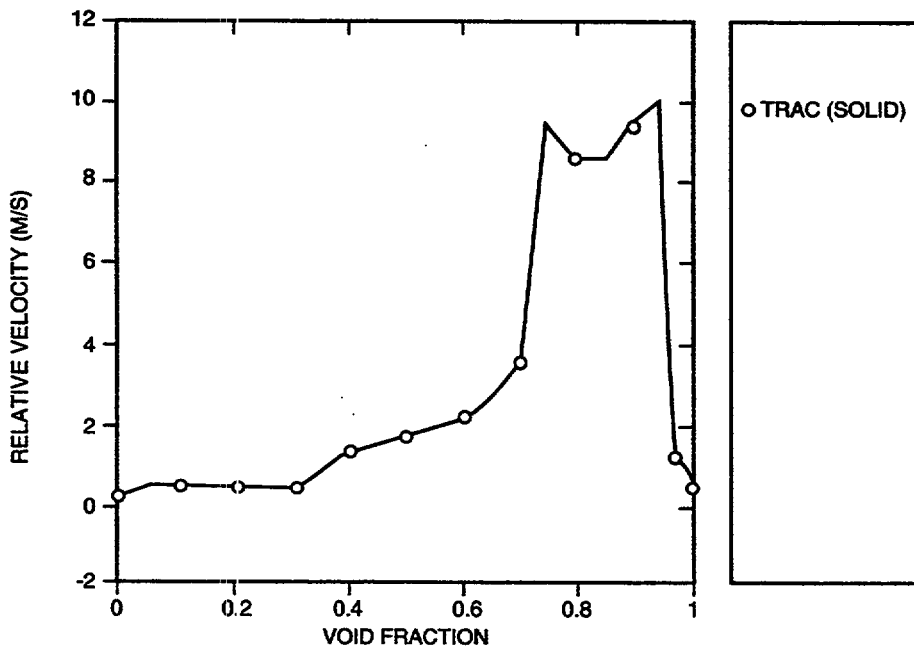


Fig. H-28. TRAC-calculated relative velocity for $p = 0.10$ MPa, $D_h = 0.7$ m, and $G = 1000$ $\text{kg} \cdot \text{m}^{-2} \cdot \text{s}^{-1}$.

Figure H-29 is a comparison of the TRAC homogeneous two-phase multiplier [Eq. (H-165)] evaluated with the two-phase viscosity static quality and flow quality. As can be seen from this figure, the approximation of using the static quality in place of the flow quality to determine the two-phase viscosity has no significant impact. Figures H-30. and H-31. compare the TRAC homogeneous two-phase multiplier with the Heat-Transfer Fluid Flow Service (HTFS) (Ref. H-38.) two-phase multiplier. As can be seen from these comparisons at low void fraction and high void fraction, both models tend to the same limits. For high slip ratios, the HTFS model tends to yield higher two-phase multipliers than does the TRAC homogeneous two-phase multiplier. The HTFS correlation (Ref. H-38.) is reported to have an uncertainty of $\pm 19\%$ for vertical flows and $\pm 51\%$ for horizontal flows. Also, according to Whatley, the homogeneous multiplier (using a two-phase viscosity) as defined by Eq. (H-166) has an uncertainty of $\pm 40\%$ for vertical steam/water flow and an uncertainty of $\pm 55\%$ for horizontal steam/water flow. These uncertainties are based on a 95% confidence level. As compared to the HTFS model, the root mean square (RMS) error of the TRAC homogeneous two-phase multiplier model is 0.21, based on 4992 points over the range of hydrodynamic conditions given in Table H-4.

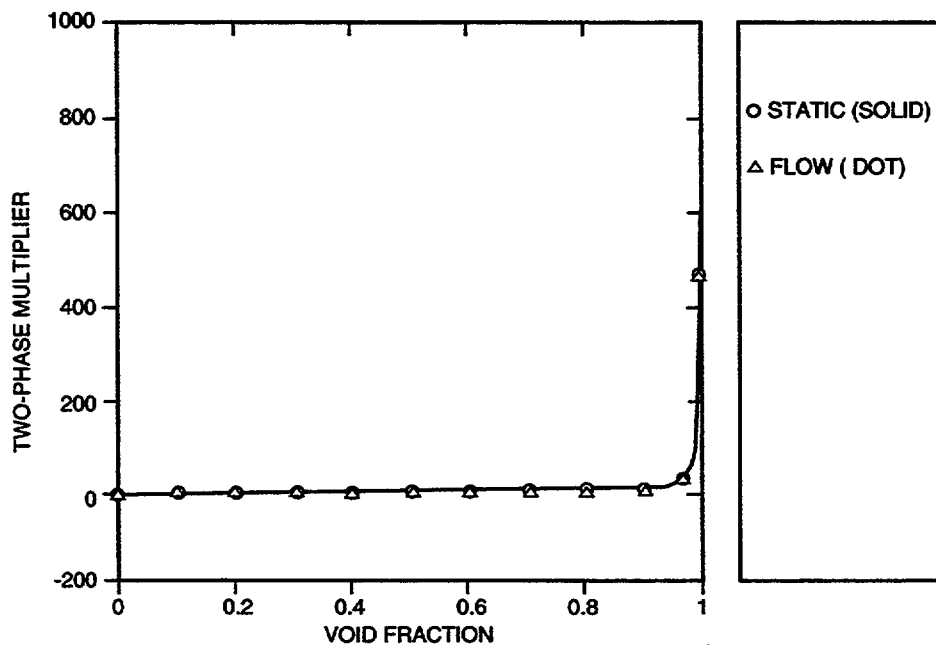


Fig. H-29. Comparison of two-phase multipliers, static vs. flow quality, for $p = 0.10$ MPa, $D_h = 0.7$ m, and $G = 1000$ $\text{kg} \cdot \text{m}^{-2} \cdot \text{s}^{-1}$.

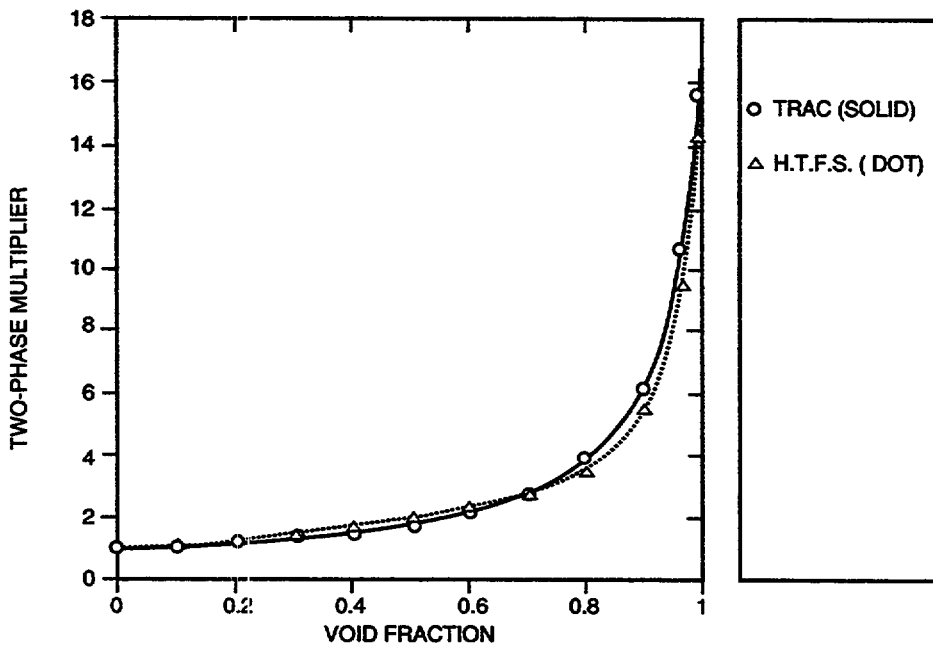


Fig. H-30. Comparison of two-phase multipliers, static vs. flow quality, for $p = 7.0$ MPa, $D_h = 0.011$ m, and $G = 10\,000$ $\text{kg}\cdot\text{m}^{-2}\cdot\text{s}^{-1}$.

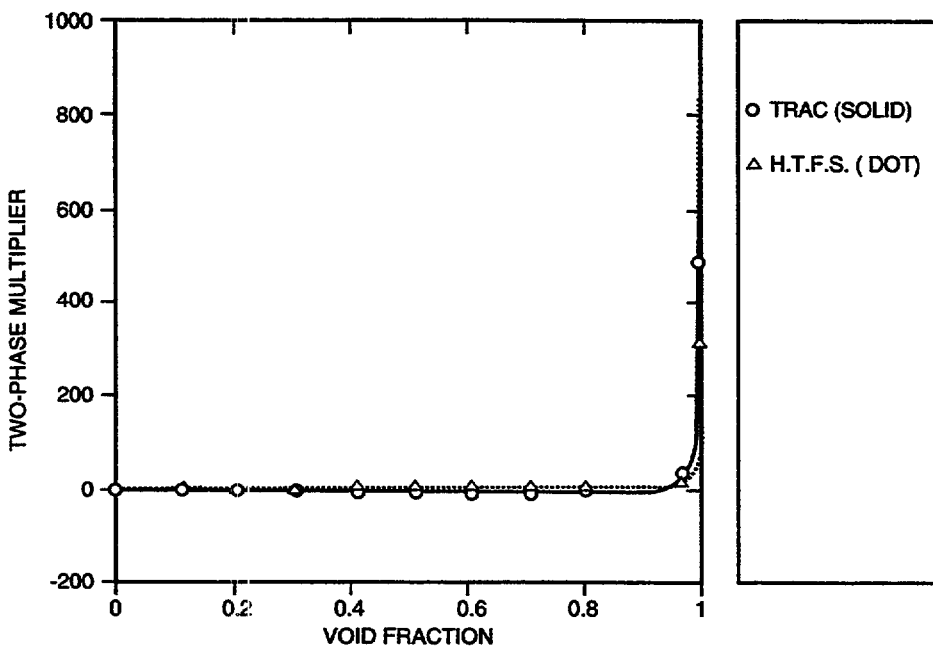


Fig. H-31. Comparison of two-phase multipliers for $p = 0.10$ MPa, $D_h = 0.7$ m, and $G = 1000$ $\text{kg}\cdot\text{m}^{-2}\cdot\text{s}^{-1}$.

TABLE H-4.
Range of Comparison Between TRAC Homogeneous Model and HTFS Correlation

Parameter	Maximum	Minimum
Mass Flux ($\text{kg} \cdot \text{m}^{-2} \cdot \text{s}^{-1}$)	10000.0	1000.0
Flow Quality	1.0	0.0
Tube Diameter (m)	0.7	0.011
Pressure (MPa)	7.0	0.10

H.2.1.1.6. Application Outside the Original Database. The TRAC homogeneous wall-drag model has no original database; however, comparisons to the HTFS correlation and the homogeneous model defined by Eq. (H-159) indicate that the model has an uncertainty of $\pm 40\%$ to $\pm 50\%$ over the range of the experimental data that formed the basis for the HTFS correlation, which is given in Table H-5. All the normal operating conditions and most of the abnormal conditions that would occur during a LOCA are covered in the database, with the exception of countercurrent flow. For countercurrent flow, it is not obvious which approach would be more accurate; however, the dominant phenomenon during countercurrent flow tends to be interfacial shear, not wall shear.

TABLE H-5.
Range of HTFS Data

Parameter	Maximum	Minimum
Mass Flux ($\text{kg} \cdot \text{m}^{-2} \cdot \text{s}^{-1}$)	24990.0	1.7
Flow Quality	1.0	0.0
Tube Diameter (m)	0.305	0.001
Pressure (MPa)	197.6	0.088
Roughness (ϵ/D)	0.068	0.0
~19000 total data points 28% of the data points were steam/water 43% of the data points were air/water 29% of the data points were fluids systems 44% of the data points were horizontal flow 31% of the data points were vertical flow 25% of the data points were inclined flow		

Eq. (H-160) is an accurate fit of the Moody Curves over a wide range of conditions. This equation includes laminar, turbulent, and rough wall effects. It is anticipated that no significant error will be introduced by using Eq. (H-160) for light-water-reactor applications. It has been observed, however, that the Churchill model is inaccurate for narrow annuli.

H.2.1.1.7. Scaling. The TRAC 1D wall-shear model is a function of Re , X_f , and S_w , all of which are nondimensional parameters that generally are accepted as independent of scale. It is also important to note that the wall shear is less important for a full-size plant (volume/surface area effect) than for the assessed experiments in which satisfactory overall answers have been obtained. As the scale increases, the importance of wall shear decreases. Inspection of the wall-shear term in the momentum equations reveals that it has a $D^{-1.2}$ dependence. The effect of this dependence on D can be illustrated by comparing the wall-shear pressure gradient for a full-size plant cold leg, for a LOFT cold leg, and for a semiscale cold leg. From Table H-6, it can be seen that the LOFT wall-shear pressure gradient in the cold leg is about three times larger than the full-size plant wall-shear pressure gradient for the same hydrodynamic conditions. The semiscale wall-shear pressure gradient in the cold leg is ~17 times larger than the full-size plant wall-shear pressure gradient for the same hydrodynamic conditions. No other term in the fluid momentum equations contains this inverse diameter effect (except for the interfacial drag during pure annular flow); therefore, as scale increases, the relative magnitude of the wall-shear term decreases. TRAC has successfully simulated both large and small breaks in both the LOFT and semiscale facilities. These subscale simulations with TRAC indicate that the wall shear is adequate for full-size plants if the flow-regime assumptions scale.

TABLE H-6.
Wall Shear Dependence Upon Pipe Diameter
for $g = 10^4 \text{ kg} \cdot \text{m}^{-2} \cdot \text{s}^{-1}$, $p = 15.8 \text{ MPa}$, $T = 551.4 \text{ K}$

Facility	Cold-leg D (m)	Wall Shear Pressure Gradient ($\text{Pa} \cdot \text{m}^{-1}$)
Full-Size Plant	0.698	446.0
LOFT	0.284	1353.0
Semiscale	0.067	7635.0

H.2.1.1.8. Summary and Conclusions. For the simulation of a typical four-loop Westinghouse plant, the total steady-state pressure loss against which the pump has to work (which is the total irrecoverable loss around a single loop and through the vessel) is ~0.6 MPa. Approximately 35% of the total loss is due to wall-friction effects. Of the pressure drop that is due to wall-friction effects, ~80% of the wall-friction pressure drop in a full-scale plant is a result of the steam-generator tubes. For plant calculations, most of the pressure drop around a loop is due to irrecoverable pressure losses at bends, flow-area changes, flow-direction changes, orifice plates, and spacers. Therefore, when modeling a plant, code users typically will simulate these irrecoverable losses by inputting additive pressure-loss factors or allowing the code to calculate the irrecoverable loss. These factors are adjusted until the user obtains the correct steady-state pressure loss around the loop at the correct loop flow rate with the correct pump speed. In addition, the user verifies that the flow splits are correct, which indicates that the flow resistances along parallel flow paths are modeled correctly. For large-break and small-break LOCAs, the transient response of the system is determined primarily by the break-flow rate (which is not dependent upon wall shear), the core and steam-generator heat-transfer rates, the gravitational heads, and the actions of all the boundary-condition systems (e.g., ECCS, secondary-side systems, etc.). The flows through the loops tend to be determined by the user-input additive losses, abrupt area-change losses, and changes in momentum fluxes. The wall-shear losses tend to be of minor importance once the transient starts. This is especially true as the flow rates drop off. The TRAC wall-drag model is accurate over a wide range of Reynolds flow. Therefore, the TRAC wall-drag model is adequate for full-scale plant calculations.

H.2.1.2. Horizontal Wall-Drag Model. A horizontal 1D interface is defined to be a 1D interface for which the angle of inclination above or below the horizon is less than 10 degrees for liquid upflow and up to 90 degrees for liquid downflow. Stratified horizontal flow occurs when the phase velocities fall below twice the critical velocity, V_c . The critical velocity for transition between stratified and dispersed or plug flow is given in [Appendix E](#) of this manual. The calculation of the wall drag for this model is described below.

H.2.1.2.1. Basis for the Model. The horizontal stratified-flow wall-shear model is based on the assumption that the wall shear for each phase can be determined by assuming smooth-pipe wall-shear models for each phase. The local-phase velocity and the hydraulic diameter based on the local-phase flow area and wetted perimeter are used to determine the phase-dependent Reynolds number. This approach for the wall shear for horizontal stratified two-phase flow is based on [Ref. H-39](#).

The horizontal 1D wall-shear coefficients are calculated from a Blasius-like relation using Reynolds numbers based on the velocities for each phase as given below:

$$Re_g = \max \left(100, \frac{\rho_g |V_g| D_g}{\mu_g} \right) \quad (\text{H-173})$$

and

$$Re_\ell = \max \left(100, \frac{\rho_\ell |V_\ell| D_\ell}{\mu_\ell} \right) , \quad (\text{H-174})$$

where D_ℓ and D_g are the hydraulic diameters based on the flow area and wetted perimeter for each phase, which are based on the height of the collapsed liquid level in the horizontal pipe. The stratified-flow wall-shear coefficients to be used in Eq. (H-156) are

$$c_{hwg} = \frac{2\alpha_g \rho_g 0.046 (Re_g)^{-0.2}}{D_g} \quad (\text{H-175})$$

and

$$c_{hw\ell} = \frac{2\alpha_\ell \rho_\ell 0.046 (Re_\ell)^{-0.2}}{D_\ell} \quad (\text{H-176})$$

This model is equivalent to the model recommended by Dukler in Ref. H-39 for the turbulent-flow regime. For laminar flow in either or both of the phases, Dukler recommends using the laminar-flow friction model given by

$$f = \frac{16}{Re} \quad (\text{H-177})$$

H.2.1.2.2. Assumptions. For Re_p (where p may be g or ℓ) below 1502, the Blasius-like friction-factor correlations in Eqs. (H-175) and (H-176) are replaced by the laminar-flow correlation given by Eq. (H-177). The total two-phase wall drag is assumed to be the sum of wall drag for both phases based on single-phase correlations evaluated with the appropriate phase velocities and hydraulic diameters. This model assumes a circular pipe geometry.

H.2.1.2.3. Constants. This model uses a Reynolds number of 1502 for laminar-to-turbulent-flow transitions.

H.2.1.2.4. Model as Coded. Interpolation between the nonstratified 1D wall-shear model defined in Sections H.2.1.1. and H.2.1.2. and the horizontal stratified wall-shear model is based on the stratified-flow-model transition logic described in Appendix E.

The interpolation function is used in the following manner:

$$c_{wg} = (WF)c_{hwg} + (1-WF)c_{vwg} \quad (\text{H-178})$$

and

$$c_{wl} = (WF)c_{hwl} + (1-WF)c_{vwl} \quad , \quad (H-179)$$

where c_{wl} and c_{wg} are the coefficients to be used in Eq. (H-156), c_{hwl} and c_{hwg} are the horizontal 1D wall-shear coefficients, and c_{vwl} and c_{vwg} are the nonstratified 1D wall-shear coefficients.

H.2.1.2.5. Weighting, Magnitude Limits, Rate Limits, and Averaging. The densities and void fractions used in the horizontal stratified-flow wall-drag correlation are based on a length-weighted average, as described by

$$\xi_{j+1/2} = \frac{\xi_j \Delta x_j + \xi_{j+1} \Delta x_{j+1}}{\Delta x_j + \Delta x_{j+1}} \quad , \quad (H-180)$$

where ξ can be any cell-center fluid property. This process yields an averaged fluid property for the TRAC momentum cell. This averaging equation will yield the same result as Eq. (H-170) if the volume-averaged flow area is not changing from cell j to $j + 1$. The length-weighted averaging process is appropriate for properties that appear in the wall-drag terms, since the wall drag is proportional to the cell length, not to the cell volume. The diameter used in the horizontal stratified-flow model is based on the volume-averaged flow area of the upstream and downstream hydrodynamic cells. The maximum pipe diameter between the two adjacent hydrodynamic cells is used in the wall-drag model for horizontal-stratified flow. The viscosity and surface tension are donor-cell properties, with the surface tension and the liquid-phase viscosity based on the liquid-phase flow direction and the gas-phase viscosity based on the gas-phase flow direction.

H.2.1.2.6. Assessment. The TRAC horizontal flow wall-shear model is compared to the homogeneous and HTFS models in Fig. H-32. For the conditions shown, TRAC calculated that the flow was stratified for void fractions between 10% and 90%. The comparison to the homogeneous and HTFS models is good except for void fractions between 0.8 and 0.9. In this region, TRAC predicts a larger two-phase multiplier than the other two correlations; however, the slip ratio chosen for this comparison is not appropriate for high-void stratified flow and may be the cause of the differences. At a more realistic slip ratio, the TRAC two-phase multiplier will be reduced for the high-void region.

According to Ref. H-38., the HTFS correlation has an uncertainty of $\pm 19\%$ for vertical two-phase flow and an uncertainty of $\pm 51\%$ for horizontal two-phase flow. The horizontal pipe two-phase flow pressure-drop data used to develop the HTFS correlation may have been stratified for some of the data points. Perhaps because the HTFS correlation attempts to include both stratified and nonstratified pressure-drop data in one correlation, it is much less accurate for horizontal pipes than for vertical pipes. Therefore, for horizontal stratified two-phase flow, the Dukler model (Ref. H-39.) used by TRAC may be more accurate than the HTFS model.

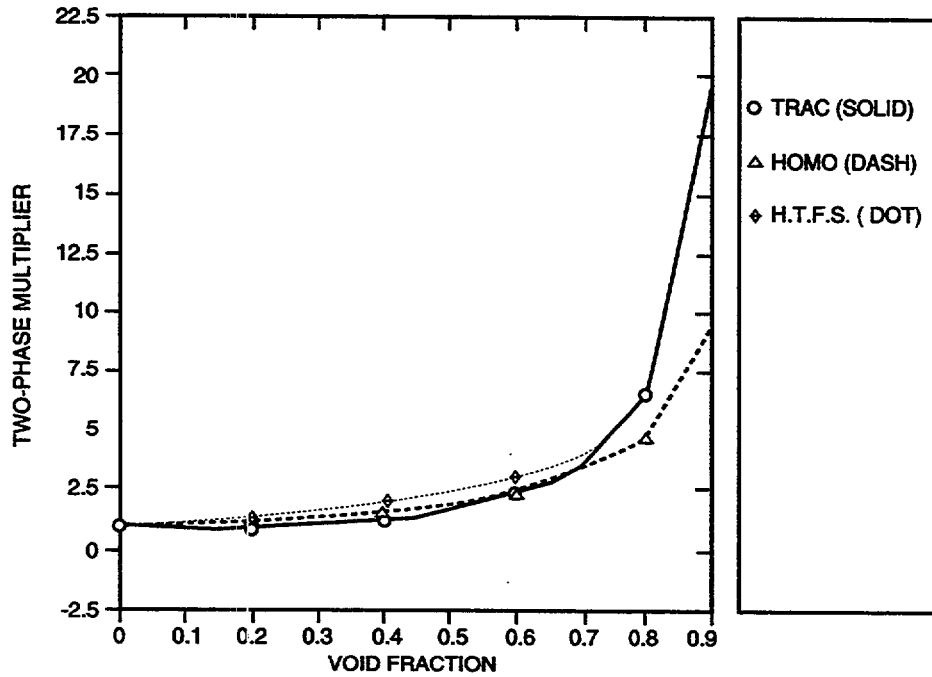


Fig. H-32. Comparison of wall drag in a horizontal pipe at $p = 1.0$ bar, $S_r = 1.012$, and $G = 500 \text{ kg} \cdot \text{m}^{-2} \cdot \text{s}^{-1}$.

H.2.1.2.7. Scaling. It is anticipated that the wall-drag correlations are independent of scale. However, there is some experimental evidence that indicates that the stratified-flow transition criteria will not scale to large-diameter pipes.

H.2.1.2.8. Summary and Conclusions. If the flow regime is predicted accurately, then the stratified-flow wall-drag model will predict accurately the wall drag on each phase.

H.2.2. 3D Models

The pressure gradient caused by wall shear for the TRAC 3D hydrodynamic equations is

$$\frac{dp}{dk} = c_{wgk} \langle V_{gk} \rangle V_{gk} + c_{w\ell k} \langle V_{\ell k} \rangle V_{\ell k} \quad , \quad (\text{H-181})$$

where k can be r , θ , or z , corresponding to the three orthogonal directions in the TRAC 3D VESSEL, and $\langle V_k \rangle$ is defined as a vector-average velocity for the k^{th} face of cell ijk . The wall-shear coefficients c_{wgk} and $c_{w\ell k}$ are defined the same way as in Eqs. (H-157) and (H-158),

$$c_{wgk} = \frac{\alpha_g \rho_g c_{fgk}}{D_{hk}} \quad (\text{H-182})$$

and

$$c_{w\ell k} = \frac{\alpha_\ell \rho_\ell c_{f\ell k}}{D_{hk}} \quad (\text{H-183})$$

As the void fraction goes to zero, Eq. (H-183) will result in the appropriate equations for the single-phase liquid wall drag based upon the $c_{f\ell k}$ coefficient. As the void fraction goes to one, Eq. (H-182) will result in the appropriate equations for the single-phase gas wall drag based upon the c_{fgk} coefficient. The following sections will address the correlations and models used to calculate α_ℓ , $c_{f\ell k}$, α_g , c_{fgk} , $\langle V_{gk} \rangle$, and $\langle V_{\ell k} \rangle$.

H.2.2.1. Basis for the Models. The laminar- and turbulent-flow friction-factor correlations for the 3D wall-drag model are based on the same references and databases as Eqs. (H-160) and (H-161) in the 1D homogeneous model.

The 3D model used the same mixture viscosity equation as defined in the 1D wall-shear-model description [Eq. (H-162)]. The flow quality used in the mixture viscosity equation is replaced with the static quality as in the 1D wall-shear model.

The Reynolds number in Eqs. (H-160) and (H-161) can be written as

$$Re_k = \frac{G_k D_{hk}}{\mu} \quad (\text{H-184})$$

where μ is the two-phase viscosity [see Eq. (H-162)], which goes to the appropriate single-phase viscosity when the void fraction is zero or one.

H.2.2.2. Assumptions. The static quality, rather than the flow quality, is used to calculate the two-phase viscosity. The flow-regime assumptions are the same as in the 1D homogeneous model.

H.2.2.3. Model as Coded. The 3D wall drag is evaluated in the WDRAG routine and the equations given above and below are evaluated as described.

H.2.2.4. Weighting, Magnitude Limits, Rate Limits, and Averaging. The vector-average velocity used in the above equations can be written as

$$\langle V_z \rangle = 0.5 \left\{ \left[2V_{zijk} \right]^2 + \left[V_{rijk} + V_{r(i-1)jk} \right]^2 + \left[V_{\theta ijk} + V_{\theta i(j-1)k} \right]^2 \right\}^{0.5} \quad (\text{H-185})$$

where V_{zijk} is the velocity in the axial direction at the z face of the ijk cell, V_{rijk} is the velocity in the radial direction at the radial face of the ijk cell, etc. The velocities used in Eq. (H-185) can be either the gas- or liquid-phase velocities.

The mass flux used in Eq. (H-184) can be written as

$$G_k = \alpha_g \rho_g \langle V_{gk} \rangle^* + \alpha_l \rho_l \langle V_{lk} \rangle^* \quad (H-186)$$

The vector-average velocities used in Eq. (H-186) are given by

$$\langle V_z \rangle^* = 0.5 \left\{ \left[2A_{zijk} V_{zijk} / A_{ijk} \right]^2 + \left[V_{rijk} + V_{r(i-1)jk} \right]^2 + \left[V_{\thetaijk} + V_{\theta(i-1)jk} \right]^2 \right\}^{0.5} \quad (H-187)$$

The vector-average velocity defined in Eq. (H-187) and used in Eq. (H-186) is the same as the vector-average velocity defined in Eq. (H-185), except for the ratio of z-face flow area A_{zijk} to volume-averaged flow area A_{ijk} that is applied to the axial-direction component of the velocity. This ratio is an attempt to relate the cell-edge velocity to the volume-average velocity. In situations in which a local flow-area restriction occurs at the z face of the ijk cell (e.g., an orifice), the wall shear should be based on the volume-average velocity rather than on the cell-edge velocity. The θ -face average vector velocity is defined by equations similar to Eqs. (H-185) and (H-187). However, the radial-face average vector velocity is set equal to the axial-face average vector velocity for the wall-shear calculation to save computational time.

H.2.2.5. Assessment. For 3D flow, the approximations for the vector-average velocities at each of the three faces for cell ijk are reasonable. However, a more accurate approximation to the averaged vector velocity at face z of cell ijk is

$$\langle V_{ijk} \rangle = \left[\left\{ \left[V_{zijk} A_{zijk} + V_{zij(k-1)} A_{zij(k-1)} \right]^2 + \left[V_{rijk} A_{rijk} + V_{r(i-1)jk} A_{r(i-1)jk} \right]^2 + \left[V_{\thetaijk} A_{\thetaijk} + V_{\theta(i-1)jk} A_{\theta(i-1)jk} \right]^2 \right\}^{0.5} \right] / \left[2A_{ijk} \right] \quad (H-188)$$

and

$$\langle V_z \rangle = \frac{\langle V_{ijk} \rangle A_{ijk} + \langle V_{ij(k+1)} \rangle A_{ij(k+1)}}{A_{ijk} + A_{ij(k+1)}} \quad (H-189)$$

Equation (H-188) results in an accurate estimation of the volume-averaged vector velocity for cell ijk , while Eq. (H-189) averages the cell ijk volume-averaged vector velocity with the cell $ij(k+1)$ volume-averaged vector velocity to obtain the average vector velocity with the z face of the ijk cell. The average vector velocity at the r and θ faces for the ijk cell can be written as

$$\langle V_r \rangle = \frac{\langle V_{ijk} \rangle A_{ijk} + \langle V_{(i+1)jk} \rangle A_{(i+1)jk}}{A_{ijk} + A_{(i+1)jk}} \quad (\text{H-190})$$

and

$$\langle V_\theta \rangle = \frac{\langle V_{ijk} \rangle A_{ijk} + \langle V_{i(j+1)k} \rangle A_{i(j+1)k}}{A_{ijk} + A_{i(j+1)k}} \quad (\text{H-191})$$

The additional accuracy obtained by using Eqs. (H-188) through (H-191) in the 3D wall-shear model is dependent upon the local geometry.

The approximations for the vector-average velocity have a negligible effect on the overall results. This is demonstrated by the following example that used typical geometry for a full-size plant with representative velocities that would occur at steady-state full-power operating conditions. The location in the VESSEL at which the largest difference in cell-average flow areas and cell-face flow areas occurs is at the core inlet location between the lower plenum and the first cell in the core region. At this location with the assumed operating conditions, Eq. (H-185) predicts a vector-average velocity of $3.51 \text{ m}\cdot\text{s}^{-1}$, while Eq. (H-189) predicts a vector-average velocity of $3.97 \text{ m}\cdot\text{s}^{-1}$. For this typical Westinghouse four-loop plant, the wall shear is ~18% of the total core pressure drop; therefore this represents ~2% error in the total core pressure-drop calculation. The user will typically adjust the user-input loss factors to account for this error.

According to Ref. H-38, the homogeneous multiplier using the mixture viscosity as defined in the 1D wall-shear model description and used in the 3D wall-shear model has an uncertainty of $\pm 40\%$ for vertical steam/water flow and an uncertainty of $\pm 55\%$ for horizontal steam/water flow. These uncertainties are based on a 95% confidence level.

REFERENCES

- H-1. M. Ishii and T. C. Chawla, "Local Drag Laws in Dispersed Two-Phase Flow," Argonne National Laboratory report ANL-79-105 (NUREG/CR-1230) (December 1979).
- H-2. J. F. Lime, "Memorandum on Interfacial Drag from M. Ishii to R. Nelson, July 28, 1987," Los Alamos National Laboratory document LA-UR-01-1591 (March 2001).
- H-3. R. B. Bird, W. E. Stewart, and E. N. Lightfoot, *Transport Phenomena* (John Wiley and Sons, New York, 1960), pp. 190-195.
- H-4. L. Shiller and A. Z. Nauman, *Ver. Deut. Ing.* **77**, 318-320 (1933).

- H-5. M. Ishii, "One-Dimensional Drift-Flux Model and Constitutive Equations for Relative Motion Between Phases in Various Two-Phase Flow Regimes," Argonne National Laboratory Report ANL-77-47 (1977).
- H-6. I. Kataoka and M. Ishii, "Drift Flux Model for Large Diameter Pipe and New Correlation for Pool Void Reaction," *Int. J. Heat Mass Transfer* **30**, 1927-1939 (1987).
- H-7. J. R. Grace, T. Wairegi, and J. Brophy, "Break-up of Drops and Bubbles in Stagnant Media," *Can. J. Chem. Eng* **56**, 3-8 (1978).
- H-8. J. Kitscha and G. Kocamustafaogullari, "Break-up Criteria for Fluid Particles," *Int. J. Multiphase Flow* **15**, 573-588 (1989).
- H-9. G. W. Govier and K. Aziz, *The Flow of Complex Mixtures in Pipes* (Von Nostrand Reinhold, New York, 1972).
- H-10. R. Clift, J. R. Grace, and M. E. Weber, *Bubbles, Drops and Particles* (Academic Press, New York, 1978), pp. 110-111.
- H-11. B. Chexal and G. Lellouche, "A Full-Range Drift-Flux Correlation for Vertical Flows (Rev. 1)," EPRI report NP-3939-SR, Rev. 1 (September 1986).
- H-12. J. Anderson and C. Chu, "BWR Refill-Reflood Program Constitutive Correlations for Shear and Heat Transfer for the BWR Version of TRAC," EPRI report NP-1582 (NUREG/CR-2134) (January 1983).
- H-13. B. Chexal, J. Horowitz, and G. Lellouche, "An Assessment of Eight Void-Fraction Models for Vertical Flows," EPRI report NSAC-107 (December 1986).
- H-14. Wilson, J. F. Grenda, R. J., and Patterson, J. F., "Steam Volume Fraction in a Bubbling Two Phase Mixture," *Trans ANS*, Nov. 1961.
- H-15. G. B. Wallis, *One Dimensional Two Phase Flow* (McGraw-Hill Book Company, New York, 1969).
- H-16. I. Kataoka and M. Ishii, "Mechanism-1 and Correlation of Droplet Entrainment and Deposition in Annular Two-phase Flow," Argonne National Laboratory report ANL82-44 (NUREG/CR-2885) (1982).
- H-17. M. Ishii and K. Mishima, "Two Fluid Model and Hydrodynamic Constitutive Relations," *Nucl. Eng. and Design*, **82**, 107-126 (1984).
- H-18. I. Kataoka, M. Ishii, and K. Mishima, "Generation and Size Distribution of Droplet in Annular Two-Phase Flow," *Transactions of the ASME*, Vol. 105, pp. 230-238 (June 1983).

- H-19. L. M. Hossfeld and D. Barathan, "Interfacial Friction in Co-current Upward Annular Flow," Electric Power Research Institute report EPRI NP-2326, Research Project 443-2 (March 1982).
- H-20. Y. Taitel and A. E. Dukler, "A Model for Predicting Flow Regime Transitions in Horizontal and Near Horizontal Gas-Liquid Flow," *AIChE J.* **22**(1), 47-55 (1976).
- H-21. A. Ohnuki, H. Adachi, and Y. Murao, "Scale Effects on Countercurrent Gas-Liquid Flow in Horizontal Tube Connected to Inclined Riser," in the ANS 1987 National Heat Transfer Conference (Pittsburgh, Pennsylvania, August 9-12, 1987), pp. 40-49.
- H-22. H. J Kim, "Heat Transfer and Interfacial Drag in Countercurrent Steam-Water Stratified Flow," *Int. J. Multiphase Flow*, **11**(5), 593-606 (1985).
- H-23. J. H. Linehan, "The Interaction of Two-Dimensional Stratified, Turbulent Air-Water and Steam-Water Flows," Ph.D. dissertation, Department of Mechanical Engineering, University of Wisconsin (1968).
- H-24. M. Ishii and G. DeJarlais, "Flow Visualization Study of Inverted Annular Flow of Post Dryout Heat Transfer Region," *Nuclear Engineering and Design*, **99**, 187-199 (1987).
- H-25. M. Ishii and G. DeJarlais, "Flow Regime Transition and Interfacial Characteristics of Inverted Annular Flow," *Nuclear Engineering and Design*, **95**, 171-184 (1986).
- H-26. N. T. Obot and M. Ishii, "Two-Phase Flow Regime Transition Criteria in Post-Dryout Region Based on Flow Visualization Experiments," *Int. J. Heat Mass Transfer*, **31**, 12, pp. 2559-2570, (1988).
- H-27. J. G. Collier, *Convective Boiling and Condensation*, (McGraw-Hill Book Company, New York, 1972).
- H-28. H. Schlichting, *Boundary-layer Theory*, (McGraw-Hill Book Company, New York, 1979).
- H-29. M. W. Cappiello, "A Model for the Interfacial Shear in Vertical, Adiabatic Annular-Mist Flow," Los Alamos National Laboratory document LA-CP-89-392 (October 1989).
- H-30. K. A. Williams, "On the Explanation and Calculation of Anomalous Reflood Hydrodynamics in Large PWR Cores," presented at the Winter ASME meeting, Miami, Florida, 85-MTA/HT-30 (November 1985).

- H-31. K. Pasamehmetoglu, "A Formula for Limiting Film Thickness on Cold Walls," Los Alamos National Laboratory memo from Pasamehmetoglu to Spore (September 1, 1989).
- H-32. "Data Report on Large Scale Reflood Test-14, CCTF Test C1-C5 (Run 14)," JAERI memo, 57-214 (August 1982).
- H-33. S. W. Churchill, "Friction-Factor Equation Spans All Fluid-Flow Regimes," *Chemical Engineering*, Nov. 7, 1977, pp. 91-92.
- H-34. P. B. Whalley, "Two-Phase Pressure Drop Design Report Part 5: The Calculation of Frictional Pressure Gradients in Two-Phase Flow," Atomic Energy Research Establishment report AERE-R9793, HTFS DR28, Rev. (February 1981).
- H-35. W. L. Owens, "Two-Phase Pressure Gradient," International Heat Transfer Conference, Boulder, Colorado, 1981.
- H-36. A. Cicchitti, C. Lombardi, M. Silvestri, G. Soldaini, and R. Zavatarelli, "Two-Phase Cooling Experiments: Pressure Drop, Heat Transfer and Burnout Measurements," *Energia Nucleare* 7, 407-425 (1960).
- H-37. A. E. Dukler, M. Wicks, and K. T. Cleveland, "Frictional Pressure Drops in Two-Phase Flow," *AIChE J.* 10, 44 (1964).
- H-38. P. B. Whalley, "Two-Phase Pressure Drop Design Report Part 6: The Calculation of Total Pressure Drop in Adiabatic Two-Phase Flow," Atomic Energy Research Establishment report AERE-R9794, HTFS DR28 (February 1981).
- H-39. Y. Taitel and A. E. Dukler, "A Model for Predicting Flow Regime Transitions in Horizontal and Near-Horizontal Gas Liquid Flows," *AIChE J.* 22 (1), 47-55 (1976).
- H-40. B. E. Boyack, J. F. Lime, D. A. Pimental, J. W. Spore, and J. L. Steiner, "TRAC-M/F77, Version 5.5, Developmental Assessment Manual, Volume I: Assessment Sections not Including 2D/3D Tests," Los Alamos National Laboratory document LA-UR-99-6480 (December 1999).
- H-41. B. E. Boyack, J. F. Lime, D. A. Pimental, J. W. Spore, and J. L. Steiner, "TRAC-M/F77, Version 5.5, Developmental Assessment Manual, Volume II: Assessment Sections for 2D/3D Tests," Los Alamos National Laboratory document LA-CP-99-345 (December 1999).

APPENDIX I

FLOW PROCESS MODELS

This section describes how the following flow processes are treated within TRAC: 1D abrupt area changes, 1D and 3D critical flow, countercurrent flow, TEE-component offtake flow, and vent valves. The following nomenclature applies to Appendix I.

NOMENCLATURE

a_{HE} :	homogeneous equilibrium sound speed
A :	area
$\underline{A}, \underline{B}$:	matrices
c_p :	specific heat at constant pressure
c_v :	specific heat at constant volume
C :	virtual mass coefficient
C_1, C_2 :	constants
C_B, M_B :	empirical parameters of Bankoff correlation
CFZ:	default additive loss coefficient
D :	diameter
e :	internal energy
E :	interpolation constant used in CCFL model
f :	Darcy friction factor
g :	gravitational constant
G :	mass flux
h :	enthalpy in <u>Section I.2.</u> and characteristic height in <u>Section I.4.</u>
h_{fg} :	latent heat of vaporization
h_b :	critical height
H :	dimensionless flux
H_L :	head losses
HD_r :	hydraulic diameter in the r -direction
j :	superficial velocity
k :	Boltzmann constant
k_c :	critical wave number
K :	form-loss coefficient
K_{TRAC} :	loss coefficient
L :	length
L^* :	Bond number

M :	Mach number
n :	number of holes
p :	pressure
Q :	volumetric flow rate
R :	ideal-gas constant in <u>Section I.2.</u> and nondimensional height ratio in <u>Section I.4.</u>
s :	entropy
s^* :	thermodynamic function defined by <u>Eq. (I-42)</u>
S :	slip ratio
t :	time
t_p :	tie-plate thickness
T :	temperature
T_{sv} :	saturation temperature corresponding to steam partial pressure
\bar{U} :	solution vector to the conservation equations
vol:	cell volume
V :	velocity
V_s :	cell-edge (throat) velocity at location of area change
V_{gc} :	cell-center (upstream) gas velocity
V_{ge} :	fluid choking velocity
V_{le} :	cell-edge (throat) liquid velocity
V_{lc} :	cell-center (upstream) liquid velocity
w :	parameter defined by <u>Eq. (I-187)</u>
W :	mass-flow rate
WFHF:	horizontal-flow weighting factor
x :	quality or axial coordinate
x_0 :	quality defined by <u>Eqs. (I-196), (I-213), and (I-234)</u>
α :	void fraction
Δp :	pressure drop
Δr :	radial length of the fluid cell that connects to the vent valve
Δx :	cell length
$\Delta \rho$:	density difference between liquid and gas
γ :	specific heat ratio
η :	ratio of the hole area to tie-plate area
λ_i :	characteristic root
ρ :	density

- ρ^* : function of the main-tube-junction cell density derivatives defined by Eq. (I-39)
- σ : surface tension

Subscripts

- 1: main-tube-junction cell
- 2nd: second pass
- a*: noncondensable gas
- actual*: actual
- c*: cell-center condition (upstream of throat) or critical
- dn*: downward offtake
- donored*: donor-cell value
- e*: cell-edge condition (at throat)
- equil: equilibrium
- g*: gas mixture
- JCELL: mesh-cell designation
- j, j+1, etc.*: cell-center quantity
- j + 1/2, etc.*: cell-edge quantity
- k*: major phase
- l*: liquid
- m*: two-phase mixture or model-predicted result
- max: maximum
- min: minimum
- nuc: nucleation
- o*: stagnation property
- ot: offtake
- re*: real root
- sat: saturation
- sc*: subcooled
- sd*: side-oriented offtake
- tp*: two-phase
- up*: upward offtake
- v*: vapor

Superscripts

+	downstream
-	upstream
1, 2, 3:	first, second, and third predictions
$n, n + 1$:	current- and new-time values
p :	predicted

I.1. 1D and 3D Abrupt Flow-Area Change Model

Here we describe the coding invoked when a user inputs a negative value for a 1D component's friction-factor variable NFF. When NFF is negative at a cell edge, TRAC calculates an additional flow loss caused by an abrupt area change encountered at a sudden expansion or contraction between mesh cells. This loss is based on user-input data for the volume-averaged mesh-cell flow area ($A_j = \text{vol}_j / \Delta x_j$) and the fluid-velocity direction. TRAC adds the additional losses into the basic momentum equations to calculate correctly the pressure drop at the location of the abrupt area change.

The flow loss of a thin-plate orifice that is modeled at a mesh-cell interface is associated with an abrupt flow-area change. This flow loss is discussed here, but it is not added as an additional loss by TRAC when NFF is negative. Such losses that are modeled at interfaces need to be defined by the user through FRIC additive friction-loss-coefficient input data.

Similarly, the user may have to account for turning losses and abrupt area changes (including expansions and contractions) at the TEE-component joining cell with the FRIC input array.

TRAC is programmed also to add abrupt flow-area change losses to the 3D VESSEL component. Because NFF is not a VESSEL-component input parameter, the negative values for the liquid additive friction-loss coefficients CFZL-T, CFZL-Z, and CFZL-R are used as a user-defined input flag that turns on the 3D abrupt area change model. TRAC evaluates the same abrupt flow-area change loss and adds it to the absolute value of the input-specified additive friction-loss coefficient. This is done for both liquid and vapor and forward and reverse flow. The volume-averaged flow area in the radial direction for cylindrical geometry is divided by $R_{\text{mean}_i} = (1/2)(R_{\text{in}_i} + R_{\text{out}_i})$ [that is, $A_i = \text{vol}_i / (R_{\text{mean}_i} \Delta r_i)$] to remove the smooth flow-area change effect from cylindrical geometry.

I.1.1. Basis for the Model

In addition to ordinary friction losses in a uniform straight pipe, other losses can occur because of sudden velocity changes resulting from abrupt area changes. In long pipes, these additional losses may be neglected in comparison to the normal friction loss of the pipe. In short pipes, however, these additional losses may actually be much larger than the ordinary friction loss.

In the case of abrupt area changes, the source of the loss is confined to a very short length of pipe, although the turbulence produced may persist for a considerable distance downstream. The flow after the change may be exceedingly complex. For the purposes of analysis, however, we assume that the effects of ordinary friction and of the additional large-scale turbulence may be separated, and that the abrupt area change loss is concentrated at the location of the area change. The total head loss in a pipe may then be considered to be the sum of the ordinary friction for the length of pipe considered and the extra loss due to the abrupt area change.

For an abrupt expansion, a theoretical determination of the loss is possible. For an abrupt contraction, however, this is not true, and experimental results must be used to determine the flow loss. Because the losses have been found to vary as the square of the mean velocity, they are frequently expressed in the form

$$\text{Head Loss} = K \frac{V^2}{2g} \quad , \quad (\text{I-1})$$

where K is the loss coefficient, V is the mean velocity, and g is the gravitational acceleration constant.

We determine corrective terms added to the TRAC momentum equations by first considering the momentum equation for single-phase flow and by neglecting the gravity head and wall shear,

$$\frac{1}{\rho} \frac{\partial p}{\partial x} + V \frac{\partial V}{\partial x} = 0 \quad . \quad (\text{I-2})$$

For a pipe noded as in Fig. I-1, integration of Eq. (I-2) with the assumptions of steady state and of constant density from point j to point $j + 1$ yields a Bernoulli-type equation for the pressure change from point j to point $j + 1$ as follows:

$$p_{j+1} - p_j = 0.5\rho(V_j^2 - V_{j+1}^2) \quad . \quad (\text{I-3})$$

If Eq. (I-3) is rewritten in terms of a pressure drop, then

$$\Delta p_{j \rightarrow (j+1)} = -(p_{j+1} - p_j) = 0.5\rho(V_{j+1}^2 - V_j^2) \quad . \quad (\text{I-4})$$

The pressure drop given by Eq. (I-4) typically is referred to as the reversible pressure drop. We use the term reversible because the pressure loss associated with a contraction can be regained by a pressure rise at an expansion of the same magnitude. Consider the following three situations. If no area change occurs between points j and $j + 1$, the velocity of the flow does not change, and Eq. (I-4) predicts

$$\Delta p_{j \rightarrow (j+1)} = 0 \quad (\text{I-5})$$

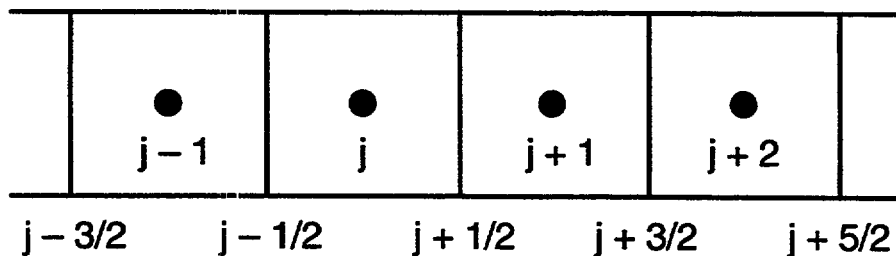


Fig. I-1. 1D TRAC noding.

as expected. If a smooth area change occurs between sections j and $j+1$, then the irreversible losses may be small, and Eq. (I-4) yields an approximation to the pressure drop from point j to $j+1$. If the area change between sections j and $j+1$ is abrupt, however, the irreversible losses cannot be ignored, and it is standard practice to add a form-loss factor to Eq. (I-4) to account for the additional irrecoverable pressure loss caused by the area change in question. This yields a general equation for the pressure drop between sections j and $j+1$ when an abrupt area change is present, such that

$$\Delta p_{j \rightarrow (j+1)} = -(p_{j+1} - p_j) = 0.5\rho(V_{j+1}^2 - V_j^2) + 0.5K\rho V_s^2 \quad , \quad (\text{I-6})$$

where V_s is the velocity at the cross section where the area change occurs. Once the loss coefficient K for the specific area change in question has been determined, either theoretically or experimentally, the pressure drop at the abrupt area change can be calculated using Eq. (I-6) above.

I.1.1.1. Abrupt Expansion. To determine the loss coefficient for an abrupt expansion, consider the expansion of Fig. I-2. If the pipes run full and the flow is assumed steady, two simplifying assumptions may be made that allow the pressure change across the expansion to be calculated. First, assume that the pressure and velocity at section j are uniform across the cross section. This assumption is valid for the high Reynolds-number flow found in most practical applications. Second, assume that the pressure and velocity at section $j+1$ are also uniform. This assumption is valid if section $j+1$ is sufficiently downstream of the expansion where the mixing caused by the turbulence has had a chance to even out the velocity profile again. A control-volume analysis using steady-flow equations may now be made on the fluid contained between sections j and $j+1$.

Application of the momentum equation for steady, incompressible flow neglecting wall friction to the fluid between sections j and $j+1$ yields the following force balance:

$$(p_j - p_{j+1})A_{j+1} = \rho Q(V_{j+1} - V_j) = \rho A_{j+1} V_{j+1} (V_{j+1} - V_j) \quad , \quad (\text{I-7})$$

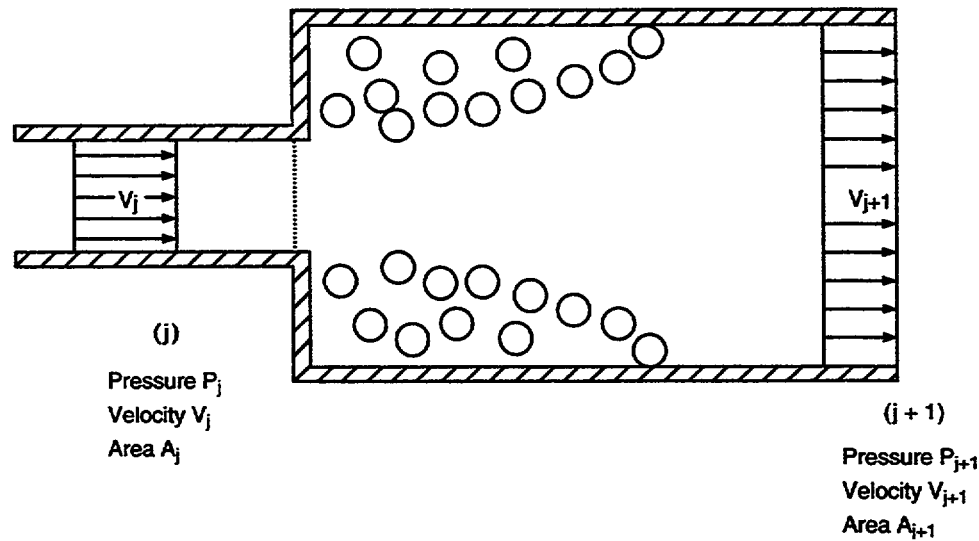


Fig. I-2. Abrupt expansion.

where Q is the volumetric flow rate and $V_j > V_{j+1}$ because of the change in the cross section at $j + 1/2$. Therefore,

$$(p_j - p_{j+1}) = \rho V_{j+1} (V_{j+1} - V_j) \quad (I-8)$$

Application of the Bernoulli equation for an incompressible fluid yields

$$\frac{p_j}{\rho g} + \frac{V_j^2}{2g} - H_L = \frac{p_{j+1}}{\rho g} + \frac{V_{j+1}^2}{2g} \quad (I-9)$$

where H_L is the total head loss across the expansion. Solving Eq. (I-9) for this head loss gives

$$H_L = \frac{p_j - p_{j+1}}{\rho g} + \frac{V_j^2 - V_{j+1}^2}{2g} \quad (I-10)$$

Substitution for the term $(p_j - p_{j+1})$ using Eq. (I-8) yields

$$H_L = \frac{(V_j - V_{j+1})^2}{2g} \quad (I-11)$$

From continuity, $A_j V_j = A_{j+1} V_{j+1}$ so that we may rewrite Eq. (I-11) as

$$H_L = \frac{V_j^2}{2g} \left(1 - \frac{A_j}{A_{j+1}} \right)^2 \quad (I-12)$$

Comparison of this result with Eq. (I-1) shows that the loss coefficient K for an abrupt expansion at the $j + 1/2$ interface is

$$K = \left(1 - \frac{A_j}{A_{j+1}} \right)^2 \quad (I-13)$$

when the mean velocity V of Eq. (I-1) is taken as V_j . Equation (I-13) is also known as the Borda-Carnot loss coefficient.

Now that the theoretical loss coefficient K has been determined, the pressure change between points j and $j + 1$ may be calculated using Eq. (I-6). Substitution of the result for K into Eq. (I-6) yields

$$\Delta p_{j \rightarrow (j+1)} = -(p_{j+1} - p_j) = \rho V_{j+1} (V_{j+1} - V_j) \quad (I-14)$$

which is exactly the result expressed in Eq. (I-8).

I.1.1.2. Abrupt Contraction. Consider the abrupt contraction of Fig. I-3. Although an abrupt contraction is geometrically the reverse of an abrupt expansion, it is not possible to solve exactly for the loss coefficient for an abrupt contraction using a control-volume analysis on the fluid between sections j and $j + 1$ as was done for the abrupt expansion of Fig. I-2. This is because the pressure at section j just upstream of the contraction varies in an unknown way as a result of the curvature of the streamlines and the acceleration of the fluid. Thus, application of the steady-flow momentum equation to the fluid at section j is not valid. Without the relationship between pressure and velocity provided by the momentum equation [as in Eq. (I-7) for the case of the abrupt expansion], it is not possible to solve explicitly for the total head loss across the contraction. Loss coefficients have been determined experimentally for circular coaxial pipes and fairly high Reynolds numbers, and Massey (Ref. I-1, p. 219) recommends the use of Table I-1 when determining values for K .

Once K has been determined using Table I-1, the pressure drop across the abrupt contraction may be calculated as follows. The flow at section j has a velocity V_j , while the flow upon reaching section $j + 1$ has a velocity V_{j+1} that is higher than V_j because of the abrupt cross-section change. Using Eq. (I-6) to calculate the change in pressure from points j to $j + 1$ caused by the abrupt area change yields

$$\Delta p_{j \rightarrow (j+1)} = -(p_{j+1} - p_j) = 0.5\rho(V_{j+1}^2 - V_j^2) + 0.5K\rho V_{j+1}^2 \quad (I-15)$$

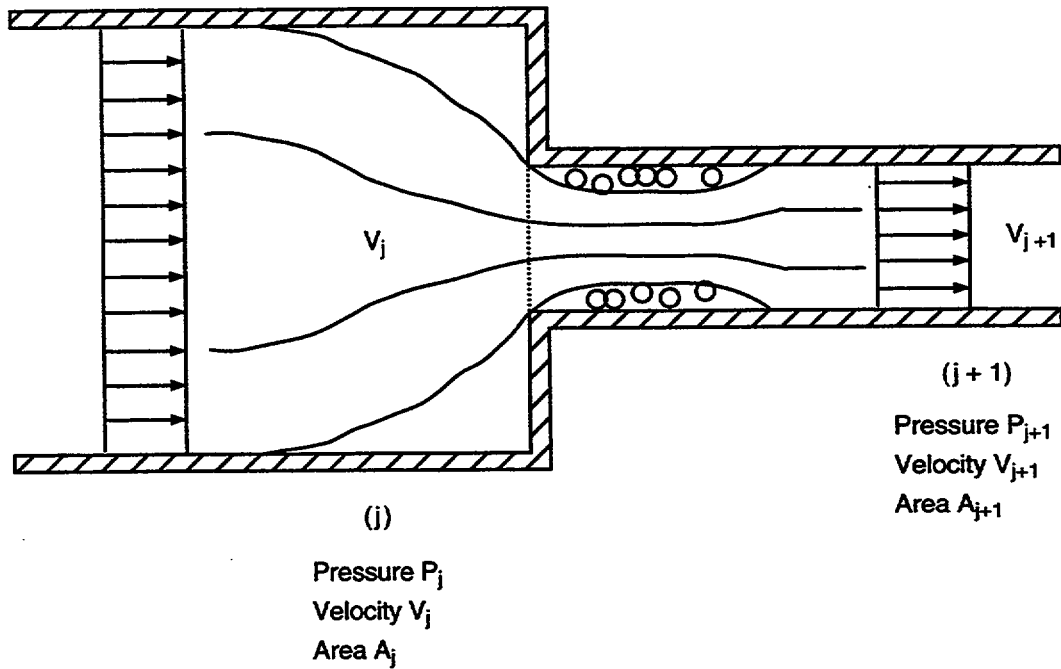


Fig. I-3. Abrupt contraction.

where K is taken from Table I-1.

I.1.1.3. Thin-Plate Orifice. As in the case of the abrupt contraction, it is not possible to determine theoretically the loss coefficient across a thin-plate orifice, and experimental data must be used. For a sharp-edged, thin-plate orifice in a straight conduit (Fig. I-4.), Idel'Chik (Ref. I-3., p. 139) suggests that the following expression be used for the loss coefficient K in the presence of high Reynolds numbers ($\geq 10^5$):

$$K = \left(1 + 0.707 \sqrt{1 - \frac{A_{j+1}}{A_j}} - \frac{A_{j+1}}{A_j} \right)^2 \quad (I-16)$$

This curve fit also agrees well with the data plotted in White (Ref. I-4., p. 384) for the irrecoverable head loss across a thin-plate orifice.

TABLE I-1.
Abrupt Contraction Standard Loss-Coefficient Data

A_{j+1}/A_j	0.0	0.04	0.16	0.36	0.64	1.0
K	0.5	0.45	0.38	0.28	0.14	0.0

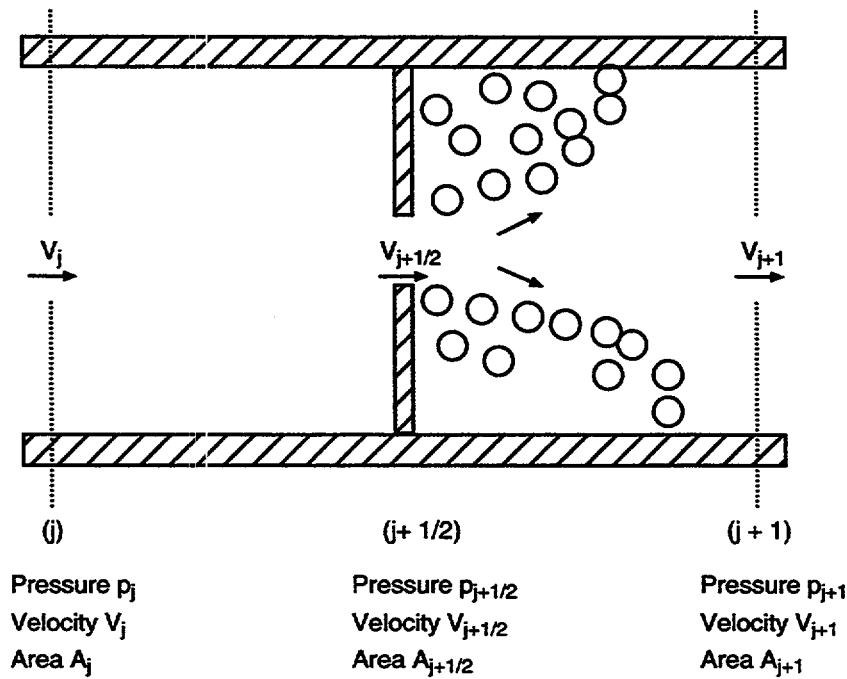


Fig. I-4. Sharp-edged, thin-plate orifice.

Once the loss coefficient K for a sharp-edged, thin-plate orifice has been determined using [Eq. \(I-16\)](#), the pressure drop across the orifice may be calculated as follows. The flow at section j has a velocity V_j , while the flow upon reaching section $j + 1/2$ has a velocity $V_{j+1/2}$, which is higher than V_j because of the abrupt cross-section change. Using [Eq. \(I-6\)](#) to calculate the change in pressure from points j to $j + 1/2$ caused by the abrupt area change yields

$$\Delta p_{j \rightarrow (j+1/2)} = -(p_{j+1/2} - p_j) = 0.5\rho(V_{j+1/2}^2 - V_j^2) + 0.5K\rho V_{j+1/2}^2 \quad (I-17)$$

where K is calculated using [Eq. \(I-16\)](#). Another abrupt area change occurs between points $j + 1/2$ and $j + 1$. The flow at section $j + 1/2$ has a velocity $V_{j+1/2}$, while the flow at section $j + 1$ has a velocity V_{j+1} , which is less than $V_{j+1/2}$ because of the expansion in cross section. Because the irreversible losses caused by the presence of the orifice have already been accounted for in the pressure drop between j and $j + 1/2$ and should not be accounted for twice, the pressure change between $j + 1/2$ and $j + 1$ is simply

$$\Delta p_{(j+1/2) \rightarrow (j+1)} = -(p_{j+1} - p_{j+1/2}) = 0.5\rho(V_{j+1}^2 - V_{j+1/2}^2) \quad (I-18)$$

Adding [Eqs. \(I-17\)](#) and [\(I-18\)](#) (noticing that $V_j = V_{j+1}$) shows that the total pressure drop from points j to $j + 1$ for the orifice of [Fig. I-4](#) is

$$\Delta p_{j \rightarrow (j+1)} = -(p_{j+1} - p_j) = 0.5 \rho K V_{j+\frac{1}{2}}^2 \quad , \quad (\text{I-19})$$

where K is calculated according to Eq. (I-16).

I.1.1.4. Turning-Flow Loss. The current TEE-component momentum-source-term logic is discussed in Section 2.0. We note here that while this model exhibits numerical stability, it does not give perfect predictions of losses at TEE internal junctions. Usually, the current model will underpredict TEE losses, although in some situations the losses will be overpredicted. The user must account for any additional losses with appropriate use of the FRIC input array that specifies friction factors (or, optionally, K-factors) at 1D mesh-cell interfaces. Reference I-2, is a source of such data. Note that the correlations in Ref. I-2, for TEE losses include velocities based on experiments that have equal flow areas in all three TEE flow channels. Also note that, as stated in Section 2.0, TRAC's flow-area logic for reversible losses is not activated at the three interfaces of the TEE joining cell and that there is no internal calculation available for abrupt expansion or contraction at those faces.

I.1.2. Assumptions and Preliminary Calculations

We make several assumptions when deriving the loss coefficients for each of the abrupt area changes discussed.

To perform a control-volume analysis on the abrupt expansion, we must assume that the pressures and velocities are uniform over the cross sections at sections j and $j+1$ (Fig. I-2). As discussed in Section I.1.1.1, this is largely true for section j at high Reynolds-number values and at section $j+1$ when it is taken sufficiently far downstream of the enlargement [about 8 times the larger diameter according to Massey (Ref. I-1, p. 217)].

For the case of the abrupt contraction, the data reported in Massey (Ref. I-1, p. 219) represent loss coefficients for coaxial circular pipes and fairly high Reynolds numbers. It is assumed that the data also apply to any abrupt contraction modeled using TRAC, and that the data give a good estimate of the loss coefficient.

For the thin-plate orifice, the loss-coefficient expression [Eq. (I-16)] recommended by Idel'Chik (Ref. I-3, p. 139) represents a curve fit to data for a sharp-edged, thin-plate orifice in a conduit for high Reynolds-number flow. As is the case for the abrupt contraction, it is assumed that this curve fit is applicable to any general sharp-edged, thin-plate orifice modeled by the user, and that the curve fit provides a good estimate of the loss coefficient.

If the correlations of Ref. I-2 are used for TEE turning losses through the FRIC array, the user still must account for any flow-area changes at the three TEE joining-cell interfaces (again, using FRIC).

I.1.3. Model as Coded

Again consider the momentum equation for single-phase flow, neglecting the gravity-head and wall-shear terms,

$$\frac{1}{\rho} \frac{\partial p}{\partial x} + \frac{1}{2} \frac{\partial V^2}{\partial x} = 0 \quad (I-20)$$

Whereas MOD1 differences the $V \partial V / \partial x$ form of the momentum-convection term, MOD2 and TRAC-M difference the momentum-convection term form in Eq. (I-20) (for the pipe noded as in Fig. I-1.) as

$$\frac{1}{\rho} (p_{j+1} - p_j) + 0.5 (V_{j+1}^2 - V_j^2) = 0 \quad (I-21)$$

Written in terms of a pressure drop between points j and $j + 1$,

$$\Delta p_{j \rightarrow (j+1)} = -(p_{j+1} - p_j) = 0.5 \rho (V_{j+1}^2 - V_j^2) \quad (I-22)$$

This finite-difference result is identical to the integral result of Eq. (I-4).

As before, if no area change occurs between points j and $j + 1$, the velocity of the flow does not change, and Eq. (I-22) predicts

$$\Delta p_{j \rightarrow (j+1)} = 0 \quad (I-23)$$

as expected. If an abrupt area change between sections j and $j + 1$ does occur, however, then a form-loss factor is again added to the pressure-drop equation to account for irreversible losses. This yields the general equation for a pressure drop between point j and $j + 1$ when an abrupt area change is present, such that,

$$\Delta p_{j \rightarrow (j+1)} = -(p_{j+1} - p_j) = 0.5 \rho (V_{j+1}^2 - V_j^2) + 0.5 K_{\text{TRAC}} \rho V_s^2 \quad (I-24)$$

where V_s is the cell-edge velocity at the location of the area change.

In TRAC, pressures are cell-centered quantities whereas velocities are cell-edge quantities. Therefore, approximating the cell-centered velocities in Eq. (I-24) by donoring the interface velocities and assuming continuity of volumetric flow gives for a positive-direction flow velocity,

$$\begin{aligned} \Delta p_{j \rightarrow (j+1)} &= -(p_{j+1} - p_j) \\ &= 0.5 \rho \left[\frac{A_{j+1/2}}{A_{j+1}} + \frac{A_{j+1/2}}{A_j} \right] V_{j+1/2} \left[\frac{A_{j+1/2}}{A_{j+1}} V_{j+1/2} - \frac{A_{j-1/2}}{A_j} V_{j-1/2} \right] \end{aligned} \quad (I-25)$$

Because the pressure-drop equation in MOD2 and TRAC-M is identical in form to Eq. (I-6), the loss coefficient K_{TRAC} calculated in subroutine FWKF is exactly that developed in the previous pages for the cases of abrupt expansion and contraction.

Namely, for an abrupt expansion noded as in Fig. I-5., subroutine FWKF calculates the loss coefficient as

$$K_{TRAC} = \left(1 - \frac{A_j}{A_{j+1}}\right)^2 \left(\frac{A_{j+1/2}}{A_j}\right)^2 \quad (I-26)$$

The factor $(1 - A_j/A_{j+1})^2$ is the K-factor to be applied to the minimum flow-area-velocity squared, v_j^2 , as presented in Eq. (I-13). The other factor $(A_{j+1/2}/A_j)^2$ converts that K-factor to K_{TRAC} , which is applied to the mesh-cell interface-velocity squared, $v_{j+1/2}^2$. This conversion is based on assuming continuity of volumetric flow; i.e., $A_j V_j = A_{j+1/2} V_{j+1/2}$. Similarly, the loss coefficient for an abrupt contraction noded as in Fig. I-6. is calculated by subroutine FWKF as a curve fit to the data of Table I-1., such that

$$K_{TRAC} = \left\{ 0.5 - 0.7 \left(\frac{A_{j+1}}{A_j}\right) + 0.2 \left(\frac{A_{j+1}}{A_j}\right)^2 \right\} \left(\frac{A_{j+1/2}}{A_{j+1}}\right)^2 \quad (I-27)$$

The bracketed factor is the K-factor to be applied to the minimum flow-area-velocity v_{j+1}^2 . Multiplying by the following factor $(A_{j+1/2}/A_{j+1})^2$ defines K_{TRAC} to be applied to the mesh-cell interface-velocity squared, $v_{j+1/2}^2$.

For the case of a thin-plate orifice noded as in Fig. I-7., the loss coefficient recommended by Idel'Chik is not evaluated by subroutine FWKF. This is because many TRAC input-data models have cell-edge flow areas that are less than both of its mesh-cell flow areas without being a model for a thin-plate orifice. The user needs to input a FRIC to account for the irreversible loss across this type of abrupt area change.

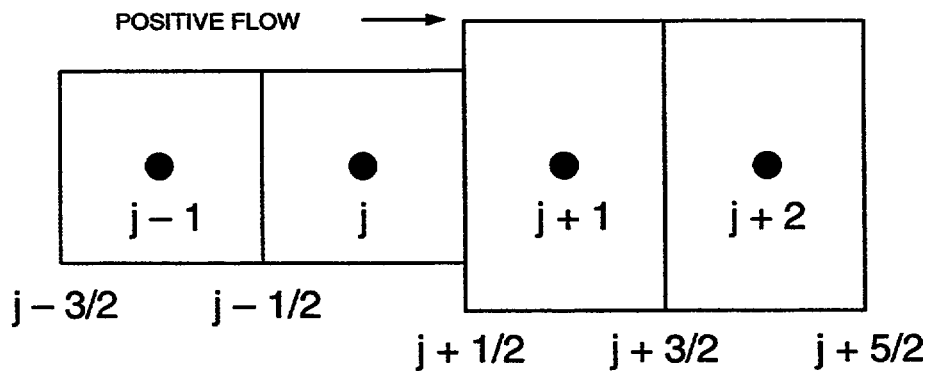


Fig. I-5. TRAC noding for abrupt expansion if $V_{j+1/2} > 0$ and for abrupt contraction if $V_{j+1/2} < 0$.

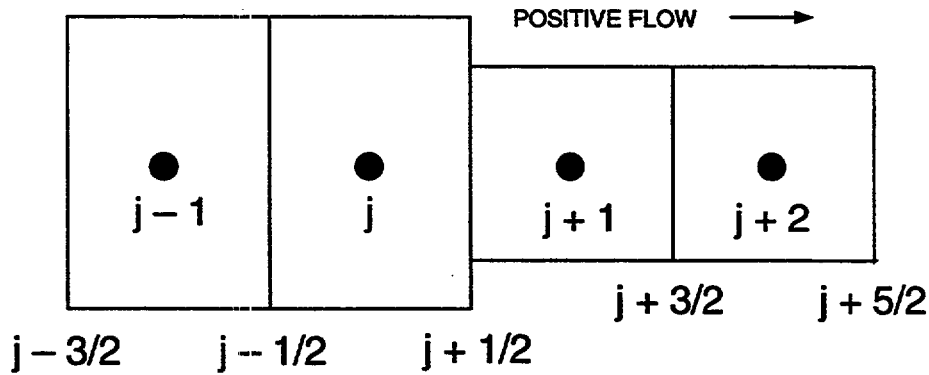


Fig. I-6. TRAC noding for abrupt contraction if $V_{j+1/2} > 0$ and for abrupt expansion if $V_{j+1/2} < 0$.

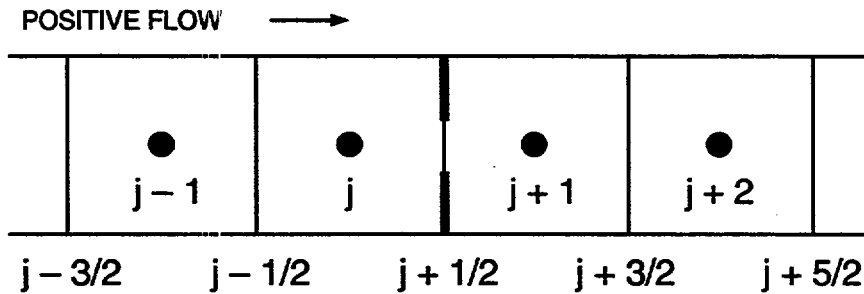


Fig. I-7. TRAC noding for sharp-edged, thin-plate orifice.

I.1.4. Assessment

The flow-area-ratio defining form of Eq. (I-25) used by MOD2 and TRAC-M predicts reversible losses across area changes, and any irreversible losses need to be accounted for by using an additional form-loss term. When the variable NFF or CFZL is set equal to a negative value at a cell edge containing an abrupt expansion, TRAC adds the theoretically derived form loss for such an area change into the momentum equations. This results in the proper pressure change being calculated and no error being introduced at cell edges containing abrupt expansions.

The data for the standard loss coefficient for an abrupt contraction cited in Massey (Ref. I-1, p. 219) (see Table I-1.) are incorporated into TRAC using a curve fit. Table I-2. compares the original data and the K -value predicted using the curve fit of Eq. (I-27). For this analysis, it is assumed that $A_{j+1/2} = A_{j+1}$. Inspection of Table I-2. shows that Eq. (I-27) very closely predicts the standard loss coefficients measured experimentally. As a result, when NFF or CFZL is set to a negative value, TRAC calculates an additional loss term that is added into the momentum equations to accurately predict the pressure drop

across an abrupt contraction. Hence, Table I-2, shows a few percent error at cell edges containing abrupt contractions when the variable NFF or CFZL is negative.

Idel'Chik (Ref. I-3, p. 139) recommends that the standard loss coefficient for a sharp-edged, thin-plate orifice be calculated using Eq. (I-16). This correlation, however, is not evaluated by subroutine FWKF. Hence, TRAC will underpredict the pressure drop across an orifice unless an appropriate FRIC, such as defined by Eq. (I-16), is input by the user.

I.1.5. Geometry Effects

A major improvement in the calculation of pressure drops was realized in the MOD2 code (and now in TRAC-M) with the incorporation of flow-area ratios in the momentum-convection term to accurately evaluate reversible Bernoulli flow losses. In the MOD1 version, finite-differencing error occurs in the momentum-convection term because variation in flow area is not modeled and momentum convection is not conserved. The pressure drop does not occur until the second cell downstream of the area change for abrupt expansions and orifices. With the introduction of the flow-area ratios in MOD2, pressure drops are now calculated to occur across the area change itself, rather than in cells downstream of the area change. Therefore, it is no longer necessary that at least two cells separate each abrupt area change to prevent unexpected results as is suggested for MOD1.

TABLE I-2.
Abrupt Contraction Standard Loss-Coefficient
Data Comparison

$\frac{A_j}{A_{j-1}}$	K_{DATA} (<u>Table I-1.</u>)	$K_{Eq. (I-27)}$	$\% \text{ error} = \frac{(K_{DATA} - K_{Eq. (I-27)})}{K_{DATA}} \times 100\%$
0.0	0.5	0.5	0.0
0.04	0.45	0.47	-4.4
0.16	0.38	0.39	-2.6
0.36	0.28	0.27	3.6
0.64	0.14	0.13	7.1
1.0	0.0	0.0	0.0

It is possible to retrieve the MOD1 form of the momentum equation using TRAC-M by setting the variable flags ARY to 0.0 and ARN to 1.0 in module OneDDat (subroutine BLKDAT in TRAC-M/F77). This causes all area ratios in Eq. (I-25) to be unity because each flow-area ratio is evaluated as $(A/A)*ARY+ARN$ by TRAC-M. A thorough discussion of the pressure drops calculated for each of the abrupt area changes is given in the MOD1 correlations and models document (Ref. I-5.), and the reader is referred to this for more information regarding this particular option.

I.1.6. Summary and Conclusions

Irrecoverable pressure losses occur across abrupt area changes. In standard practice, these losses are accounted for in the momentum equation using an additional form-loss term. If the user sets the 1D-component variable NFF or the 3D VESSEL-component additive friction-loss coefficients CFZL to a negative value at the cell edge where the abrupt area change (an expansion or a contraction) is located, TRAC will calculate a form-loss coefficient based on the user-input cell-edge flow area, the volume-averaged mesh-flow flow areas, and the velocity direction. TRAC then adds this additional form-loss term to the momentum equation to account for the irrecoverable losses caused by the abrupt area change.

The abrupt flow-area change coding invoked when NFF or CFZL is negative is contained in subroutine FWKF. For an abrupt expansion or contraction, TRAC accurately calculates the pressure drop across the area change by adding an additional form-loss term into the momentum equations to account for the irrecoverable head loss. Although an additional loss coefficient should also be calculated for the case of an orifice, the recommended correlation is not evaluated by subroutine FWKF. The user is currently advised to account for irreversible losses through the use of input-specified FRICs.

The user may have to account for irrecoverable turning pressure loss through a TEE internal junction with appropriate FRICs. The current TEE model does not implement the area-ratio logic for reversible losses at the three joining-cell interfaces, nor is there evaluation of abrupt area changes at those faces when NFF is negative.

Modeling the momentum-convection term with area ratios conserves momentum flux convection between momentum cells and provides an accurate evaluation of reversible Bernoulli flow losses. The TRAC user has the responsibility then to account for all irreversible flow losses either by setting NFF or CFZL negative, so that TRAC internally evaluates and adds in abrupt flow-area-change losses for abrupt expansions and contractions, or by providing appropriate irreversible form-loss FRIC values at selected mesh-cell edges.

I.2. 1D Critical-Flow Model

The TRAC 1D critical-flow model comprises three separate models: a subcooled-liquid choked-flow model; a two-phase, two-component, choked-flow model; and a single-phase vapor choked-flow model.

I.2.1. Basis for the Models

The subcooled-liquid choked-flow model is a modified form of the Burnell model. The two-phase, two-component, choked-flow model is based on first principles and a characteristic analysis approach. The single-phase vapor choked-flow model uses an ideal-gas isentropic expansion assumption. Each model basis is now described in more detail.

I.2.1.1. Subcooled Liquid. The subcooled choked-flow model is a modified form of the Burnell model (Ref. I-6.). During the subcooled blowdown phase, the fluid changes phase at the break because the downstream pressure is much lower than the saturation pressure corresponding to the system fluid temperature. The transition from single- to two-phase flow, which is accompanied by discontinuous change in the fluid bulk modulus, leads to a large discontinuity in the sound speed at the break. The physical process that occurs during the subcooled blowdown phase is described briefly in the following paragraphs. Reference I-6. discusses this phenomenon in greater detail.

Figure I-8. shows a converging-diverging nozzle. The pressure downstream is such that the fluid just begins to flash at the throat. The flow upstream of the throat is subsonic. Because the sound speed is discontinuous when the fluid becomes saturated, however, and because mass conservation dictates that the velocity just upstream of the throat must be equal to the velocity just downstream of the throat (where the fluid has only a minuscule void fraction), the flow is supersonic throughout the diverging section. Thus, the nozzle does not contain any point in which the Mach number, M , equals one. Figure I-8. also shows the velocity profile and the sound speeds for this situation.

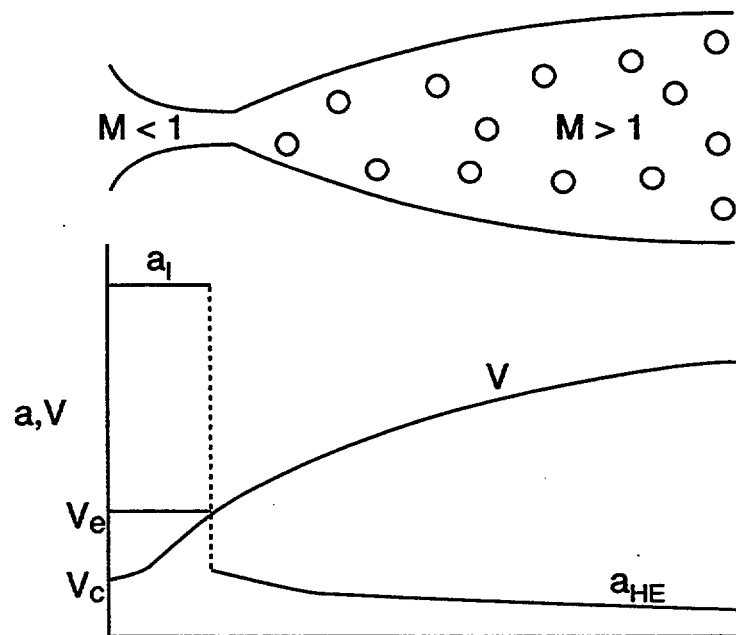


Fig. I-8. Subcooled choking process when nucleation begins at the throat.

The liquid velocity at the throat is calculated from Bernoulli's equation, assuming steady frictionless incompressible flow, such that

$$V_{le} = \left[V_{lc}^2 + \frac{2(p_c - p_e)}{\rho_l} \right]^{\frac{1}{2}}, \quad (I-28)$$

where subscripts c and e refer to the cell-center (upstream) and the cell-edge (throat) conditions, respectively. The throat pressure, p_e , is equal to the nucleation pressure, p_{nuc} , and can be considerably lower than the local saturation pressure, p_{sat} , because thermal nonequilibrium causes nucleation delay.

Any further reduction in the downstream pressure does not affect the flow because the disturbance cannot move upstream where the flow is supersonic in the diverging section. Thus, Eq. (I-28) gives the liquid throat velocity for any downstream pressure lower than the pressure necessary to cause the subcooled liquid to begin flashing at the throat (which is the case for most problems of interest in LWR applications).

Next we consider the situation in which the subcooled choked flow, as described above, exists initially, and the upstream pressure is lowered. As the upstream pressure decreases, the pressure at the throat remains equal to p_{nuc} , and again Eq. (I-28) can be used to calculate the liquid throat velocity. The liquid throat velocity decreases, however, because the upstream pressure decreases. If the upstream pressure is lowered further, a point is reached at which the liquid exit velocity is just equal to the homogeneous equilibrium sound speed, that is,

$$V_{le} = a_{HE} . \quad (I-29)$$

Any further reduction in the upstream pressure moves the point where $p = p_{nuc}$ upstream. In this case, the flow in the subcooled zone and two-phase zone upstream of the throat is subsonic. The flow at the throat is sonic with $V_{le} = a_{HE}$; the flow in the diverging section is supersonic. If the upstream pressure is reduced further, the p_{nuc} point moves upstream until complete two-phase flow exists. Therefore, the maximum of the Bernoulli expression and the homogeneous equilibrium sound speed give the subcooled choking criterion. Thus,

$$V_{le} = \max \left\{ a_{HE}, \left[V_{lc}^2 + \frac{2(p_c - p_e)}{\rho_l} \right]^{\frac{1}{2}} \right\} . \quad (I-30)$$

In TRAC, a nucleation delay model, developed by Jones (Ref. I-7.), determines the cell-edge pressure, p_e , from the saturation pressure, p_{sat} (corresponding to the donor-cell liquid temperature, T_d), such that

$$p_e = p_{\text{sat}} - \max \left\{ 0.0, 0.258 \frac{\sigma^{1.5} \left(\frac{T_\ell}{T_c} \right)^{13.76} \left[1 + 13.25 \left(-\frac{1}{1.01325 \times 10^{11}} \frac{Dp}{Dt} \right)^{0.8} \right]^{0.5}}{(kT_c)^{0.5} \left(1 - \frac{\rho_g}{\rho_\ell} \right)} - 27(0.072)^2 \left(\frac{A_e}{A_c} \right)^2 \frac{\rho_\ell V_\ell^2}{2} \right\} \quad (\text{I-31})$$

where σ is the surface tension, T_ℓ is the donor-cell liquid temperature, T_c is the critical temperature, Dp/Dt is the substantial derivative of the pressure, k is the Boltzmann constant, ρ_ℓ and ρ_g are cell-edge phasic densities, V_ℓ is the cell-edge liquid velocity as calculated by the standard momentum solution, and A_e and A_c are cell-edge and cell-center flow areas. The calculational sequence for the TRAC subcooled-liquid choking model is described in Section I.2.4.

I.2.1.2. Two-Phase, Two-Component Fluid. We developed the two-phase, two-component, choked-flow model from first principles using the characteristic analysis approach. The TRAC model is an extension of a model developed by Ransom and Trapp (Ref. I-8) that incorporates an additional inert-gas component and nonequilibrium effects. As suggested by Ransom and Trapp, we assume that thermal equilibrium exists between the phases. The validity of this assumption has not been investigated in the presence of an inert gas. This assumption, however, is not an inherent feature of the TRAC model and can be changed easily, if necessary.

The two-fluid field under thermal equilibrium is described by the overall continuity equation, two-phasic momentum equations, the mixture energy equation, and the inert-gas continuity equation. When the nondifferential source terms are omitted (because they do not enter into characteristic analysis), the equations are

$$\frac{\partial \rho_m}{\partial t} + \frac{\partial}{\partial x} (\rho_m V_m) = 0, \quad (\text{I-32})$$

$$\alpha \rho_g \left[\frac{\partial V_g}{\partial t} + V_g \frac{\partial V_g}{\partial x} \right] + \alpha \frac{\partial p}{\partial x} + C \alpha (1 - \alpha) \rho_m \left[\frac{\partial V_g}{\partial t} + V_\ell \frac{\partial V_g}{\partial x} - \frac{\partial V_\ell}{\partial t} - V_g \frac{\partial V_\ell}{\partial x} \right] = 0, \quad (\text{I-33})$$

$$(1-\alpha)\rho_\ell \left[\frac{\partial V_\ell}{\partial t} + V_\ell \frac{\partial V_\ell}{\partial x} \right] + (1-\alpha) \frac{\partial p}{\partial x} \\ + C\alpha(1-\alpha)\rho_m \left[\frac{\partial V_\ell}{\partial t} + V_g \frac{\partial V_\ell}{\partial x} - \frac{\partial V_g}{\partial t} - V_\ell \frac{\partial V_g}{\partial x} \right] = 0 \quad , \quad (I-34)$$

$$\frac{\partial}{\partial t}(\rho_m s_m) + \frac{\partial}{\partial x}[\alpha\rho_g V_g s_g + (1-\alpha)\rho_\ell V_\ell s_\ell] = 0 \quad , \quad (I-35)$$

and

$$\frac{\partial}{\partial t}(\alpha\rho_a) + \frac{\partial}{\partial x}(\alpha\rho_a V_g) = 0 \quad , \quad (I-36)$$

where C is the virtual mass coefficient; s is the entropy; and subscripts a , g , ℓ , and m refer to the noncondensable gas, steam/gas mixture, liquid, and total mixture, respectively. The last terms in Eqs. (I-33) and (I-34) represent interphasic force terms caused by relative acceleration. These terms are discussed in detail in Refs. I-6 and I-8. Following Ransom and Trapp's formulation, the energy equation is written in the form of the mixture-specific entropy that is conserved for adiabatic flow (with the irreversibilities associated with interphasic mass transfer and relative phase acceleration neglected). No basic difficulty in the analysis is experienced, however, if the mixture energy equation is written in terms of the internal energy or enthalpy.

In the thermal-equilibrium case, ρ_v , ρ_ℓ , s_g , s_ℓ , and ρ_a are known functions of p_a and p_v . If we assume that Dalton's law of partial pressures applies, Eqs. (I-32) through (I-36) can be written in terms of the five unknowns p_v , α , V_g , V_ℓ , and p_a . The matrix representation of these equations is

$$A(\bar{U}) \frac{\partial \bar{U}}{\partial t} + B(\bar{U}) \frac{\partial \bar{U}}{\partial x} = 0 \quad , \quad (I-37)$$

where the \bar{U} consists of p_v , α , V_g , V_ℓ , and p_a .

An example of one of the equations in the system given by Eq. (I-37) is the mixture or overall continuity equation, Eq. (I-32). We will provide here the details of the derivation of that equation, then merely list the other equations. Under equilibrium, we know that

$$\begin{aligned} T_\ell &= T_g = T \quad , \\ \rho_a &= \rho_a(p_a, T) \quad , \\ \rho_v &= \rho_v(p_v \text{ only}) \quad , \text{ and} \\ \rho_\ell &= \rho_\ell(p, T) \quad , \end{aligned} \quad (I-38)$$

which results in

$$\begin{aligned}
 d\rho_a &= \left(\frac{\partial \rho_a}{\partial p_a}\right)_T dp_a + \left(\frac{\partial \rho_a}{\partial T}\right)_{p_a} dT \\
 &= \left(\frac{\partial \rho_a}{\partial p_a}\right)_T dp_a + \left(\frac{\partial \rho_a}{\partial T}\right)_{p_a} \frac{dT}{dp_v} dp_v, \\
 d\rho_\ell &= \left(\frac{\partial \rho_\ell}{\partial p}\right)_T dp + \left(\frac{\partial \rho_\ell}{\partial T}\right)_p dT \\
 &= \left(\frac{\partial \rho_\ell}{\partial p}\right)_T (dp_a + dp_v) + \left(\frac{\partial \rho_\ell}{\partial T}\right)_p \frac{dT}{dp_v} dp_v \\
 &= \left(\frac{\partial \rho_\ell}{\partial p}\right)_T dp_a + \left[\left(\frac{\partial \rho_\ell}{\partial p}\right)_T + \left(\frac{\partial \rho_\ell}{\partial T}\right)_p \frac{dT}{dp_v} \right] dp_v \\
 &\doteq \left(\frac{\partial \rho_\ell}{\partial p}\right)_T dp_a + \rho_\ell^* dp_v, \quad \text{and} \\
 d\rho_v &= \left(\frac{\partial \rho_v}{\partial p_v}\right)_T dp_v + \left(\frac{\partial \rho_v}{\partial T}\right)_{p_v} dT \\
 &= \left(\frac{\partial \rho_v}{\partial p_v}\right)_T dp_v + \left(\frac{\partial \rho_v}{\partial T}\right)_{p_v} \frac{dT}{dp_v} dp_v \\
 &\doteq \rho_v^* dp_v.
 \end{aligned} \tag{I-39}$$

Expanding the differential terms of Eq. (I-32),

$$d\rho_m = \alpha d\rho_a + \alpha d\rho_v + \rho_g d\alpha + (1-\alpha)d\rho_\ell - \rho_\ell d\alpha$$

and

$$\begin{aligned}
 d(\rho_m V_m) &= \alpha \rho_g dV_g + \alpha V_g (d\rho_a + d\rho_v) + \rho_g V_g d\alpha \\
 &\quad + (1-\alpha)\rho_\ell dV_\ell + (1-\alpha)V_\ell d\rho_\ell - \rho_\ell V_\ell d\alpha.
 \end{aligned} \tag{I-40}$$

Using the relationships derived above and rearranging, Eq. (I-32) can be written as

$$\begin{aligned}
 & \left\{ \alpha \left[\left(\frac{\partial \rho_a}{\partial T} \right)_{p_a} \frac{dT}{dp_v} + \rho_v^* \right] + (1-\alpha) \rho_\ell^* \right\} \frac{\partial p_v}{\partial t} + (\rho_g - \rho_\ell) \frac{\partial \alpha}{\partial t} \\
 & + 0 \cdot \frac{\partial V_g}{\partial t} + 0 \cdot \frac{\partial V_\ell}{\partial t} + \left[\alpha \left(\frac{\partial \rho_a}{\partial p} \right)_T + (1-\alpha) \left(\frac{\partial \rho_\ell}{\partial p} \right)_T \right] \frac{\partial p_a}{\partial t} \\
 & + \left\{ V_g \alpha \left[\left(\frac{\partial \rho_a}{\partial T} \right)_{p_a} \frac{dT}{dp_v} + \rho_v^* \right] + V_\ell (1-\alpha) \rho_\ell^* \right\} \frac{\partial p_v}{\partial x} + (\rho_g V_g - \rho_\ell V_\ell) \frac{\partial \alpha}{\partial t} \\
 & + \alpha \rho_g \frac{\partial V_g}{\partial x} + (1-\alpha) \rho_\ell \frac{\partial V_\ell}{\partial x} + \left[V_g \alpha \left(\frac{\partial \rho_a}{\partial p} \right)_T + V_\ell (1-\alpha) \left(\frac{\partial \rho_\ell}{\partial p} \right)_T \right] \frac{\partial p_a}{\partial t} \\
 & = 0 \quad .
 \end{aligned} \tag{I-41}$$

The complete matrices for the system are given in Figs. I-9.a and I-9.b, where

$$s_v^* = \frac{1}{T} \left[\left(\frac{\partial e_v}{\partial p_v} \right)_T + \left(\frac{\partial e_v}{\partial T} \right)_{p_v} \frac{dT}{dp_v} \right] - \frac{p_v}{\rho_v^2 T} \left[\left(\frac{\partial \rho_v}{\partial p_v} \right)_T + \left(\frac{\partial \rho_v}{\partial T} \right)_{p_v} \frac{dT}{dp_v} \right]$$

and

$$s_\ell^* = \frac{1}{T} \left[\left(\frac{\partial e_\ell}{\partial p} \right)_T + \left(\frac{\partial e_\ell}{\partial T} \right)_p \frac{dT}{dp_v} \right] - \frac{p}{\rho_\ell^2 T} \left[\left(\frac{\partial \rho_\ell}{\partial p} \right)_T + \left(\frac{\partial \rho_\ell}{\partial T} \right)_p \frac{dT}{dp_v} \right] \quad . \tag{I-42}$$

With p , p_a , and T known, all of the thermodynamic partial derivatives used in the above equations are obtained by a call to subroutine THERMO.

The characteristic roots, λ_i , of the above system of equations are defined as the roots of the fifth-order polynomial,

$$\text{determinant } (\underline{A}\lambda - \underline{B}) = 0 \quad . \tag{I-43}$$

Choking occurs when the signal propagating with the largest velocity relative to the fluid is stationary; that is, the maximum value of the real part of a characteristic root, $\lambda_{i, \text{re, max}}$, is zero. Equation (I-43) is extremely difficult to solve analytically. Thus, TRAC obtains the characteristic roots of Eq. (I-43) numerically. This method advantageously maintains generality and facilitates computations under different assumptions. The calculational sequence for the TRAC two-phase choking model is described in Section I.2.4.

$$\underline{\underline{A}} = \begin{bmatrix} \alpha \left[\left(\frac{\partial \rho_a}{\partial T} \right)_{p_a} \frac{dT}{dp_v} + \rho_v^* \right] + (1-\alpha) \rho_\ell^* & \rho_g - \rho_\ell & 0 & 0 & \alpha \left(\frac{\partial \rho_a}{\partial p} \right)_T + (1-\alpha) \left(\frac{\partial \rho_\ell}{\partial p} \right)_T \\ 0 & 0 & \alpha \rho_g + C\alpha(1-\alpha)\rho_m & -C\alpha(1-\alpha)\rho_m & 0 \\ 0 & 0 & -C\alpha(1-\alpha)\rho_m & (1-\alpha)\rho_\ell + C\alpha(1-\alpha)\rho_m & 0 \\ \alpha \left[-\rho_v s_v^* + s_v \rho_v^* + \frac{dT}{dp_v} \left(\rho_a \left(\frac{\partial s_a}{\partial T} \right)_{p_a} + s_a \left(\frac{\partial \rho_a}{\partial T} \right)_{p_a} \right) \right] + (1-\alpha) \left[\rho_\ell s_\ell + \rho_\ell s_\ell^* \right] & (\rho_g s_g - \rho_\ell s_\ell) & 0 & 0 & \alpha \left[\rho_a \left(\frac{\partial s_a}{\partial p_a} \right)_T + s_a \left(\frac{\partial \rho_a}{\partial p_a} \right)_T \right] + (1-\alpha) \left[\rho_\ell \left(\frac{\partial s_\ell}{\partial p} \right)_T + s_\ell \left(\frac{\partial \rho_\ell}{\partial p} \right)_T \right] \\ \alpha \left(\frac{\partial \rho_a}{\partial T} \right)_{p_a} \frac{dT}{dp_v} & \rho_a & 0 & 0 & \alpha \left(\frac{\partial \rho_a}{\partial p_a} \right)_T \end{bmatrix} \begin{bmatrix} \frac{\partial p_v}{\partial t} \\ \frac{\partial \alpha}{\partial t} \\ \frac{\partial V_g}{\partial t} \\ \frac{\partial V_\ell}{\partial t} \\ \frac{\partial p_a}{\partial t} \end{bmatrix}$$

Fig. I-9.a Matrix A.

$$\underline{\underline{B}} = \begin{bmatrix} V_g \alpha \left[\left(\frac{\partial \rho_a}{\partial T} \right)_{p_a} \frac{dT}{dp_v} + \rho_v^* \right] + V_\ell (1-\alpha) \rho_\ell^* & \rho_g V_g - \rho_\ell V_\ell & \alpha \rho_g & (1-\alpha) \rho_\ell & V_g \alpha \left(\frac{\partial \rho_a}{\partial p} \right)_T + V_\ell (1-\alpha) \left(\frac{\partial \rho_\ell}{\partial p} \right)_T \\ \alpha & 0 & V_g \alpha \rho_g + V_\ell C \alpha (1-\alpha) \rho_m & -V_g C \alpha (1-\alpha) \rho_m & \alpha \\ (1-\alpha) & 0 & -V_\ell C \alpha (1-\alpha) \rho_m & V_g C \alpha (1-\alpha) \rho_m + V_\ell (1-\alpha) \rho_\ell & (1-\alpha) \\ V_g \alpha \left[-\rho_v s_v^* + s_v \rho_v^* + \frac{dT}{dp_v} \left(\rho_a \left(\frac{\partial s_a}{\partial T} \right)_{p_a} + s_a \left(\frac{\partial \rho_a}{\partial T} \right)_{p_a} \right) \right] + V_\ell (1-\alpha) \left[\rho_\ell s_\ell + s_\ell \rho_\ell^* \right] & V_g \rho_g s_g - V_\ell \rho_\ell s_\ell & \alpha \rho_g s_g & (1-\alpha) \rho_\ell s_\ell & V_g \alpha \left[\rho_a \left(\frac{\partial s_a}{\partial p_a} \right)_T + s_a \left(\frac{\partial \rho_a}{\partial p_a} \right)_T \right] + V_\ell (1-\alpha) \left[\rho_\ell \left(\frac{\partial s_\ell}{\partial p} \right)_T + s_\ell \left(\frac{\partial \rho_\ell}{\partial p} \right)_T \right] \\ V_g \alpha \left(\frac{\partial \rho_a}{\partial T} \right)_{p_a} \frac{dT}{dp_v} & V_g \rho_a & \alpha \rho_a & 0 & V_g \alpha \left(\frac{\partial \rho_a}{\partial p_a} \right)_T \end{bmatrix} \begin{bmatrix} \frac{\partial p_v}{\partial x} \\ \frac{\partial \alpha}{\partial x} \\ \frac{\partial V_g}{\partial x} \\ \frac{\partial V_\ell}{\partial x} \\ \frac{\partial p_a}{\partial x} \end{bmatrix}$$

Fig. I-9.b Matrix B.

I.2.1.3. Single-Phase Vapor. The single-phase vapor choked-flow model is based on isentropic expansion of an ideal gas (Ref. I-4, p. 515). A throat pressure, p_e , is calculated from the stagnation pressure, p_o , such that

$$p_e = p_o \left(\frac{2}{\gamma + 1} \right)^{\gamma/\gamma - 1}, \quad (I-44)$$

where γ is the specific-heat ratio. A downstream throat temperature, T_e , is calculated from the stagnation temperature, T_o , using the ideal-gas relation

$$T_e = T_o \left(\frac{2}{\gamma + 1} \right). \quad (I-45)$$

When T_e is greater than the saturation temperature at p_e , the fluid flow at the throat is predicted to be superheated by the ideal-gas relations. The continuity equation, in conjunction with the ideal-gas relations, yields a fluid choking velocity,

$$V_{ge} = \sqrt{\frac{2\gamma}{\gamma + 1} RT_o}, \quad (I-46)$$

where R is the gas constant.

If T_e is less than or equal to the saturation temperature at p_e , then the fluid flow at the throat is not predicted to be superheated by the ideal-gas relations, and the choking velocity is calculated using iterations to maximize mass flux along the isentrope that extends from the superheated conditions upstream of the throat to the two-phase conditions at the throat. This method assumes that no delay in condensation occurs as the steam expands to the saturated two-phase state at the throat.

The calculational sequence for the TRAC single-phase vapor choking model is described in Section I.2.4.

I.2.1.4. Transition Regions. Because there is a discontinuity in the sound speed during the transition from liquid to two-phase flow, the flow during this transition regime must be analyzed carefully. In TRAC, this transition is handled by linear interpolation between the subcooled ($\alpha \leq 0.01$) and the two-phase ($\alpha \geq 0.1$) regimes. The calculational sequence for the TRAC transition region is described in Section I.2.4.

The transition from the two-phase to the vapor-phase regime is smooth because the two-phase characteristic solution approaches the homogeneous equilibrium limit as $\alpha \rightarrow 1$. Thus, this transition is made by switching the calculational logic at $\alpha = 0.999$.

I.2.2. Assumptions and Preliminary Calculations

I.2.2.1. Cell-Center Momentum-Solution Velocities. The velocities obtained from the momentum solution are cell-edge values. However, in order to evaluate stagnation conditions (in subroutine SOUND), it is necessary to know the phasic velocities at cell center. This transition between cell edge and cell center is accomplished in subroutine VOLV by averaging the mass flux between cell edges, such that

$$V_{gc} = \frac{\frac{1}{2} \left[(\rho_g \alpha)_{e^-} V_{g,e^-} A_{e^-} + (\rho_g \alpha)_{e^+} V_{g,e^+} A_{e^+} \right]}{\rho_{gc} \alpha_c A_c} \quad (I-47)$$

and

$$V_{lc} = \frac{\frac{1}{2} \left[(\rho_l (1-\alpha))_{e^-} V_{l,e^-} A_{e^-} + (\rho_l (1-\alpha))_{e^+} V_{l,e^+} A_{e^+} \right]}{\rho_{lc} (1-\alpha)_c A_c} \quad (I-48)$$

where V_{gc} and V_{lc} are the transformed cell-center velocities, ρ_g and ρ_l are the steam/gas-mixture and liquid densities, α is the void fraction, V_l and V_g are the liquid and steam/gas-mixture velocities, and A is the cross-sectional flow area. The subscripts e^- and e^+ refer to upstream cell-edge and downstream cell-edge quantities, while the subscript c refers to cell-center quantities for the particular cell in question. It is assumed that $\rho\alpha$ at the upstream face is equal to the upstream cell product value, whereas $\rho\alpha$ at the downstream face is taken to be equal to the current cell value because densities and void fractions are normally associated with cell-center rather than with cell-edge positions.

I.2.2.2. Subroutine SOUND. The evaluation of Eqs. (I-30) and (I-31) in the subcooled-liquid choking model and the solution of Eq. (I-43) in the two-phase, two-component choking model require that conditions at the cell-edge where the choking criterion is applied be known. Subroutine CHOKE calls subroutine SOUND to calculate a homogeneous equilibrium sound speed and to estimate the corresponding cell-edge conditions, given the conditions at cell center. Three basic calculational sequences exist in subroutine SOUND:

1. If the cell contains pure noncondensable gas, the homogeneous equilibrium sound speed and corresponding cell-edge conditions are computed by assuming an isentropic expansion of an ideal gas.
2. If the cell length-to-hydraulic-diameter ratio, L/D , is greater than or equal to 1.5, or if some noncondensable gas is present in the vapor phase of a two-phase flow at cell center (regardless of the value of L/D), then the conditions at cell center are required to come to equilibrium by means of an isenthalpic process before stagnation conditions are calculated. Once the stagnation conditions have been determined, a homogeneous equilibrium sound speed and the corresponding cell-edge conditions are calculated by first assuming thermal equilibrium and no slip at the cell

edge and an isentropic expansion from stagnation to cell edge. We then iterate for the cell-edge pressure, which results in the maximum or critical mass flux at the cell edge (a classical technique used in generating the HEM tables).

3. If the cell length-to-hydraulic-diameter ratio, L/D , is less than 1.5, or if only the superheated vapor phase or the subcooled-liquid phase exists at the cell center, then the stagnation conditions are calculated from the actual cell-center properties, rather than from the effective equilibrium properties as in (2). Once stagnation conditions have been determined, a homogeneous equilibrium sound speed and the corresponding cell-edge conditions are determined either by assuming an isentropic expansion of an ideal gas (for the case of superheated vapor phase at the cell edge) or by iterating for the cell-edge pressure, which gives the maximum mass flux as in (2) above. The details of each procedure follow.

I.2.2.2.1. Isentropic Expansion of Ideal Gas. When the cell-center conditions represent a pure noncondensable-gas field, the sound speed and cell-edge conditions are calculated using ideal-gas theory. First, a cell-edge temperature and a cell-edge pressure are computed, such that

$$T_e = \frac{2T_g}{\gamma_a + 1} \left(1 + \frac{V_{gc}^2}{2c_{pa}T_g} \right) \quad (I-49)$$

and

$$p_e = p \left[\frac{2}{\gamma_a + 1} \left(1 + \frac{V_{gc}^2}{2c_{pa}T_g} \right) \right]^{\gamma_a/(\gamma_a - 1)} \quad (I-50)$$

where T_g is the cell-center gas temperature, γ_a is the specific heat ratio for the noncondensable gas (as defined in subroutine SETEOS), V_{gc} is the cell-center gas velocity [as computed in Eq. (I-47)], c_{pa} is the constant-pressure specific heat for the noncondensable gas (as defined in subroutine SETEOS), and p is the cell-center total pressure.

Next, a cell-edge noncondensable-gas density is calculated according to

$$\rho_{ae} = \frac{p_e}{R_a T_e} \quad (I-51)$$

where R_a is the noncondensable-gas constant (as defined in subroutine SETEOS), and p_e and T_e are the cell-edge pressure and temperature calculated above.

The gas sound speed now becomes

$$a_{HE} = \sqrt{\gamma_a R_a T_e} \quad , \quad (I-52)$$

where γ_a is the specific heat ratio for the noncondensable gas (as defined in subroutine SETEOS), R_a is the noncondensable-gas constant (also defined in subroutine SETEOS), and T_e is the cell-edge temperature calculated in Eq. (I-49) above.

This concludes the calculation of the gas sound speed and cell-edge conditions for the case of pure noncondensable gas at cell center. At this point, the logic returns to subroutine CHOKe.

I.2.2.2.2. $L/D \leq 1.5$ or Noncondensable Gas Present in Two-Phase Flow at Cell Center. Subroutine SOUND calculates the stagnation conditions using the effective equilibrium void fraction, rather than the actual void fraction, if the cell center is not in equilibrium. The calculational sequence to arrive at the cell-edge conditions and the homogeneous equilibrium sound speed is as follows.

Initially, subroutine THERMO is called with the actual cell-center total pressure, p ; the partial pressure of any noncondensable gas that may be present, p_a ; and the steam/gas-mixture and liquid temperatures, T_g and T_ℓ . With these variables, THERMO calculates the actual mixture density, actual quality, and liquid, steam, noncondensable-gas, steam/gas-mixture, and steam/liquid-water-mixture enthalpies:

$$\rho_m = \alpha_{\text{actual}} \rho_g + (1 - \alpha_{\text{actual}}) \rho_\ell \quad , \quad (I-53)$$

$$x_{\text{actual}} = \alpha_{\text{actual}} \left(\frac{\rho_g}{\rho_m} \right) \quad , \quad (I-54)$$

$$h_\ell = e_\ell + \frac{p}{\rho_\ell} \quad , \quad (I-55)$$

$$h_v = e_v + \frac{p - p_a}{\rho_g - \rho_a} \quad , \quad (I-56)$$

$$h_a = e_a + \frac{p_a}{\rho_a + 1.0 \times 10^{-20}} \quad , \quad (I-57)$$

$$h_g = e_g + \frac{p}{\rho_g} \quad , \quad (I-58)$$

and

$$h_m = x_{\text{actual}} h_v + (1 - x_{\text{actual}}) h_\ell \quad , \quad (\text{I-59})$$

where α_{actual} is the actual cell-center void fraction, x_{actual} is the actual cell-center quality, and all fluid properties are actual cell-center values.

If the cell-center conditions do not represent an equilibrium state, an effective equilibrium void fraction at the cell center is determined assuming an isenthalpic process from the actual cell-center state. A call to subroutine THERMO with the saturation temperature corresponding to the cell-center partial pressure of steam allows cell-center liquid, steam, noncondensable-gas, and steam/gas-mixture saturated enthalpies to be determined. From this the equilibrium quality at cell center and equilibrium void fraction at cell center may be calculated, such that

$$x_{\text{equil}} = \frac{h_m - h_{\ell,\text{equil}}}{h_{v,\text{equil}} - h_{\ell,\text{equil}} + \frac{\rho_{a,\text{equil}}}{\rho_{g,\text{equil}}} (h_{a,\text{equil}} - h_a - h_{v,\text{equil}} + h_v)} \quad (\text{I-60})$$

and

$$\alpha_{\text{equil}} = \frac{x_{\text{equil}} \rho_{\ell,\text{equil}}}{\rho_{g,\text{equil}} + x_{\text{equil}} (\rho_{\ell,\text{equil}} - \rho_{g,\text{equil}})} \quad , \quad (\text{I-61})$$

where h_m is the cell-center steam/liquid-water-mixture actual enthalpy from Eq. (I-59); $h_{\ell,\text{equil}}$, $h_{v,\text{equil}}$, and $h_{a,\text{equil}}$ are the cell-center liquid, steam, and noncondensable-gas equilibrium enthalpies for the saturation temperature corresponding to the cell-center partial pressure of steam; h_v and h_a are the cell-center steam and noncondensable-gas actual enthalpies [Eqs. (I-56) and (I-57)]; and $\rho_{\ell,\text{equil}}$, $\rho_{a,\text{equil}}$, and $\rho_{g,\text{equil}}$ are the cell-center liquid, noncondensable-gas, and steam/gas-mixture equilibrium densities for the saturation temperature corresponding to the cell-center partial pressure of steam.

Such quantities as constant-pressure specific heats, constant-volume specific heats, and specific-heat ratios are now defined for the fluid. If the fluid at cell center is a single-phase saturated vapor, the steam specific-heat ratio is defined as

$$\gamma_v = 1.3 \quad . \quad (\text{I-62})$$

However, if the fluid at cell center is two-phase or subcooled, the steam ratio of specific heats is defined as

$$\gamma_v = 1.035 + 0.1 \alpha_{\text{equil}} \left(\frac{\rho_{g,\text{equil}} - \rho_{a,\text{equil}}}{\alpha_{\text{equil}} \rho_{g,\text{equil}} + (1 - \alpha_{\text{equil}}) \rho_{\ell,\text{equil}}} \right) \quad , \quad (\text{I-63})$$

where α_{equil} is the cell-center equilibrium void fraction and $\rho_{g,\text{equil}}$, $\rho_{a,\text{equil}}$, and $\rho_{l,\text{equil}}$ are cell-center steam/gas-mixture, noncondensable-gas, and liquid equilibrium densities at the saturation temperature corresponding to the cell-center partial pressure of steam.

The steam and steam/gas-mixture specific heats are then defined, such that

$$c_{pv} = \frac{\gamma_v R_v}{\gamma_v - 1} \quad , \quad (\text{I-64})$$

$$c_{vv} = c_{pv} - R_v \quad , \quad (\text{I-65})$$

$$c_{pg} = c_{pa} \left(\frac{\rho_{a,\text{equil}}}{\rho_{g,\text{equil}}} \right) + c_{pv} \left(1 - \frac{\rho_{a,\text{equil}}}{\rho_{g,\text{equil}}} \right) \quad , \quad (\text{I-66})$$

and

$$c_{vg} = c_{va} \left(\frac{\rho_{a,\text{equil}}}{\rho_{g,\text{equil}}} \right) + c_{vv} \left(1 - \frac{\rho_{a,\text{equil}}}{\rho_{g,\text{equil}}} \right) \quad , \quad (\text{I-67})$$

where γ_v is the steam specific-heat ratio [as defined by Eqs. (I-62) or (I-63)], R_v is the steam gas constant (defined by subroutine SETEOS), and $\rho_{a,\text{equil}}$ and $\rho_{g,\text{equil}}$ are the cell-center noncondensable-gas and steam/gas-mixture equilibrium densities at the saturation temperature corresponding to the cell-center partial pressure of steam.

The steam/gas-mixture ratio of specific heats becomes

$$\gamma_g = \frac{c_{pg}}{c_{vg}} \quad . \quad (\text{I-68})$$

Cell-center liquid, steam, noncondensable-gas, steam/gas-mixture, and steam/liquid-water-mixture equilibrium entropies for the saturation temperature corresponding to the cell-center partial pressure of steam are calculated, such that

$$s_{l,\text{equil}} = c_{vl} \ln \left(\frac{T_{sv}}{273.15} \right) \quad , \quad (\text{I-69})$$

$$s_{v,\text{equil}} = c_{vl} \ln \left(\frac{T_{sv}}{273.15} \right) + \frac{h_{fg,\text{equil}}}{T_{sv}} \quad , \quad (\text{I-70})$$

$$s_{a,\text{equil}} = c_{pa} \ln \left(\frac{T_{sv}}{273.15} \right) - R_a \ln \left(\frac{\max\{p_a, 1.0 \times 10^{-5}\}}{1.0 \times 10^5} \right) , \quad (\text{I-71})$$

$$s_{g,\text{equil}} = s_{a,\text{equil}} \left(\frac{\rho_{a,\text{equil}}}{\rho_{g,\text{equil}}} \right) + s_{v,\text{equil}} \left(1 - \frac{\rho_{a,\text{equil}}}{\rho_{g,\text{equil}}} \right) , \quad (\text{I-72})$$

and

$$s_{m,\text{equil}} = x_{\text{equil}} s_{v,\text{equil}} + (1 - x_{\text{equil}}) s_{\ell,\text{equil}} , \quad (\text{I-73})$$

where T_{sv} is the saturation temperature corresponding to the cell-center partial pressure of steam, c_{v1} is the liquid constant-volume specific heat (defined in subroutine SETEOS), $h_{fg,\text{equil}}$ is the latent heat of vaporization at T_{sv} , c_{pa} is the noncondensable-gas constant-pressure specific heat (defined by subroutine SETEOS), R_a is the noncondensable-gas constant (defined in subroutine SETEOS), p_a is the cell-center partial pressure of the noncondensable gas, $\rho_{a,\text{equil}}$ and $\rho_{g,\text{equil}}$ are the cell-center noncondensable-gas and steam/gas-mixture equilibrium densities at the saturation temperature corresponding to the cell-center partial pressure of steam, and x_{equil} is the cell-center effective equilibrium quality as computed in Eq. (I-60).

Finally, stagnation conditions are computed according to the following:

$$h_o = x_{\text{equil}} \left(h_{g,\text{equil}} + \frac{1}{2} V_{gc}^2 \right) + (1 - x_{\text{equil}}) \left(h_{\ell,\text{equil}} + \frac{1}{2} V_{lc}^2 \right) , \quad (\text{I-74})$$

$$p_o = x_{\text{equil}} p \left(1 + \frac{1}{2} \frac{V_{gc}^2}{c_{pg} T_{sv}} \right)^{\frac{\gamma_g}{\gamma_g - 1}} + (1 - x_{\text{equil}}) \left(p + \frac{1}{2} \rho_{\ell} V_{lc}^2 \right) , \quad (\text{I-75})$$

and

$$s_o = x_{\text{equil}} s_{g,\text{equil}} + (1 - x_{\text{equil}}) s_{\ell,\text{equil}} , \quad (\text{I-76})$$

where x_{equil} is the cell-center effective equilibrium quality as computed in Eq. (I-60), $h_{\ell,\text{equil}}$ and $h_{g,\text{equil}}$ are the cell-center liquid and steam/gas-mixture equilibrium enthalpies evaluated at the saturation temperature corresponding to the cell-center partial pressure of steam, V_{lc} and V_{gc} are the cell-center liquid and steam/gas-mixture velocities [as computed in Eqs. (I-47) and (I-48)], p is the cell-center total pressure, γ_g is the ratio of specific heats [as defined in Eq. (I-68)], c_{pg} is the steam/gas-mixture specific heat at constant pressure [as defined in Eq. (I-66)], T_{sv} is the saturation temperature corresponding to the cell-center partial pressure of steam, ρ_{ℓ} is the cell-center liquid actual density, and $s_{\ell,\text{equil}}$ and $s_{g,\text{equil}}$ are the cell-center liquid and steam/gas-mixture

equilibrium entropies evaluated at the saturation temperature corresponding to the cell-center partial pressure of steam [as in Eqs. (I-69) and (I-72)].

Iterations can now be performed to determine the maximum mass flux and the corresponding cell-edge conditions.

An initial cell-edge pressure equal to that predicted by ideal-gas expansion theory is guessed by using the relationship

$$p_e = p_o \left(\frac{2}{\gamma_g + 1} \right)^{\gamma_g / (\gamma_g - 1)} \quad , \quad (I-77)$$

where p_o is the stagnation pressure [as in Eq. (I-75)] and γ_g is the steam/gas-mixture specific-heat ratio [as in Eq. (I-68)].

Subroutine THERMO is then called to determine the saturation properties at the cell edge corresponding to the cell-edge pressure, p_e .

Saturated cell-edge values for liquid, steam, and steam/gas-mixture enthalpies and for liquid, steam, and noncondensable-gas entropies are computed, such that

$$h_{le} = e_{le} + \frac{p_e}{\rho_{le}} \quad , \quad (I-78)$$

$$h_{ve} = e_{ve} + \frac{p_e - p_{ae}}{\rho_{ge} - \rho_{ae}} \quad , \quad (I-79)$$

$$h_{ge} = e_{ge} + \frac{p_e}{\rho_{ge}} \quad , \quad (I-80)$$

$$s_{le} = c_{vl} \ln \left(\frac{T_e}{273.15} \right) \quad , \quad (I-81)$$

$$s_{ve} = s_{le} + \frac{h_{ve} - h_{le}}{T_e} \quad , \quad (I-82)$$

and

$$s_{ae} = c_{pa} \ln \left(\frac{T_e}{273.15} \right) - R_a \ln \left(\frac{\min\{p_{ae}, 1.0 \times 10^{-5}\}}{1.0 \times 10^{-5}} \right) \quad , \quad (I-83)$$

where e_{le} , e_{ve} , and e_{ge} are the cell-edge liquid, steam, and steam/gas-mixture saturated internal energies for the pressure p_e ; p_e is the cell-edge pressure; p_{ae} is the cell-edge partial pressure of the noncondensable gas given by $p_{ae} = p_a(p_e)/p$; ρ_{le} , ρ_{ae} , and ρ_{ge} are the cell-edge liquid, noncondensable-gas, and steam/gas-mixture saturated densities for the pressure p_e ; c_{vl} is the liquid constant-volume specific heat (as defined in subroutine SETEOS); T_e is the cell-edge temperature equal to the saturation temperature at p_e ; c_{pa} is the noncondensable-gas constant-pressure specific heat (as defined in subroutine SETEOS); and R_a is the noncondensable-gas constant (as defined in subroutine SETEOS).

Then, assuming a constant entropy expansion from the stagnation condition, a cell-edge quality may be calculated from

$$x_e = \frac{s_{m, \text{equil}} - s_{le}}{s_{ve} - s_{le} + \left(\frac{\rho_{ae}}{\rho_{ge}}\right) (s_{ae} - s_{a, \text{equil}} - s_{ve} - s_{v, \text{equil}})} \quad , \quad (\text{I-84})$$

where $s_{m, \text{equil}}$, $s_{v, \text{equil}}$, and $s_{a, \text{equil}}$ are the cell-center steam/liquid-water-mixture, steam, and noncondensable-gas equilibrium entropies for the saturation temperature corresponding to the cell-center partial pressure of steam [as in Eqs. (I-73), (I-70), and (I-71)]; s_{le} , s_{ve} , and s_{ae} are the cell-edge liquid, steam, and noncondensable-gas saturated entropies for the pressure p_e [as computed above in Eqs. (I-81), (I-82), and (I-83)]; and ρ_{ae} and ρ_{ge} are the cell-edge noncondensable-gas and steam/gas-mixture saturated densities for the pressure p_e .

Once the cell-edge quality has been determined, a cell-edge total mixture enthalpy and cell-edge total mixture density are calculated as follows:

$$h_{me} = x_e h_{ge} + (1 - x_e) h_{le} \quad (\text{I-85})$$

and

$$\rho_{me} = \frac{\rho_{le} \rho_{ge}}{x_e (\rho_{le} - \rho_{ge}) + \rho_{ge}} \quad , \quad (\text{I-86})$$

where x_e is the cell-edge quality [as in Eq. (I-84)]; h_{le} and h_{ge} are the cell-edge liquid and steam/gas-mixture saturated enthalpies for the pressure p_e [as in Eqs. (I-78) and (I-80)]; and ρ_{le} and ρ_{ge} are the cell-edge liquid and steam/gas-mixture saturated densities for the pressure p_e .

The mass flux, then, for a cell-edge pressure of p_e becomes

$$G = \rho_{me} \sqrt{2(h_o - h_{me})} \quad , \quad (\text{I-87})$$

where ρ_{me} is the cell-edge total mixture density [as in Eq. (I-86)], h_o is the stagnation enthalpy [as in Eq. (I-74)], and h_{me} is the cell-edge total mixture enthalpy [as in Eq. (I-85)].

The pressure is varied slightly and the iteration is repeated until the pressure that gives the maximum or critical mass flux as predicted by Eq. (I-87) is determined. Once the cell-edge pressure corresponding to the critical flux has been found, the saturated cell-edge conditions become known, and a homogeneous equilibrium sound speed, a_{HE} , is computed as follows:

$$a_{HE} = \frac{G_{\max}}{\rho_{me}} \quad (I-88)$$

This concludes the calculation of the homogeneous equilibrium sound speed and the corresponding cell-edge conditions for the case of nonsuperheated vapor phase at cell center when $L/D \geq 1.5$ or when noncondensable gas is present in two-phase cell-center flow. At this point, the logic returns to subroutine CHOKe.

I.2.2.2.3. $L/D < 1.5$ or Only Superheated Vapor Phase, or Only Subcooled-Liquid Phase Present at Cell Center. In this case, instead of allowing the cell-center conditions to come to equilibrium along an isenthalpic process (if the cell center is not originally in equilibrium), the stagnation conditions are derived from the cell-center actual properties. The method of arriving at these stagnation conditions follows that of the $L/D \geq 1.5$ case, except that actual properties are used instead of equilibrium properties. Then, as in the case for $L/D \geq 1.5$, SOUND determines a homogeneous equilibrium sound speed and the corresponding cell-edge conditions by again assuming thermal equilibrium, no slip at the cell edge, and a constant entropy expansion between stagnation and cell edge, and by again iterating for the cell-edge pressure that gives the maximum mass flux at the cell edge if two-phase flow is predicted at the cell edge. Otherwise, the homogeneous equilibrium sound speed and corresponding cell-edge conditions are found by assuming an isentropic expansion of the superheated vapor phase existing at cell center according to ideal-gas behavior. The following gives the exact coding in detail.

As before, subroutine THERMO is called with the actual cell-center total pressure, p ; the partial pressure of any noncondensable gas that may be present, p_{ai} ; and the steam/gas-mixture and liquid-phase temperatures, T_g and T_ℓ . With these variables, THERMO calculates such properties as actual mixture density, actual quality, and liquid, steam, noncondensable-gas, steam/gas-mixture, and steam/liquid-water-mixture enthalpies, such that,

$$\rho_m = \alpha_{\text{actual}} \rho_g + (1 - \alpha_{\text{actual}}) \rho_\ell \quad , \quad (I-89)$$

$$x_{\text{actual}} = \alpha_{\text{actual}} \left(\frac{\rho_g}{\rho_m} \right) \quad , \quad (I-90)$$

$$h_l = e_l + \frac{p}{\rho_l} \quad , \quad (I-91)$$

$$h_v = e_v + \frac{p - p_a}{\rho_g - \rho_a} \quad , \quad (I-92)$$

$$h_a = e_a + \frac{p_a}{\rho_a + 1.0 \times 10^{-20}} \quad , \quad (I-93)$$

$$h_g = e_g + \frac{p}{\rho_g} \quad , \quad (I-94)$$

and

$$h_m = x_{\text{actual}} h_v + (1 - x_{\text{actual}}) h_l \quad , \quad (I-95)$$

where α_{actual} is the actual cell-center void fraction, x_{actual} is the actual cell-center quality, and all fluid properties are actual cell-center values.

Such quantities as constant-pressure specific heats, constant-volume specific heats, and specific-heat ratios are now defined for the fluid. If the fluid at cell center is a superheated vapor, the steam specific-heat ratio is defined as

$$\gamma_v = 1.3 \quad . \quad (I-96)$$

However, if the fluid at cell center is two-phase or subcooled, the steam ratio of specific heats is defined as

$$\gamma_v = 1.035 + 0.1 \alpha_{\text{actual}} \left(\frac{\rho_g - \rho_a}{\rho_m} \right) \quad , \quad (I-97)$$

where α_{actual} is the cell-center actual void fraction and ρ_g , ρ_a , and ρ_m are cell-center steam/gas-mixture, noncondensable-gas, and total mixture actual densities.

Next the steam and steam/gas-mixture specific heats are defined, such that

$$c_{pv} = \frac{\gamma_v R_v}{\gamma_v - 1} \quad , \quad (I-98)$$

$$c_{vv} = c_{pv} - R_v \quad , \quad (I-99)$$

$$c_{pg} = c_{pa} \left(\frac{\rho_a}{\rho_g} \right) + c_{pv} \left(1 - \frac{\rho_a}{\rho_g} \right) , \quad (\text{I-100})$$

and

$$c_{vg} = c_{va} \left(\frac{\rho_a}{\rho_g} \right) + c_{vv} \left(1 - \frac{\rho_a}{\rho_g} \right) , \quad (\text{I-101})$$

where γ_v is the steam specific-heat ratio [as defined by Eqs. (I-96) or (I-97)], R_v is the steam gas constant (defined by subroutine SETEOS), and ρ_a and ρ_g are the cell-center noncondensable-gas and steam/gas-mixture actual densities.

The steam/gas-mixture ratio of specific heats becomes

$$\gamma_g = \frac{c_{pg}}{c_{vg}} . \quad (\text{I-102})$$

Cell-center liquid, steam, noncondensable-gas, steam/gas-mixture, and steam/liquid-water-mixture actual entropies are calculated, such that

$$s_\ell = c_{v\ell} \ln \left(\frac{T_\ell}{273.15} \right) , \quad (\text{I-103})$$

$$s_v = c_{v\ell} \ln \left(\frac{T_{sv}}{273.15} \right) + \frac{h_{fg, \text{equil}}}{T_{sv}} + c_{pv} \ln \left(\frac{T_g}{T_{sv}} \right) , \quad (\text{I-104})$$

$$s_a = c_{pa} \ln \left(\frac{T_g}{273.15} \right) - R_a \ln \left(\frac{\max\{p_a, 1.0 \times 10^{-5}\}}{1.0 \times 10^5} \right) , \quad (\text{I-105})$$

$$s_g = s_a \left(\frac{\rho_a}{\rho_g} \right) + s_v \left(1 - \frac{\rho_a}{\rho_g} \right) , \quad (\text{I-106})$$

and

$$s_m = x_{\text{actual}} s_v + (1 - x_{\text{actual}}) s_\ell , \quad (\text{I-107})$$

where T_l is the cell-center liquid temperature, T_{sv} is the saturation temperature corresponding to the cell-center partial pressure of steam, c_{vl} is the liquid constant-volume specific heat (defined in subroutine SETEOS), $h_{fg, \text{equil}}$ is the latent heat of vaporization at T_{sv} , c_{pv} and c_{pa} are the steam and noncondensable-gas constant-pressure specific heats [defined by Eq. (I-98) and subroutine SETEOS, respectively], T_g is the cell-center steam/gas-mixture temperature, R_a is the noncondensable-gas constant (defined in subroutine SETEOS), p_a is the cell-center partial pressure of the noncondensable gas, ρ_a and ρ_g are the cell-center noncondensable-gas and steam/gas-mixture actual densities, and x_{actual} is the cell-center actual quality as computed in Eq. (I-1).

Finally, stagnation conditions are computed according to the following:

$$h_o = x_{\text{actual}} \left(h_g + \frac{1}{2} V_{gc}^2 \right) + (1 - x_{\text{actual}}) \left(h_l + \frac{1}{2} V_{lc}^2 \right) , \quad (\text{I-108})$$

$$p_o = x_{\text{actual}} p \left(1 + \frac{1}{2} \frac{V_{gc}^2}{c_{pg} T_g} \right)^{\frac{\gamma_g}{\gamma_g - 1}} + (1 - x_{\text{actual}}) \left(p + \frac{1}{2} \rho_l V_{lc}^2 \right) , \quad (\text{I-109})$$

and

$$s_o = x_{\text{actual}} s_g + (1 - x_{\text{actual}}) s_l , \quad (\text{I-110})$$

where x_{actual} is the cell-center actual quality as computed in Eq. (I-90), h_l and h_g are the cell-center liquid and steam/gas-mixture actual enthalpies, V_{gc} and V_{lc} are the cell-center steam/gas-mixture and liquid velocities [as computed in Eqs. (I-47) and (I-48)], p is the cell-center total pressure, γ_g is the ratio of specific heats [as defined in Eq. (I-102)], c_{pg} is the steam/gas-mixture specific heat at constant pressure [as defined in Eq. (I-100)], T_g is the cell-center steam/gas-mixture temperature, ρ_l is the cell-center liquid actual density, and s_l and s_g are the cell-center liquid and steam/gas-mixture actual entropies [as in Eqs. (I-103) and (I-106)]. At this point, the logic splits to handle either superheated vapor phase at cell center or nonsuperheated vapor phase at cell center based on a check of the cell-center steam/gas-mixture temperature and the cell-center actual quality [Eq. (I-90)].

I.2.2.2.3.1. Superheated Vapor Phase at Cell Center. If the cell-center steam/gas-mixture temperature, T_g , is greater than the saturation temperature corresponding to the cell-center partial pressure of steam or if the cell-center actual quality [Eq. (I-90)] is equal to 1, then TRAC determines the cell-center fluid to be a superheated vapor phase, and the homogeneous equilibrium sound speed and corresponding cell-edge conditions are computed as follows.

A cell-edge pressure, p_e , is calculated from the stagnation pressure, p_o , using the ideal-gas expansion theory, such that

$$p_e = p_o \left(\frac{2}{\gamma_g + 1} \right)^{\gamma_g / (\gamma_g - 1)} , \quad (I-111)$$

where γ_g is the steam/gas-mixture specific-heat ratio [as in Eq. (I-102)]. A downstream cell-edge temperature, T_e , is estimated from the cell-center steam/gas-mixture temperature, T_g , again using the ideal-gas expansion theory,

$$T_e = T_g \left(\frac{2}{\gamma_g + 1} \right) , \quad (I-112)$$

where T_g is assumed to be close to the stagnation temperature.

When T_e is greater than the saturation temperature at p_e , the fluid flow at cell-edge is predicted to be superheated by the ideal-gas relations, and the following logic occurs. Subroutine THERMO is called to determine the cell-edge properties for the superheated steam/gas mixture at pressure p_e and temperature T_e . The continuity equation, in conjunction with the ideal-gas relations, then yields a cell-edge steam/gas-mixture choking velocity,

$$V_{ge} = \frac{p_o}{\rho_{ge} \sqrt{T_g}} \sqrt{\frac{\gamma_g \left(\frac{2}{\gamma_g + 1} \right)^{(\gamma_g + 1) / (\gamma_g - 1)}}{R_g}} , \quad (I-113)$$

where p_o is the stagnation pressure [as in Eq. (I-109)]; ρ_{ge} is the cell-edge steam/gas-mixture density; T_g is the cell-center steam/gas-mixture temperature, which is assumed to be approximately equal to the stagnation temperature; and γ_g is the steam/gas-mixture specific-heat ratio [as in Eq. (I-102)]. R_g is the steam/gas-mixture gas constant and is defined by

$$R_g = R_a \left(\frac{\rho_a}{\rho_g} \right) + R_v \left(1 - \frac{\rho_a}{\rho_g} \right) , \quad (I-114)$$

where R_v and R_a are the steam and noncondensable-gas constants (defined by subroutine SETEOS), ρ_a and ρ_g are the cell-center noncondensable-gas and steam/gas-mixture actual densities.

If, in addition, the enthalpy at cell edge is greater than the stagnation enthalpy, the first law of thermodynamics also is used to calculate a cell-edge steam/gas-mixture choking velocity,

$$V_{ge} = \sqrt{2(h_o - h_{ge})} , \quad (I-115)$$

where h_o is the stagnation enthalpy [as in Eq. (I-107)] and h_{ge} is the steam/gas-mixture cell-edge enthalpy calculated from the cell-edge properties as

$$h_{ge} = e_{ge} + \frac{p_e}{\rho_{ge}} \quad (I-116)$$

When both Eqs. (I-113) and (I-115) are used to compute a velocity, the actual steam/gas-mixture choking velocity is chosen to be the larger of the two calculated values. This concludes the calculation of the homogeneous equilibrium sound speed and the corresponding cell-edge conditions for the case of a superheated vapor phase at cell edge. At this point, the logic returns to subroutine CHOKE.

When T_e is less than or equal to the saturation temperature at p_e , one additional check is made to determine whether the fluid at cell edge is a superheated vapor phase. A steam/gas-mixture sound speed at cell edge is calculated from

$$V_{ge} = \sqrt{2 \left[h_o - \left(e_{ge} + \frac{p_e}{\rho_{ge}} \right) \right]} \quad (I-117)$$

where h_o is the stagnation enthalpy [as in Eq. (I-108)], p_e is the cell-edge pressure [as in Eq. (I-111)], and e_{ge} and ρ_{ge} are the cell-edge steam/gas-mixture internal energy and density as determined in the call to THERMO for the pressure p_e and the temperature T_e .

In addition, a sound speed for an ideal gas at the same temperature is calculated from

$$a_{HE} = \sqrt{\gamma_g R_g T_e} \quad (I-118)$$

where γ_g is the steam/gas-mixture specific-heat ratio [Eq. (I-102)], R_g is the steam/gas-mixture gas constant [Eq. (I-114)], and T_e is the cell-edge temperature [Eq. (I-112)].

If the steam/gas-mixture velocity at the cell edge computed in Eq. (I-117) is greater than (or equal to) the ideal-gas sound speed of Eq. (I-118), then a superheated vapor phase is assumed to occur at the cell edge, and the choking velocity is calculated by maximizing the mass flux through pressure iterations in the following way.

Initially, the code chooses the cell-edge pressure and temperature to be equal to those values predicted by ideal-gas theory as in Eqs. (I-111) and (I-112). After calling THERMO to determine the cell-edge steam/gas-mixture properties corresponding to p_e and T_e , a steam/gas-mixture sound speed at cell edge is calculated using Eq. (I-117). A mass flux may then be computed from

$$G = V_{ge} \rho_{ge} \quad (I-119)$$

where ρ_{ge} is the steam/gas-mixture cell-edge density and V_{ge} is the steam/gas-mixture cell-edge sound speed [Eq. (I-117)].

The cell-edge pressure guess is varied slightly, and the calculation of cell-edge mass flux is repeated until the pressure that gives the maximum mass flux is located. Once the maximum mass flux and the cell-edge properties for that particular cell-edge pressure have been found, a homogeneous equilibrium sound-speed velocity is calculated according to

$$a_{HE} = \frac{G_{\max}}{\rho_{ge}} \quad (I-120)$$

This concludes the calculation of the homogeneous equilibrium sound speed and the corresponding cell-edge conditions for the case of a slightly superheated vapor phase at cell edge. At this point, the logic returns to subroutine CHOKe.

If neither T_e is greater than the saturation temperature corresponding to the partial pressure of steam at cell edge, nor is the steam/gas-mixture sound speed greater than the ideal-gas sound speed [Eqs. (I-117) and (I-118)], then two-phase saturated fluid is assumed to be present at the cell edge. In this case, the pressure iteration necessary to determine the maximum mass flux and corresponding cell-edge conditions is exactly that described in the $L/D \geq 1.5$ section. This method assumes that no delay in condensation occurs as the steam/gas mixture expands to the saturation temperature corresponding to the cell-edge partial pressure of steam. The equations are repeated here for completeness.

An initial cell-edge pressure equal to that predicted by ideal-gas expansion theory is guessed as

$$p_e = p_o \left(\frac{2}{\gamma_g + 1} \right)^{\gamma_g / (\gamma_g - 1)} \quad (I-121)$$

where p_o is the stagnation pressure [as in Eq. (I-109)] and γ_g is the steam/gas-mixture specific-heat ratio [as in Eq. (I-102)].

Subroutine THERMO is then called to determine the saturation properties at the cell edge corresponding to the cell-edge pressure, p_e .

Saturated cell-edge values for liquid, steam, and steam/gas-mixture enthalpies and for liquid, steam, and noncondensable-gas entropies are computed, such that

$$h_{te} = e_{te} + \frac{p_e}{\rho_{te}} \quad (I-122)$$

$$h_{ve} = e_{ve} + \frac{p_e - p_{ae}}{\rho_{ge} - \rho_{ae}}, \quad (\text{I-123})$$

$$h_{ge} = e_{ge} + \frac{p_e}{\rho_{ge}}, \quad (\text{I-124})$$

$$s_{le} = c_{vl} \ln \left(\frac{T_e}{273.15} \right), \quad (\text{I-125})$$

$$s_{ve} = s_{le} + \frac{h_{ve} - h_{le}}{T_e}, \quad (\text{I-126})$$

and

$$s_{ae} = c_{pa} \ln \left(\frac{T_e}{273.15} \right) - R_a \ln \left(\frac{\min\{p_{ae}, 1.0 \times 10^{-5}\}}{1.0 \times 10^5} \right), \quad (\text{I-127})$$

where e_{le} , e_{ve} , and e_{ge} are the cell-edge liquid, steam, and steam/gas-mixture saturated internal energies for the pressure p_e ; p_e is the cell-edge pressure; p_{ae} is the cell-edge partial pressure of the noncondensable gas given by $p_{ae} = p_a(p_d/p)$; ρ_{le} , ρ_{ae} , and ρ_{ge} are the cell-edge liquid, noncondensable-gas, and steam/gas-mixture saturated densities for the pressure p_e ; c_{vl} is the liquid constant-volume specific heat (as defined in subroutine SETEOS); T_e is the cell-edge temperature equal to the saturation temperature at p_e ; c_{pa} is the noncondensable-gas constant-pressure specific heat (as defined in subroutine SETEOS); and R_a is the noncondensable-gas constant (as defined in subroutine SETEOS).

Then, assuming a constant entropy expansion from the stagnation condition, a cell-edge quality may be calculated from

$$x_e = \frac{s_m - s_{le}}{s_{ve} - s_{le} + \left(\frac{\rho_{ae}}{\rho_{ge}} \right) (s_{ae} - s_a - s_{ve} - s_v)}, \quad (\text{I-128})$$

where s_m , s_v , and s_a are the cell-center steam/liquid-water-mixture, steam, and noncondensable-gas actual entropies for the saturation temperature corresponding to the cell-center partial pressure of steam [as in Eqs. (I-107), (I-104), and (I-105)]; s_{le} , s_{ve} , and s_{ae} are the cell-edge liquid, steam, and noncondensable-gas saturated entropies for the pressure p_e [as computed above in Eqs. (I-125), (I-126), and (I-127)]; and ρ_{ae} and ρ_{ge} are the cell-edge noncondensable-gas and steam/gas-mixture saturated densities for the pressure p_e .

Once the cell-edge quality has been determined, a cell-edge total mixture enthalpy and cell-edge total mixture density are calculated as

$$h_{me} = x_e h_{ge} + (1 - x_e) h_{le} \quad (\text{I-129})$$

and

$$\rho_{me} = \frac{\rho_{le} \rho_{ge}}{x_e (\rho_{le} - \rho_{ge}) + \rho_{ge}} \quad (\text{I-130})$$

where x_e is the cell-edge quality [as in Eq. (I-128)]; h_{le} and h_{ge} are the cell-edge liquid and steam/gas-mixture saturated enthalpies for the pressure p_e [as in Eqs. (I-122) and (I-124)]; and ρ_{le} and ρ_{ge} are the cell-edge liquid and steam/gas-mixture saturated densities for the pressure p_e .

The mass flux, then, for a cell-edge pressure of p_e , becomes

$$G = \rho_{me} \sqrt{2 (h_o - h_{me})} \quad (\text{I-131})$$

where ρ_{me} is the cell-edge total mixture density [as in Eq. (I-130)], h_o is the stagnation enthalpy [as in Eq. (I-108)], and h_{me} is the cell-edge total mixture enthalpy [as in Eq. (I-129)].

The pressure is varied slightly and the iteration is repeated until the pressure that gives the maximum or critical mass flux as predicted by Eq. (I-131) is determined. Once the cell-edge pressure corresponding to the critical flux has been found, the saturated cell-edge conditions become known, and a homogeneous equilibrium sound speed, a_{HE} , is computed as follows:

$$a_{HE} = \frac{G_{\max}}{\rho_{me}} \quad (\text{I-132})$$

This concludes the calculation of the homogeneous equilibrium sound speed and the corresponding cell-edge conditions for the case of a nonsuperheated vapor phase at the cell edge when a superheated vapor phase existed at cell center. At this point, the logic returns to subroutine CHOKE.

I.2.2.3.2. Nonsuperheated Vapor Phase at Cell Center. If the cell-center steam/gas-mixture temperature, T_{gr} , is less than or equal to the saturation temperature corresponding to the cell-center partial pressure of steam, or if the cell-center actual quality [Eq. (I-90)] is less than 1, the cell-center fluid is determined to be a nonsuperheated vapor phase, and the homogeneous equilibrium sound speed and corresponding cell-edge conditions are computed using the same iterative process

outlined in Section I.2.2.2, once the stagnation properties have been identified. The equations are repeated here for completeness.

An initial cell-edge pressure equal to that predicted by ideal-gas expansion theory is guessed as

$$p_e = p_o \left(\frac{2}{\gamma_g + 1} \right)^{\gamma_g / (\gamma_g - 1)} \quad , \quad (I-133)$$

where p_o is the stagnation pressure [as in Eq. (I-109)] and γ_g is the steam/gas-mixture specific-heat ratio [as in Eq. (I-102)].

Subroutine THERMO is then called to determine the saturation properties at the cell edge corresponding to the cell-edge pressure, p_e .

Saturated cell-edge values for liquid, steam, and steam/gas-mixture enthalpies and for liquid, steam, and noncondensable-gas entropies are computed, such that

$$h_{le} = e_{le} + \frac{p_e}{\rho_{le}} \quad , \quad (I-134)$$

$$h_{ve} = e_{ve} + \frac{p_e - p_{ae}}{\rho_{ge} - \rho_{ae}} \quad , \quad (I-135)$$

$$h_{ge} = e_{ge} + \frac{p_e}{\rho_{ge}} \quad , \quad (I-136)$$

$$s_{le} = c_{vl} \ln \left(\frac{T_e}{273.15} \right) \quad , \quad (I-137)$$

$$s_{ve} = s_{le} + \frac{h_{ve} - h_{le}}{T_e} \quad , \quad (I-138)$$

and

$$s_{ae} = c_{pa} \ln \left(\frac{T_e}{273.15} \right) - R_a \ln \left(\frac{\min \{ p_{ae}, 1.0 \times 10^{-5} \}}{1.0 \times 10^5} \right) \quad , \quad (I-139)$$

where e_{le} , e_{ve} , and e_{ge} are the cell-edge liquid, steam, and steam/gas-mixture saturated internal energies for the pressure p_e ; p_e is the cell-edge pressure; p_{ae} is the cell-edge partial

pressure of the noncondensable gas given by $p_{ae} = p_a(p_e/p)$; ρ_{le} , ρ_{ae} , and ρ_{ge} are the cell-edge liquid, noncondensable-gas, and steam/gas-mixture saturated densities for the pressure p_e ; c_{vl} is the liquid constant-volume specific heat (as defined in subroutine SETEOS); T_e is the cell-edge temperature equal to the saturation temperature at p_e ; c_{pa} is the noncondensable-gas constant-pressure specific heat (as defined in subroutine SETEOS); and R_a is the noncondensable-gas constant (as defined in subroutine SETEOS).

Then, assuming a constant entropy expansion from the stagnation condition, the code calculates a cell-edge quality from

$$x_e = \frac{s_m - s_{le}}{s_{ve} - s_{le} + \left(\frac{\rho_{ae}}{\rho_{ge}}\right)(s_{ae} - s_a - s_{ve} - s_v)} \quad , \quad (\text{I-140})$$

where s_m , s_v , and s_a are the cell-center steam/liquid-water-mixture, steam, and noncondensable-gas actual entropies for the saturation temperature corresponding to the cell-center partial pressure of steam [as in Eqs. (I-107), (I-104), and (I-105)]; s_{le} , s_{ve} , and s_{ae} are the cell-edge liquid, steam, and noncondensable-gas saturated entropies for the pressure p_e [as computed above in Eqs. (I-137), (I-138), and (I-139)]; and ρ_{ae} and ρ_{ge} are the cell-edge noncondensable-gas and steam/gas-mixture saturated densities for the pressure p_e .

Once the cell-edge quality has been determined, a cell-edge total mixture enthalpy and cell-edge total mixture density are calculated as

$$h_{me} = x_e h_{ge} + (1 - x_e) h_{le} \quad (\text{I-141})$$

and

$$\rho_{me} = \frac{\rho_{le} \rho_{ge}}{x_e (\rho_{le} - \rho_{ge}) + \rho_{ge}} \quad , \quad (\text{I-142})$$

where x_e is the cell-edge quality [as in Eq. (I-140)]; h_{le} and h_{ge} are the cell-edge liquid and steam/gas-mixture saturated enthalpies for the pressure p_e [as in Eqs. (I-134) and (I-136)]; and ρ_{le} and ρ_{ge} are the cell-edge liquid and steam/gas-mixture saturated densities for the pressure p_e .

The mass flux, then, for a cell-edge pressure of p_e becomes

$$G = \rho_{me} \sqrt{2(h_o - h_{me})} \quad , \quad (\text{I-143})$$

where ρ_{me} is the cell-edge total mixture density [as in Eq. (I-142)], h_o is the stagnation enthalpy [as in Eq. (I-108)], and h_{me} is the cell-edge total mixture enthalpy [as in Eq. (I-141)].

The pressure is varied slightly and the iteration is repeated until the pressure that gives the maximum or critical mass flux as predicted by Eq. (I-143) is determined. Once the cell-edge pressure corresponding to the critical flux has been found, the saturated cell-edge conditions become known and a homogeneous equilibrium sound speed, a_{HE} , is computed as follows:

$$a_{HE} = \frac{G_{max}}{\rho_{me}} \quad (I-144)$$

This concludes the calculation of the homogeneous equilibrium sound speed and the corresponding cell-edge conditions for the case of a nonsuperheated vapor at cell center when $L/D < 1.5$ or the case of only subcooled liquid at cell center. At this point, the logic returns to subroutine CHOKE.

I.2.3. Constants

Several thermodynamic properties, such as the constant-pressure and constant-volume specific heats, are defined as constants in subroutine THERMO. These constants are fully described in Appendix A of this document.

I.2.4. Models as Coded

Subroutines CHOKE and SOUND contain the Fortran coding for the critical flow models. The necessary input to CHOKE includes the following:

AREA	Cell-edge area.
ARATIO	Ratio of cell-edge to donor-cell flow areas.
DADX	(Cell-edge area - cell area) / (0.5 x cell length).
DXC	Donor-cell length.
FAC	Donor-cell flow area.
ALPC	Donor-cell void fraction.
PC	Donor-cell pressure.
PAC	Donor-cell partial pressure of air.
TLC	Donor-cell liquid temperature.
RHOLC	Donor-cell liquid density.
RHOVC	Donor-cell steam/gas-mixture density.
SIGMA	Donor-cell surface tension.
VL	Momentum-solution liquid velocity.
VV	Momentum-solution steam/gas-mixture velocity.
VLO	Old-time liquid velocity.
VVO	Old-time steam/gas-mixture velocity.
VLC	Donor-cell cell-center liquid velocity.
VVC	Donor-cell cell-center steam/gas-mixture velocity.
ICHOKE	Choking indicator: ICHOKE = 0, unchoked flow. ICHOKE = 1, subcooled choked flow. ICHOKE = 2, two-phase choked flow. ICHOKE = 3, single-phase vapor choked flow.

I.2.4.1. Initial Calculations. Upon entry to subroutine CHOKe, several preliminary calculations are performed to prepare for either a subcooled-liquid choking calculation; a two-phase, two-component choking calculation; or a single-phase vapor choking calculation.

The two choked-flow multipliers are set to the user-input values as specified in the INOPTS NAMELIST data or are defaulted to 1.0 if no user-input values are specified.

The cell length-to-hydraulic-diameter ratio, L/D , is checked to determine how subroutine SOUND will calculate the stagnation properties given the cell-center conditions.

For $L/D \geq 1.5$, complete thermal equilibrium is assumed to exist at the cell edge. If the cell-center conditions are not initially in thermal equilibrium, thermal equilibrium conditions are calculated at the cell center assuming a constant-enthalpy process. Once thermal equilibrium has been established at cell center, the equilibrium void fraction is used to determine which choking model to use (subcooled-liquid; two-phase, two-component; or single-phase vapor). Stagnation properties computed in subroutine SOUND to determine the homogeneous equilibrium sound speed and the corresponding cell-edge conditions are calculated using the cell-center thermal equilibrium conditions, rather than any nonequilibrium cell-center conditions that may exist.

For $0.0000011111 \leq L/D < 1.5$, the actual cell-center void fraction is used to determine which choking model is used (either subcooled-liquid; two-phase, two-component; or single-phase vapor). Complete thermal equilibrium is still assumed to exist at the cell edge, but the stagnation conditions computed in subroutine SOUND to calculate the homogeneous equilibrium sound speed and the corresponding cell-edge conditions are calculated using the actual cell-center conditions (which may be either equilibrium or nonequilibrium conditions).

For $L/D < 0.0000011111$, complete nonequilibrium is assumed to exist at the choking plane (cell edge).

In TRAC, the low value of 0.0000011111 for the L/D check means that nonequilibrium equations are not evaluated. In addition, when a noncondensable gas is present in the vapor component, the logic described above for the case when $L/D \geq 1.5$ is followed throughout the choking calculation, regardless of the actual value of L/D .

Next the mixture density, mixture velocity, and slip ratio are calculated from the momentum-solution velocities according to the following:

$$\rho_{mc} = \alpha_c \rho_{gc} + (1.0 - \alpha_c) \rho_{lc} \quad , \quad (I-145)$$

$$V_m = \frac{\alpha_c \rho_{gc} V_g + (1.0 - \alpha_c) \rho_{lc} V_l}{\rho_{mc}} \quad , \quad (I-146)$$

and

$$S = \frac{V_g}{V_l} \quad , \quad (I-147)$$

where α_c is the cell-center void fraction, ρ_{gc} and ρ_{lc} are the cell-center phasic densities, and V_g and V_l are the momentum-solution phasic velocities. If a negative slip is calculated, the slip is reset to 1.0, and the calculational sequence proceeds. This should never occur, but in the event that countercurrent flow is sent to CHOKe, a slip of 1.0 will allow CHOKe to run without failing. (Choked flow will not occur in this case anyway.)

I.2.4.2. Determination of Choking Velocities Using the Appropriate Model.

At this point, subroutine CHOKe branches to the appropriate choked-flow model based on the void fraction (either actual or equilibrium as determined by the L/D check described above).

If $\alpha \leq 0.01$, a subcooled-liquid choking calculation is done.

If $0.01 < \alpha < 0.1$, an interpolation between the subcooled-liquid and the two-phase, two-component choking calculation is performed to determine the choking velocities.

If $0.1 \leq \alpha \leq 0.999$, a two-phase, two-component choking calculation is done.

And if $\alpha > 0.999$, a single-phase vapor choking calculation is performed.

I.2.4.2.1. Subcooled Liquid. If $\alpha \leq 0.01$, a subcooled-liquid calculation is done to determine the choking velocities.

First, subroutine SOUND is called to determine the maximum mass flux and the corresponding cell-edge conditions, as described in Section I.2.2. From this maximum mass flux, the value of the homogeneous equilibrium sound speed to be used in conjunction with the donor-cell conditions to give the correct mass flow is then calculated, such that

$$a_{HE} = \frac{G_{max}}{\rho_{mc}} \quad , \quad (I-148)$$

where G_{max} is the critical mass flux returned by SOUND and ρ_{mc} is the (donor-cell) cell-center mixture density calculated in Eq. (I-145).

Next, a nucleation pressure, which may be lower than the saturation pressure corresponding to the local (donor-cell) liquid temperature, is calculated for the cell edge using the Jones nucleation delay model [Eq. (I-31)]. With the critical temperature, T_c , equal to 647.3 K and Boltzmann's constant, k , equal to 1.380622×10^{-23} J·K⁻¹ Eq. (I-31) becomes

$$p_{\text{nuc}} = p_{\text{sat}} - \max \left\{ 0.0, \frac{5.691364 \times 10^{-30} \sigma^{1.5} T_\ell^{13.76} \left[1 + 13.25 \left(-\frac{1}{1.01325 \times 10^{11}} \frac{Dp}{Dt} \right)^{0.8} \right]^{0.5}}{\left(1 - \frac{\rho_{ge}}{\rho_{le}} \right)} \right. \\ \left. - 0.069984 \left(\frac{A_e}{A_c} \right)^2 \rho_\ell V_\ell^2 \right\} , \quad (\text{I-149})$$

where p_{sat} is the saturation pressure corresponding to T_ℓ , the donor-cell liquid temperature; σ is the surface tension; ρ_{le} and ρ_{ge} are cell-edge densities; A_e and A_c are cell-edge and cell-center flow areas; and V_ℓ is the momentum-solution liquid velocity. The term Dp/Dt is the substantial derivative of pressure and is given by

$$\frac{Dp}{Dt} = \max \left\{ 1.0 \times 10^{-10}, -\frac{2|V_\ell|(p_e - p_c)}{\Delta x} \right\} , \quad (\text{I-150})$$

where V_ℓ is again the momentum-solution liquid velocity, p_e is the cell-edge (choke-plane or throat) pressure returned by subroutine SOUND, p_c is the cell-center pressure, and Δx is the cell length.

The code then evaluates Bernoulli's equation to give the following cell-edge velocity:

$$V_{\ell e, \text{Bernoulli}} = \left[V_{\ell c}^2 + \frac{2 \max\{0.0, (p_c - p_{\text{nuc}})\}}{\rho_{le}} \right]^{\frac{1}{2}} , \quad (\text{I-151})$$

where $V_{\ell c}$ is the cell-center liquid velocity calculated from Eq. (I-48) as described in Section I.2.2., ρ_{le} is the cell-edge liquid density as evaluated in subroutine SOUND, p_c is the cell-center pressure, and p_{nuc} is the cell-edge nucleation pressure [Eq. (I-149)].

The liquid choking velocity is taken as the maximum of the Bernoulli-predicted velocity and the homogeneous equilibrium sound speed as determined in SOUND. That is,

$$V_{\ell e} = \max \{ a_{\text{HE}}, V_{\ell e, \text{Bernoulli}} \} . \quad (\text{I-152})$$

If a sound-speed multiplier was specified through the user-input INOPTS NAMELIST data, this is applied to the liquid choking velocity to give a final predicted value of

$$V_{le}^p = CHMLT1 \cdot \max \{ a_{HE}, V_{le, \text{Bernoulli}} \} \quad (I-153)$$

If the liquid velocity as determined in the momentum solution is less than this maximum choking velocity, the flow is flagged as being unchoked and the calculation is ended. If, however, the liquid velocity determined in the momentum solution is greater than or equal to this maximum choking velocity, then the liquid velocity is reset to be equal to the choking velocity. In addition, a predicted steam/gas-mixture velocity is calculated according to

$$V_{ge}^p = V_{le}^p S \quad (I-154)$$

where S is the slip ratio [as determined in Eq. (I-147)]. If the predicted steam/gas-mixture choking velocity, v_{ge}^p , has changed directions from the momentum-solution steam/gas-mixture velocity, V_{ge} , the steam/gas-mixture choking velocity is reset to zero.

I.2.4.2.2. Two-Phase, Two-Component Fluid. If $0.1 \leq \alpha \leq 0.999$ a two-phase, two-component choking calculation is done to determine the predicted choking velocities.

Equation (I-43) is extremely difficult to solve analytically. Thus, TRAC obtains the characteristic roots of Eq. (I-43) numerically. This method advantageously maintains generality and facilitates computations under different assumptions.

The solution of Eq. (I-43) requires that $p_a, p_v, \alpha, \rho_a, \rho_v, \rho_l, s_a, s_v,$ and s_l and their derivatives be specified at the cell edge, where the choking criterion is applied. However, these quantities are known only at the cell center. Direct use of the cell-center quantities yields erroneous results caused by the presence of steep gradients near the choking plane. Therefore, an estimate of the thermodynamic state at the cell edge is necessary. To obtain this estimate, subroutine SOUND is called. In addition to determining the thermodynamic state at the cell edge, SOUND also calculates the homogeneous equilibrium sound speed which is used as a first estimate for the largest characteristic root. (When the non-homogeneous effects are not dominant, the desired root is close to the homogeneous equilibrium sound speed.) The procedure used by SOUND to arrive at the cell-edge thermodynamic state and the homogeneous equilibrium sound speed is described in full detail in Section I.2.2.

Because equilibrium is assumed to occur at the cell edge, subroutine THERMO is called to determine saturation properties at the cell edge corresponding to the cell-edge pressure, p_e , estimated in the call to SOUND. The cell-edge void fraction may then be calculated, such that

$$\alpha_e = \frac{\rho_{le} - \rho_{me}}{\rho_{le} - \rho_{ge}} \quad (I-155)$$

where ρ_{me} is the cell-edge mixture density calculated by subroutine SOUND, and ρ_{le} and ρ_{ge} are the saturated liquid and steam/gas-mixture densities for a cell-edge pressure of p_e .

In addition, entropies and the quantities ρ_{le}^* , ρ_{ge}^* , s_{le}^* , and s_{ge}^* necessary for evaluating the elements of matrix $\underline{\underline{B}}$ (as shown in Fig. I-9.b) are defined at the cell-edge, such that

$$s_{le} = c_{vl} \ln \left(\frac{T_e}{273.15} \right) , \quad (I-156)$$

$$s_{ve} = c_{vl} \ln \left(\frac{T_e}{273.15} \right) + \left(\frac{1}{\rho_{ve}} - \frac{1}{\rho_{le}} \right) \frac{dT}{dp_v} , \quad (I-157)$$

$$s_{ae} = c_{pa} \ln \left(\frac{T_e}{273.15} \right) - R_a \ln \left(\frac{\max \{p_{ae}, 1.0 \times 10^{-5}\}}{1.0 \times 10^5} \right) , \quad (I-158)$$

$$s_{ge} = s_{ae} \left(\frac{\rho_{ae}}{\rho_{ge}} \right) + s_{ve} \left(1 - \frac{\rho_{ae}}{\rho_{ge}} \right) , \quad (I-159)$$

and

$$\rho_{le}^* = \left(\frac{\partial \rho_{le}}{\partial p} \right)_T + \left(\frac{\partial \rho_{le}}{\partial T} \right)_p \frac{dT}{dp_v} , \quad (I-160)$$

$$\rho_{ve}^* = \left(\frac{\partial \rho_{ve}}{\partial p_v} \right)_T + \left(\frac{\partial \rho_{ve}}{\partial T} \right)_{p_v} \frac{dT}{dp_v} , \quad (I-161)$$

$$s_{ve}^* = \frac{1}{T_e} \left[\left(\frac{\partial e_{ve}}{\partial p_v} \right)_T + \left(\frac{\partial e_{ve}}{\partial T} \right)_{p_v} \frac{dT}{dp_v} \right] - \frac{p_{ve}}{\rho_{ve}^2 T_e} \left[\left(\frac{\partial \rho_{ve}}{\partial p_v} \right)_T + \left(\frac{\partial \rho_{ve}}{\partial T} \right)_{p_v} \frac{dT}{dp_v} \right] , \quad (I-162)$$

and

$$s_{le}^* = \frac{1}{T_e} \left[\left(\frac{\partial e_{le}}{\partial p} \right)_T + \left(\frac{\partial e_{le}}{\partial T} \right)_p \frac{dT}{dp_v} \right] - \frac{p_e}{\rho_{le}^2 T} \left[\left(\frac{\partial \rho_{le}}{\partial p} \right)_T + \left(\frac{\partial \rho_{le}}{\partial T} \right)_p \frac{dT}{dp_v} \right] , \quad (I-163)$$

where T_e is the cell-edge saturation temperature corresponding to the cell-edge partial pressure of steam, p_{ve} ; c_{vl} is the liquid constant-volume specific heat (defined in subroutine SETEOS); ρ_{ae} , ρ_{ve} , ρ_{ge} , and ρ_{le} are the cell-edge saturation densities corresponding to the cell-edge pressure, p_e ; c_{pa} and R_a are the noncondensable-gas constant-pressure specific heat and the gas constant (both defined in subroutine SETEOS); and p_{ae} is the cell-edge partial pressure of the noncondensable gas as estimated by SOUND.

Next, CHOKe tries to determine the mass flux such that none of the characteristic roots of the governing system of partial differential equations given by Eqs. (I-32) through (I-36) has a positive real part and that the maximum root is zero.

The solution of Eq. (I-43) for a set of λ that includes $\lambda_1 = 0$ requires that

$$\det |\underline{\underline{B}}| = 0 . \quad (I-164)$$

Therefore, CHOKe first tries to solve Eq. (I-164).

To set up the elements of matrix $\underline{\underline{B}}$, CHOKe calculates first-guess approximations of the steam/gas-mixture and liquid cell-edge velocities from the homogeneous equilibrium sound speed, a_{HE} , and the cell-center momentum-solution slip value [computed in Eq. (I-147)], such that

$$V_{ge} = \frac{a_{HE} S \rho_{me}}{\alpha_e \rho_{ge} S + (1 - \alpha_e) \rho_{le}} \quad (I-165)$$

and

$$V_{le} = \frac{V_{ge}}{(S + 1.0 \times 10^{-20})} , \quad (I-166)$$

where a_{HE} is the homogeneous equilibrium sound speed by returned subroutine SOUND, S is the slip ratio calculated from the momentum-solution steam/gas-mixture and liquid velocities [as in Eq. (I-147)], α_e is the cell-edge void fraction [computed in Eq. (I-155)], ρ_{me} is the cell-edge total mixture density returned by subroutine SOUND, and ρ_{le} and ρ_{ge} are the saturated cell-edge liquid and steam/gas-mixture densities for the cell-edge pressure p_e .

The virtual mass coefficient in the two phasic momentum equations [Eqs. (I-33) and (I-34)] is assumed to be fixed at a value of 10. Values for the virtual mass coefficient such as 5, 10, and 20 were found to give good mass-flow predictions when compared to data. The value of 10 was arbitrarily chosen because small variations in the virtual mass coefficient in this range (5 to 20) did not significantly affect the calculation.

The determinant of matrix \underline{B} may now be evaluated. An iterative procedure is used to vary the mixture velocity around a_{HE} until the rate of change of V_{ge} is less than (or equal to) $0.001a_{HE}$ per iteration step while satisfying the requirement that the determinant be zero.

Once converged values of V_{ge} and V_{le} have been found using the iteration above, CHOKE sets up the elements in matrix \underline{A} and solves for the eigenvalues and eigenvectors of $\underline{A}^{-1}\underline{B}$. This is equivalent to solving Eq. (I-43) if the signs of the eigenvalues are reversed. CHOKE also checks that the absolute value of the root with the largest real part is indeed real and less than (or equal to) $0.01a_{HE}$.

The predicted values of the choking velocities to be used in conjunction with the donor-cell conditions to give the correct mass-flow rate are now calculated, such that

$$V_{me}^p = \frac{\alpha_e \rho_{ge} V_{ge} + (1 - \alpha_e) \rho_{le} V_{le}}{\rho_{mc}} \quad , \quad (I-167)$$

$$V_{le}^p = \text{CHMLT2} \cdot \frac{V_{me}^p \rho_{mc}}{\rho_{gc} \alpha_c S + \rho_{lc} (1 - \alpha_c)} \quad , \quad (I-168)$$

and

$$V_{ge}^p = S V_{le}^p \quad , \quad (I-169)$$

where α_e is the cell-edge void fraction calculated in Eq. (I-155); ρ_{ge} and ρ_{le} are the cell-edge saturation densities corresponding to the cell-edge pressure, p_e ; ρ_{gc} , ρ_{lc} , and ρ_{mc} are the cell-center steam/gas-mixture, liquid, and total mixture densities; S is the slip ratio calculated from the momentum-solution steam/gas-mixture and liquid velocities as in Eq. (I-147); and CHMLT2 is a user-input choked-flow multiplier.

If the mixture velocity as determined in the momentum solution is less than this predicted mixture velocity, the flow is flagged as being unchoked and the calculation is ended. If, however, the mixture velocity determined in the momentum solution is greater than (or equal to) the predicted mixture choking velocity, then the steam/gas-mixture, liquid, and total mixture velocities are reset to the predicted choking values.

I.2.4.2.3. Interpolation Region Between Subcooled and Two-Phase Models. If $0.01 < \alpha < 0.1$, an interpolation between the subcooled-liquid and the two-phase, two-component choking calculation is performed to determine the predicted choking velocities.

Initially, liquid and steam/gas-mixture choking velocities are calculated using the two-phase, two-component model. In addition, liquid and steam/gas-mixture choking velocities are calculated using the subcooled-liquid choking model. These velocities are combined to produce the predicted liquid and steam/gas-mixture choking velocities using a linear interpolation in alpha, such that,

$$V_{le}^p = V_{l,sc} + \left(\frac{\alpha_c - \alpha_{\min}}{\alpha_{\max} - \alpha_{\min}} \right) (V_{l,tp} - V_{l,sc}) \quad (I-170)$$

and

$$V_{ge}^p = V_{g,sc} + \left(\frac{\alpha_c - \alpha_{\min}}{\alpha_{\max} - \alpha_{\min}} \right) (V_{g,tp} - V_{g,sc}) \quad (I-171)$$

where $V_{l,sc}$ and $V_{g,sc}$ are the liquid and steam/gas-mixture choking velocities calculated using the subcooled-liquid model; $V_{l,tp}$ and $V_{g,tp}$ are the liquid and steam/gas-mixture choking velocities calculated using the two-phase, two-component choking model; α_c is the cell-center void fraction (either actual or equilibrium, depending on the value of L/D); and α_{\min} and α_{\max} are the limits on the void fraction for the interpolation region, currently set to 0.01 and 0.1, respectively.

I.2.4.2.4. Single-Phase Vapor. If $\alpha > 0.999$, a single-phase vapor model is used to determine the choking velocities. Subroutine SOUND is first called to determine cell-edge conditions and the maximum mass flux as described in [Section I.2.2](#). From this maximum mass flux, the value of the homogeneous equilibrium sound speed to be used in conjunction with donor-cell conditions to give correct mass flow is then calculated, such that

$$a_{HE} = \frac{G_{\max}}{\rho_{mc}} \quad (I-172)$$

where G_{\max} is the critical mass flux returned by SOUND and ρ_{me} is the (donor-cell) cell-center mixture density calculated in Eq. (I-145). If a sound-speed multiplier was specified through the user-input INOPTS NAMELIST data, this is applied to the steam/gas-mixture sound speed to give a predicted steam/gas-mixture choking velocity of

$$V_{ge}^p = \text{CHMLT2} \cdot a_{HE} \quad (\text{I-173})$$

If the momentum-solution steam/gas-mixture velocity, V_g , is less than this predicted steam/gas-mixture choking velocity, the flow is flagged as being unchoked and the calculation is ended. If, however, the steam/gas-mixture velocity as determined in the momentum solution is greater than or equal to the predicted choking velocity, then the steam/gas-mixture velocity is reset to be equal to the predicted steam/gas-mixture choking velocity. In addition, a predicted liquid velocity is calculated according to

$$V_{le}^p = \frac{V_{ge}^p}{(S + 1.0 \times 10^{-20})} \quad (\text{I-174})$$

where S is the slip ratio as determined in Eq. (I-147). If the predicted liquid choking velocity at the cell edge, v_{le}^p , has changed directions from the momentum-solution liquid velocity, V_l , it is reset to zero.

I.2.4.3. New-Time Choking Velocities. Finally, new-time phasic choking velocities are computed by time-averaging the old-time velocities with the predicted choking velocities just calculated, such that

$$V_l^{n+1} = 0.1 V_{le}^p + 0.9 V_l^n \quad (\text{I-175})$$

and

$$V_g^{n+1} = 0.1 V_{ge}^p + 0.9 V_g^n \quad (\text{I-176})$$

where v_{le}^p and v_{ge}^p are the predicted liquid and steam/gas-mixture choking velocities just calculated, and v_l^n and v_g^n are the old-time liquid and steam/gas-mixture velocities (either momentum solution or choking). This old-time, new-time method of weighting limits the change in the choking velocity for either phase to only 10% of the actual calculated change and ensures that the choking model lags slightly behind any pressure transients so that the effects of unnatural pressure changes caused by fluid inertia are limited.

This concludes the first pass through the choking model calculation. A second pass is necessary to evaluate the velocity derivatives. This is described in the next section.

I.2.4.4. Second-Pass Velocity m Derivatives. To calculate the derivatives of the liquid and steam/gas-mixture choking velocities with respect to pressure, a second pass through subroutine CHOKe is made with the pressure at cell center equal to 0.99 of the actual cell-center value. A second set of predicted liquid and steam/gas-mixture choking velocities is calculated for this 99% pressure value, using either a subcooled-liquid, a two-phase two-component fluid, or a superheated vapor calculation, exactly as was done in the first pass through subroutine CHOKe. These second-pass predicted choking velocities are then time-averaged to determine new-time choking velocities for the 99% pressure value in a manner similar to that used in the first pass, such that

$$V_{\ell,2nd}^{n+1} = 0.1V_{\ell,2nd}^p + 0.9V_{\ell}^n \quad (I-177)$$

and

$$V_{g,2nd}^{n+1} = 0.1V_{g,2nd}^p + 0.9V_g^n \quad (I-178)$$

where $V_{\ell,2nd}^p$ and $V_{g,2nd}^p$ are the second-pass predicted liquid and steam/gas-mixture choking velocities, and V_{ℓ}^n and V_g^n are the old-time liquid and steam/gas-mixture velocities (either momentum-solution or choked).

Once the actual and second-pass new-time liquid and steam/gas-mixture choking velocities have been determined, the derivatives with respect to pressure are calculated as follows:

$$\begin{aligned} \frac{dV_{\ell}}{dp} &\approx \frac{\Delta V_{\ell}}{\Delta p} \\ &= \frac{(V_{\ell}^{n+1} - V_{\ell,2nd}^{n+1})}{(p - 0.99p)} = 100.0 \frac{(V_{\ell}^{n+1} - V_{\ell,2nd}^{n+1})}{p} \end{aligned} \quad (I-179)$$

and

$$\frac{dV_g}{dp} \approx 100.0 \frac{(V_g^{n+1} - V_{g,2nd}^{n+1})}{p} \quad (I-180)$$

where V_{ℓ}^{n+1} and V_g^{n+1} are the actual new-time choking velocities, and $V_{\ell,2nd}^{n+1}$ and $V_{g,2nd}^{n+1}$ are the second-pass, new-time choking velocities for a cell-center pressure of 0.99p.

With the determination of the new-time choking velocities and their derivatives with respect to pressure, the choking calculation performed in subroutines CHOKe and SOUND is now complete. At this point, the logic returns to the calling subroutine.

I.2.5. Weighting, Magnitude Limits, Rate Limits, and Averaging

This next section describing the averaging technique used to compute cell-center momentum-solution velocities is copied exactly from Section I.2.2.1. It is included here also for completeness.

I.2.5.1. Cell-Center Momentum-Solution Velocities. The velocities obtained from the momentum solution are cell-edge values. However, to evaluate stagnation conditions (in subroutine SOUND), it is necessary to know the phasic velocities at cell center. This transition between cell edge and cell center is accomplished in subroutine VOLV by averaging the mass flux between cell edges, such that

$$V_{gc} = \frac{\frac{1}{2} \left[(\rho_g \alpha)_{e^-} V_{g,e^-} A_{e^-} + (\rho_g \alpha)_{e^+} V_{g,e^+} A_{e^+} \right]}{\rho_{gc} \alpha_c A_c} \quad (\text{I-181})$$

and

$$V_{lc} = \frac{\frac{1}{2} \left[(\rho_l (1 - \alpha))_{e^-} V_{l,e^-} A_{e^-} + (\rho_l (1 - \alpha))_{e^+} V_{l,e^+} A_{e^+} \right]}{\rho_{lc} (1 - \alpha)_c A_c} \quad (\text{I-182})$$

where V_{gc} and V_{lc} are the transformed cell-center velocities, ρ_g and ρ_l are the liquid and steam/gas-mixture densities, α is the void fraction, V_l and V_g are the liquid and steam/gas-mixture velocities, and A is the cross-sectional flow area. The subscripts e^- and e^+ refer to upstream cell-edge and downstream cell-edge quantities, while the subscript c refers to cell-center quantities for the particular cell in question. It is assumed that $\rho\alpha$ at the upstream face is equal to the upstream cell product value, whereas $\rho\alpha$ at the downstream face is taken to be equal to the current cell value, because densities and void fractions are normally associated with cell-center rather than cell-edge positions.

This next section describing the weighting technique used to compute new-time choking velocities from predicted and old-time velocities is copied from Section I.2.4.3. It is included here also for completeness.

I.2.5.2. New-Time Choking Velocities. New-time phasic choking velocities are computed by time-averaging the old-time velocities with the predicted choking velocities, such that

$$V_{le}^{n+1} = 0.1 V_{le}^p + 0.9 V_{le}^n \quad (\text{I-183})$$

and

$$V_g^{n+1} = 0.1 V_{ge}^p + 0.9 V_g^n \quad (\text{I-184})$$

where v_{le}^p and v_{ge}^p are the predicted liquid and steam/gas-mixture choking velocities, and v_{le}^o and v_{ge}^o are the old-time liquid and steam/gas-mixture velocities (either momentum solution or choking). This old-time, new-time method of weighting limits the change in the choking velocity for either phase to only 10% of the actual calculated change and ensures that the choking model lags slightly behind any pressure transients so that the effects of unnatural pressure changes caused by fluid inertia are limited.

I.2.6. Assessment

Two types of assessment are performed on the TRAC-PF1/MOD2 critical flow model: comparing the MOD2 model to other models and comparing calculations using the critical flow model against fine-mesh calculations and test data. Results of the comparisons follow. The results and conclusions presented throughout this section apply to TRAC-M as well.

I.2.6.1. Comparing TRAC-PF1/MOD2 Choked-Flow Model with Other Models.

The primary requirement for an accurate choked-flow model is that it yield results that are close to the homogeneous equilibrium calculations when the flow approaches such a homogeneous limit, because the nonhomogeneous effects are of only secondary importance in most situations. Therefore, the homogeneous equilibrium sound speed calculated by MOD2 should agree with the true sound speed. [Figure I-10](#) compares the MOD2-calculated homogeneous equilibrium sound speed with that obtained from the tables of Hall ([Ref. I-9](#)) for different void fractions at a 560 K saturation temperature. The agreement between the calculations and the tables is excellent.

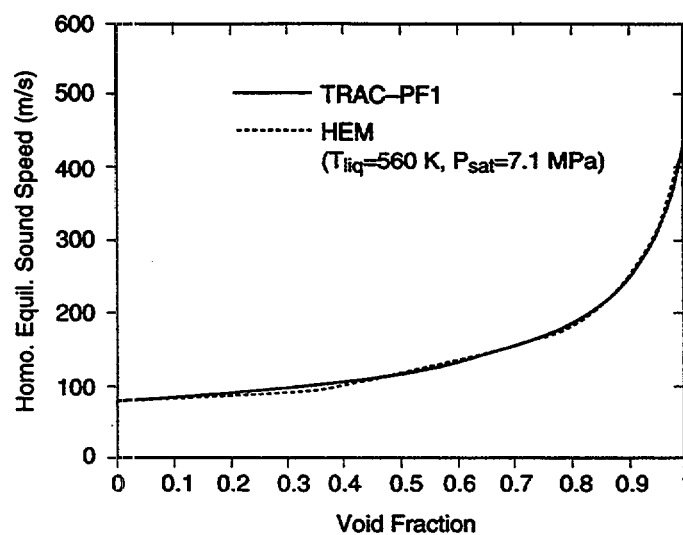


Fig. I-10. Comparison of the two-phase homogeneous equilibrium sound speed.

Figure I-11. compares the MOD2-calculated subcooled critical flow with that from the Burnell model and from the Homogeneous Equilibrium Model (HEM) for stagnation pressures ranging from 7.1 MPa (saturated liquid) to 15.0 MPa (subcooled liquid) at a constant 560 K temperature. The Burnell model is the modified Burnell model from RELAP4/MOD6 (Ref. I-10.) that accounts for nucleation delay by an empirical expression. The HEM mass flux represents a lower limit on the mass flux. As desired, the MOD2 model calculations give results that are similar to those for the Burnell model. The minor discrepancy between the MOD2 choked-flow models and the Burnell models is caused primarily by the difference between the nucleation-delay models.

Figure I-12. compares the MOD2 two-phase critical-flow model calculations with the HEM data at 560 K saturation temperature. Again, the agreement is good. The MOD2-calculated results differ from the HEM data because the nonhomogeneous effects are not accounted for in the HEM. Larger differences between the results obtained from the two models are expected when the upstream phasic velocities differ. (The flow upstream of the break was assumed to be stagnant for this calculation.)

I.2.6.2. Comparing the MOD2 Choked-Flow Model Calculations with the Fine-Mesh Calculations and the Test Data. A true test of the accuracy of a choking model is its ability to predict results similar to those obtained using an extremely fine mesh (natural choking) for geometries with smooth area changes. Therefore, the MOD2 choking calculations are compared with the fine-mesh results and the test data from Tests 4 (Ref. I-11.) and 24 (Ref. I-12.) of the Marviken test facility and the Edwards blowdown experiment (Ref. I-13.).

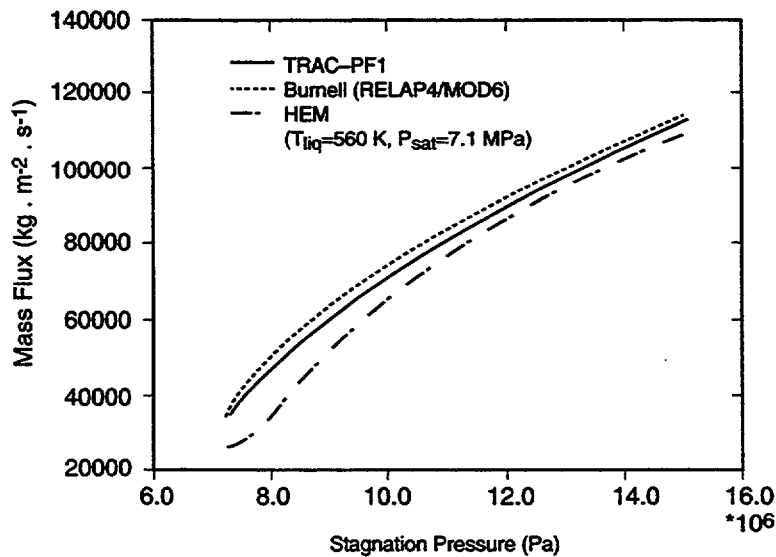


Fig. I-11. Comparison of the subcooled critical mass flux.

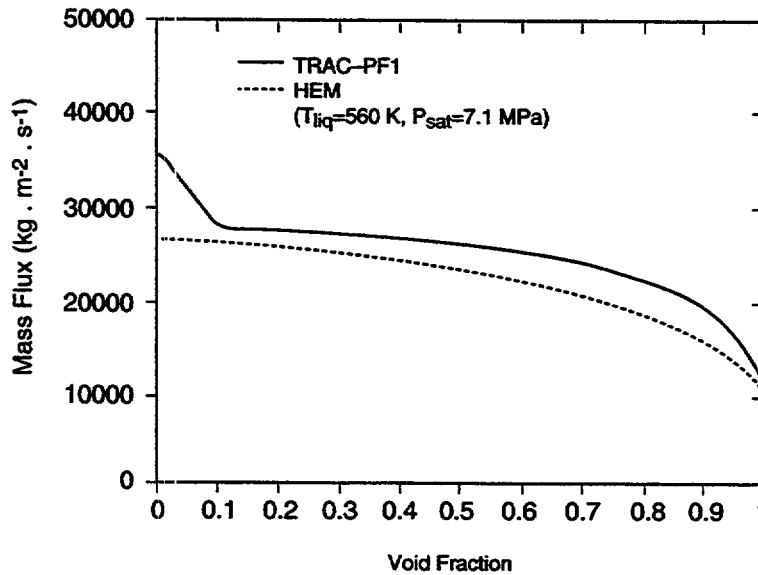


Fig. I-12. Comparison of the two-phase critical mass flux.

I.2.6.2.1. Marviken Test Facility. The Marviken full-scale critical-flow tests assess the ability of computer codes to predict large pressure-vessel blowdowns. The four major components of this facility are a pressure vessel, originally designed to be part of the Marviken nuclear power plant; a discharge pipe; a test nozzle with the minimum flow area in the system; and a rupture-disk assembly. Figure I-13 shows the vessel that still includes part of the core superstructure and the moderator tank plus three gratings installed to eliminate vortex formation. Figure I-14 shows the other components. All elevations in both figures are measured relative to the vessel bottom. Pressure and temperature transducers are located along the vessel and the discharge pipe, as shown in Figs. I-13 and I-14. The signals from the various transducers are processed through a signal-conditioning unit with its channels connected to a pulse-code modulation system.

Before a test is run, the vessel is partially filled with deionized water and heated by removing water from the vessel bottom, passing it through an electric heater, and returning it to the steam dome at the vessel top. This procedure produces a complicated initial temperature distribution in the vessel. A saturated steam dome fills the vessel region above the initial water level. The test is initiated by releasing the rupture disks and is terminated by closing a ball valve in the discharge pipe. We specifically chose Marviken Tests 4 and 24 because Test 4 had the longest nozzle and Test 24 the shortest in the entire test series.

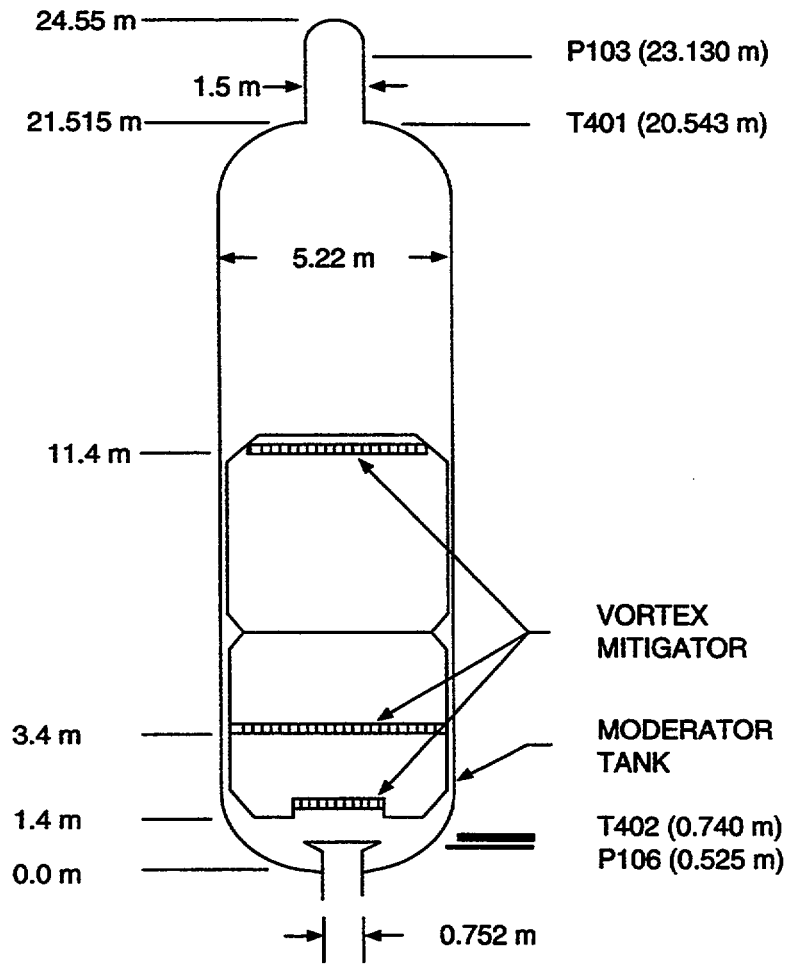


Fig. I-13. Marviken pressure vessel.

The MOD2 model for Marviken Tests 4 and 24 included four components. A zero-velocity FILL component modeled the vessel upper boundary. A PIPE component modeled the vessel above 2.6 m, including the maximum-diameter region plus the top cupola. Another PIPE component modeled the lower part of the vessel, the discharge pipe, the nozzle, and the rupture-disk assembly. A BREAK component provided a pressure boundary condition at the rupture-disk assembly lower boundary. For the fine-noding cases, the nozzles were modeled with 30 cells (15 in the converging section and 15 in the straight portion with a minimum cell length of 0.025 m) for Test 4 and with 12 cells (5 in the converging section and 7 in the straight portion with a minimum cell length of 0.02 m) for Test 24. When using the choked-flow model, the nozzles in both tests were modeled by only two cells, one in the converging section and the other simulating the entire straight section, with the choked-flow model invoked at the downstream edge of the second cell. The default choked-flow multipliers were used in these calculations.

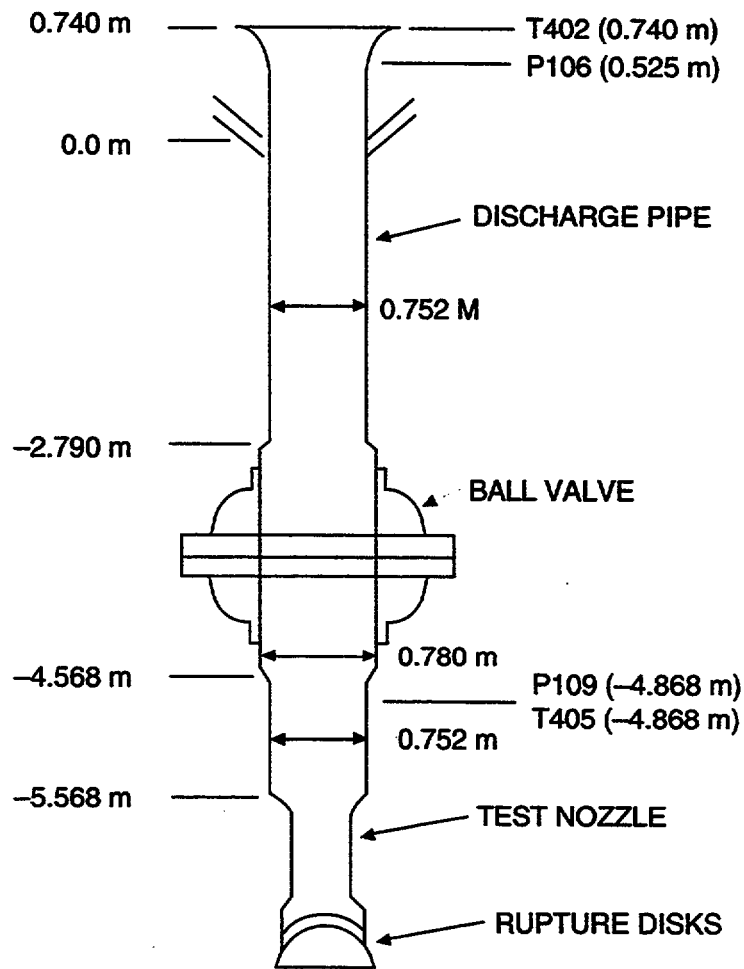


Fig. I-14. Marviken discharge pipe, test nozzle, and rupture-disk assembly.

Figures I-15 and I-16 show the MOD2 mass flows and pressure histories with the choking model and the fine noding compared with the test data. The measured mass flows are derived from velocity (pitot-static) and vessel differential-pressure measurements. The pitot-static data curve is valid throughout the transient, whereas the vessel differential-pressure curve is valid only after ~5 s. The choking calculations give almost identical results to those for the fine-mesh case. Both the choked-flow and the fine-mesh calculations also agree well with the test data except during the subcooled blowdown phase when the mass flow is under-predicted by an average of ~10%. The dip in the measured pressure during the first 3 s of the transient indicates a significantly more pronounced nucleation delay than predicted by the MOD2 model.

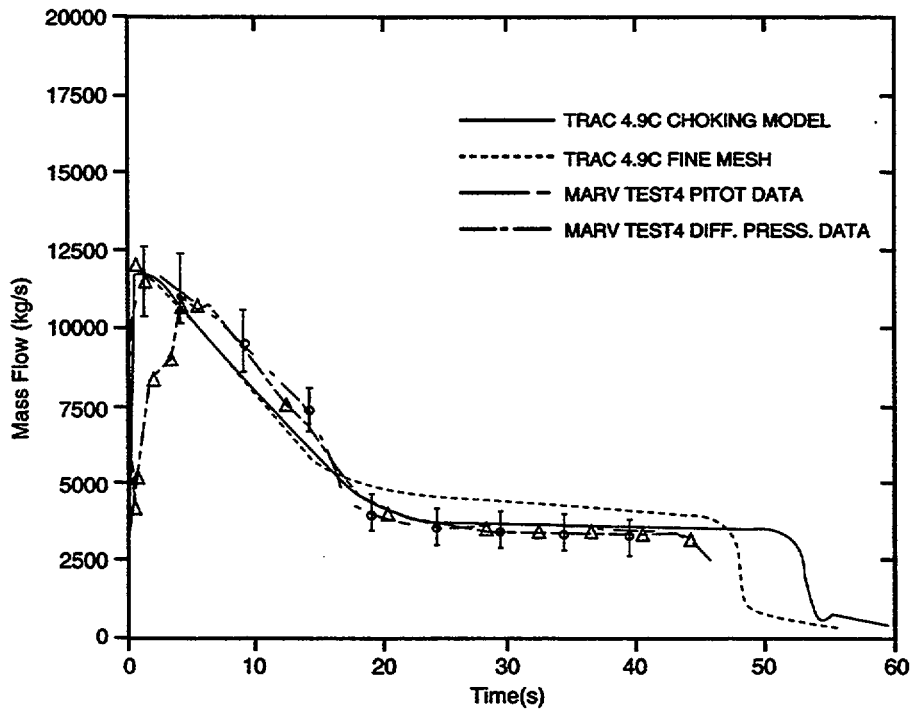


Fig. I-15. Comparison of the nozzle mass flows for Marviken Test 4.

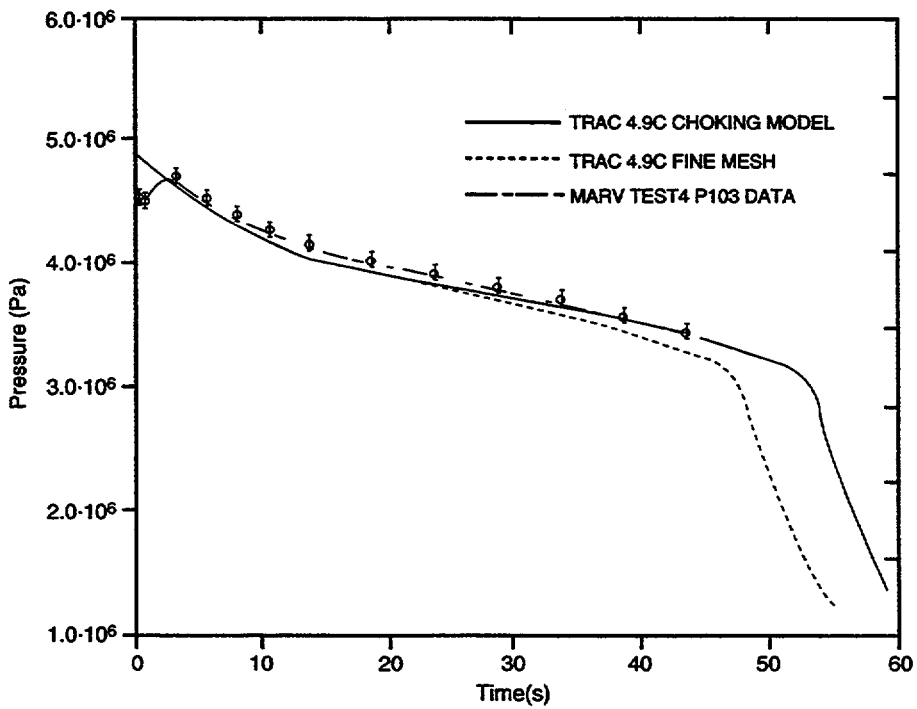


Fig. I-16. Comparison of the system pressure histories for Marviken Test 4.

Figures I-17. and I-18. show the mass flows and pressure histories for Test 24. The agreement between the choking calculation and the results obtained from the fine-mesh case is not as good as for Test 4. This discrepancy is attributed to the predominance of nonequilibrium effects between the phases caused by the short nozzle length. These nonequilibrium effects are not modeled in the MOD2 choking calculation. (The straight sections of the nozzles for Tests 4 and 24, respectively, were 1.5 and 0.166 m long, with L/D ratios of 2.95 and 0.33.)

To investigate the importance of nonequilibrium effects in Test 24, a sensitivity run, with the "frozen" assumption in the characteristic solution (using a seven-equation characteristic model without differential-type mass-transfer terms), will be performed as time permits.

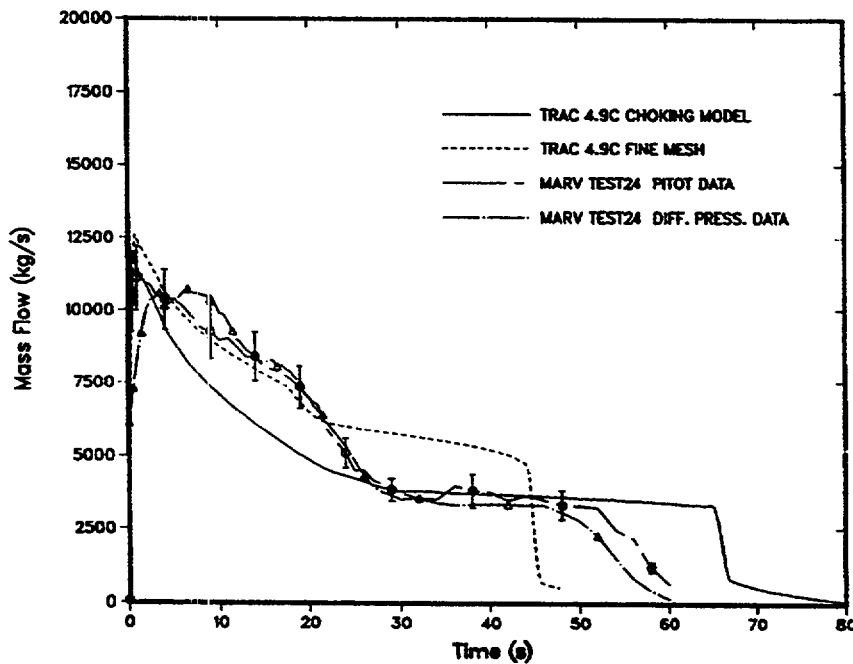


Fig. I-17. Comparison of the nozzle mass flows for Marviken Test 24.

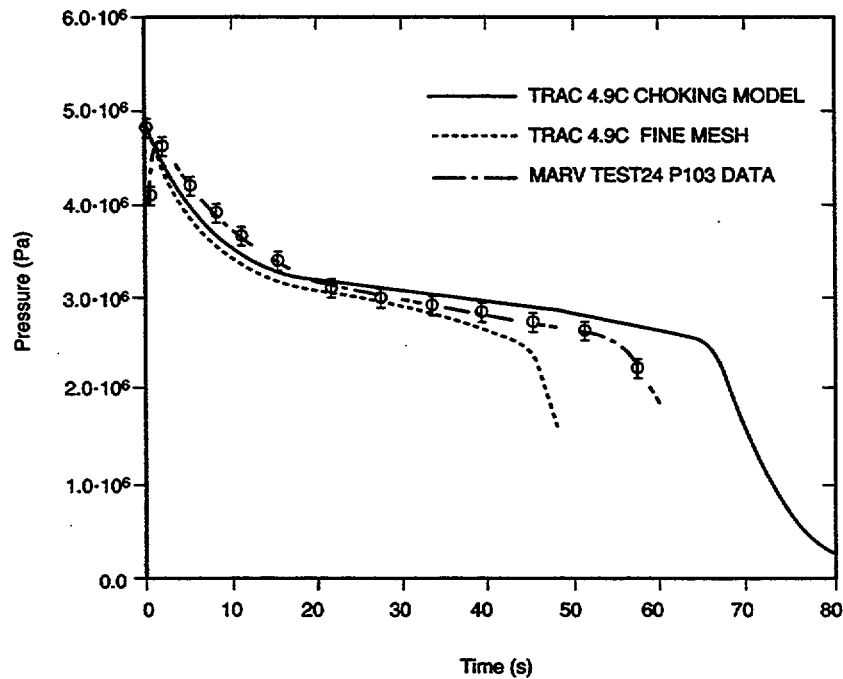


Fig. I-18. Comparison of the system pressure histories for Marviken Test 24.

I.2.6.2.2. Edwards Blowdown Experiment. The Edwards horizontal-pipe blowdown experiment studied depressurization phenomena of initially nonflowing subcooled water. The experimental apparatus consisted of a 4.096-m-long straight steel pipe with a 0.073-m i.d. The apparatus was designed for a maximum 17.24-MPa pressure at temperatures to 616.5 K. The discharge end of the horizontal pipe was sealed with a 0.0127-m-thick glass disk.

The pipe was filled with demineralized water; a hydraulic pump and a control valve regulated the system pressure. The pipe was evacuated by a vacuum pump before it was filled with water. Before the glass disk was ruptured, the pipe was isolated from the supply tank to prevent the discharge of cold water into the pipe during blowdown. Pressure transducers were located at gauge stations GS-1 to GS-7, and a temperature transducer was located at GS-5 (Fig. I-19). Also provided at GS-5 were two aluminum-alloy disk windows for transient void-fraction measurements, which used an x-ray absorption system. The pipe was insulated and heated electrically. The operating procedure required that degassed water completely fill the pipe. The pipe was pressurized cold to ~25% above the initial depressurization 7-MPa test pressure and checked for leaks. Next, the pressure was reduced to 3.45 MPa and heat was applied gradually for ~1.5 h. During the heating of the water, the system pressure was maintained at ~3.45 MPa above the saturation pressure to prevent liquid flashing. The temperature variation along the pipe was limited by adjusting the voltage control for each heater. Initially the system was brought to an approximately uniform 515 K

temperature¹ and 7-MPa pressure. Because the isolating valve between the pipe and storage tank was closed, the glass disk ruptured, and the data were recorded automatically.

The MOD2 model consisted of a zero-velocity FILL component to simulate the closed end of the pipe, two PIPE components coupled in series, and a BREAK component. Near the discharge end of the pipe, the minimum cell lengths were 0.00509 m for the fine-mesh case and 0.17325 m for the choked-flow model. The choking model was applied at the discharge end, which had the minimum cross-sectional area in the system. We had to estimate this area because fragments of glass remained intact during the experiment. The default choked-flow multipliers were used in these calculations.

Figure I-20 compares the measured and calculated pressure histories near the middle of the pipe (GS-4). The choking and the fine-mesh calculations again agree well, with the choking calculational results closer to the data than the fine-mesh results. Although the discharge mass flow was not measured, the good pressure comparison between the calculations and the test data suggests good mass-flow calculations as well.

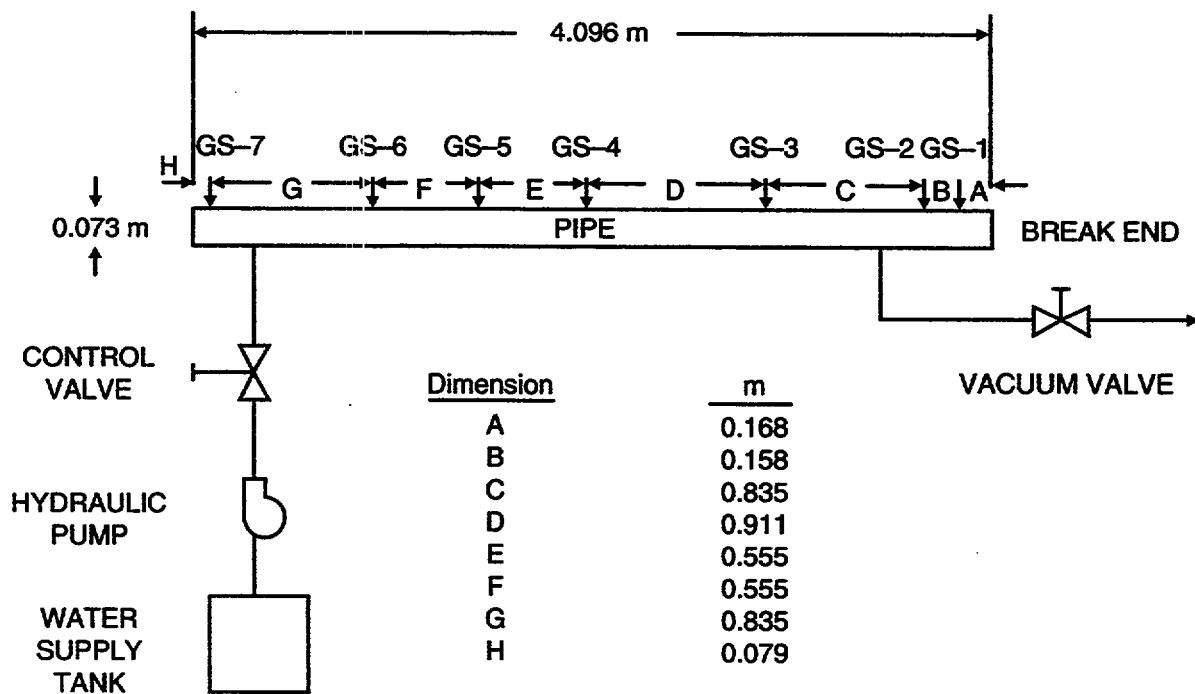


Fig. I-19. The Edwards horizontal-pipe blowdown experiment (adapted from Ref. I-13.).

1. There is some uncertainty in the initial temperature profile. However, we used exactly identical initial conditions in the choking and the fine-mesh calculations to maintain the validity of the comparison between the two calculations.

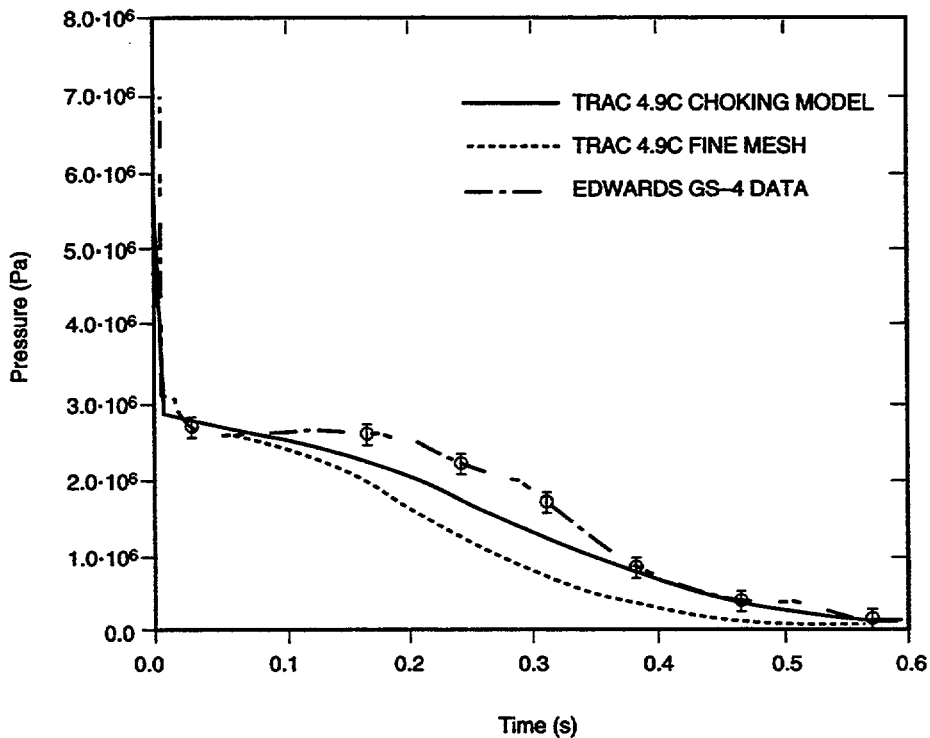


Fig. I-20. Comparison of the system pressure histories for the Edwards blowdown experiment.

I.2.7. Geometry Effects

To account for any geometry effects, the choked-flow model allows the user to input subcooled and two-phase choked-flow multipliers in the INOPTS NAMELIST data. Depending on which choking model is used (either subcooled-liquid, two-phase two-component fluid, or superheated vapor), these multipliers allow the user to adjust the predicted liquid, steam/gas-mixture, or both choking velocities to account for break or nozzle geometry effects. The use of the multipliers is described fully in [Section I.2.4](#).
Scaling Considerations

The choking model in TRAC is applicable to large- and small-scale geometries. The favorable results obtained in the Marviken Test 4 and Test 24 comparisons support the large-scale applicability, while the favorable results obtained in the Edwards blowdown test comparison show the model's ability to predict small-scale choking.

I.2.8. Summary and Conclusions

The two-phase, two-component, choked-flow model in TRAC was developed from first principles with a minimal amount of empiricism. The model assumes that thermal equilibrium exists between the phases in the presence or absence of an inert gas. The eigenvalues for the system of coupled differential equations are obtained

numerically. This generality gives the user the freedom to investigate and incorporate differential equations derived under different assumptions. The model yields results similar to those obtained using a fine mesh for components with smooth area changes. However, the quantitative agreement with the fine-mesh calculations is deficient for Marviken Test 24, which has a short nozzle, because the equilibrium assumption may be improper in that case. The results also compare well with other conventional models (the modified Burnell and the HEM). A good mass-flow comparison between the TRAC two-phase model and the HEM was obtained because the upstream fluid was stagnant, which gives minimal nonhomogeneous effects. However, for other two-phase situations, where the upstream liquid and vapor velocities differ significantly from each other, the nonhomogeneous effects may be very important. Comparisons of the TRAC calculations with the data from the separate-effects Marviken tests and the Edwards blowdown experiment also were favorable.

I.3. Countercurrent Flow Limitation (CCFL)

A special model exists in the code that allows the user to invoke characteristic CCFL correlations at specific locations in the 3D VESSEL component or in 1D vertical components. This capability exists in the axial direction in the 3D VESSEL component.

Countercurrent flow and CCFL can occur at any location in the reactor system. For instance, in the case of a reflux-condensation transient associated with a small-break LOCA, countercurrent flow is predicted to exist in the hot leg and in the entrance to the steam-generator inlet plenum. In the VESSEL, CCFL can occur during blowdown as ECC liquid is attempting to fill the downcomer. During reflood, CCFL can occur at the tie plate, where the upflow of steam prevents or limits the fallback of liquid. This is especially important for those systems that employ upper-plenum ECC injection.

Excluding mass transfer, the accurate prediction of the flow rates is dependent primarily on the interfacial drag between the phases (which is itself dependent on the accurate prediction of the flow regime). In a given flow system, CCFL usually occurs at a flow-area restriction. Typically, without the use of the CCFL model, the code predicts the complete turnaround point (zero liquid delivery), but overpredicts the amount of liquid downflow in the region of countercurrent flow. To improve the prediction in the countercurrent region, we added a special CCFL model to the 3D VESSEL and to vertical 1D components.

I.3.1. CCFL in the 3D VESSEL

We designed the CCFL model primarily for use in the tie-plate region of a PWR. The mechanism for countercurrent flow tie-plate geometry is very complex. For instance, in a single-bundle experiment, it has been observed that downflow can exist at the periphery of the plate, whereas upflow may occur in the center region. On the average over time, this behavior can be described by a CCFL (or flooding) correlation. CCFL correlations typically provide a superficial mass flux of liquid downflow versus a superficial mass flux of gas upflow. The correlations are developed from the integral over time of the amount of liquid accumulation below the plate for a given gas-injection

rate. The correlation therefore provides a 1D empirical model of the time-averaged multidimensional countercurrent-flow behavior. These correlations are geometry dependent. For tie plates, the plate thickness, hole diameter (or slot dimensions), number of holes, as well as the type of hardware above and below the tie plate can affect the CCFL characteristics. Rather than try to develop a new mechanistic CCFL model that could predict these complex behaviors in a variety of geometrical configurations, we decided to make use of the vast amount of correlated data already available. Therefore, the TRAC CCFL model provides the user the option to implement a CCFL correlation for the specific geometry available and to apply it at specific locations in the VESSEL. The input is general so that Wallis (Ref. I-14.), Kutateladze (Ref. I-15.), or Bankoff (Ref. I-16.) scaling can be accommodated.

I.3.2. Basis for the Model

The TRAC CCFL model is designed to provide the user with an alternative method for calculating countercurrent flow in geometrically complex reactor hardware. This model allows the user to input the characteristic flooding curve parameters for a specific geometry applied at a particular location in the vessel. Typically, these parameters have been developed from experimental data for the geometry of interest or for hardware of at least similar dimensions. Bankoff (Ref. I-16.) has shown that the data correlate well with the relationship

$$H_g^{1/2} + M_B H_l^{1/2} = C_B \quad , \quad (I-185)$$

where H_g is the dimensionless gas flux, H_l is the dimensionless liquid delivery, C_B is the abscissa intercept, and M_B is the slope.

This relationship is used in the CCFL model because it allows the user to implement either the Wallis scaling (diameter dependence), Kutateladze scaling (surface-tension dependence), or a combination of the two. This is done by defining as follows a variable-length scale in the determination of the dimensionless flux:

$$H_k = j_k \left(\frac{\rho_k}{g w \Delta \rho} \right)^{1/2} \quad , \quad (I-186)$$

$$w = D^{1-E} L^E \quad , \quad (I-187)$$

and

$$L = \left(\frac{\sigma}{g \Delta \rho} \right)^{1/2} \quad , \quad (I-188)$$

where

- k refers to the phase (gas or liquid),
- j is the superficial velocity,
- D is the diameter of the holes
- g is the gravitational constant,
- σ is the surface tension,
- ρ is the density,
- $\Delta\rho$ is the difference between the phasic densities, and
- E is an interpolation constant between 0 and 1.

Note that for $E = 0$, the correlation reverts to the Wallis scaling, and for $E = 1$, reverts to the Kutateladze scaling. For E between 0 and 1, the user can input the scaling proposed by Bankoff. This scaling can be calculated for tie-plate geometry even if no experimental data are available based on the critical wave number, $k_c = 2\pi / t_p$ (Ref. I-16.), so that

$$E = \tanh(\eta k_c D) \quad , \quad (\text{I-189})$$

where η is the ratio of the area of the holes to the area of the tie plate and t_p is the thickness of the tie plate. Also, Bankoff developed a correlation for C_B based on the Bond number $L^* = n\pi D(g\Delta\rho/\sigma)^{1/2}$, so that

$$C_B = 1.07 + 4.33 \times 10^{-3} L^* \text{ for } L^* \leq 200 \quad (\text{I-190})$$

and

$$C_B = 1.94 \text{ for } L^* > 200 \quad , \quad (\text{I-191})$$

where n is the number of holes.

I.3.3. Input Required

The user supplies the correlation constants M_B , E , and C_B , and the location where the CCFL model is to be applied. Alternatively, the values of C_B and E can be calculated by the code from thermodynamic properties and the input of n , t_p , h , and D . The void fraction in the cell below the interface is used to calculate the vapor flux. The void fraction in the cell above the interface is used to calculate the liquid flux. The surface tension, liquid density, and vapor density in the cell below the interface are used in the CCFL model.

I.3.4. Parametric Range and Scaling Considerations

For the TRAC CCFL model, the user supplies the correlation to be used at a specific location. Thus, the database is dependent on user input because the correlation constants are determined either from experimental data or from estimates based on physical dimensions. If the user provides a correlation that represents data that are similar to the

cell dimensions in geometry and scale, then the code should adequately predict countercurrent flow. Also, CCFL correlations normally scale with pressure because the form of the equations includes the effect of the change in density.

I.4. TEE-Component Offtake Model

The TRAC TEE-component offtake model is designed specifically to handle the case when a small break is made in a large pipe containing horizontal stratified flow (Ref. I-17). One example of a transient that is particularly well-suited for use with the offtake model is the LOCA, in which a small break occurs in one of the large-diameter horizontal pipes of the reactor inlet or outlet legs. During this transient, horizontal stratified flow may occur, and the flow quality discharged at the break will depend on whether the break is above or below the liquid level. To accurately follow the progression of the transient, it is essential that the offtake flow be predicted correctly.

The TRAC TEE-component offtake model predicts the offtake flow quality that exits the break based on conditions in the main pipe in a manner similar to that developed for use in the RELAP5/MOD2 code (Ref. I-18). When the entrance plane to the break is submerged, the offtake flow consists mostly of liquid with possibly an entrained gas component. When the entrance plane is above the liquid level, the offtake flow is mostly gas with possibly an entrained liquid component.

The model is implemented as an option that the user may turn on using the INOPTS namelist data flag IOFFTK. When IOFFTK = 1 (default = 0), the user is required to insert an additional line of input for each TEE component within the TRAC input deck specifying the value of the variable IENTRN. This new Card Number 15 requires IENTRN = 1 to implement the offtake model for a particular TEE. Similarly, no offtake model is implemented for any TEE for which IENTRN = 0. To use the model for its intended purpose, the following input guidelines are suggested.

1. The side tube of the TEE is required to be either top, bottom, or centrally located off the main tube.
2. The angle from the low-numbered side of the main tube to the side tube must be 90°. (Variable COST on Card Number 2 in TEE-component input.)
3. The main-tube-junction cell must be horizontal.

If these three conditions are not met by the input deck TEE geometry, the problem currently terminates in the initialization stage with a fatal error concerning inappropriate offtake geometry.

I.4.1. Basis for the Model

Several studies have been performed to investigate the discharge characteristics of a small break located on a horizontal pipe containing stratified flow. In these studies, the offtake was either top, bottom, or centrally oriented from the main tube as shown in Fig. I-21. The following discussion briefly describes each of these three offtake

geometries and the flow correlations developed by Ref. I-18. More detailed descriptions of the original experimental work may be found in Refs. I-19, through I-22.

In each of the three offtake geometries, a critical height at which gas or liquid entrainment begins, h_b , may be calculated using major-phase conditions at the entrance plane such that

$$h_b = \frac{C_1 W_k^{0.4}}{(g \rho_k \Delta \rho)^{0.2}} \quad , \quad (I-192)$$

where C_1 = a constant determined from data, W_k = major-phase mass-flow rate, g = gravitational constant, ρ_k = major-phase density, and $\Delta \rho = \rho_l - \rho_g$ = phasic density difference. For an upward offtake or for a side-oriented offtake with a liquid level *below* the offtake center, the major phase comprises the gas component. For a downward offtake or for a side-oriented offtake with a liquid level *above* the offtake center, the liquid component constitutes the major phase. The values of the constant C_1 recommended for use by Ref. I-18, are summarized in Table I-3. This formulation for h_b can be derived theoretically for each of the three offtake geometries by considering the force exerted on the liquid particles by the accelerating gas flow for liquid entrainment in upward or side-oriented offtakes and by considering surface instability effects for gas entrainment in downward offtakes (Refs. I-19, I-23, and I-24).

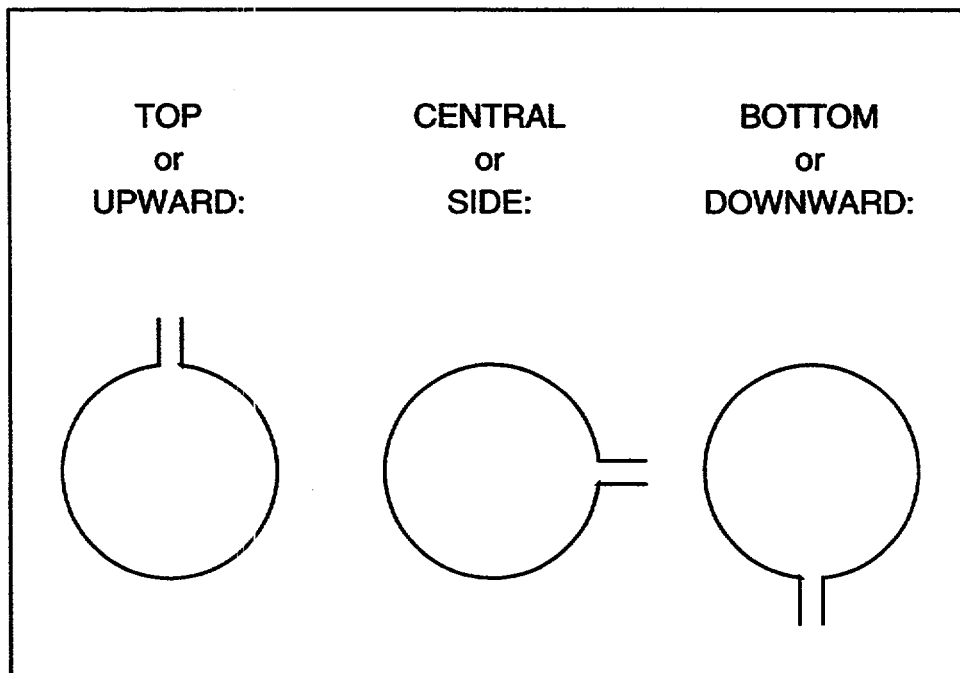


Fig. I-21. Possible offtake geometries.

TABLE I-3.
Critical Height Correlation Constant

Offtake Geometry	Correlation Constant, C_1
Upward	1.67
Downward	1.50
Side (gas entrain.)	0.75
Side (liquid entrain.)	0.69

An actual characteristic height, h , measured as the distance from the offtake entrance plane to the liquid level, may be determined for each of the three offtake geometries as shown in Fig. I-22. The nondimensional height ratio, R , then may be represented as

$$R = \frac{h}{h_b} \quad , \quad (I-193)$$

where h = actual characteristic height (see Fig. I-22.) and h_b = critical height [as defined by Eq. (I-192)].

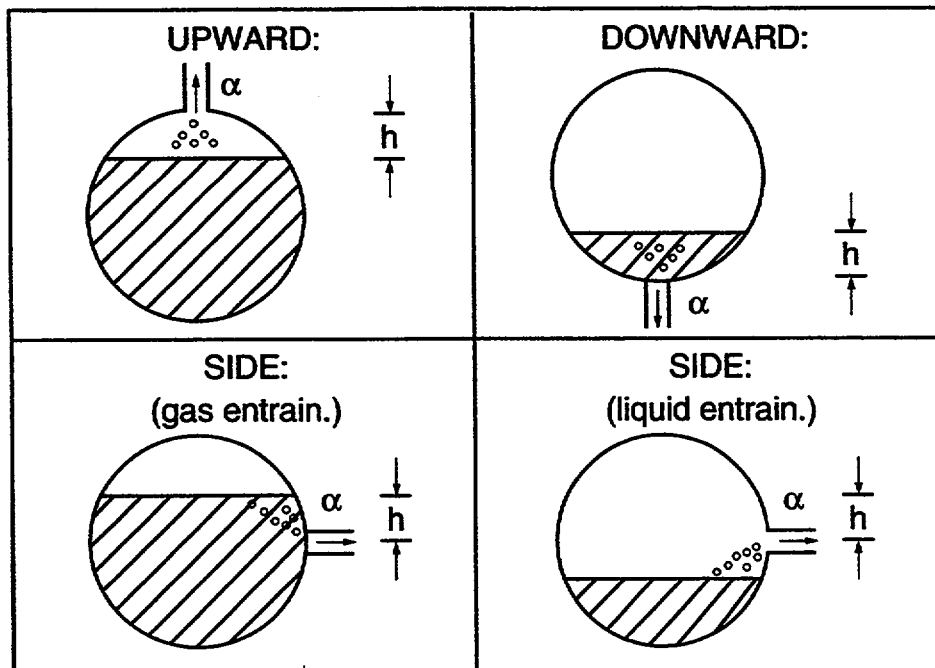


Fig. I-22. Determination of actual characteristic height, h .

Reference I-18 recommends the offtake flow quality, which has been correlated as a function of the nondimensional height ratio, R , be calculated for each of the three offtake geometries as follows.

For an upward offtake,

$$x = R^{3.25(1-R)^2} \quad , \quad (I-194)$$

where R = nondimensional height ratio [as defined by Eq. (I-193)].

For a side-oriented offtake,

$$x = x_o^{(1+C_2R)} \left[1 - 0.5R(1+R)x_o^{(1-R)} \right]^{0.5} \quad , \quad (I-195)$$

where

$$x_o = \frac{1.15}{1 + \sqrt{\frac{\rho_l}{\rho_g}}} \quad , \quad (I-196)$$

R = nondimensional height ratio [as defined by Eq. (I-193)], ρ_l = liquid-phase density at the entrance plane, ρ_g = gas-phase density at the entrance plane, and $C_2 = 1.09$ for gas entrainment or 1.00 for liquid entrainment.

For a downward offtake,

$$x = x_o^{2.5R} \left[1 - 0.5R(1+R)x_o^{(1-R)} \right]^{0.5} \quad , \quad (I-197)$$

where x_o is given by Eq. (I-196), R = nondimensional height ratio [as defined by Eq. (I-193)], ρ_l = liquid-phase density at the entrance plane, and ρ_g = gas-phase density at the entrance plane.

The actual coding for the TRAC offtake model is contained in subroutine OFFTKE and is outlined in Sections I.4.2 and I.4.3.

I.4.2. Assumptions and Preliminary Calculations

The coding for the TEE-component offtake model is contained in subroutine OFFTKE, and the main calculation is described in the next section. However, upon entry into subroutine OFFTKE, several preliminary calculations take place, and these are described here. The offtake void fraction is initialized to be the same as the void fraction of the main-tube-junction cell. In addition, the average flow diameter of the offtake is calculated such that

$$D_{ot} = \sqrt{\frac{4.0A_j}{\pi}} \quad , \quad (I-198)$$

where A_j = offtake flow area at the entrance plane.

Next, several tests are performed to determine whether to continue the calculation. Subroutine OFFTKE is designed to handle only the case of two-phase, co-current flow out of the main tube break. If these conditions are not met, the offtake calculation ends and the logic returns to the calling subroutine. This is also true if horizontal stratified flow does not exist in the main-tube-junction cell (as indicated by the variable WFHF) or if the average diameter of the offtake is greater than or equal to the main-tube-junction cell average diameter.

However, if co-current, horizontal stratified flow out of the main-tube-junction cell does exist, subroutine OFFTKE continues with its preliminary calculations. The liquid level in the main-tube-junction cell is calculated from the void fraction and average diameter in a call to subroutine LEVEL. In addition, an old-time slip ratio at the offtake entrance plane is calculated as the ratio of old-time gas and liquid velocities such that

$$S = \frac{V_g^n}{V_l^n} , \quad (\text{I-199})$$

where v_g^n = old-time, entrance-plane gas velocity and v_l^n = old-time, entrance-plane liquid velocity. This slip is limited to a minimum value of 1.0×10^{-7} . After the preliminary calculations have been performed, the logic splits to handle each of the three possible geometries: upward offtake, side-oriented offtake, or downward offtake.

I.4.3. Model as Coded

The TEE-component offtake model was added into TRAC using subroutine OFFTKE. Based on the offtake geometry and the liquid level conditions in the junction cell of the main tube, subroutine OFFTKE calculates the void fraction that exits out the main tube break. Upon entry into subroutine OFFTKE, several preliminary calculations take place that are detailed in the previous section. Once the preliminary calculations are complete, the logic splits to handle each of the three possible geometries: upward offtake, side-oriented offtake, or downward offtake.

I.4.3.1. Upward Offtake. For the case of the upward offtake, the major-flow component is the gas phase. The actual characteristic height for the upward offtake as shown in Fig. I-22, is approximated as

$$h_{\text{up}} = D_1 - h_1 , \quad (\text{I-200})$$

where D_1 = main-tube-junction cell average diameter and h_1 = main-tube-junction cell liquid depth (as defined by a call to subroutine LEVEL).

The major-phase mass-flow rate at the offtake entrance plane is calculated as

$$W_g = \alpha_{\text{ot}}^n \rho_g^{n+1} A_j V_g^{n+1} , \quad (\text{I-201})$$

where α_{ot}^n = old-time offtake void fraction, ρ_g^{n+1} = new-time donor-cell gas density, A_j = offtake entrance-plane flow area, and v_g^{n+1} = new-time entrance-plane gas velocity.

The critical entrainment height then may be calculated such that

$$h_b = \frac{C_1 W_g^{0.4}}{\left[g \rho_g^{n+1} (\rho_\ell^{n+1} - \rho_g^{n+1}) \right]^{0.2}} \quad (I-202)$$

where $C_1 = 1.67$ for an upward offtake (as defined by Table I-3.), W_g = major-phase (gas) mass-flow rate [as defined by Eq. (I-201)], g = gravitational constant, ρ_g^{n+1} = new-time donor-cell gas density, and ρ_ℓ^{n+1} = new-time donor-cell liquid density. This critical entrainment height is limited to a minimum value of 1.0×10^{-6} .

The offtake flow quality at the entrance plane is then

$$x = R^{3.25(1-R)^2} \quad (I-203)$$

where R = nondimensional height ratio of h_{up} [as defined by Eq. (I-200)] to h_b [as defined by Eq. (I-202)], which is limited such that $0.0 \leq R \leq 1.0$.

Thus, the first prediction of the new-time offtake-model void fraction at the entrance plane is calculated as

$$\alpha_m^{n+1,1} = \frac{x \rho_\ell^{n+1}}{x \rho_\ell^{n+1} + (1-x) \rho_g^{n+1} S} \quad (I-204)$$

where x = offtake entrance-plane flow quality [as defined by Eq. (I-203)], ρ_ℓ^{n+1} = new-time donor-cell liquid density, ρ_g^{n+1} = new-time donor-cell gas density, and S = old-time slip ratio [as defined by Eq. (I-199)]. At this point, this first prediction of the offtake void fraction is sent through several interpolations, averages, and limits to arrive at the final offtake void fraction.

First, if the liquid level in the main-tube-junction cell is above the offtake entrance plane, the offtake void fraction predicted by Eq. (I-204) is modified to ensure that it approaches the value of the void fraction in the main-tube-junction cell as the liquid level reaches the top of the main-tube-junction cell. This interpolation is performed linearly with the main-tube-junction cell liquid depth, h_1 , such that

$$\alpha_m^{n+1,2} = f \alpha_m^{n+1,1} + (1-f) \alpha_1^{n+1} \quad (I-205)$$

where

$$f = \frac{h_1 - D_1}{h_c - D_1} \quad (I-206)$$

h_1 = main-tube-junction cell liquid depth, D_1 = main-tube-junction cell average diameter, h_c = critical main-tube-junction cell liquid depth at which the liquid level just reaches the offtake entrance plane, $\alpha_m^{n+1,1}$ = first offtake void-fraction prediction [as defined by Eq. (I-204)], and α_1^{n+1} = new-time main-tube-junction cell void fraction.

Next, this offtake void-fraction result is weighted using the horizontal stratified-flow weighting factor to ensure that the offtake void fraction tends toward the main-tube-junction cell void fraction as the flow, moves away from a stratified-flow regime such that

$$\alpha_m^{n+1,3} = \text{WFHF} \cdot \alpha_m^{n+1,2} + (1 - \text{WFHF})\alpha_1^{n+1} \quad , \quad (\text{I-207})$$

where WFHF = horizontal-flow weighting factor, $\alpha_m^{n+1,2}$ = second offtake void-fraction prediction [as defined by Eq. (I-205)], and α_1^{n+1} = new-time main-tube-junction cell void fraction.

Finally, the offtake void-fraction prediction is limited to ensure that the volume of liquid entrained does not exceed the volume that exists in the main-tube-junction cell such that

$$\alpha_{\text{ot}}^{n+1} = \max(\alpha_m^{n+1,3}, \alpha_1^{n+1}), \quad (\text{I-208})$$

where $\alpha_m^{n+1,3}$ = third offtake void-fraction prediction [as defined by Eq. (I-207)] and α_1^{n+1} = new-time main-tube-junction cell void fraction. This concludes the calculative sequence for the case of the upward offtake. At this point, the new-time offtake void fraction, α_{ot}^{n+1} , is returned to the calling subroutine.

I.4.3.2. Side-Oriented Offtake. For the case of the side-oriented offtake, the major-flow component may be either the gas phase or the liquid phase. When the liquid level in the main tube is below the offtake center, the gas phase is the major-flow component and liquid entrainment may occur. However, if the liquid level in the main tube is above the offtake center, the liquid phase becomes the major-flow component and gas entrainment may be possible. The following description first details the case of when the gas phase is the major-flow component and liquid entrainment may occur, and then outlines the case when the liquid phase is the major-flow component and gas entrainment may be possible.

For the case of the side-oriented offtake with a gas major-flow component (the case of possible liquid entrainment), the actual characteristic height as shown in Fig. I-22, is approximated as

$$h_{\text{sd}} = h_1 - 0.5D_1 \quad , \quad (\text{I-209})$$

where h_1 = main-tube-junction cell liquid depth (as defined by a call to subroutine LEVEL) and D_1 = main-tube-junction cell average diameter. Notice that for this offtake configuration, h_{sd} is a negative value, which later causes the nondimensional height ratio, R , to also be negative in value.

The major-phase mass-flow rate at the offtake entrance plane is calculated as

$$W_g = \alpha_{ot}^n \rho_g^{n+1} A_j V_g^{n+1} \quad , \quad (I-210)$$

where α_{ot}^n = old-time offtake void fraction, ρ_g^{n+1} = new-time donor-cell gas density, A_j = offtake entrance-plane flow area, and V_g^{n+1} = new-time entrance-plane gas velocity.

The critical entrainment height then may be calculated such that

$$h_b = \frac{C_1 W_g^{0.4}}{\left[g \rho_g^{n+1} (\rho_\ell^{n+1} - \rho_g^{n+1}) \right]^{0.2}} \quad , \quad (I-211)$$

where $C_1 = 0.69$ for a side-oriented offtake with a gas major-flow component (as defined by Table I-3.), W_g = major-phase (gas) mass-flow rate [as defined by Eq. (I-210)], g = gravitational constant, ρ_g^{n+1} = new-time donor-cell gas density, and ρ_ℓ^{n+1} = new-time donor-cell liquid density. This critical entrainment height is limited to be no less than the larger of 1.0×10^{-6} and $0.5 D_{ct}$ [see Eq. (I-198)].

The offtake flow quality at the entrance plane is then

$$x = x_o^{(1+C_2R)} \left[1 - 0.5R(1+R)x_o^{(1-R)} \right]^{0.5} \quad , \quad (I-212)$$

where

$$x_o = \frac{1.15}{1 + \sqrt{\frac{\rho_\ell^{n+1}}{\rho_g^{n+1}}}} \quad , \quad (I-213)$$

R = nondimensional height ratio of h_{sd} [as defined by Eq. (I-209)] to h_b [as defined by Eq. (I-211)], ρ_ℓ^{n+1} = new-time donor-cell liquid density, ρ_g^{n+1} = new-time donor-cell gas density, and $C_2 = 1.00$ for liquid entrainment.

Thus, the first prediction of the new-time offtake-model void fraction at the entrance plane is calculated as

$$\alpha_m^{n+1,1} = \frac{x \rho_\ell^{n+1}}{x \rho_\ell^{n+1} + (1-x) \rho_g^{n+1} S} \quad , \quad (I-214)$$

where x = offtake entrance-plane flow quality [as defined by Eq. (I-212)], ρ_ℓ^{n+1} = new-time donor-cell liquid density, ρ_g^{n+1} = new-time donor-cell gas density, and S = old-time slip ratio [as defined by Eq. (I-199)]. At this point, this first prediction of the offtake void

fraction is sent through the same interpolations, averages, and limits as was the case for the upward offtake to arrive at the final offtake void fraction.

First, if the liquid level in the main-tube-junction cell is between the bottom and the centerline of the offtake entrance, the offtake void fraction predicted by Eq. (I-214) is modified to ensure that it approaches the value of the void fraction in the main-tube-junction cell as the diameter of the offtake approaches the diameter of the main-tube-junction cell. This interpolation is performed linearly with the main-tube-junction cell liquid depth, h_1 such that

$$\alpha_m^{n+1,2} = f\alpha_m^{n+1,1} + (1-f)\alpha_1^{n+1} \quad , \quad (\text{I-215})$$

where

$$f = \frac{h_c}{h_1} \quad , \quad (\text{I-216})$$

and where h_c = critical main-tube-junction cell liquid depth at which the liquid level just reaches the offtake entrance, h_1 = main-tube-junction cell liquid depth, $\alpha_m^{n+1,1}$ = first offtake void-fraction prediction [as defined by Eq. (I-214)], and α_1^{n+1} = new-time main-tube-junction cell void fraction.

Next, this offtake void-fraction result is weighted using the horizontal stratified-flow weighting factor to ensure that the offtake void fraction tends toward the main-tube-junction cell void fraction as the flow moves away from a stratified-flow regime such that

$$\alpha_m^{n+1,3} = \text{WFHF} \cdot \alpha_m^{n+1,2} + (1 - \text{WFHF})\alpha_1^{n+1} \quad , \quad (\text{I-217})$$

where WFHF = horizontal-flow weighting factor, $\alpha_m^{n+1,2}$ = second offtake void-fraction prediction [as defined by Eq. (I-215)], and α_1^{n+1} = new-time main-tube-junction cell void fraction.

Finally, the offtake void-fraction prediction is limited to ensure that the volume of liquid entrained does not exceed the volume that exists in the main-tube-junction cell such that

$$\alpha_{\text{ot}}^{n+1} = \max(\alpha_m^{n+1,3}, \alpha_1^{n+1}) \quad , \quad (\text{I-218})$$

where $\alpha_m^{n+1,3}$ = third offtake void-fraction prediction [as defined by Eq. (I-217)] and α_1^{n+1} = new-time main-tube-junction cell void fraction. This concludes the calculative sequence for the case of the side-oriented offtake with a gas major-flow component. At this point, the new-time offtake void fraction, α_{ot}^{n+1} , is returned to the calling subroutine.

For the case of the side-oriented offtake with a liquid major-flow component (the case of possible gas entrainment), the actual characteristic height as shown in Fig. I-22 is approximated as

$$h_{sd} = h_1 - 0.5D_1 \quad , \quad (I-219)$$

where h_1 = main-tube-junction cell liquid depth (as defined by a call to subroutine LEVEL) and D_1 = main-tube-junction cell average diameter.

The major-phase mass-flow rate at the offtake entrance plane is calculated as

$$W_\ell = (1 - \alpha_{ot}^n) \rho_\ell^{n+1} A_j V_\ell^{n+1} \quad , \quad (I-220)$$

where α_{ot}^n = old-time offtake void fraction, ρ_ℓ^{n+1} = new-time donor-cell liquid density, A_j = offtake entrance-plane flow area, and v_ℓ^{n+1} = new-time entrance-plane liquid velocity.

The critical entrainment height then may be calculated such that

$$h_b = \frac{C_1 W_\ell^{0.4}}{\left[g \rho_\ell^{n+1} (\rho_\ell^{n+1} - \rho_g^{n+1}) \right]^{0.2}} \quad , \quad (I-221)$$

where $C_1 = 0.75$ for a side-oriented offtake with a liquid major-flow component (as defined by Table I-3), W_ℓ = major-phase (liquid) mass-flow rate [as defined by Eq. (I-220)], g = gravitational constant, ρ_ℓ^{n+1} = new-time donor-cell liquid density, and ρ_g^{n+1} = new-time donor-cell gas density. This critical entrainment height is limited to be no less than the larger of 1.0×10^{-6} and $0.5D_{ot}$ [see Eq. (I-198)].

The offtake flow quality at the entrance plane is then

$$x = x_o^{(1+C_2R)} \left[1 - 0.5R(1+R) x_o^{(1-R)} \right]^{0.5} \quad (I-222)$$

for the range

$$0.0 \leq R < 0.9 \quad ,$$

where

$$x_o = \frac{1.15}{1 + \sqrt{\frac{\rho_\ell^{n+1}}{\rho_g^{n+1}}}} \quad , \quad (I-223)$$

R = nondimensional height ratio of h_{sd} [as defined by Eq. (I-219)] to h_b [as defined by Eq. (I-221)], ρ_l^{n+1} = new-time donor-cell liquid density, ρ_g^{n+1} = new-time donor-cell gas density, and $C_2 = 1.09$ for gas entrainment.

In Eq. (I-222), as R approaches 1, x approaches 0 very rapidly. To avoid an exponential approach toward zero, the term $R(1 + R)$ was replaced with a linear function for the range $0.9 \leq R \leq 1.0$, resulting in the following formulation for flow quality:

$$x = -10.0x_0^{(1+C_2R)} [1 - 0.855x_0^{0.1}]^{0.5} (R - 1.0) \quad (\text{I-224})$$

for the range

$$0.9 \leq R \leq 1.0 \quad ,$$

where x_0 is defined by Eq. (I-223), $C_2 = 1.09$ for gas entrainment, and R is again the nondimensional height ratio.

Thus, the first prediction of the new-time offtake-model void fraction at the entrance plane is calculated as

$$\alpha_m^{n+1,1} = \frac{x\rho_l^{n+1}}{x\rho_l^{n+1} + (1-x)\rho_g^{n+1}S} \quad , \quad (\text{I-225})$$

where x = offtake entrance-plane flow quality [as defined by Eq. (I-222) or (I-224)], ρ_l^{n+1} = new-time donor-cell liquid density, ρ_g^{n+1} = new-time donor-cell gas density, and S = old-time slip ratio [as defined by Eq. (I-199)]. At this point, this first prediction of the offtake void fraction is sent through the same type interpolations, averages, and limits as was the case for the upward offtake to arrive at the final offtake void fraction.

First, if the liquid level in the main-tube-junction cell is between the centerline and the top of the offtake entrance, the offtake void fraction predicted by Eq. (I-225) is modified to ensure that it approaches the value of the void fraction in the main-tube-junction cell as the diameter of the offtake approaches the diameter of the main-tube-junction cell. This interpolation is performed linearly with the main-tube-junction cell liquid depth, h_1 such that

$$\alpha_m^{n+1,2} = f\alpha_m^{n+1,1} + (1-f)\alpha_1^{n+1} \quad , \quad (\text{I-226})$$

where

$$f = \frac{D_1 - h_c}{D_1 - h_1} \quad , \quad (\text{I-227})$$

D_1 = main-tube-junction cell average diameter, h_c = critical main-tube-junction cell liquid depth at which the liquid level just reaches the offtake entrance, h_1 = main-tube-junction cell liquid depth, $\alpha_m^{n+1,1}$ = first offtake void-fraction prediction [as defined by Eq. (I-225)], and α_1^{n+1} = new-time main-tube-junction cell void fraction.

Next, this offtake void-fraction result is weighted using the horizontal stratified-flow weighting factor to ensure that the offtake void fraction tends toward the main-tube-junction cell void fraction as the flow moves away from a stratified-flow regime such that

$$\alpha_m^{n+1,3} = \text{WFHF} \cdot \alpha_m^{n+1,2} + (1 - \text{WFHF}) \alpha_1^{n+1} \quad , \quad (\text{I-228})$$

where WFHF = horizontal-flow weighting factor, $\alpha_m^{n+1,2}$ = second offtake void-fraction prediction [as defined by Eq. (I-226)], and α_1^{n+1} = new-time main-tube-junction cell void fraction.

Finally, the offtake void-fraction prediction is limited to ensure that the volume of gas entrained does not exceed the volume that exists in the main-tube-junction cell such that

$$\alpha_{\text{ot}}^{n+1} = \min(\alpha_m^{n+1,3}, \alpha_1^{n+1}) \quad , \quad (\text{I-229})$$

where $\alpha_m^{n+1,3}$ = third offtake void-fraction prediction [as defined by Eq. (I-228)] and α_1^{n+1} = new-time main-tube-junction cell void fraction. This concludes the calculative sequence for the case of the side-oriented offtake with a liquid major-flow component. At this point, the new-time offtake void fraction, α_{ot}^{n+1} , is returned to the calling subroutine.

I.4.3.3. Downward Offtake. For the case of the downward offtake, the major-flow component is the liquid phase. The actual characteristic height for the downward offtake as shown in Fig. I-22 is approximated as

$$h_{\text{dn}} = h_1 \quad , \quad (\text{I-230})$$

where h_1 = main-tube-junction cell liquid depth (as defined by a call to subroutine LEVEL).

The major-phase mass-flow rate at the offtake entrance plane is calculated as

$$W_\ell = (1 - \alpha_{\text{ot}}^n) \rho_\ell^{n+1} A_j V_\ell^{n+1} \quad , \quad (\text{I-231})$$

where α_{ot}^n = old-time offtake void fraction, ρ_ℓ^{n+1} = new-time donor-cell liquid density, A_j = offtake entrance-plane flow area, and v_ℓ^{n+1} = new-time entrance-plane liquid velocity.

The critical entrainment height then may be calculated such that

$$h_b = \frac{C_1 W_\ell^{0.4}}{\left[g \rho_\ell^{n+1} (\rho_\ell^{n+1} - \rho_g^{n+1}) \right]^{0.2}} \quad , \quad (I-232)$$

where $C_1 = 1.50$ for a downward offtake (as defined by Table I-3.), $W_\ell =$ major-phase (liquid) mass-flow rate [as defined by Eq. (I-231)], $g =$ gravitational constant, $\rho_\ell^{n+1} =$ new-time donor-cell liquid density, and $\rho_g^{n+1} =$ new-time donor-cell gas density. This critical entrainment height is limited to a minimum value of 1.0×10^{-6} .

The offtake flow quality at the entrance plane is then

$$x = x_o^{2.5R} \left[1 - 0.5R(1+R)x_o^{(1-R)} \right]^{0.5} \quad (I-233)$$

for the range

$$0.0 \leq R < 0.9 \quad ,$$

where

$$x_o = \frac{1.15}{1 + \sqrt{\frac{\rho_\ell^{n+1}}{\rho_g^{n+1}}}} \quad , \quad (I-234)$$

$R =$ nondimensional height ratio of h_{dn} [as defined by Eq. (I-230)] to h_b [as defined by Eq. (I-232)], $\rho_\ell^{n+1} =$ new-time donor-cell liquid density, and $\rho_g^{n+1} =$ new-time donor-cell gas density.

In Eq. (I-233), as R approaches 1, x approaches 0 very rapidly. To avoid an exponential approach toward zero, the term $R(1+R)$ was replaced with a linear function for the range $0.9 \leq R \leq 1.0$ resulting in the following formulation for flow quality:

$$x = -10.0x_o^{2.5R} \left[1 - 0.855x_o^{0.1} \right]^{0.5} (R - 1.0) \quad (I-235)$$

for the range

$$0.9 \leq R \leq 1.0 \quad ,$$

where x_o is defined by Eq. (I-232) and R is again the nondimensional height ratio.

Thus, the first prediction of the new-time model void fraction at the entrance plane is calculated as

$$\alpha_m^{n+1,1} = \frac{x\rho_l^{n+1}}{x\rho_l^{n+1} + (1-x)\rho_g^{n+1}S} \quad (I-236)$$

where x = offtake entrance-plane flow quality [as defined by Eq. (I-233) or (I-235)], ρ_l^{n+1} = new-time donor-cell liquid density, ρ_g^{n+1} = new-time donor-cell gas density, and S = old-time slip ratio [as defined by Eq. (I-199)]. At this point, this first prediction of the offtake void fraction is sent through the same type of interpolations, averages, and limits as was the case for both the upward and side-oriented offtakes to arrive at the final offtake void fraction.

First, if the liquid level in the main-tube-junction cell is below the offtake entrance plane, the offtake void fraction predicted by Eq. (I-236) is modified to ensure that it approaches the value of the void fraction in the main-tube-junction cell as the liquid level reaches the bottom of the main-tube-junction cell. This interpolation is performed linearly with the main-tube-junction cell liquid depth, h_1 such that

$$\alpha_m^{n+1,2} = f\alpha_m^{n+1,1} + (1-f)\alpha_1^{n+1} \quad (I-237)$$

where

$$f = \frac{h_1}{h_c} \quad (I-238)$$

h_1 = main-tube-junction cell liquid depth, h_c = critical main-tube-junction cell liquid depth at which the liquid level reaches the offtake entrance plane, $\alpha_m^{n+1,1}$ = first offtake void-fraction prediction [as defined by Eq. (I-236)], and α_1^{n+1} = new-time main-tube-junction cell void fraction.

Next, this offtake void-fraction result is weighted using the horizontal stratified-flow weighting factor to ensure that the offtake void fraction tends toward the main-tube-junction cell void fraction as the flow moves from a stratified-flow regime such that

$$\alpha_m^{n+1,3} = \text{WFHF} \cdot \alpha_m^{n+1,2} + (1 - \text{WFHF})\alpha_1^{n+1} \quad (I-239)$$

where WFHF = horizontal-flow weighting factor, $\alpha_m^{n+1,2}$ = second offtake void-fraction prediction [as defined by Eq. (I-237)], and α_1^{n+1} = new-time main-tube-junction cell void fraction.

Finally, the offtake void-fraction prediction is limited to ensure that the volume of gas entrained does not exceed the volume that exists in the main-tube-junction cell such that

$$\alpha_{ot}^{n+1} = \min(\alpha_m^{n+1,3}, \alpha_1^{n+1}) \quad (I-240)$$

where $\alpha_m^{n+1,3}$ = third offtake void-fraction prediction [as defined by Eq. (I-239)] and α_1^{n+1} = new-time main-tube-junction cell void fraction. This concludes the calculative sequence for the case of the downward offtake. At this point, the new-time, offtake void fraction, α_{ot}^{n+1} , is returned to the calling subroutine.

I.4.4. Weighting, Magnitude Limits, Rate Limits, and Averaging

For each of the three possible offtake geometries, the solution procedure within subroutine OFFTKE follows the same logic. Once a first prediction of the offtake void fraction is determined, three adjustments are performed to obtain the final offtake void-fraction prediction. The first adjustment is an interpolation based on liquid level to ensure that the predicted offtake void fraction tends toward certain limits as the liquid level approaches certain limits. For example, as the liquid level approaches the top of the main-tube-junction cell, the offtake void fraction for an upward offtake is expected to approach the value of the main-tube-junction cell void fraction. The second adjustment is a simple weighting using the horizontal weighting factor to ensure that the offtake void fraction tends toward the main-tube-junction cell void fraction as the flow moves away from a stratified-flow regime. The final adjustment is a limit to ensure that the volume of liquid or gas being entrained does not exceed the volume of the entrained component that exists in the main-tube-junction cell. Each of these adjustments is performed once the first prediction of the offtake void fraction is obtained, regardless of the offtake geometry. The specific algebraic equations used for these interpolations, weightings, or limits is detailed in the appropriate subsection of the model description in Section I.4.3.

I.4.5. Assessment

Two very simple test cases have been developed to demonstrate how the offtake option works. These tests were chosen because of the existence of "obvious answers" and are meant only to demonstrate that the technique used to implement the offtake model into the TRAC two-step numerics functions properly. Three additional, more detailed assessment calculations are planned for the offtake model using the data from Tests SB-CL-12, SB-CL-15, and SB-CL-16 of the ROSA-IV facility performed by the Japan Atomic Energy Research Institute (JAERI). The three JAERI tests, which involve a 0.5% cold-leg break oriented in each of the three offtake positions, will enable a more rigorous assessment of the offtake model to be performed.

The geometry for both of the two simple analytical problems consists of a horizontal TEE component with a specified mass-flow rate at one end of the main tube and a large drain tank at the other end. The side tube of the TEE forms the offtake and is upwardly oriented for one test and downwardly oriented for the other. A schematic of the input used to model the test case with the upward offtake is shown in Fig. I-23. The mass-flow rate at the inlet FILL was chosen such that a low-velocity, horizontal stratified flow would exist in the TEE main tube. In addition, a mass-flow rate was selected that could maintain a relatively high void fraction in the main-tube-junction cell for the upward offtake and a relatively low void fraction for the downward offtake test case. Pressure boundaries were selected to encourage flow from the main tube into the offtake.

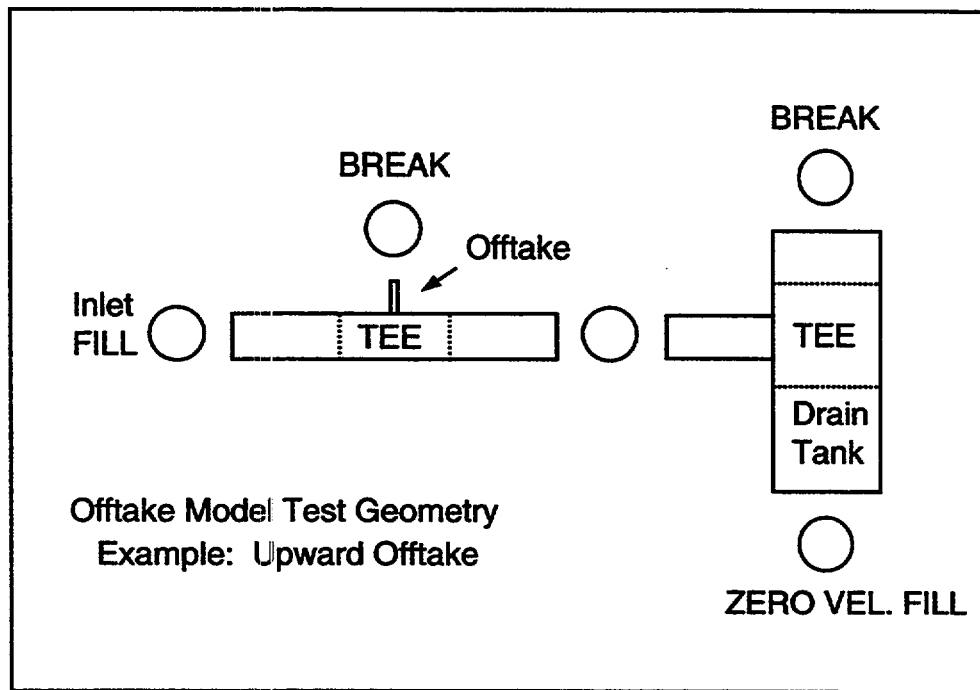


Fig. I-23. Sample input deck schematic.

The results of the upward offtake test case are shown in Figs. I-24. and I-25. Figure I-24. shows the void fractions that TRAC calculates to exist in the main-tube-junction cell and in the offtake cell when the offtake option is not selected. Notice that although the main-tube-junction cell has only a small volume fraction of liquid in it, TRAC shows that the same volume fraction is convected up out of the offtake. For the low-velocity, horizontal stratified flow of this test case, this prediction is not physical. Figure I-25. shows the same example with the offtake option selected. As expected, only the gas exits the offtake for this particular case of low-velocity, high-void, horizontal stratified flow in the main tube.

Similar results are achieved in the downward offtake test case. For low-velocity, low-void flow in the main tube, one expects that only liquid will drain out of a downward offtake. Figure I-26. shows that TRAC does not calculate this result when the offtake option is off. Instead, the flow exiting the offtake is calculated incorrectly as being of nearly the same void fraction as that which exists in the main-tube-junction cell. However, Fig. I-27. shows that if the offtake model is turned on, TRAC is able to predict correctly that only liquid is draining out of the offtake as expected physically.

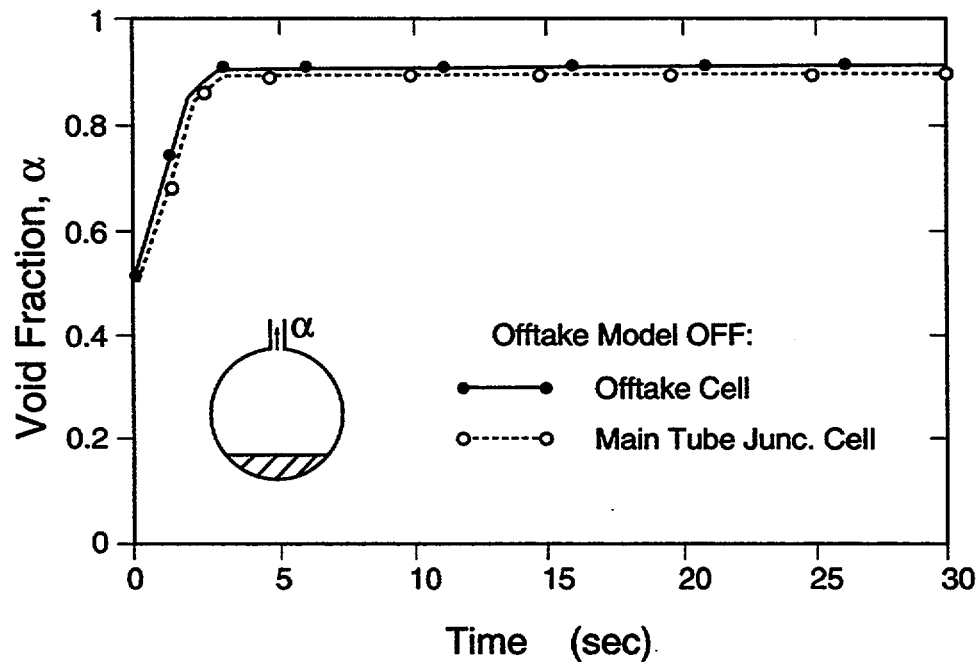


Fig. I-24. Upward offtake test results—no offtake model implemented.

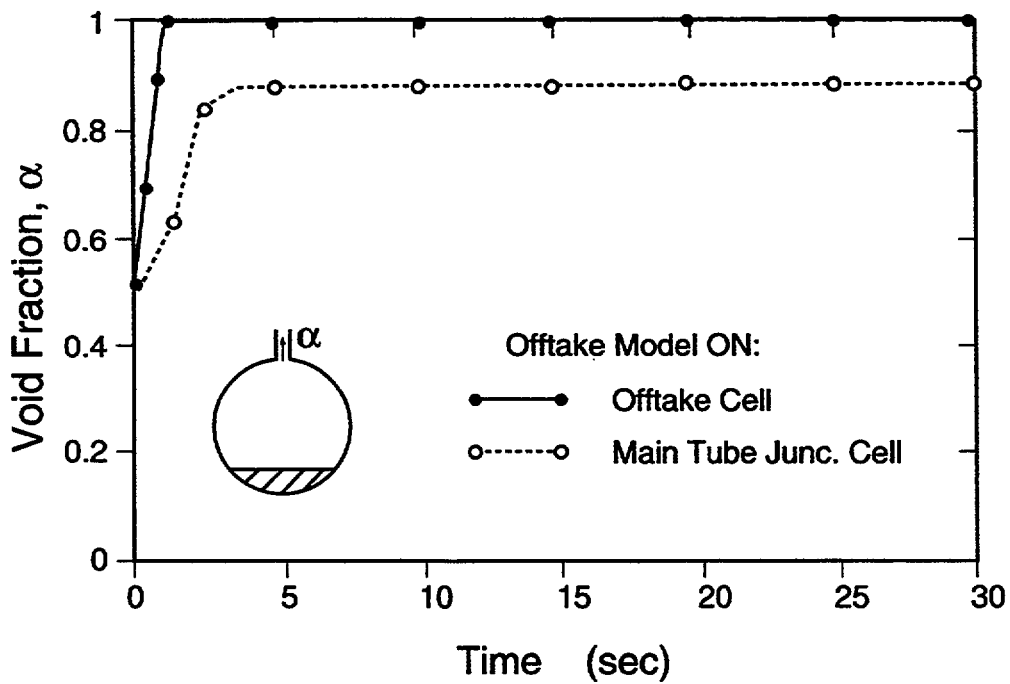


Fig. I-25. Upward offtake test results—offtake model option implemented.

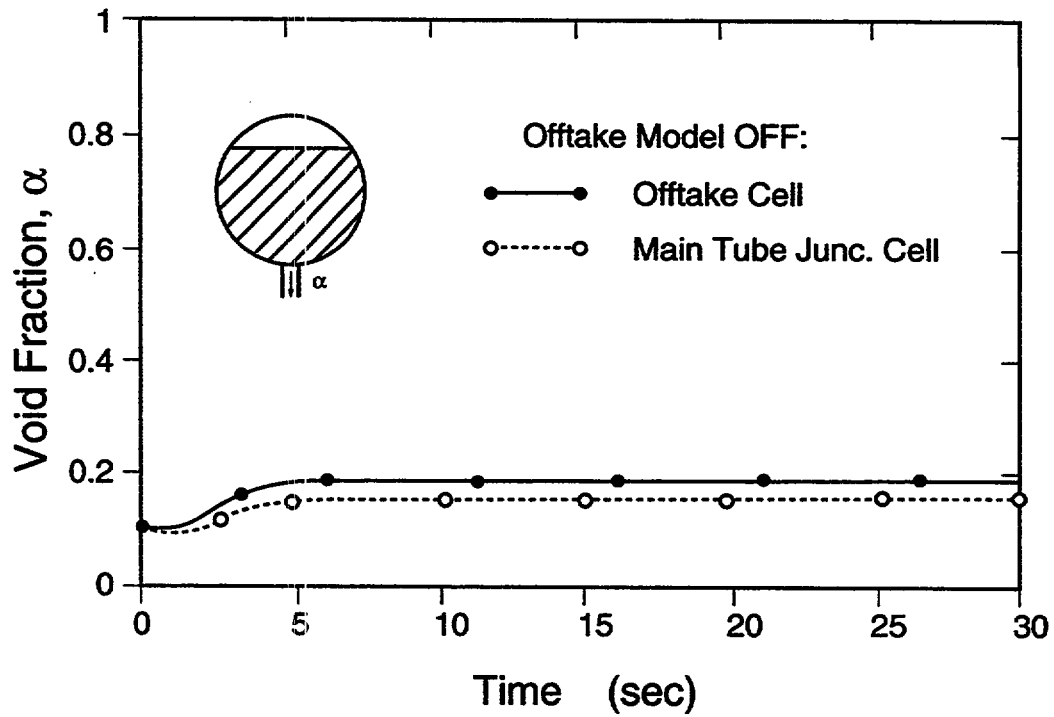


Fig. I-26. Downward offtake test results—no offtake model implemented.

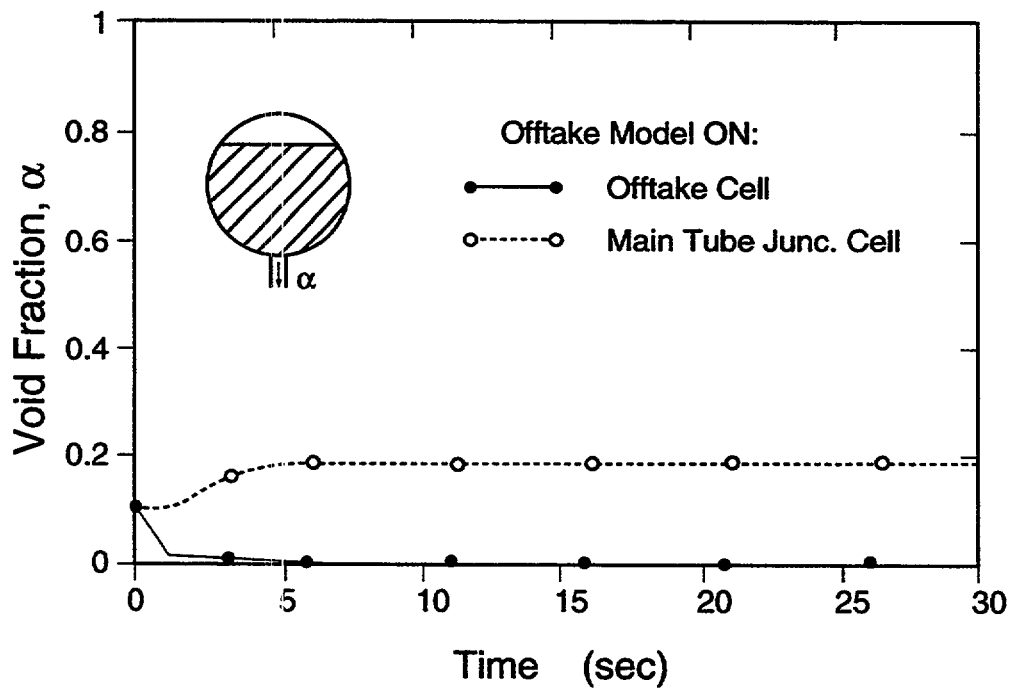


Fig. I-27. Downward offtake test results—offtake model option implemented.

I.4.6. Geometry Effects

In an effort to ensure that the offtake model be used only as was originally intended, the following specific offtake geometry restrictions apply.

1. The side tube of the TEE is required to be either top, bottom, or centrally located off the main tube.
2. The angle from the low-numbered side of the main tube to the side tube must be 90°. (Variable COST on Card Number 2 in TEE-component input.)
3. The main-tube-junction cell must be horizontal.

If these three conditions are not met by the input deck TEE geometry, the problem currently terminates in the initialization stage with a fatal error concerning inappropriate offtake geometry.

I.4.7. Scaling Considerations

The offtake model is most applicable when the transient being modeled includes a small break in a large pipe containing horizontal stratified flow. As the offtake diameter becomes larger and begins to approach the diameter of the main tube, the offtake model will predict an offtake void fraction that tends toward the main-tube-junction cell void fraction.

I.4.8. Summary and Conclusions

The TRAC TEE-component offtake model predicts the flow discharged from a small break in a large pipe containing horizontal stratified flow. The current model is able to accommodate three different offtake geometries: upward offtake, side-oriented offtake, and downward offtake. Using subroutine OFFTKE, TRAC calculates a prediction for the offtake void fraction from flow correlations for the particular offtake geometry being modeled. This first prediction of the offtake void fraction is then sent through one interpolation based on the liquid level, one weighting based on the degree of horizontal stratification, and one limit based on the maximum allowable entrainment volume to arrive at the final offtake void fraction. The technique used to implement the offtake model into the two-step numerics scheme is demonstrated to work effectively by two simple thought problems.

I.5. Reactor-Vessel Vent Valve

Reactor-vessel vent valves, such as those used in Babcock and Wilcox (B & W) plants, are modeled in the VESSEL component with a specific set of input data. The number of vent valves, the vent-valve locations in terms of axial level and azimuthal/radial cell number, and the vent-valve maximum flow areas (i.e., for the valves when fully open) are specified in the VESSEL input. The user then specifies the vent-valve behavior by providing a valve's flow-loss resistance as a function of pressure drop across the valve. As the pressure drop decreases across the vent valve, the valve opening decreases. The flow reduction caused by the partial opening is accounted for by increasing the resistance factor as the vent valve closes. During each time step in a calculation, the

vent-valve resistance factor is determined from the pressure drop across the valve and is used in the radial momentum equations. The inertial effects of the vent valve opening and closing are not modeled in TRAC.

Vent-valve characteristics may be found in B & W final safety analysis reports (FSARs) as well as in other B & W documents. Figure I-28 shows a typical vent-valve resistance curve. The resistance approaches infinity as the pressure drop decreases and the valve openings decrease to zero. The resistance factor at very low pressure drops may be set to a very high value to obtain near-zero flow, or it may be adjusted to reflect an overall leakage flow between the downcomer and upper plenum, such as the leakage flow that occurs between the hot-leg nozzle flange and downcomer.

In the MOD2 code (and TRAC-M), the vent-valve resistance factor input must be of the form

$$\frac{K}{\Delta r_i + \Delta r_{i+1}} = \frac{CFZ}{HD_r} = \text{internally stored value used ,} \quad (I-241)$$

where K = K -factor loss coefficient, CFZ = default additive-loss coefficient used in MOD2 (and TRAC-M), and Δr_i and Δr_{i+1} = the radial lengths of the fluid cells that connect to the vent valve.

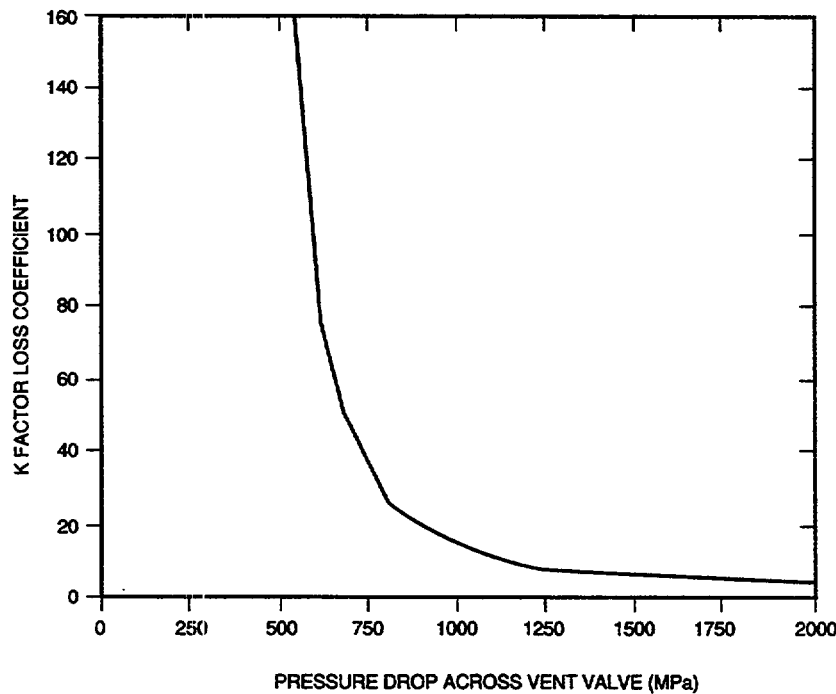


Fig. I-28. Vent-valve resistance vs. pressure drop across the valve.

The namelist variable IKFAC, which is used to change the additive-loss coefficient, does not affect the vent-valve resistance factors because the IKFAC conversion is done before the transient calculations are performed. The vent-valve resistance factors are determined during the transient calculation.

The user specifies the cells that have vent valves by giving the axial level, cell number, and total area of vent valves for each cell with vent valves in the outer radial surface. The user also specifies the vent-valve resistance factor, which can be done in two different ways. In the first option, the user specifies the following for each cell with vent valves: (1) the maximum pressure drop when the vent valve is closed, DPCVN; (2) the minimum pressure drop when the valve is open, DPOVN; (3) the vent-valve resistance when the valve is closed to model leakage, FRCVN (in the input form specified above); and (4) the vent-valve resistance when the valve is open, FRCVO. The code uses FRCVN when the pressure drop is less than DPCVN, uses FRCVO when the pressure drop is greater than DPOVN, and interpolates for pressure drops between DPCVN and DPOVN.

This input option allows only two points to describe the vent-valve resistance characteristics and may not be accurate enough. Therefore, a second option is provided that allows the input of a multiple-point resistance table, which specifies flow-loss resistance versus pressure drop.

For the first option, the two pressure drops and the two resistances are provided for each vent valve. In the second option, a single table is input for all vent valves.

Only one vent valve may be specified in a given VESSEL cell [at the cell's outer radial (or x) face]. Actual vent valves at a given cell interface may have to be lumped together.

REFERENCES

- I-1. B. S. Massey, *Mechanics of Fluids* (D. Van Nostrand Co., New York, 1968).
- I-2. R. C. Blevins, *Applied Fluid Dynamics Handbook* (Krieger Publishing Co., Malabar, Florida, 1992).
- I-3. I. E. Idel'Chik, *Handbook of Hydraulic Resistance, Coefficients of Local Resistance and of Friction*, National Technical Information Service Report NTIS AEC-TR-6630 (1960).
- I-4. F. M. White, *Fluid Mechanics* (McGraw-Hill Book Co., New York, 1979).
- I-5. D. R. Liles, J. W. Spore, T. D. Knight, R. A. Nelson, M. W. Cappiello, K. O. Pasamehmetohlu, et al., "TRAC-PF1/MOD1, Correlations and Models," Los Alamos National Laboratory report LA-11208-MS (NUREG/CR-5069) (December 1988).

- I-6. "RELAP5/MOD1 Code Manual, Volume 1: System Models and Numerical Methods," Idaho National Engineering Laboratory report EGG-2070 Draft, Rev. 1 (NUREG/CR-1826) (March 1981).
- I-7. O. C. Jones, Jr., "Flashing Inception in Flowing Liquids," Brookhaven National Laboratory report (BNL-NUREG-51221) (1980).
- I-8. V. H. Ransom and J. A. Trapp, "The RELAP5 Choked Flow Model and Application to a Large Scale Flow Test," in *ANS/ASME/NRC International Topical Meeting on Nuclear Reactor Thermal-Hydraulics* (Saratoga Springs, New York, 1980), pp. 799-819.
- I-9. Douglas G. Hall and Linda S. Czapyry, "Tables of Homogeneous Equilibrium Critical Flow Parameters for Water in SI Units," Idaho National Engineering Laboratory report EGG-2056 (September 1980).
- I-10. "RELAP4/MOD6, A Computer Program for Transient Thermal-Hydraulic Analysis of Nuclear Reactors and Related Systems," Idaho National Engineering Laboratory report CDAP-TR-003 (January 1978).
- I-11. "Results from Test 4, The Marviken Full-Scale Critical Flow Tests," Joint Reactor Safety Experiments in the Marviken Full Power Station, Sweden, Marviken report MXC204 (September 1979).
- I-12. "Results from Test 24, The Marviken Full-Scale Critical Flow Tests," Joint Reactor Safety Experiments in the Marviken Power Station, Sweden, Marviken report MXC224 (September 1979).
- I-13. A. R. Edwards and T. P. O'Brien, "Studies of Phenomena Connected with the Depressurization of Water Reactors," *J. Br. Nucl. Energy Soc.* 9, 125-135 (1970).
- I-14. G. B. Wallis, *One Dimensional Two-Phase Flow* (McGraw-Hill, Inc., New York, 1969).
- I-15. S. S. Kutateladze, *Izv. Akad. Nauk SSSR, Otd. Tekhn. Nauk* 8, 529 (1951).
- I-16. S. G. Bankoff, R. S. Tankin, M. C. Yuen, and C. L. Hsieh, "Countercurrent Flow of Air/Water and Steam/Water Through a Horizontal Perforated Plate," *Int. J. Heat Mass Transfer* 24 (8), 1381-1395 (1981).
- I-17. L. A. Crotzer, "TRAC-PF1/MOD2 TEE Component Offtake Model: A Completion Report," Los Alamos National Laboratory report LA-UR-91-4052 (November 1991).
- I-18. K. H. Ardron and W. M. Bryce, "Assessment of Horizontal Stratification Entrainment Model in RELAP5/MOD2," United Kingdom Atomic Energy Authority, AEE Winfrith draft report AEEW-R 2345 (April 1988).

- I-19. C. Smoglie, "Two Phase Flow Through Small Break Branches in a Horizontal Pipe with Stratified Flow," Kernforschungszentrum Karlsruhe report KfK 3861 (December 1984).
- I-20. V. E. Schrock, S. T. Revankar, R. Mannheimer, and C. H. Wang, "Small Break Critical Discharge—The Roles of Vapor and Liquid Entrainment in a Stratified Two-Phase Region Upstream of the Break," Lawrence Berkeley Laboratory report LBL-22024 (NUREG/CR-4761) (December 1986).
- I-21. T. Maciaszek and A. Menponteil, "Experimental Study on Phase Separation in a Tee Junction for Steam-Water Stratified Inlet Flow," European Two-Phase Flow Group Meeting, Munich, Germany, June 10-13, 1986.
- I-22. J. L. Anderson and R. L. Benedetti, "Critical Flow Through Small Pipe Breaks," Electric Power Research Institute report EPRI NP-4532 (May 1986).
- I-23. D. R. L. Harleman, R. L. Morgan, and R. A. Purple, "Selective Withdrawal from a Vertically Stratified Fluid," International Association for Hydraulic Research, 8th Congress, Montreal, Canada, August 24-29, 1959.
- I-24. B. T. Lubin and G. S. Springer, "The Formation of a Dip on the Surface of a Liquid Draining from a Tank," *J. Fluid Mech.* **29**, 385-390 (1976).